Thermoelectric skutterudites: why and how high zT can be achieved

Thesis by

Yinglu Tang

In Partial Fulfillment of the Requirements for the degree
of
Doctor of Philosophy

CALIFORNIA INSTITUTE OF TECHNOLOGY
Pasadena, California

2016
(Defended Dec 11, 2015)

ACKNOWLEDGEMENTS

The path to a PhD degree is not easy and many times in the moments that I feel lost and weak, I would practice writing this part of my thesis, as a way of encouraging myself to continue. It is silly, but helpful. Now finally, here I am.

I would like to thank Jesus Christ for being my savior. I got to know him in my fourth year and ever since I have been blessed by his unconditional love. I am grateful that he lifts me up through every hardship and difficulty.

I would like to thank my parents, for their love and support over the past 27 years and many years to come. I apologize for my constant absence from their lives due to the path I have chosen, and thank them for accepting all without complaint. The completion of this work would be impossible without their support. I hope I can make a better living for them in the future.

I would like to thank my advisor Prof. Jeff Snyder. Through the past 5 years, Jeff has been a great mentor to me. He not only gives me research freedom but also ignites my passion and curiosity with his abundant knowledge and sharp research insights, not to mention all those enlightening discussions whenever I encounter problems in my research. I owe him endless thanks for his patience to help me strengthen my confidence throughout the course as well. He knows my potential better than I do myself and I will be grateful forever for his guidance in both research and life.

I thank Prof. Sinn-wen Chen and his group at National Tsinghua University for their generous help about phase diagram studies. I learnt a lot from our productive communications (skype, in person, email). I thank Prof. Lidong Chen as well as his group at SICCAS in China for valuable scientific discussions about skutterudites. Former postdocs of the group (Teruyuki, Shiho and Aaron) and my labmates (Nick, Heng and Alex) helped me with instruments when I first started as a graduate student, for which I appreciate greatly their patience. I am grateful to Yuting Qiu and Zach Gibbs for our successful collaborations. Thanks to Yulong Li for transport property measurements, Luis

Agapito, Guodon Li, and Lily Xi for DFT calculations and Riley Hanus for APT measurements in this work. Dr. Chi Ma at Caltech helped me a lot with microscopy. My student Estelle Sanz was a gift to my first mentor experience. Her intelligence, diligence as well as passion for life inspired me a lot during her four-month stay at Caltech. Prof. Yanzhong Pei at Tongji University, Prof. Tiejun Zhu at Zhejiang University, Prof. Eric Toberer at Colorado School of Mines, and Prof. Holger Kleinke at University of Waterloo offered me incisive suggestions regarding carrier path. I thank DOE-Gentherm and National Science Council of Taiwan for supporting my research.

My lab mates are great for building a supportive, relaxing yet productive working environment. It was a pleasure to work with all of them during the past 5 years. Special thanks to Nick, Alex and Alex, Heng and Jie, Tristan and Alice, Hyun-sik and Ok-young, and Saneyuki and Stephen for their constant encouragement. Life will never be the same without you guys around.

All my friends along the way, including Yulia, Amanda, Ho-cheng, Chu Hao, Juying, Sijia, Vanessa, Hanhui, Haiyang, Ning Xin, Chenguang, Liu Fan, Siying, Yan Qu, Cindy, Megan, Audrey, Jian Li, Zhichang Liu, Yu Zhang, Min Zhang, Betty, Huijian Li, Qiao Liang, and many more not listed here, I thank you all for being there for me when needed you.

ABSTRACT

Thermoelectric materials have been widely studied over the past few decades due to their ability to convert waste heat into useful electricity. Among various thermoelectric materials, skutterudite distinguishes itself in both space and terrestrial applications with its excellent thermoelectric performance, robust mechanical properties, and thermal stability. The thermoelectric excellence of skutterudites is mostly attributed to the low thermal conductivity due to the addition of filler atoms (R) into the void (one per primitive cell Co_4Sb_{12}). Essential though this is to high *zT*, the importance of the intrinsic electronic structure in skutterudites is often understated or ignored completely. In this thesis, by combining experimental and computational studies, the electronic origin of high thermoelectric performance of $CoSb_3$-based skutterudites is investigated. The high *zT* was shown to be a direct result of the high valley degeneracy inherent to $CoSb_3$, which is further enhanced by band convergence at high temperatures. This successfully explains why the optimum doping carrier concentration in *n*-$CoSb_3$ skutterudites is independent on the type of fillers. With the electronic origin of high thermoelectric performance clarified, the thesis moves on to elaborate how to achieve high *zT* in skutterudite with the aid of phase diagram study. By mapping out the phase regions near the skutterudite phase on the isothermal section of the R-Co-Sb ternary phase diagram, the solubility region of the $CoSb_3$ skutterudite phase can be determined along with the solubility limit of R, both of which are often determined in stable compositions resulting in a synthesis window. The temperature dependence of the filler solubility is also demonstrated experimentally. This overturns the general understanding that the filler solubility is a single value only dependent on the filler type. The temperature dependence of stable compositions enables easy carrier concentration tuning which allows the optimization of thermoelectric performance. High *zT* values are achieved in single In, Yb, Ce-$CoSb_3$ skutterudites. The methodology applied here are not confined to *n*-$CoSb_3$, but can be generalized to any other ternary systems.

PUBLISHED CONTENT AND CONTRIBUTIONS

Yinglu Tang, Zachary M. Gibbs, Luis Agapito, Guodong Li, Hyun-Sik Kim, Marco Buongiorno-Nardelli, Stefano Curtarolo, G. Jeffrey Snyder, " Convergence of the Multivalley Bands as the Electronic Origin of High Thermoelectric Performance in $CoSb_3$ Skutterudites" ***Nature Materials*** *14, 1223-1228 (2015)* DOI: 10.1038/NMAT4430

Y.T. participated in the conception of the work, performed sample synthesis, structural characterization and thermoelectric transport property measurements, confirmed Kane band model effective mass relation and participated in band modelling and writing up the manuscript.

Chapter 3 is readapted and reproduced with permission from the copyright holder, Nature Publishing Group.

Yinglu Tang, Riley Hanus, Sinn-wen Chen, G. Jeffrey Snyder, "Solubility Design Leading to High *zT* in Low-Cost Ce-$CoSb_3$ Skutterudites" ***Nature Communications*** 6, 7584(1-7) (2015) DOI: 10.1038/ncomms8584

Y.T. contributed to design the study and write the manuscript. Y.T. contributed to sample synthesis, structure characterization and property measurements.

Section 5.5 is readapted and reproduced with permission from the copyright holder, Nature Publishing Group.

Yinglu Tang, Sinn-wen Chen, G. Jeffrey Snyder, "Temperature Dependent Solubility of Yb in Yb-$CoSb_3$ Skutterudite and its Effect on Preparation, Optimization and Lifetime of Thermoelectrics" ***Journal of Materiomics*** 1, 75-84 (2015) DOI:10.1016/j.jmat.2015.03.008

Y.T. contributed to design the study and write the manuscript. Y.T. contributed to sample synthesis, structure characterization and property measurements.

Sections 5.2, 5.4 and 5.6 are readapted and reproduced with permission from the copyright holder, The Chinese Ceramic Society. Production and hosting by Elsevier B.V.

Yinglu Tang, Yuting Qiu, Lili Xi, Xun Shi, Wenqing Zhang, Lidong Chen, Ssu-Ming Tseng, Sinn-wen Chen and G. Jeffrey Snyder "Phase Diagram of In-Co-Sb System and Thermoelectric Properties of In-containing Skutterudites" ***Energy and Environmental Science*** 7, 812-819 (2014) DOI: 10.1039/C3EE43240H

Y.T. contributed to design the study and write the manuscript. Y.T. contributed to sample synthesis, structure characterization and property measurements.

Section 5.3 is readapted and reproduced with permission from the copyright holder, Royal Society of Chemistry.

Yuting Qiu, Lili Xi, Pengfei Qiu, James R. Salvador, Jung Y. Cho, Jihui Yang, Xun Shi, Wenqing Zhang, Lidong Chen, Yuan-chun Chen, Sinn-wen Chen, **Yinglu Tang**, and G. Jeffrey Snyder "Charge-Compensated Compound Defects in Ga-containing Thermoelectric Skutterudites" ***Advanced Functional Materials*** 23, 3194-3203 (2013) DOI: 10.1002/adfm.201202571

Y.T. contributed to data analysis and writing of the manuscript.

Section 5.3 is readapted and reproduced with permission from the copyright holder, Wiley-VCH Verlag GmbH & Co. KGaA.

TABLE OF CONTENTS

LIST OF FIGURES

LIST OF TABLES

LIST OF SYMBOLS AND NOTATIONS

S or α: Seebeck coefficient (thermopower)

Π: Peltier coefficient

K: Thompson coefficient

σ: electrical conductivity

κ: thermal conductivity

κ_e: electronic contribution to thermal conductivity

κ_l: lattice contribution to thermal conductivity

κ_b: bipolar contribution to thermal conductivity

L: Lorentz number

zT: thermoelectric figure of merit

η_{max}: maximum thermoelectric efficiency

D: mass diffusion coefficient

l_D: diffusion length

t_D: diffusion time

N_V: number of valley degeneracy

E_g: energy band gap

ΔE: energy offset

e: electron charge

k_B: Boltzmann constant

$\hbar$: reduced Planck constant

r: scattering parameter

n: carrier concentration

r_H: Hall factor

R_H: Hall coefficient

μ_H: Hall mobility

n_H: Hall carrier concentration

μ_D: drift mobility

m_S^*: density of states effective mass obtained from Seebeck measurements using the single parabolic band (SPB) model (referred to as the Seebeck mass)

m_0^*: band-edge effective mass

m_P^*:energy-dependent effective mass derived from the electron momentum

m_C^*: conductivity mass

λ: correction factor in Mott relation for Seebeck in kane band model

B: quality factor

E_{def}: deformation potential

C_l: elastic constant in longitudinal direction

Ω: atomic volume

Θ: Debye temperature

w_D: Debye frequency

v_s: speed of sound

V_g: group velocity

w_0: resonant frequency

τ_r: resonant scattering relaxation time

Γ: scattering parameter for point defect scattering

τ_{PD}: point defect scattering relaxation time

τ_{ep}: electron-phonon scattering relaxation time

v_e: velocity of electron

λ_e: mean free path of electron

d: mass density

τ_B: boundary scattering relaxation time

τ_U: Umklapp scattering relaxation time

K, G: bulk and shear modulus respectively

ε_F: Fermi level

q: charge state of the point defect

E_V: valence band maximum

e_c : number of available valence electrons of the cation element

b_c : number of cation-cation two-electron bonds and nonbonding lone pair electrons.

b_a : number of anion-anion two-electron bonds

η: reduced electrochemical potential

$\mathcal{E}$: electron energy

μ: chemical potential

Φ: electrostatic potential

E: electric field

H: magnetic field

j: electrical current density

$f(k, r)$: electron distribution function of momentum k and position r

TE: thermoelectric

PGEC: phonon glass electron crystal

FFL: filling fraction limit

SPB: single parabolic band

SKB: single kane band

SEM: scanning electron microscopy

XRD: X-ray diffraction

EPMA: electron probe microprobe

EDS: energy dispersive spectroscopy

WDS: wavelength dispersive spectroscopy

APT: atomic probe topographic

HP: hot pressing

BM: ball milling

MMS: melt-melt-spinning

DRIFTS: diffuse reflectance infrared fourier transform spectroscopy

PAW: projector augmented wave

VASP: Vienna ab initio simulation package

PBE: Perdew-Burke-Ernzerhof

GGA: generalized gradient approximation

DFT: density functional theory

DOS: density of states

JDOS: joint density of states

CB_2: secondary conduction band

ADP: atomic displacement parameter

PDOS: partial density of phonon states

NIS: nuclear inelastic spectroscopy

INS: inelastic neutron scattering

EXAFS: extended X-ray fine absorption measurements

CCCD: charge-compensated compound depects

BTE: Boltzmann transport equation

Chapter 1

Introduction

1.1 Thermoelectric (TE) materials

Thermoelectricity was discovered and developed in Western Europe by academic scientists in the 100 years between 1820 and 1920 [1]. The thermoelectric effect is the direct conversion of temperature differences to electric voltage and vice versa. By the 1950s, generator efficiencies had reached 5% and cooling from ambient to below 0°C was demonstrated. Many thought thermoelectric would soon replace conventional heat engines and refrigeration. However, by the end of the 1960s the pace of progress had stagnated and many research programs were dismantled. Since 1970, the need for reliable, remote power sources enabled niche applications for thermoelectric materials such as space exploration missions (Voyager, Curiosity etc.) even while conventional processes are more efficient. Interest in thermoelectricity renewed in the 1990s with the influx of new ideas such as nano-scale engineered structures. The global need for alternative sources of energy has revived interest in commercial applications and in developing inexpensive and environmentally benign thermoelectric materials.[1]

There are three separately identified thermoelectric effects: the Seebeck effect, the Peltier effect, and the Thompson effect. Seebeck effect can be observed when electric voltage is produced between a pair of dissimilar materials with their junction subjected to a different temperature. Seebeck effect is illustrated in Figure 1.1.

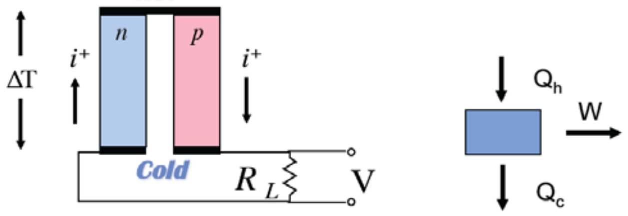

Figure 1.1 Illustration of Seebeck effect. An open circuit voltage V is generated in the presence of a temperature difference ΔT in a pair of n- and p- thermoelectric materials. Thermal energy Q_h can then be partly converted to work W.

The ratio between the voltage and the temperature difference is called Seebeck coefficient S, which is also called thermopower α. As shown in Eq. 1.1, ΔV denotes the voltage difference whereas ΔT denotes the temperature difference across the material. The minus sign is added such that for *p*-type material, the Seebeck coefficient is positive; while for *n*-type material, the Seebeck coefficient is negative.

$$S = -\frac{\Delta V}{\Delta T} = \frac{E}{\nabla T} \qquad \text{(Eq. 1.1)}$$

Peltier effect refers to the presence of heating or cooling at the junction between a pair of dissimilar materials when electric current is passed through. Peltier effect is illustrated in Figure 1.2.

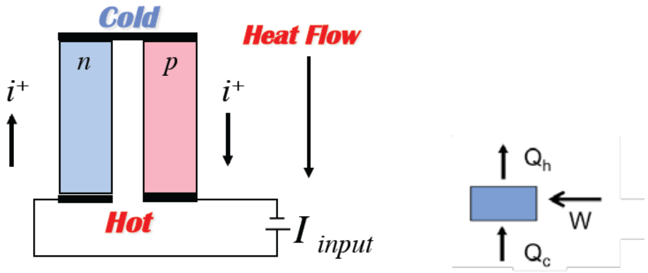

Figure 1.2 Illustration of Peltier effect. The temperature difference across a pair of *n*- and *p*-thermoelectric materials is generated in the presence of an electric current i^+. The "Hot" side is attached to a heat sink so that it remains at ambient temperature, while the "Cold" side goes below room temperature. Electrical work W is consumed to move thermal energy Q from the cold side to the hot side.

The ratio between the heat absorption/creation rate ($\dot{Q}$) and the electric current (I) is called the Peltier coefficient Π, as shown in Eq. 1.2.

$$\Pi = \frac{\dot{Q}}{I} \qquad \text{(Eq. 1.2)}$$

While the Seebeck coefficient represents the entropy carried per unit charge, the Peltier coefficient represents heat carried per unit charge. These two coefficients are interrelated by thermodynamics. For time-reversal symmetric materials, Peltier coefficient is simply the Seebeck coefficient times the absolute temperature (known as the second Kelvin relationship shown in Eq. 1.3).

$$\Pi = ST \qquad \text{(Eq. 1.3)}$$

Thompson effect can be observed in a single material with both electric current and temperature gradient applied. The heat absorption/creation rate is proportional to both the electric current and the temperature gradient. The proportionality constant is called Thompson coefficient (*K*), which relates to both the Seebeck coefficient and the temperature dependence of Peltier coefficient, as shown in Eq.1.4. This equation is also called the first Kelvin relationship. By substituting Eq. 1.3 into Eq. 1.4, we get the simple form relating all three coefficients, as shown in Eq. 1.5.

$$K = \frac{d\Pi}{dT} - S \qquad \text{(Eq. 1.4)}$$

$$K = T\frac{dS}{dT} \qquad \text{(Eq. 1.5)}$$

The Thomson coefficient is unique among the three main thermoelectric coefficients because it is the only one directly measurable for individual materials. The Peltier and Seebeck coefficients can only be easily determined for pairs of materials.

Thermoelectric effects enable thermoelectric materials in many applications such as power generation and refrigeration. The thermoelectric performance of materials is characterized by the dimensionless figure of merit, *zT*.

$$zT = \frac{S^2\sigma T}{\kappa} = \frac{S^2\sigma T}{\kappa_e + \kappa_l} \qquad \text{(Eq. 1.6)}$$

where *S* is the Seebeck coefficient, σ is the electrical conductivity, *T* is the absolute temperature, and κ is the total thermal conductivity. There is no theoretical upper limit in *zT* [2], and as *zT* approaches infinity, the thermoelectric efficiency η_{max} approaches the Carnot limit ($\frac{T_H - T_C}{T_H}$) (Eq. 1.7).

$$\eta_{max} = \frac{T_H - T_C}{T_H}\frac{1+\sqrt{zT}-1}{1+\sqrt{zT}+\frac{T_C}{T_H}} \qquad \text{(Eq. 1.7)}$$

For thermoelectric materials to be competitive in efficiency compared to traditional energy converters such as internal combustion engines or vapor-compression refrigerators, *zT* > 3 (about 20-30% efficiency with $\frac{T_H}{T_C} \geq 2$) is required.[3] However, *zT* > 2 is rarely achieved in bulk thermoelectric materials. Good thermoelectric materials should possess large Seebeck coefficient (large voltage difference), high electrical conductivity (to minimize Joule heating due to electrical resistance), and low thermal conductivity (to minimize heat loss). Due to the inter-correlating nature among these variables (i.e., high electrical conductivity would also lead to high electronic thermal conductivity, large Seebeck coefficient also happens at the band edge which leads to small electrical conductivity), increasing *zT* is still a major challenge in the field of thermoelectrics. The optimum carrier concentration range for thermoelectric performance is in the heavily doped semiconductor regime, e.g., 10^{19}~10^{21} cm^{-3}, as shown in Figure 1.3 [4].

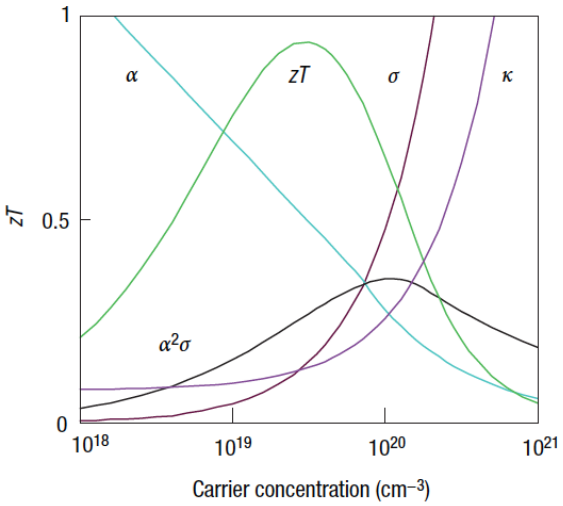

Figure 1.3 Optimizing *zT* through carrier concentration tuning. Maximizing the efficiency (*zT*) of a thermoelectric involves a compromise of thermal conductivity (κ; plotted on the *y* axis from 0 to a top value of 10 Wm^{-1}K^{-1}) and Seebeck coefficient (α; 0 to 500 μVK^{-1}) with electrical conductivity (σ; 0 to 5,000 Ω^{-1}cm^{-1}).[4]

1.2 Skutterudites

Among various state-of-the-art thermoelectric materials, skutterudite is a promising candidate for mid-temperature range (400℃ - 600℃) applications with excellent thermoelectric properties, good mechanical properties, and thermal stability. Skutterudite was named after Skutterud, a small mining town in Norway, where a $CoAs_3$-based mineral was discovered in 1845. Compounds with the structure identical to $CoAs_3$ have since become known as Skutterudites. Binary skutterudites have the general formula MX_3, where M stands for one of the group 9 transition metals Co, Ir, or Rh, and X represents P, As, or Sb. Binary skutterudites form with all 9 possible combinations of the M and X elements and crystalize in the body-centered-cubic structure in the space group (#204) of

$Im\bar{3}$. The unit cell M_8X_{24} contains 32 atoms in eight MX_3 blocks, as shown in Figure 1.4a. There are three different atomic positions: Co sites (8c), Sb sites (24g), and void sites (2a).

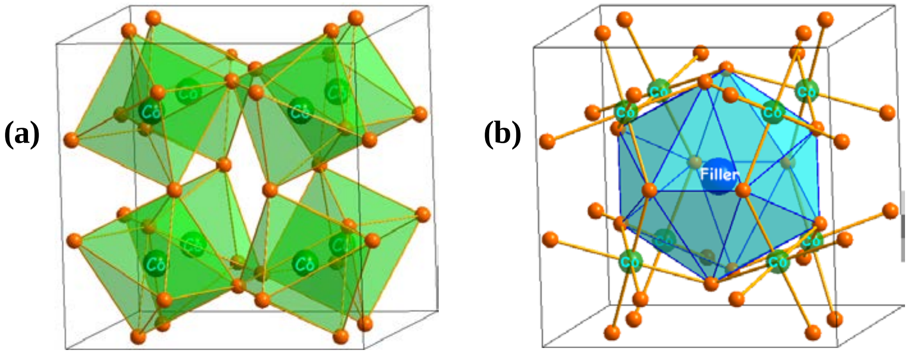

Figure 1.4 Crystal structure of (a) unfilled $CoSb_3$ and (b) filled $CoSb_3$ in a unit cell.

Study of binary skutterudites for thermoelectric purposes started in the 1950s, and soon it was realized that even though they have high electrical conductivity (10^4 Sm^{-1}) and large Seebeck coefficient (hundreds of μVK^{-1}), their high thermal conductivity ($10Wm^{-1}K^{-1}$) limits their application as thermoelectric materials[5-7]. In the 1970s, it was discovered[8] that skutterudites have one void (with radius r = 1.89Å)[9] per primitive cell ($R_xM_4X_{12}$, $0 < x < 1$), which allows foreign atoms R to actively fill the structure. These weakly bound atoms can "rattle" around their equilibrium positions. The addition of fillers not only largely decreases the lattice thermal conductivity but also could contribute to *n*-type doping. This makes skutterudite a perfect example of the phonon glass electron crystal (PGEC) concept, proposed by Slack in 1994 [10]. Since then, the search for filler type and multiple filling in filled skutteurdites has been a major research trend. Up to date the choice of fillers has been among alkali elements (Na[11], K[12]), alkali earth elements (Ba[13], Ca[14], Sr[15]), group 13 elements (Ga[16], In[17]), and rare earth elements (La[18], Ce[19,20], Nd[21], Eu[22], Yb[23,24]) etc. In *n*-type $CoSb_3$-based skutterudites, the highest zT achieved is 1.3 and 1.9 for single and multiple filling respectively at 850K [11,17,20,23,25]. In *p*-type skutteurdites, the highest zT reported is around 1.3 at 850K, significantly lower compared to its *n*-type counterpart [26,27].

1.3 Summary of research

My research focuses on *n*-type $CoSb_3$-based skutterudites. In Chapter 2, a detailed description of experimental methods is provided. Chapter 3 and 4 answer the question of why high zT can be achieved in *n*-type $CoSb_3$-based skutterudites, regardless of the various filler types. High zT in skutterudites is often attributed to the addition of the filler atoms and subsequent reduction in thermal conductivity due to alloying disorder and the complex phonon modes of the filler atom[28-30]. Although low thermal conductivity is essential to high *zT*, the importance of the intrinsic electronic structure in skutterudites is often understated or ignored completely, especially given that the optimum doping carrier concentration is independent on the filler type. In Chapter 3, the electronic origin of high thermoelectric performance in *n*-type $CoSb_3$-based skutterudites is discussed based on experimental and computational results, which is the convergence of a secondary multi-valley conduction band to the primary conduction band at high temperatures. In Chapter 4, the role of fillers in decreasing lattice thermal conductivity is discussed, including resonant scattering, avoided crossing mechanism, point defect scattering, umklapp scattering, and electron-phonon scattering.

The maximum thermoelectric performance of a material depends on the charge carrier concentration, which is often controlled by the solubility limit of fillers; therefore the study of the solubility limit of fillers is essential. There has been a lot of debate concerning the solubility limit of various fillers such as Ga, In, Yb, and Ce, etc. When a foreign atom R is added to the $CoSb_3$ system, a phase diagram study of these ternary R-Co-Sb systems is necessary in determining the solubility limit. However this was rarely performed previously, and instead the solubility limit (or filling fraction limit when the filler R only goes to the void position) was mostly considered to be a single value only dependent on the filler type. The necessity and methodology of integrating phase diagram study in skutterudites is elaborated in Chapter 5 to clarify the previous solubility debates with examples of Ga-Co-Sb, In-Co-Sb, Yb-Co-Sb, and Ce-Co-Sb systems. The existence of solubility direction as well as the dependence of the solubility limit on the phase region and annealing temperature should refresh previous understanding in the skutterudite community. These knowledge serves as guidance in reliable precise doping control, which alleviates the influence of synthesis uncertainty on thermoelectric performance and could potentially benefit large-scale commercialization of high *zT* skutterudites.

In Chapter 6, the defect study of intrinsic $CoSb_3$ is discussed combining bonding chemistry, binary phase diagram study, and experimental results from carrier concentration characterization. In Chapter 7, the phase diagram study of quaternary Ce-Co-Fe-Sb system is discussed which sheds light on optimizing *p*-type $(Co,Fe)Sb_3$-based skutterudites. In Chapter 8, the possibility of nano-structured precipitation driven by temperature dependent filler solubility was demonstrated with experimental results. Lastly, possible future work is discussed in Chapter 9.

Appendix A gives a detailed derivation from Boltzmann transport equation to thermoelectric properties with a single parabolic band (SPB) approximation. Appendix B gives the equations for TE properties with a SPB model and acoustic phonon scattering, which is the most common electron scattering mechanism for skutteurdites above 300K. Appendix C gives the equations for TE properties with a SPB model in both non-degenerate and degenerate limits. Appendix D gives the equations to calculate thermoelectric properties with a multi-band model. Appendix E compares the Mott relation derived from both single parabolic band model and kane band model and explains why linear band does not benefit thermoelectric performance.

Chapter 2

Experimental methods

2.1 Summary

Synthesis of single-phase homogeneous skutterudites is a non-trivial task due to the complexity of the equilibrium phase diagram of binary Co-Sb system. As can be seen from the Co-Sb phase diagram in Figure 2.1, when the temperature cools down, CoSb (γ-phase, metal) forms congruently first from a melt with nominal composition $CoSb_3$, then $CoSb_2$ (δ-phase, semiconductor) and $CoSb_3$ (ε-phase, semiconductor) form peritectically at 936℃ and 874℃, respectively. The skutterudite phase $CoSb_3$ is formed in a peritectic reaction from a solid $CoSb_2$ phase and a liquid at 874℃. Because of the slow kinetics, this reaction can hardly be completed during a quenching process. Figure 2.2 shows the Scanning Electron Microscopy (SEM) photo of a melt-quenched sample with nominal composition $CoSb_{3.}$ As shown in the photo, the $CoSb_2$ phase forms around the CoSb phase whereas the $CoSb_3$ skutterudite phase is barely formed after melting and quenching. The remaining Sb phase confirms the incomplete peritectic reaction of $CoSb_3$ formation. In order to get a single-phase homogeneous skutterudite phase, long time annealing (usually a week) after melting and quenching is thus needed.

Besides the traditional melt-annealing method, solid-state reaction such as mechanical alloying (ball milling)[31,32] is also widely used. The ball milling process can greatly reduce the grain size and consequently the diffusion length.

$$t_D = \frac{l_D^2}{D} \qquad \text{(Eq. 2.1)}$$

where D is the mass diffusion coefficient. From equation 2.1 we can see that by reducing the diffusion length l_D, the diffusion time t_D required could be greatly reduced due to its square dependence on the diffusion length. Thus subsequent annealing time could be largely shortened after ball milling. The same principle works for the melt-spinning method[33]. In a melt-spinning method, by ejecting the molten charge onto a cold rotating drum of copper, an ultra-fast solidification of the melt happens which yields materials with a very fine grain structure.

These methods (melt-annealing method, mechanical alloying or ball milling[31,32], melt-spinning method[33], high pressure assisted synthesis[34], etc.) all result in polycrystalline skutterudites. Single crystalline skutterudites are also synthesized and studied by many researchers (gradient freeze technique[5,6], flux-assisted growth[35], chemical vapor deposition[36], etc.). Readers can refer to the referenced papers and the review paper by Prof Ctirad Uher for more details[37].

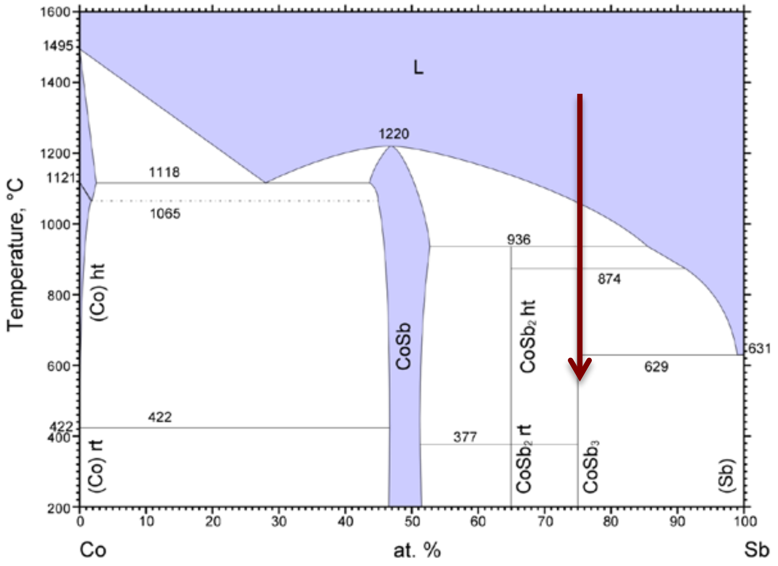

© ASM International 2006. Diagram No. 979952

Figure. 2.1 The Co-Sb (Cobalt-Antimony) phase diagram[38].

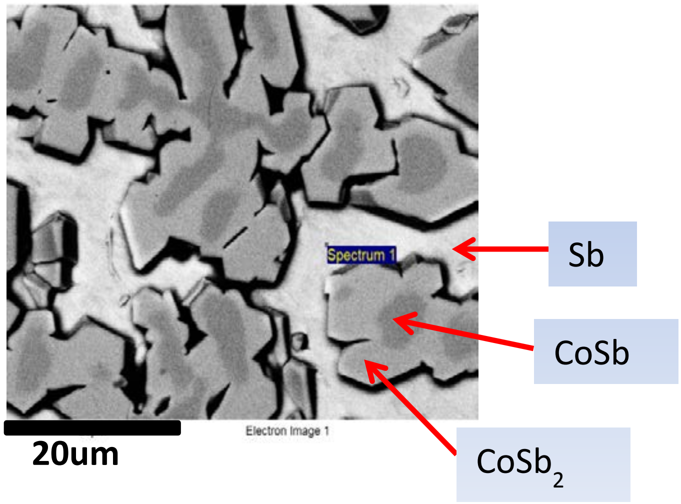

Figure 2.2 Scanning Electron Microprobe (SEM) photo of a melt-quenched sample with nominal composition $CoSb_3$.

The choice of synthesis method depends on the goal of research. For electronic band structure study such as Shubnikov-de Haas effect measurement or a detailed study of the crystal structure of a material by techniques such as Bragg diffraction, single crystalline skutterudite is preferred. However, for thermoelectric property investigation, polycrystalline skutterudite is sufficient due to its cubic structure and isotropy nature resulting from various crystalline orientations. Among polycrystalline skutterudite synthesis methods, ball milling and melt-spinning can largely reduce grain size, thus decreasing the lattice thermal conductivity. However, these processes risk throwing the nominal composition off the desired $CoSb_3$ stoichiometry due to possible contaminants (such as Fe, oxygen) and sublimation of volatile Sb, which leads to easy formation of secondary phases. To determine precisely the solubility region of skutterudites such that pure skutterudites can be synthesized for thermoelectric investigation, we adopt the melt-annealing method in this study in order to avoid external compositional perturbations and get thermodynamically stable materials. Samples after melting and quenching are annealed at a specific temperature below the peritectic temperature for one week to ensure thermodynamic homogeneity. Phase analysis is performed on an annealed and quenched ingot to avoid possible compositional drift due to any post-annealing process.

2.2 Synthesis procedures

There are two types of samples in this study. One is related to determination of isothermal sections of either ternary systems (Yb-Co-Sb, In-Co-Sb, etc.) or quaternary systems (Ce-Co-Fe-Sb). Nominal compositions of these samples were chosen based on a preliminary phase diagram study with the knowledge of related binary or ternary phase diagrams, which can be quite different from the skutterudite stoichiometry (Co: Sb = 1: 3). The other type of samples is related to an *n*-type doping study. Samples with skutterudite stoichiometry (nominal compositions $Yb_xCo_4Sb_{12.012}$, with x ranging from 0.0025 to 0.3) were synthesized with 0.1at% excess of Sb added to compensate for possible Sb evaporation.

High-purity elements (Co, Fe (99.95%, slug), Sb (99.9999%, shot), and Ce (99.9%, rod), Yb (99.9%, ingot) etc.) purchased from Alfa Aesar were used as raw materials. The samples were sealed in carbon-coated fused silica tubes under vacuum. The silica tubes were heated slowly up to 923K in 4 hours, held at 923K for 2 hours, then heated up to 1373K in 6 hours, held at this temperature for 12 hours, and then quenched in water to room temperature. The 2-hour saturation at

923K was performed such that Sb (with melting temperature 904K) in liquid form will promote mass diffusion and reaction.

Samples were then annealed at temperatures ranging from 773K to 1123K for 7 days. After annealing samples were quenched in water to room temperature again. The resulting ingots were taken out of the ampoule and taken to X-ray diffraction (XRD) and SEM, Electron Probe Microanalysis (EPMA) for phase identification and chemical composition determination. Note that the amount of fillers in annealed and quenched samples is “frozen” from high temperature annealing and thus could be indicative of their corresponding high temperature solubility. Ingots were then hand ground into fine powders and consolidated by rapid hot pressing (HP) at 973K for 1h under a pressure of about 60MPa, yielding fully dense bulk samples[39]. High density (> 95% of the theoretical density of $CoSb_3$) was achieved in all hot pressed samples. Hot pressed samples were sealed in fused tubes under vacuum for further annealing at the same annealing temperatures as before for 7 days again to erase the temperature effect of the hot pressing process before thermoelectric properties were measured.

Several tips:

1. Ampoules should be baked prior to the loading the elements in order to clean out possible contaminants (dust, water, etc.). Close attention needs to be paid to possible fissures, which should be gotten rid of by applying the torch, otherwise they may lead to ampoule breakage during the quenching process later.
2. A baked ampoule can be carbon-coated using acetone. Note that if the order is reversed (to bake the already carbon-coated ampoule instead) the carbon coating will disappear upon baking. After rinsing with water for several times, carbon-coated ampoules could be stored in a desiccator to get rid of the remaining water inside of the ampoule.
3. All starting elements are chosen to be in either slug, rod, or shot form. Powder form is avoided such that oxygen contamination is minimized. For elements easy to oxidize such as Yb and Ce, usage of brush or electronic drill is recommended to clean off the oxidized layer before cutting and weighing. Also when using an electronic drill, pay attention to the drilling speed such that no flame comes out due to the reactive nature of these elements.
4. When loading the elements into the ampoule, the element with highest melting point (Co in most samples) is loaded first, whereas the element with lowest melting point (Sb in most samples) is loaded last. This can assure that the whole sample is wrapped in liquid Sb after Sb melts and maximizes the contact and reaction between elements.

5. When sealing ampoules, the length of fused ampoule should be controlled to be short enough (not too short to burn the fingers holding it, also usage of cotton gloves are required for protection during sealing) such that even if the temperature distribution in the furnace is not entirely homogeneous, the precipitation of volatile Sb on the colder part of the ampoule can be minimized.
6. Before breaking the ampoule to get the ingot out, always check the vacuum inside the ampoule first by placing the torch close to the top of ampoule. If the ampoule wall curves in (in the appearance of a dip), then it is in good condition. Otherwise, the sample has to be discarded.

2.3 Characterization

2.3.1 Phase and chemical composition identification

Ingots after annealing were cut and characterized by room temperature X-ray diffraction (XRD), with data collected on a Panalytical X'Pert Pro diffractometer equipped with Cu Kα radiation to check phase purity and lattice constant. Microstructures of the annealed samples were checked with a ZEISS 1550VP Field Emission Scanning Electron Microscope (SEM). Quantitative elemental analyses of the annealed samples were performed with a JEOL JXA-8200 electron probe microanalysis (EPMA) using an accelerating voltage of 15KeV and a current of 25nA in a WDS mode and averaged over 10 randomly selected locations in the skutterudite phase.

Atomic Probe Topographic (APT) measurements were conducted to check possible dopant segregation on sample with $x = 0.20$ Ce doping content (nominal composition $Ce_{0.5}Co_4Sb_{12}$)[20] on a Cameca LEAP-4000X Si equipped with a picosecond UV laser (wavelength 355 nm). Microtip samples of the nominal composition $Ce_{0.5}Co_4Sb_{12}$ were prepared using a dual-beam focused–ion beam microscope (FEI Helios Nanolab) equipped with a micromanipulator (similar to the lift-out method)[40]. Microtips with a diameter of ~100 nm were fabricated to contain a grain boundary and the last step of the tip sharpening process utilized a low voltage and current (5 kV, 16 pA) Ga^+ ion beam to minimized Ga implantation in the sample (Ga content of the region analyzed was <0.01 at%). The sample was maintained at 30K and laser energy of 10 pJ $pulse^{-1}$ was used at a pulse rate of 250 Hz with a target evaporation rate of 0.5% atom $pulse^{-1}$. The primary ions detected were Co^{2+}, Co^+, Ce^{3+}, Ce^{2+}, Sb^{3+}, Sb^{2+}, and Sb^+. Very small amounts of Sb^{2+} and $CoCe^+$, Ga^+, and O^{2+} were also detected. Ions were detected using a 2D microchannel plate detector with a detector efficiency of 50%. This detection efficiency is the same for all ions evaporated. The data collected were analyzed and a 3D reconstruction was created using the program IVAS v.3.6.6.

2.3.2 Transport property characterization

Electrical transport properties for published data, including electrical conductivity (σ) and Seebeck coefficient (S) were measured using the ZEM-3 (ULVAC) apparatus under a helium atmosphere from 300 to 850 K. Some unpublished data are measured on our home-built high temperature Hall measurement system[41] and high temperature Seebeck measurement system[42]. Thermal conductivity (κ) was calculated using $\kappa = dD_T C_P$, with the thermal diffusivity D_T measured along the cross-plane direction by the laser flash method (Netzsch LFA 457) under argon flow with the Cowan model plus pulse correction. The density of the samples was measured using the geometrical method. The specific heat capacity C_P was determined using the Dulong-Petit law $C_P = 3k_B$ per atom throughout the temperature range 300K to 850K. The in-plane Hall coefficient (R_H) was measured using the Van der Pauw method in a magnetic field up to 2 T [41]. Hall carrier concentration (n_H) was then estimated to be equal to $1/R_He$ assuming a single type of carrier, where e is the elementary charge. The Hall carrier mobility ($\boldsymbol{\mu_H}$) was calculated according to the relation $\boldsymbol{\mu_H} = R_H\sigma$. The estimated measurement uncertainties are listed as follows: 5% for electrical resistivity, 7% for Seebeck coefficient, 5% for thermal diffusivity, and 1% for density. The data precision (reproducibility) is smaller than the accuracy, leading to zT values within the range of ±0.2.

2.3.3 Optical property characterization

Optical band gap was measured on an intrinsic $CoSb_3$ powder sample (*p*-type, with carrier concentration 2E17cm^{-3}). Diffuse reflectance infrared Fourier transform spectroscopy (DRIFTS) measurements were performed on a Nicolet 6700 FTIR Spectrometer fitted with a Harrick Praying Mantis Diffuse Reflectance attachment and a low-temperature stage (Harrick CHC). The spectral range of the instrument was from 0.05 to 0.8 eV. The Kubelka Munk function, *F(R)*, was obtained from the measured diffuse reflectance (R), $F(R) = \frac{(1-R)^2}{2R}$, which is known to be proportional to the absorption coefficient (α) ratioed to the scattering coefficient (K).

2.4 *Ab initio* DFT Calculation

For Ga-Co-Sb and In-Co-Sb systems, Lily Xi from SICCAS in China performed the first-principle calculations. The details of her calculation are as follows: All the calculations were carried out using the projector augmented wave (PAW) method, as implemented in the Vienna ab initio Simulation Package (VASP). The Perdew-Burke-Ernzerhof generalized gradient approximation (GGA) for the exchange-correlation potential was used for all the calculations, and computational details[9] can be found in our earlier publications. All calculations of pure and gallium/indium doped $CoSb_3$ skutterudites were carried out on a supercell (2×2×2 primitive cell) with a total of 128 atoms and 8 voids. A 3×3×3 Monkhorst-Pack uniform *k*-point sampling was used for energy calculations of the supercell. Different configuration structures were considered and the one that had the lowest energy was used for further analysis.

For Yb-Co-Sb sytem, Luis Agapito from University of North Texas performed both the DFT calculation and ultrafine evaluation of Fermi surfaces. The details of his calculation are described as follows.

The positions of the 16 atoms in the $CoSb_3$ unit cell (with conventional lattice parameter of 9.07 Å) are relaxed using norm-conserving pseudopotentials and the Perdew-Burke-Ernzerhof (PBE)[43] density functional, as implemented in the *ab initio* package Quantum Espresso[44]. The plane-wave basis set is defined by an energy cutoff of 270 Ry. Although PBE is generally known for the systematic underestimation of the band gap of semiconductors, it can usually predict the correct topology of the bands, which is desired in this study; for such cases, the PBE electronic structure can simply be corrected by an energy shift of the unoccupied manifold via the scissor operator. Previous literature also suggests that the specific band gap value is extremely sensitive to the Sb positions and lattice parameter[45] and that the exact functional is less important. The obtained theoretical band gap using PBE density functional agrees well with experimental optical band gap in this study.

A 9x9x9 Monkhorst-Pack sampling of the reciprocal space is sufficient to converge the DFT wavefunctions. However, ultrafine *k*-meshes are needed in order to obtain smooth isosurfaces (180x180x180 *k*-points in the reciprocal unit cell) and resolve the low-energy features of the DOS (100x100x100, with low smearing energy of 0.02 eV). Highly accurate real-space tight-binding

Hamiltonian matrices are built by projecting the DFT Bloch states onto a "small" set of atomic orbitals (4*p*, 3*d*, 4*s* for Co; and 5*p*, 5*s* for Sb) while filtering out states of low projectability[46]. Reciprocal- and real-space Hamiltonian matrices are obtained by Fourier transformation and then diagonalized at each point of the ultrafine mesh to obtain the eigenenergies. The resulting tight-binding and the actual DFT values are numerically equivalent for all practical purposes. We used the parallel implementation of the method available in the WanT code[47]. XCrySDen[48] is used for visualizing the isosurfaces.

Chapter 3

Electronic origin of high *zT* in *n*-$CoSb_3$ skutterudites

3.1 Summary

N-type filled skutterudites $R_xCo_4Sb_{12}$ are excellent thermoelectric materials owing to their high electronic mobility and high effective mass combined with low thermal conductivity associated with the addition of filler atoms into the void site. The favorable electronic band structure in *n*-type $CoSb_3$ is typically attributed to three-fold degeneracy at the conduction band minimum accompanied by linear band behavior at higher carrier concentrations, which is thought to be related to the increase in effective mass as the doping level increases. Using combined experimental and computational studies, we show instead that a secondary conduction band with 12 conducting carrier pockets (that probably converge with the primary band at high temperatures) is responsible for the extraordinary thermoelectric performance of *n*-type $CoSb_3$ skutterudites. A theoretical explanation is also provided as to why the linear (or Kane-type) band feature is not beneficial for thermoelectrics. This chapter is reproduced with permission obtained from the published paper: *Nature Materials* DOI:10.1038/NMAT4430 [49]. Section 3.2 gives a background introduction. Section 3.3 shows the results and discussion. Conclusion and future work are in Section 3.4.

3.2 Background introduction

Among the best thermoelectric materials are *n*-type filled skutterudites based on $CoSb_3$. The addition of filler atoms, for example Yb, into a void site ($Yb_xCo_4Sb_{12}$) can lead to high *zT* by reducing the thermal conductivity while simultaneously doping the material (adding electrons as charge carriers) [6,50]. High *zT* values (greater than 1) have been reported for both single-element filling (Na[11], Ba[13], In[17], Ce[20], and so on) and multiple filling (In+Ce[51], Sr+Ba+Yb[52], Ba+La+Yb[53]). High *zT* in skutterudites is most often attributed to the addition of the filler atoms and subsequent reduction in thermal conductivity due to alloying disorder and the complex phonon modes of the filler atom[28-30].

Although low thermal conductivity is essential to high *zT*, the importance of the intrinsic electronic structure in skutterudites is often understated or ignored completely. It has become increasingly apparent that complex band structures -- including: multi-valley Fermi surfaces[54,55], convergence of bands (PbTe[55], PbSe[56], Mg_2Si[57]), or even threads of Fermi-surface-connecting band extrema[58] -- are key features of many good thermoelectric materials because the thermoelectric quality factor, B, is proportional to N_v [54,59], the number of degenerate valleys in the electronic structure (or pockets of Fermi surface). While most common semiconductors or metals have simple Fermi surfaces with one or three pockets, thermoelectric materials with $zT > 1$ often have $N_v = 6$ or more[54,56]. Researchers have shown that $CoSb_3$ has very light bands, making a very small (0.05 - 0.22 eV) direct band gap[45,60]. The single, light valence band has an approximately linear ($E \sim k$ rather than the usual parabolic $E = \frac{\hbar^2 k^2}{2m^*}$) dispersion. The light effective mass explains the high mobility observed in lightly doped p-type $CoSb_3$ [6] and is beneficial to zT [61], but it also makes the thermopower (magnitude of the Seebeck coefficient) decrease more quickly as the material is doped. The conduction bands in n-type $CoSb_3$ skutterudites are also very light, with one of the three bands mirroring the linear valence band. The n-type thermopower, however, remains high at high doping, where the linear band concept has been used to explain the apparent increase in effective mass[6,62-65]. This high thermopower at high doping is essential for achieving the high zT in all n-type skutterudites. Here we show that this essential feature of the electronic structure cannot be due to the linear band, but instead is due to a new band (or bands) with high valley degeneracy of $N_v = 12$ or more.

3.3 Results and discussion

3.3.1 Multiple conduction band behavior in n-$CoSb_3$

Here we shall describe the transport properties of $Yb_xCo_4Sb_{12}$ using a rigid band approximation[66,67], meaning that the conduction band structure does not significantly change with doping (Yb content) from that of unfilled $CoSb_3$. Experimentally, similar electronic properties are obtained whether $CoSb_3$ is doped through filling or by substitution on the Co or Sb sites[6,62,64,65] (with optimum thermoelectric performance of the order of 10^{20} cm^{-3} or 0.5 electrons per unit cell)[53,67] in accordance with the rigid band model. Filled $Yb_xCo_4Sb_{12}$ is shown theoretically to be an essentially rigid band up to x=0.25 (0.5 electrons per unit cell[67]). In other thermoelectric materials, such as PbTe, rigid band models have been used successfully and have been confirmed theoretically[68].

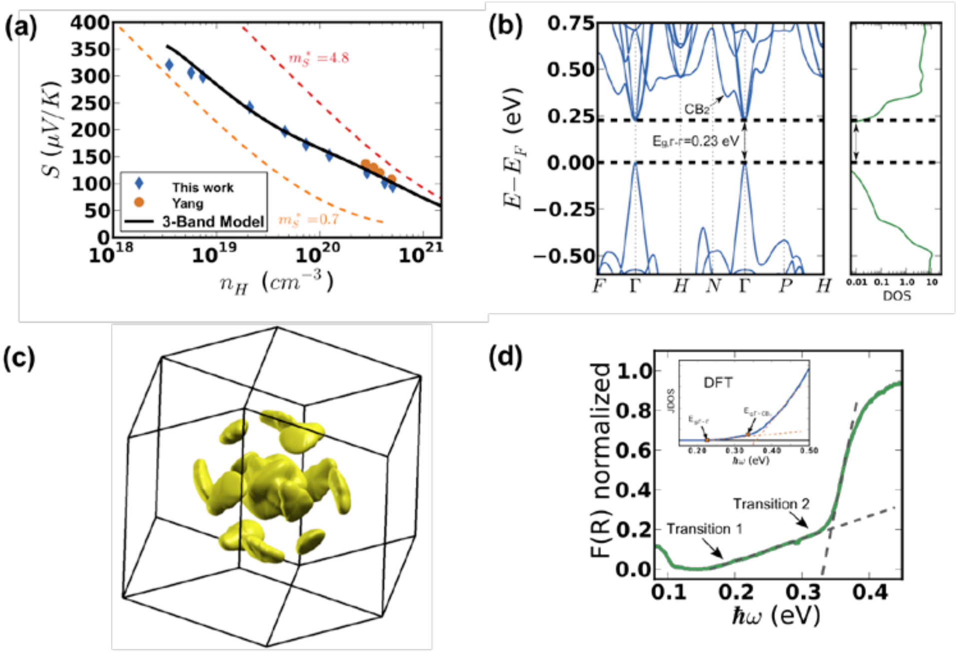

Figure 3.1 Experimental and theoretical evidence showing multiple conduction bands in *n*-type $CoSb_3$. (a) Pisarenko plot of Seebeck coefficient (S) vs. Hall carrier concentration (n_H) at 300K. The solid black line (three-band model) represents the prediction of a semi-empirical model with two conduction bands plus one valence band. Orange and red dashed lines show the expected S vs n_H behavior for single parabolic bands with masses equal to the two individual conduction bands. The data of Yang *et al*[69] on Yb-filled $CoSb_3$ are included for comparison. (b) DFT calculated electronic band structure and density of states (DOS) for $CoSb_3$. (c) Fermi surface calculation for Fermi level 0.11eV above the conduction band minimum showing the 12 pockets of the second conduction band CB_2 observed as a valley between $\Gamma - N$. (d) Room temperature optical absorption measurement with estimated joint density of states from DFT showing two distinct transitions.

Multiple band effects that are responsible for the exceptionally high zT in *n*-type $CoSb_3$ are observable through several methods, both experimental and theoretical, as presented in Figure 3.1. A clear demonstration of complex band behavior is seen in the doping-dependent Seebeck coefficient (Pisarenko plot at 300K) shown in Figure 3.1a. In the degenerate limit the relationship between S, m_S^* and n can be described by:

$$S = \frac{2k_B^2 T}{3e\hbar^2}\left(\frac{\pi}{3n}\right)^{\frac{2}{3}} m_S^*(1+r) \tag{Eq. 3.1}$$

where e is the electron charge, k_B is the Boltzmann constant, $\hbar$ is the reduced Planck constant, r is the scattering parameter ($r = 0$ for acoustic phonon scattering, which is fairly common above 300K and is most appropriate for $CoSb_3$), and m_S^* is the density of states (DOS) effective mass obtained from Seebeck measurements using the single parabolic band (SPB) model (which will be referred to as the Seebeck mass herein). At low carrier concentrations (n_H less than ~1×10^{19} cm^{-3}), $CoSb_3$

shows light mass behavior ($m_S^*{\sim}0.7\ m_e$); as the carrier concentration increases, the system transitions to a much heavier mass, requiring $m_S^* = 4.8\ m_e$ in the heavily doped regime (n_H larger than 3×10^{20} cm^{-3}). By considering two conduction bands[70-72] plus one valence band in a three-band transport model (with a conduction band offset ΔE of ~0.08 eV), we capture the behavior of both the lightly and the heavily doped regions (black line in Figure 3.1a).

The calculated electronic band structure is consistent with an increasing m_S^*, that becomes gradually heavier with doping, if we consider not only the primary conduction bands (Γ point), but also the bands higher in energy (labelled CB$_2$ in Figure 3.1b) for heavily doped CoSb$_3$. The *ab initio* density functional theory (DFT) calculated band structure (Figure 3.1b) shows a direct band gap at the Γ point ($E_{g,\Gamma-\Gamma} = 0.23\ eV$), which yields a triply degenerate (N_v = 3) conduction band edge. However, as a result of heavy doping and relatively light bands at the conduction band minimum, the Fermi level quickly moves up the conduction band, allowing a large population of electrons to form in the secondary conduction band (CB$_2$). Calculations show that this secondary conduction band minimum (CB$_2$) exists about 0.11eV above the conduction band minimum along $\Gamma - N$, and that the Fermi level (E_F) should be well within CB$_2$ with 0.5 electrons/unit cell[67,73] (E_F reaches CB$_2$ minimum with $n_H \approx 2 \times 10^{20}\ cm^{-3}$ at T = 300K). The iso-energy Fermi surface for an energy level just at CB$_2$ (Figure 3.1c) has a high degeneracy with 12 isolated pockets[73]. Only PbTe, which reaches a *zT* of ~2 [54], has such a high value of N_v; it has been shown that this high N_v plays a crucial role in the high Seebeck values and *zT*. In CoSb$_3$, at higher energies these 12 pockets join at corners along $\Gamma - F$ (N_v = 24, 0.013 eV above CB$_2$) [73] and then to the Γ Fermi surface before closing up an opening at $\Gamma - H$ (N_v = 6, 0.034 eV above CB$_2$).

In addition to thermoelectric transport and DFT calculations, multi-band features in CoSb$_3$ can be directly observed by infrared (IR) optical absorption. Optical absorption edge spectra for a nearly intrinsic sample of CoSb$_3$ ($n_H = 1.7 \times 10^{17} cm^{-3}$) show two distinct features (Figure 3.1d). The lower-energy (~0.2eV optically, 0.23eV from DFT) transition can be associated with the direct, $\Gamma - \Gamma$ transition, and the second transition (~0.3eV optically, 0.34eV from DFT) indicates the onset of a $\Gamma - CB_2$ transition. Although direct transitions have been shown to exhibit more than ten times the strength of absorption of the indirect transitions[74], the transition rate is also proportional to the DOS. Because both VB_Γ and CB_Γ have very low DOS in comparison to *CB*$_2$, the $\Gamma - \Gamma$ transition, despite the fact that it is a direct transition, may occur with a lower intensity than the $\Gamma - CB_2$ transition. We roughly estimate the strength of all transitions by calculating the joint density of states (JDOS) from the DFT band structure in the inset of Figure 3.1d, which weights both direct and indirect transitions equally. The JDOS agrees with the observation of two slopes from optical data. Historically, optical measurements in the skutterudite system have been limited, showing an optical band gap for CoP_3 of 0.45 eV; no optical gap had been found for $CoSb_3$ or $CoAs_3$[75]. This was probably because the lowest photon energy that they had measured was 0.4 eV. Other optical measurements have focused on very low energies (<0.1 eV) to probe optical phonons[76], just missing the frequency range important for interband transitions.

3.3.2 Linear or kane bands do not increase Seebeck mass

The unexpectedly high thermopower at high carrier density in $Yb_xCo_4Sb_{12}$ observed in the Pisarenko plot of Figure 3.1a can also be represented as an increase in m_S^*, the Seebeck effective mass, as a function of carrier concentration, as shown in Figure 3.2a. This apparent increase in effective mass with doping has previously been attributed to non-parabolic (Kane) bands[6,62-65], rather than multi-band effects. A non-parabolic dispersion (shown in Figure 3.2b, Eq. 3.2) can arise as a result of interaction between the valence and conduction bands, common in narrow gap semiconductors, which can be described using $k \cdot p$ perturbation theory[77]. Such bands are often described by a dispersion relation where the band is approximately parabolic near the band edge (at E = 0, with band-edge effective mass m_0^*), but they become more linear as the electron energy, E, becomes large relative to the band gap E_g.

$$E\left(1+\frac{E}{E_g}\right)=\frac{\hbar^2 k^2}{2m_0^*} \qquad \text{(Eq. 3.2)}$$

where k is the electron wave vector. For non-parabolic bands, effective mass is not well defined because there are different definitions for m^*, based on different classical relationships. In non-parabolic transport theory, the commonly used energy-dependent effective mass derived from the electron momentum is:

$$m_P^*(E)=\hbar^2 k\left(\frac{dE}{dk}\right)^{-1}=m_0^*(1+\frac{2E}{E_g}) \qquad \text{(Eq. 3.3)}$$

This is a different definition than that found in most solid-state physics textbooks, $m^*=\hbar^2\left(\frac{d^2E}{dk^2}\right)^{-1}$, which relates the effective mass to the band curvature directly. Many common semiconducting materials are reported to show $m^*(E)$ increasing with energy (Fermi level, E_F) including InSb[78], InAs[79], GaAs[79], PbTe[80], and others in a variety of different measurements including: electrical susceptibility (measured using optical reflectance)[80,81], Shubnikov-De Haas/De Haas-Van Alphen oscillations[36], Faraday rotation[78,79], and combined galvano thermomagnetic measurements (Seebeck and Nernst coefficients)[82]. In general these measurements are analyzed based on the dispersion relation Eq. 3.2 to derive the $m_P^*(E)$ of Eq. 3.3. However, we will show that such an increasing trend with energy should not be expected on the Seebeck Pisarenko plot, and instead a decrease in Seebeck mass $m_S^*(E)$ is predicted in the case of a non-parabolic band with a dispersion given by Eq. 3.2.

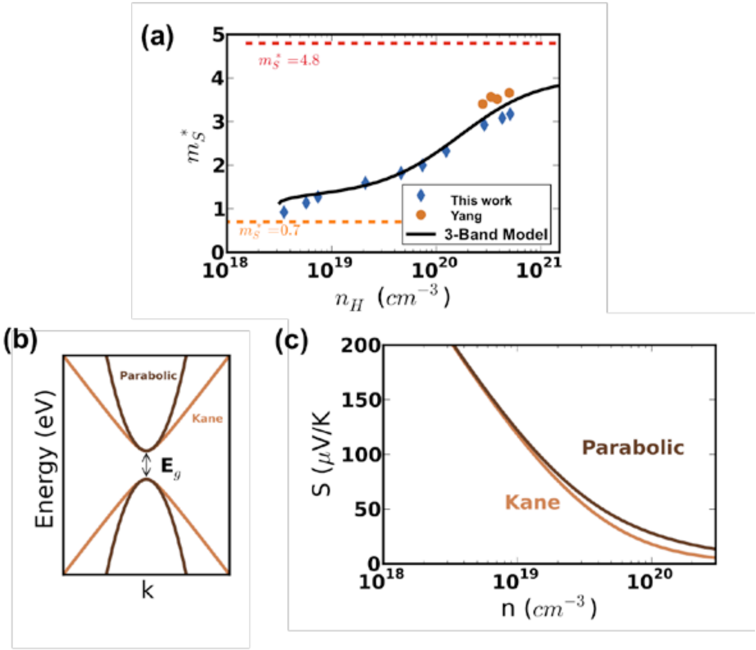

Figure 3.2 Band non-parabolicity and its effect on the Seebeck coefficient and energy-dependent Seebeck effective mass $m_S^*(E)$. a) Effective mass $m_S^*(E)$ derived from Seebeck coefficient and Hall effect measurements. The solid black line (three-band model) represents the prediction of a semi-empirical model with two conduction bands plus one valence band. Orange and red dashed lines indicate the band masses of the two individual conduction bands. The data of Yang *et al.* [69] is included for comparison. b) Parabolic and Kane band dispersions with the same band-edge effective mass ($m_S^*(E=0)$). c) Seebeck Pisarenko plot for both Kane and Parabolic bands, illustrating that $m_S^*(E)$ actually decreases for Kane bands at high carrier concentration.

For thermoelectric materials we define the Seebeck mass $m_S^*(E)$ as the DOS effective mass that would give the measured Seebeck coefficient with the measured n_H using a SPB model[1] (that is, Eq. 3.1 in the degenerate limit). In $CoSb_3$, this carrier-concentration-dependent DOS effective mass $m_S^*(E)$ is observed to increase with n_H in both *n*-type (Figure 3.2a) and *p*-type materials; this increase is commonly attributed to band non-parabolicity using Eq. 3.2 and 3.3.[6,36,62-65] However, we must realize that these two distinct definitions of effective mass, $m_S^*(E)$ and $m_P^*(E)$, are qualitatively different. For example, the degenerate limit of the Seebeck coefficient with a Kane dispersion relation (the equation analogous to Eq. 3.1 using the Kane dispersion, Eq. 3.2) can be expressed as[83]:

$$S = \frac{2k_B^2 T}{3e\hbar^2}\left(\frac{\pi}{3n}\right)^{\frac{2}{3}} m_P^*(E)(1 + r - \lambda) \qquad \text{(Eq. 3.4)}$$

where an additional correction factor $\lambda = \frac{\frac{4E}{E_g}\left(1+\frac{E}{E_g}\right)}{\left(1+\frac{2E}{E_g}\right)^2}$ has been added to the equation for that of a parabolic band (Eq. 3.1). Thus, m_S^*, as used in thermoelectric studies, does not necessarily increase with doping or Fermi level as the momentum mass does. In fact, when *r* = 0, as is commonly found in thermoelectric materials, the m_S^* mass in a Kane band should actually decrease according to:

$$m_S^*(E) = \frac{m_0^*}{1+\frac{2E}{E_g}} \qquad \text{(Eq. 3.5)}$$

which is derived by substituting the expression for λ into Eq. 3.4 and comparing the result to the SPB result (Eq. 3.1). Additional details regarding this derivation are included in the Appendix E. The effect of this relation can be seen in Figure 3.2c, which shows a Seebeck coefficient that is lower for the Kane band ($m_S^*(E)$ decreased).

In other words, even though $m_P^*(E)$ increases with energy in a Kane band, the Seebeck coefficient and $m_S^*(E)$ should actually decrease relative to that of a parabolic band as shown in Figure 3.2c. This may be surprising because both $m_P^*(E)$ and $m_S^*(E)$ are described as a density of states effective mass and often implicitly expected to exhibit the same trends. Instead, Eq. 3.5 shows that the Kane band dispersion and linear bands in general do not increase $m_S^*(E)$ or benefit thermoelectric performance relative to a parabolic band with the same band-edge effective mass. For $CoSb_3$, Eq. 3.5 demonstrates that the increasing m_S^* in Figure 3.2a is not evidence of Kane-type behavior, but rather that multiple conduction bands are necessary to explain the properties of $CoSb_3$.

3.3.3 Band convergence at high temperatures

We have shown that a second band is required to explain the room-temperature transport and optical properties. However, it is at high temperatures where the thermoelectric performance of $CoSb_3$ excels. At high temperatures, we show that these exceptional properties are probably the result of band convergence, as indicated by optical absorption edge measurements that show that the two conduction bands approach each other, leading to convergence at $T_{cvg} \approx 800 \pm 100\ K$ (with effective convergence, i.e., $\Delta E < 1k_BT$, for T > 500 K). This band convergence further increases the effective valley degeneracy to $N_v \approx 12 - 15$. The optical absorption measured from

20 to 400 °C clearly shows that the strong $\Gamma - CB_2$ absorption decreases in onset energy with temperature (Figure 3.3a). The extrapolated absorption edges (Figure 3.3b) indicate that the primary ($\Gamma - \Gamma$, direct) transition does not shift much with temperature (and actually is overtaken by free carrier absorption at high temperatures), whereas the secondary band ($\Gamma - CB_2$) shows a clear temperature-dependent decrease in energy at a rate of ~-2.0×10^{-4} eVK^{-1}. As the two bands become closer in energy, both bands will contribute significantly to thermoelectric transport and improve the thermoelectric quality factor and zT in the same way that band convergence enables high zT in *p*-type PbTe[54].

The high zT in $Yb_xCo_4Sb_{12}$ can now be shown to be a direct result of the high valley degeneracy inherent to $CoSb_3$, which is further enhanced by band convergence at high temperatures. Figure 3.3c shows the carrier-concentration-dependent zT for a series of Yb-doped samples at 800 K along with the calculated results of a three-band model (two conduction bands and one valence band). From this plot, we can see the benefits that having a second conduction band allows, resulting in a significantly higher zT than the primary conduction band at Γ can provide alone. If we consider both the primary (CB_Γ, N_v=3) and the secondary band (CB_2, $N_v = 12$) in the context of band engineering and the quality factor $B = \frac{2k_B^2\hbar}{3\pi}\frac{N_v C_L}{m_c^* E_{def}^2 \kappa_L} T$ ($m_\Gamma^* \approx 0.42$, $m_{CB_2}^* \approx 2.88$ at 800 K), we determine that B_{CB2} is about four times that of B_{CB2} (as indicated by the much larger maximum zT in Figure 3.3c at 800 K). Because CB_Γ and CB_2 are very near converged at high temperatures ($\Delta E \approx 0$ for 800 K), the overall quality factor is enhanced by the presence of the second band, as both bands can be thought to conduct in parallel, thereby increasing the electrical conductivity without being detrimental to the Seebeck coefficient (in the limit of converged bands $B_{total} = B_{CB\Gamma} + B_{CB2}$ [84]). Thus both bands are contributing to the high thermoelectric performance.

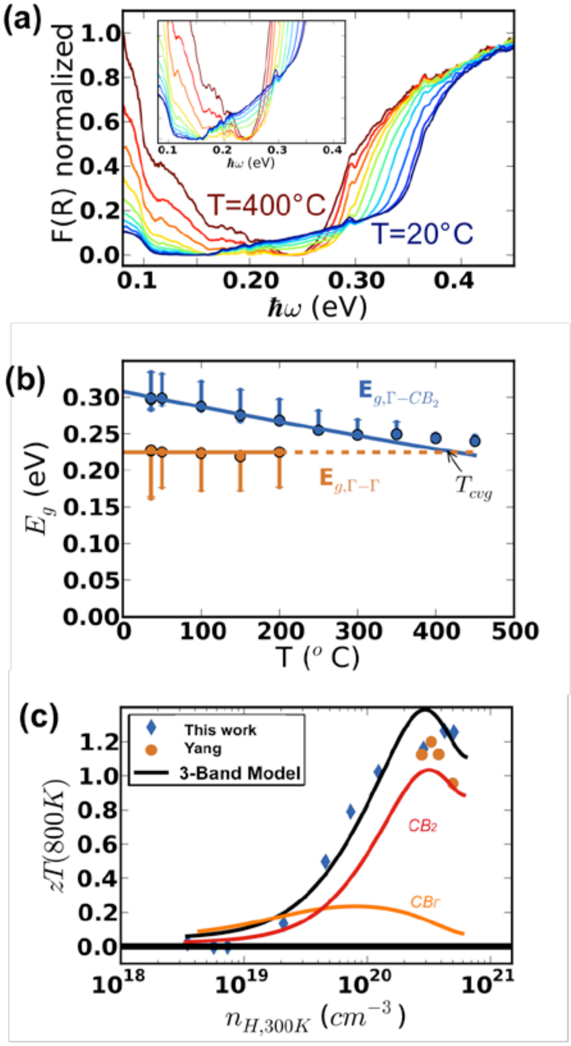

Figure 3.3 Band convergence at high temperatures in $CoSb_3$ as shown from optical absorption and thermoelectric figure of merit. (a) Temperature dependent optical absorption for $CoSb_3$ from 20 to 400°C. (b) Temperature dependent band gap for the direct ($E_{g,\Gamma-\Gamma}$) and indirect ($E_{g,\Gamma-CB_2}$) transitions indicating band convergence at $800 \pm 100\,K$. Error bars represent the range of extrapolations obtained for both the primary and secondary transitions. (c) zT at 800K vs carrier concentration n_H measured at 300K compared with that predicted with the model (solid black line). Colored lines labeled CB_Γ and CB_2 represent the zT that could have been attained by the primary and secondary conduction bands, respectively, with the valence band. Yang *et al.*'s data shows the measured zT for comparison. [69]

3.4 Conclusion and future work

A unified picture explaining the extraordinary thermoelectric properties of skutterudites has emerged from a combined analysis of transport measurements, optical absorption, and theory on a series of $Yb_xCo_4Sb_{12}$ samples. The primary light conduction bands at Γ have a reasonable thermoelectric quality factor, but they are significantly aided by a secondary conduction band, which has extremely high valley degeneracy $N_v = 12$. At high temperatures these two bands converge, enabling the extraordinarily high $zT > 1$ that is observed in many $CoSb_3$ based skutterudites with a variety of filling and doping elements. The contribution of band convergence to the performance at high temperatures suggests that band engineering methods[59] to converge the two conduction bands at lower temperatures would improve the low temperature zT. The analysis of linear and kane bands presented here suggests that non-parabolic band dispersions do not lead to an increase in thermopower (Seebeck coefficient) and are not beneficial to thermoelectric performance.

The investigation of the electronic origin of high zT in *n*-type $CoSb_3$-based skutterudites is rooted in the successful synthesis of single-phase Yb-doped skutterudites, which benefits from a thorough phase diagram study elaborated in Chapter 5. The methodology described in this chapter can be generalized and applied to study other systems as well, i.e., *p*-type skutterudites and half heuslers. For *p*-type skutterudite, this will enable us to find out why it is less competent compared to its *n*-type counterpart. For the latter, pure phase half heusler material is difficult to be synthesized and thus its electronic origin of TE performance is hardly investigated.

Chapter 4

Role of filler in thermal transport

4.1 Summary

The unique crystal structure of skutterudites allows the addition of fillers into the void site. Besides the doping effect that fillers have on electrical transport, the influence of fillers on thermal transport is also prominent and quite complex. The lattice thermal conductivity can be expressed by a simplified version of the Callaway model[85,86]:

$$\kappa_{lattice} = \frac{1}{3}\int_0^{w_{max}} C_v(w) V_g^2\,(w)\tau(w)dw \qquad \text{(Eq. 4.1)}$$

where C_v is the heat capacity, V_g the group velocity, τ the scattering time and w_{max} is related to Debye temperature $\Theta = v_s(\hbar/k_B)(6\pi^2/\Omega)^{1/3}$ by $w_{max} = w_D = \frac{k_B\Theta}{\hbar} = v_s(6\pi^2/\Omega)^{1/3}$. v_s is speed of sound and Ω is the atomic volume.

By adding atoms into the skutterudite cell, the heat capacity C_v increases because the number of atom per unit cell increases, which leads to the increase of thermal conductivity. The guest atoms might also influence the stiffness of the crystal structure, and thus change the group velocity V_g (as discussed in Section 4.4.2). The scattering time could be influenced the most, through various scattering mechanisms associated with the filler atom. The widely acknowledged rattling effect of fillers is an important factor that requires consideration, albeit its microscopic nature remains unclear (discussed in Section 4.2.1). Point defect scattering could be significant due to partial filling as discussed in Section 4.2.2. Large carrier concentration due to the doping can potentially scatter phonon propagation as well (electron-phonon scattering, discussed in Section 4.2.3). Increased Umklapp scattering due to large anharmonicity associated with the fillers can also influence scattering time.

In this chapter, first the complex phonon modes associated with the fillers (resonant scattering/avoided crossing, point defect scattering, and electron-phonon scattering) will be discussed in Section 4.2. Section 4.3 describes how thermal transport properties are calculated as guidance in material design including calculation of minimum thermal conductivity (Section 4.3.1), electronic contribution to thermal conductivity (Section 4.3.2) and theoretical calculation of thermal conductivity using Callaway model (Section 4.3.3). In Section 4.4 a few attempts in revealing the underlying mechanisms of lattice thermal conductivity reduction in $R_xCo_4Sb_{12}$ are presented, with the possibility of electron-phonon scattering (Section 4.4.1) and lattice softening (Section 4.4.2) discussed. Lastly, possible future work is mentioned in Section 4.5.

4.2 Complex phonon modes

4.2.1 Rattling – resonant scattering or avoided crossing

The decrease of lattice thermal conductivity in $R_xCo_4Sb_{12}$ skutterudites has been largely attributed to the "rattling" effect of filler atom R. Due to the size difference between the void and filler atoms (see Table 4.1)[9,87,88], fillers are under-constrained and weakly bound, which allows them to "rattle" in the void. The concept of fillers as "rattlers" was first proposed by Slack[89]. Rattlers are supposed to scatter phonon propagation effectively such that the material behaves as a glass whereas the electron conduction is mostly unaffected as it is in a crystal. Materials with such characteristic features are known as PGEC (phonon glass electron crystal).

Even though the concept of rattling has been widely accepted in the skutterudite community, the microscopic mechanism of rattling, as to be more precise, the interaction between guest atom phonon modes and host atom phonon modes, is still unclear and often debated.

The first and most common explanation is resonant scattering by guest atom vibrations. In this mechanism, a localized mode of the guest atom (Einstein or so-called rattling mode) within the acoustic frequency range is introduced which is uncorrelated to the phonon modes of the framework described by the usual Debye model. The rattling mode can be approximated as a quantized harmonic oscillator, with a single-frequency $w_0 = \sqrt{K/M}$, where K is the force constant which depends on the bonding strength between R and Sb atoms and M is the rattler mass. A few Einstein frequencies calculated along [100] direction for different fillers with comparison to experimental results are listed in Table 4.1 [9,87,88]. As we can see from this equation, the heavier the rattler and the smaller its ionic radius, the lower the rattling frequency would be. The scattering mechanism due to the guest atom vibrations is called resonant scattering, in which only the lattice phonons with the energy similar to that of the local mode introduced by guest atoms would get scattered. The resonant scattering relaxation time can be expressed as:

$$\tau_r^{-1} = C_0 \frac{w^2}{(w^2 - w_0^2)^2} \tag{Eq. 4.2}$$

where C_0 is a constant that is proportional to the concentration of rattlers, and w_0 is the frequency of Einstein mode of rattlers. Since the majority of heat is transferred by acoustic phonons with relatively low frequencies, the lower the rattling frequency, the more acoustic phonons are scattered. This can explain why Yb is such good filler in decreasing lattice thermal conductivity.

Evidence of resonant scattering has been found in many experiments. Large atomic displacement parameter (ADP) of fillers was observed from Rietveld refinements of X-ray diffraction data[37]. The existence of single-frequency Einstein modes was also found either from specific heat data, or from peaked response close to the supposed Einstein mode frequency in the partial densities of phonon states (PDOS) from either nuclear inelastic spectroscopy (NIS)[90] or time-of-flight inelastic neutron scattering (INS). Moreover, as the void size increases, the decrease in the lattice thermal conductivity and Einstein temperature (vibration frequency) also supports the resonant scattering mechanism[37,91].

Table 4.1 Ionic radii, atomic mass, and rattling frequency of different filler atoms. Coordination for all fillers is chosen to be eight except for Ga (coordination = 6).

Filler type	Charge	Ionic radius (Å)	Atomic Mass	w_{0_calc} (cm^{-1})	w_{0_exp} (cm^{-1})
Na	+1	1.18	22.99	113	-
K	+1	1.51	39.10	142	-
Ca	+2	1.12	40.08	-	-
Sr	+2	1.26	87.62	91	-
Ba	+2	1.42	137.33	94	-
Eu	+2	1.25	151.96	59	-
Yb	+2	1.14	173.05	43	40
Ga	+3	0.62	69.72	-	-
In	+3	0.92	114.82	-	-
Ce	+3	1.14	140.12	55	55
La	+3	1.16	138.91	68	55
Void	-	1.89	-	-	-

The resonant scattering mechanism has been challenged when evidence of avoided crossing mechanism was discovered in recent years. In the resonant scattering picture, the rattling mode is considered to be a vibration motion lacking phase coherence compared to the host motion. However recent studies from both experimental work (the lower reduced mass compared to rattler mass from Extended X-ray fine absorption measurements (EXAFS)[91], inelastic neutron[29], and nuclear inelastic scattering[90]) and theoretical calculations[92] cast doubt on this assumption. From inelastic neutron scattering data, Koza *et al.*[29] showed coherency of coupling between the localized guest mode and host lattice mode in Ce and La-filled Fe_4Sb_{12} skutterudites. This interaction between the localized rattling mode and the host acoustic modes could lead to avoided crossing on the phonon spectra and thus effectively lower group velocity, largely scattering the acoustic phonons and reducing thermal conductivity. In addition, this coupling also leads to an increased anharmonicity for the rattling mode manifested as a higher Gruneisen parameter, which will contribute to more Umklapp scattering, as we will discuss later. Recently it was also discovered that the anharmonicity associated with phonon hybridization can decrease as the phonons modes decouple at high pressure, meaning the rattling mode can be switched off at high pressure[90].

The different origin in decreasing lattice thermal conductivity between resonant scattering and avoided crossing can be understood as follows. From Eq. 4.1 we know that the lattice thermal conductivity can be expressed as $\kappa_{lattice} = \frac{1}{3}\int_0^{w_{max}} C_v(w)V_g^2\,(w)\tau(w)dw$; while resonant scattering reduces the scattering time near the rattling mode frequency $\tau(w)$ (Figure 4.1a and blue curve in 4.1d), the avoided crossing due to coupling of localized guest atom and host lattice modes leads to a large reduction in the group phonon velocity $V_g^2(w)$ near the guest vibration mode frequency, as illustrated in Figure 4.1b, 4.1c and orange curve in 4.1d [93].

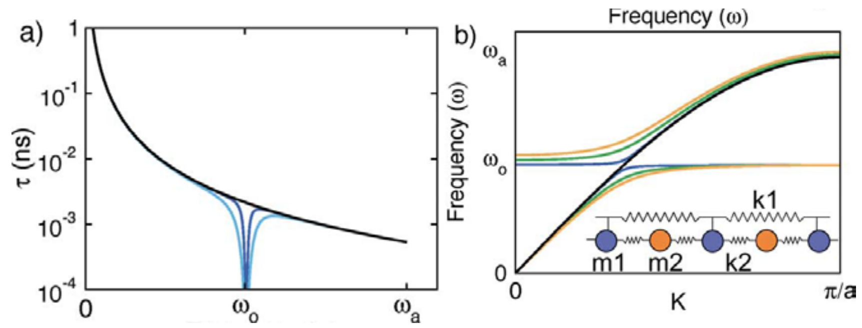

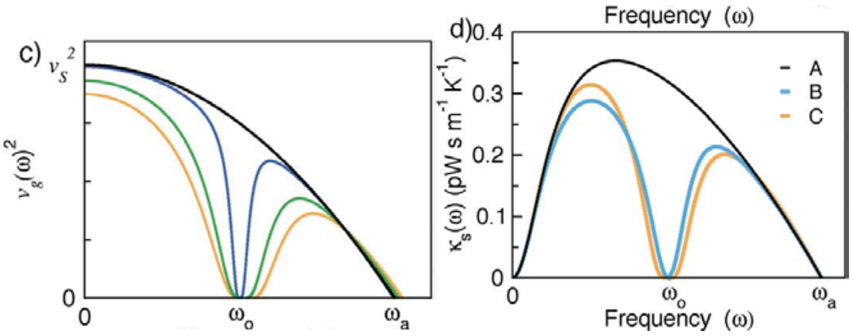

Figure 4.1 Different mechanisms in reducing lattice thermal conductivity between resonant scattering and avoided crossing on the phonon spectra. a) The resonant scattering model targets phonons near w_0. b) BvK phonon dispersions for a stiff framework (m_1, k_1) and loosely bound guest atoms (m_2, k_2). Increased k_2 stiffness results in increased coupling (extent of avoided crossing) between the framework and guest modes. c) The avoided crossing reduces $V_g^2(w)$ in the vicinity of w_0. d) $\kappa_s(w)$for an empty BvK framework, using Umklapp and boundary scattering terms (curve A). Including resonant scattering reduces $\kappa_s(w)$ near w_0 (curve B). If instead the effect of coupling on $V_g^2(w)$ is accounted for, a similar reduction is observed (curve C). Reproduced with copyright permission obtained © Royal Society of Chemistry [2011] (http://pubs.rsc.org/en/Content/ArticleLanding/2011/JM/C1JM11754H#!divAbstract).

From Figure 4.1 we can see that both the resonant scattering effect (reduction of scattering time $\tau(w)$) and the effect of avoided crossing on the phonon spectra (reduction of group velocity $V_g^2(w)$) will result in the similar reduction of lattice thermal conductivity. It is thus difficult to distinguish between the two effects. Temperature dependent thermal conductivity measurements are not enough but rather frequency-dependent measurements of $V_g^2(w)$ and $\tau(w)$ are required to unravel the intertwined effects on κ_L.

4.2.2 Point defect scattering

By partially filling R into the skutterudite structure ($R_xCo_4Sb_{12}$, $0 < x < 1$), due to the mass and size differences between R and the void, point defects are introduced into the system, which can effectively scatter phonon propagation and thus decrease lattice thermal conductivity. The relaxation time due to point defect scattering can be expressed as:

$$\tau_{PD}^{-1} = \frac{\Omega}{4\pi {v_s}^3}\omega^4\Gamma \qquad \text{(Eq. 4.3)}$$

where Ω, v_s, and Γ are the average atomic volume (volume per atom), the average lattice sound velocity, and the disorder scattering parameter, respectively. Γ can be estimated from experimental lattice thermal conductivity values (as shown below from a Klemens model): the larger the scattering parameter, the lower the lattice thermal conductivity.

According to Callaway and Klemens[94-96], if we consider a combined scattering mechanism including Umklapp scattering for the pure crystal without disorder, and extra point defect scattering process for the crystal with disorder, then the ratio of κ_L of the crystal with disorder to that without disorder, κ_L^P is:

$$\frac{\kappa_L}{\kappa_L^P} = \frac{\arctan(u)}{u} \qquad \text{(Eq. 4.4)}$$

$$u^2 = \frac{\pi^2 \theta_D \Omega}{h {v_s}^2} \kappa_L^P \Gamma_{expt} \qquad \text{(Eq. 4.5)}$$

where u, h, and Γ_{expt} are the disorder scaling parameter, the Planck constant, and the experimental disorder scattering parameter, respectively. Thus, Γ_{expt} can be derived from κ_L measurements using Eq. 4.4 and 4.5. It can then be compared to calculated values, as detailed in the following.

Γ can be separated into two components:

$$\Gamma = \Gamma_M + \Gamma_S \qquad \text{(Eq. 4.6)}$$

where the scattering parameters Γ_M and Γ_S represent mass and strain field fluctuations due to the introduction of point defects (e.g., R into the void), respectively.

$$\Gamma_S = x(1-x)\varepsilon\left(\frac{\Delta a}{a}\right)^2 \qquad \text{(Eq. 4.7)}$$

where ε is an empirical fitting parameter related to Gruneisen parameter and elastic properties. a is the lattice constant of pure alloy whereas Δa is the difference in lattice constant between the alloy with point defects and the pure alloy.

When there is more than one constituent element in the compound (as in the case of skutterudites $R_xCo_4Sb_{12}$), there is some discrepancy regarding the definition of Γ_M.

According to Klemens:

$$\Gamma_M = x(1-x)\left(\frac{\Delta M}{M}\right)^2 \qquad \text{(Eq. 4.8)}$$

where ΔM is the mass difference between two species on the same site and M is the molar mass of the compound.

In the case of skutterudite compound, with Yb filling, we are comparing $Yb_xCo_4Sb_{12}$ to unfilled Co_4Sb_{12}, $\Delta M = M_{Yb} = 173.04$ and

$$M = xM_{YbCo4Sb12} + (1-x)M_{Co4Sb12} = 173.04 * x + 4 * 58.93 + 12 * 121.76$$

So $\Gamma_M = x(1-x)\left(\frac{\Delta M}{M}\right)^2 = x(1-x)\left(\frac{173.04}{173.04*x+4*58.93+12*121.76}\right)^2$ (Eq. 4.9)

Later, Yang[97] proposed a different way of calculating Γ_M which weighs the influence of mass fluctuation on each site by its degeneracy. To be more specific, it takes into account not only the number of atoms on a specific site but also the mass contrast between the specific site and the rest of the sites. For example, the chemical composition of a material can be expressed as $A_{1c1}A_{2c2}A_{3c3}A_{4c4}\ldots A_{ncn}$, where the A_i are crystallographic sublattices in the structure and the ci are the relative degeneracies of the respective sites. In this context, the skutterudite compound $Yb_xCo_4Sb_{12}$ has n=3, A_1=Yb, A_2=Co, A_3=Sb, and c1=1, c2=4, c3=12. In general there will be several different types of atoms that occupy each sublattice, and the *k*th atom of the *i*th sublattice has mass M_i^k, radius r_i^k, and fractional occupation f_i^k. The average mass and radius of atoms on the *i*th sublattice are:

$$\overline{M_i} = \sum_k f_i^k M_i^k \quad \text{(Eq. 4.10)}$$

$$\overline{r_i} = \sum_k f_i^k r_i^k \quad \text{(Eq. 4.11)}$$

The mass fluctuation scattering parameter is then given by:

$$\Gamma_M = \frac{\sum_{i=1}^{n} c_i \left(\frac{\overline{M_i}}{\overline{\overline{M}}}\right)^2 \Gamma_{M,i}}{\left(\sum_{i=1}^{n} c_i\right)} \quad \text{(Eq. 4.12)}$$

where the mass fluctuation scattering parameter for the ith sublattice is:

$$\Gamma_{M,i} = \sum_k f_i^k \left(1 - \frac{M_i^k}{\overline{M_i}}\right)^2 \quad \text{(Eq. 4.13)}$$

and the average atomic mass of the compound is:

$$\overline{\overline{M}} = \frac{\sum_{i=1}^{n} c_i \overline{M_i}}{\left(\sum_{i=1}^{n} c_i\right)} \quad \text{(Eq. 4.14)}$$

In the case of skutterudite compound $Yb_xCo_4Sb_{12}$, there is no mass fluctuation on sites A_2 (Co) and A_3 (Sb).

$\overline{M_2} = M(Co) = 58.93$,

$\overline{M_3} = M(Sb) = 121.76$.

Consequently $\Gamma_{M,2} = \Gamma_{M,3} = 0$

For site A$_1$ (Yb/void), $\overline{M_1} = f_1^{Yb} M_1^{Yb} + f_1^{void} M_1^{void} = 173.04 * x$

$$\Gamma_{M,1} = f_1^{Yb}\left(1-\frac{M_1^{Yb}}{\overline{M_1}}\right)^2 + f_1^{void}\left(1-\frac{M_1^{void}}{\overline{M_1}}\right)^2$$

$$= x\left(1-\frac{173.04}{173.04*x}\right)^2 + (1-x)\left(1-\frac{0}{173.04*x}\right)^2$$

$$= \frac{(x-1)^2}{x} + (1-x) = (1-x)(1+\frac{1-x}{x}) = \frac{1-x}{x}$$

$$\overline{\overline{M}} = \frac{\sum_{i=1}^{n} c_i \overline{M_i}}{\left(\sum_{i=1}^{n} c_i\right)} = \frac{\overline{M_1} + 4\overline{M_2} + 12\overline{M_3}}{1+4+12} = \frac{173.04*x + 4*58.93 + 12*121.76}{17}$$

$$\Gamma_M = \frac{\sum_{i=1}^{n} c_i \left(\frac{\overline{M_i}}{\overline{\overline{M}}}\right)^2 \Gamma_{M,i}}{\left(\sum_{i=1}^{n} c_i\right)} = \frac{\left(\frac{\overline{M_1}}{\overline{\overline{M}}}\right)^2 \Gamma_{M,1}}{17}$$

$$= \frac{\left(\frac{173.04*x}{\frac{173.04*x+4*58.93+12*121.76}{17}}\right)^2}{17}\frac{1-x}{x} \qquad \text{(Eq. 4.15)}$$

$$= 17\left(\frac{173.04}{173.04*x+4*58.93+12*121.76}\right)^2 (1-x)x$$

Now if we compare Eq. 4.15 to Klemens's result in Eq. 4.9, we can see that there is clearly a difference of 17 times which equals to the total number of atoms per compound formula.

If we modify Yang' formula such that the degeneracy of each site is still taken into account but with a less complicated form, we get

$$\Gamma_M = x(1-x)f\left(\frac{\Delta M}{\overline{M}}\right)^2 \qquad \text{(Eq. 4.16)}$$

This formula is quite similar to Klemens's formula (Eq. 4.8) except with an extra term f and a different definition for $\overline{M}$, which stand for the fraction of substituted lattice sites and the average atomic mass per number of atoms in the compound (rather than the previous molar mass for the compound) respectively. ΔM still holds for the mass difference between the host and impurity atom. In the case of skutterudite compound, $\Delta M = M_{Yb} = 173.04$ and

$$\overline{M} = \left[xM_{YbCo4Sb12} + (1-x)M_{Co4Sb12} = 173.04*x + 4*58.93 + 12*121.76\right]/17$$

So $$\Gamma_M = x(1-x)\,f\left(\frac{\Delta M}{\overline{M}}\right)^2 = \frac{1}{17}x(1-x)\left(\frac{173.04}{\frac{173.04*x+4*58.93+12*121.76}{17}}\right)^2 \qquad \text{(Eq. 4.17)}$$

$$= 17x(1-x)\left(\frac{173.04}{173.04*x+4*58.93+12*121.76}\right)^2$$

Compare Eq. 4.9, Eq. 4.15 and Eq.17, we get

$$\Gamma_{M,Modified} = \Gamma_{M,Yang} = 17\Gamma_{M,Klemens} \qquad \text{(Eq. 4.18)}$$

Let us take $Cu_2ZnGeSe_xS_{4-x}$ for another example. Using Klemens model, we have:

$A = Cu_2ZnGeSe_4$

$B = Cu_2ZnGeS_4$

$Cu_2ZnGeSe_xS_{4-x} = (x/4)*Cu_2ZnGeSe_4 + (1-x/4)*Cu_2ZnGeS_4$

$$\Gamma_{M,Klemens} = \frac{x}{4}(1-\frac{x}{4})\left(\frac{\Delta M}{M}\right)^2 = \frac{x}{4}(1-\frac{x}{4})\left(\frac{4\left(M_{Se}-M_S\right)}{x*M_{Se}+(4-x)*M_S+M_{Zn}+M_{Ge}+2*M_{Cu}}\right)^2 \qquad \text{(Eq. 4.19)}$$

$$= \frac{x}{4}(1-\frac{x}{4})\left(\frac{\left(M_{Se}-M_S\right)}{\overline{\overline{M}}}\right)^2\frac{1}{4}$$

$$\Gamma_{M,Modified} = x(1-x)\,f\left(\frac{\Delta M}{\overline{\overline{M}}}\right)^2 = \frac{x}{4}(1-\frac{x}{4})\frac{4}{8}\left(\frac{M_{Se}-M_S}{\overline{\overline{M}}}\right)^2 \qquad \text{(Eq. 4.20)}$$

$$= \frac{1}{2}*\frac{x}{4}(1-\frac{x}{4})\left(\frac{M_{Se}-M_S}{\overline{\overline{M}}}\right)^2$$

$$\Gamma_{M,Yang} = \frac{\sum_{i=1}^{n}c_i\left(\frac{\overline{M_i}}{\overline{\overline{M}}}\right)^2\Gamma_{M,i}}{\left(\sum_{i=1}^{n}c_i\right)} = \frac{4*\left(\frac{\overline{M_{Se/S}}}{\overline{\overline{M}}}\right)^2\Gamma_{M,Se/S}}{8}$$

$$= \frac{4*\left(\frac{M_{Se}*x/4+M_S*(1-x/4)}{\overline{\overline{M}}}\right)^2}{8}\left(\frac{x}{4}*\left(1-\frac{M_{Se}}{M_{Se}*x/4+M_S*(1-x/4)}\right)^2+\frac{4-x}{4}*\left(1-\frac{M_S}{M_{Se}*x/4+M_S*(1-x/4)}\right)^2\right) \qquad \text{(Eq. 4.21)}$$

$$= \frac{1}{2}*\frac{x}{4}*\frac{4-x}{4}\left(\frac{M_{Se}-M_S}{\overline{\overline{M}}}\right)^2$$

Compare Eq. 4.19, Eq. 4.20, and Eq. 4.21, and we get

$$\Gamma_{M,Modified} = \Gamma_{M,Yang} = 2\Gamma_{M,Klemens} \qquad \text{(Eq. 4.22)}$$

Thus the modified equation for calculating Γ_M gives the same result as Yang's formula, yet it is easier to implement. From now on, we will only compare Yang's formula and Klemens's formula.

In a more general case, for compound $A_{1c1}A_{2c2}A_{3c3}A_{4c4}\ldots A_{ncn}$, the relationship between the calculated scattering parameters from Klemens's formula (Eq. 4.8) and Yang's formula (Eq. 4.12) will be:

$$\Gamma_{M,Yang} = \frac{\sum_{i=1}^{n} c_i}{c_i}\Gamma_{M,Klemens} \qquad \text{(Eq. 4.23)}$$

with the i^{th} element being substituted and A_i position having a C_i degeneracy.

The difference between Yang's formula and Klemens' formula is that Yang's formula takes the degeneracy of each site as the weighing factor in calculating scattering parameter, which makes more sense because doping on the Co site ($Co_xNi_{1-x}Sb_3$) should result in a smaller scattering parameter from doping on the Sb site ($Co(Sb_xTe_{1-x})_3$) even when the doping content x is the same.

Since $\sum_{i=1}^{n} c_i$ is always larger than c_i, the scattering parameter of Yang's formula is always larger than Klemens', which leads to a smaller lattice thermal conductivity.

4.2.3 Electron-phonon scattering

In binary $CoSb_3$ skutterudites, even adding a few percent of dopant (Fe, Pd, Pt, Ni, Te etc.) can result in large reduction in the lattice thermal conductivity. This was first reported by Dudkin and Abrikosov, who observed a 50% reduction of the lattice thermal conductivity at 300K in $CoSb_3$ doped with 10at% Ni, 10at%Fe or 0.25at% Te [98]. Later the influence of different dopant on lattice thermal conductivity reduction was confirmed and explored by many researchers, such as Caillat[7], Stokes[99], Anno[100] etc. A plot with lattice thermal conductivity of $CoSb_3$ versus the carrier concentration of *n*-type dopants (Ni, Pd, Pt) is shown in Figure 4.2, with data exacted from Anno's paper[100] (1999).

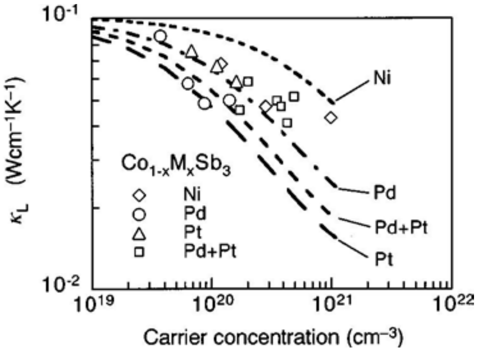

Figure 4.2. Lattice thermal conductivity κ_L at room temperature as a function of carrier concentration for $Co_{1-x}M_xSb_3$ (M=Ni, Pd, Pt, and Pd+Pt) samples. The dashed lines present the calculations based on the Debye model. Reproduced with permission from [Anno, H., Matsubara, K., Notohara, Y., Sakakibara, T. & Tashiro, H. Effects of doping on the transport properties of $CoSb_3$. *Journal of Applied Physics* **86**, 3780, doi:10.1063/1.371287 (1999).]. Copyright [1999], AIP Publishing LLC.

A Debye model including the Umklapp scattering, point defect scattering and electron-phonon scattering is used to compare with experimental value. It was concluded that the point defect scattering and electron-phonon scattering are the main processes that result in the reduction of lattice thermal conductivity of *n*-$CoSb_3$ at room temperature. The relative strength of these two scattering mechanisms depends on the type of dopant. For example, point defect scattering is more dominant for Pd and Pt dopants due to the large difference in atomic mass and size compared to Co, whereas for Ni as dopant, the electron-phonon scattering plays a more crucial role due to the similar atomic mass and size between Ni and Co.

Electron-phonon scattering occurs when the doping concentration is high and the temperature is low. This electron-phonon scattering is often ignored at high temperatures because it gets overwhelmed by Umklapp scattering. The relaxation time for electron-phonon scattering is expressed[101,102] as Eq. 4.24-25 when the wavelength of electrons is shorter than the wavelength of phonons:

$$\tau_{ep}^{-1} = C_{ep}\omega^2 \quad \text{(Eq. 4.24)}$$

where $C_{ep} = \frac{4nm^* v_e \lambda_e}{15 d v_s{}^2}$ (Eq. 4.25)

Here n is the electron concentration, m^* is the effective electron mass, v_e is the electron velocity, λ_e is the mean free path of the electrons, and d is the mass density, v_s is the speed of sound.

In the region where the electron-phonon scattering dominates, the lattice thermal conductivity increases proportionally with temperature $\kappa_L \propto T$. While it is reasonable to expect a carrier concentration dependent κ_L, the exact relation $w_L = \frac{1}{\kappa_L} \propto n^a$ remains unclear with different values of $a(= \frac{4}{3}\, or\ 2)$ reported[103,104]. Shi *et al*[103] made an estimate of the coefficient C_{ep}:

$$C_{ep} \propto \frac{n^{4/3}}{E_{def}^2 m^{*2} k_B T} \qquad \text{(Eq. 4.26)}$$

which is based on the acoustic phonon scattering approximation and a single parabolic band model in the degenerate limit $(v_e = v_F, \lambda_e = v_e \tau_e = v_e \tau_0 E^{-\frac{1}{2}}, E = \frac{1}{2} m^* v_F^2, E \propto \frac{n^{\frac{2}{3}}}{m^*})$. The obtained relation $C \propto n^{\frac{4}{3}}$ holds when the other parameters are either constant (such as T) or independent of carrier concentration such as E_{def}, m^*. Eq. 4.26 explains why the electron-phonon scattering is more evident in heavily doped samples and at low temperatures.

In filled skutterudites, due to the donor nature of filler atoms, the *n*-type carrier concentration can be quite high (10^{19} ~ 10^{21} cm^{-3}). So besides the well-known “rattling” effect and point defect scattering effect of fillers, the electron-phonon scattering should also play an important role in the decrease of lattice thermal conductivity, as it does in binary skutterudites. Unfortunately, it has been challenging to separate the effect of electron-phonon scattering from other scattering processes with the uncertainty of carrier concentration dependence of κ_L. The difficulty in getting experimental data with pure electron-phonon scattering also makes it hard to confirm.

4.3 Thermal transport calculation

4.3.1 Minimum thermal conductivity

It is important for us to know the minimum thermal conductivity of skutterudites when trying to decrease the lattice thermal conductivity. There are two frequently used formulas for minimum thermal conductivity calculation. The one proposed by Cahill[105] was initially for amorphous materials and based on a physical picture of a modified Einstein model, which consists of a random walk of energy between uncorrelated localized oscillators of varying sizes and frequencies. The dominant energy transport is between nearest neighbors. The minimum phonon mean free path is one half of its wavelength (relaxation time equals to one half of one period of vibration). The Cahill minimum thermal conductivity can be expressed as:

$$\kappa_{\min} = \left(\frac{\pi}{6}\right)^{1/3} k_B \Omega^{-2/3} \sum_i v_i \left(\frac{T}{\Theta_i}\right) \int_0^{\Theta_i/T} \frac{x^3 e^x}{(e^x - 1)^2} dx \qquad \text{(Eq. 4.27)}$$

where the summation is over the three sound modes (one longitudinal and two transverse modes), and Ω represents the average volume per atom, v_i is the sound velocity for the longitudinal and transverse modes, and $\Theta_i = v_i(\hbar/k_B)(6\pi^2/\Omega)^{1/3}$ is the Debye temperature for each polarization in degrees K. Equation 4.27 contains no free parameters, since both Ω and v_i are known.

In the high temperature limit, $\frac{x^3 e^x}{(e^x-1)^2} \approx x$, so the equation becomes:

$$\kappa_{\min} = \frac{1}{2}\left(\frac{\pi}{6}\right)^{1/3} k_B \Omega^{-2/3} \sum_i v_i = \frac{1}{2}\left(\frac{\pi}{6}\right)^{1/3} k_B \Omega^{-2/3}\left(2v_t + v_l\right) \qquad \text{(Eq. 4.28)}$$

Slack[89] proposed a different formula to calculate minimum thermal conductivity based on the notion that heat is carried by waves, and for this they must live longer than one period of vibration. The minimum mean free path is thus one wavelength instead of one half according to Cahill.

According to Slack, the minimum thermal conductivity at high temperatures can also be estimated using a Debye approximation as:

$$\kappa_{\min}(acoustic) = \frac{3}{2}\left(\frac{4\pi}{3}\right)^{1/3} \frac{v k_B}{(\Omega N)^{2/3}} \qquad \text{(Eq. 4.29)}$$

$$\kappa_{\min}(optic) = \frac{k_B^2 \Theta}{2\hbar \Omega^{1/3}}\left(1 + \frac{1}{N^{1/3}}\right) \qquad \text{(Eq. 4.30)}$$

$$\kappa_{\min} = \kappa_{\min}(acoustic) + \kappa_{\min}(optic) \qquad \text{(Eq. 4.31)}$$

where N is the number of atoms per primitive cell. The optic contribution is calculated from a sum of $3(N-1)$ equally spaced optic modes.

For $CoSb_3$, $v_l = 4743 m/s$, $v_t = 2830 m/s$ according to speed of sound measurement, see Section 4.4.2.

The average velocity $\bar{v}$ can be calculated from:

$$\frac{3}{(\bar{v})^3} = \frac{2}{v_t^3} + \frac{1}{v_l^3} \qquad \text{(Eq. 4.32)}$$

we get $\boldsymbol{V}$ =3132m/s. The Debye temperature Θ can be calculated from:

$$\Theta = v(\hbar/k_B)(6\pi^2/\Omega)^{1/3} \tag{Eq. 4.33}$$

With $\Omega = \frac{a^3}{2N} = \frac{9.0348^3}{2*16} * 10^{-30}m^{-3} = 23.05 * 10^{-30}m^{-3}$, $\Theta = 327.8$K. Both the speed of sound measurement data and the Debye temperature match well with literature data ($v_l = 4590m/s$, $v_t = 2643m/s, \Theta = 307$K) [6].

With the values obtained we get the minimum thermal conductivity for $CoSb_3$ skutterudites:

$$\kappa_{\min,Slack} = \kappa_{\min}(acoustic) + \kappa_{\min}(optic) = 0.204+0.232\ (W/m/K) = 0.436\ W/m/K \tag{Eq. 4.34}$$

$$\kappa_{\min,Cahill} = 0.713\,W/m/K \tag{Eq. 4.35}$$

These values (Eq. 4.34 and Eq. 4.35) should serve as a guide in search of lower lattice thermal conductivity. Notice there is some discrepancy between the values obtained from both methods. The Cahill method surprisingly gives a higher thermal conductivity with only half of the wavelength used in the Slack model.

4.3.2 Electronic contribution to thermal conductivity

The data from thermal diffusivity measurements D_T gives us experimental estimations of thermal conductivity κ ($\kappa = dD_TC_P, C_P = 3k_B, d\ is\ density$). κ is the sum of electronic contribution to the thermal conductivity κ_e and lattice thermal conductivity κ_l. In order to probe the role of fillers in reducing lattice thermal conductivity, we have to separate κ_e from κ first. κ_e can be expressed as in Eq. 4.36:

$$\kappa_e = \kappa_{e,e} + \kappa_{e,h} + \kappa_b \tag{Eq. 4.36}$$

where $\kappa_{e,i}$ denotes the electronic thermal conductivity from the carrier type i. κ_b denotes the electronic thermal conductivity from bipolar conduction, which usually occurs when the band gap E_g is small and temperature T is high enough that intrinsic conduction can happen ($k_BT > E_g$) with both electrons and holes excited in pairs.

The values of $\kappa_{e,i}$ is large in heavily doped semiconductor and can be easily calculated using the Wiedemann-Franz law. The Wiedemann-Franz relationship states that the electronic contribution from species *i* is related to the electrical conductivity of species *i* (σ_i), temperature *T*, and the corresponding Lorenz number L_i via:

$$k_{e,i} = L_i \sigma_i T \qquad \text{(Eq. 4.37)}$$

In a single parabolic band model with carrier scattering time of the form $\tau = \tau_0 \varepsilon^r$:

$$L = \left(\frac{k_B}{e}\right)^2 \left[\frac{r+7/2}{r+3/2} \times \frac{F_{r+5/2}(\eta)}{F_{r+1/2}(\eta)} - \left(\frac{r+5/2}{r+3/2}\right)^2 \times \frac{F_{r+3/2}(\eta)^2}{F_{r+1/2}(\eta)^2}\right] \qquad \text{(Eq. 4.38)}$$

For acoustic phonon scattering, $r = -1/2$, so the Lorenz number can be expressed as:

$$L = \frac{k^2}{e^2} \frac{3F_0(\eta)F_2(\eta) - 4F_1(\eta)^2}{F_0(\eta)^2} \qquad \text{(Eq. 4.39)}$$

For electronic thermal conductivity due to bipolar conduction,

$$k_b = \frac{\sigma_e \sigma_h}{\sigma_e + \sigma_h} \left(\alpha_e - \alpha_h\right)^2 T \qquad \text{(Eq.}$$

4.40)

For more details, please refer to Appendix A-D.

4.3.3 Callaway model

Once the electronic thermal conductivity is exacted from the total thermal conductivity, the lattice contribution can be estimated experimentally. A Callaway model can be used to calculate theoretical lattice thermal conductivity, taking into account of various phonon scattering mechanisms. By comparing results from Callaway model to experimental values, underlying phonon scattering mechanisms can be revealed. This is quite useful in accessing the role of fillers in reducing the lattice thermal conductivity.

The Callaway model is based on a Debye approximation, with which the lattice thermal conductivity can be calculated as:

$$\kappa_L = \frac{k_B^4}{2\pi^2 \hbar^3 v} T^3 \int_0^{\Theta/T} \tau_{total} \frac{x^4 e^x}{(e^x - 1)^2} dx \qquad \text{(Eq. 4.41)}$$

$$\tau_{total}^{-1} = \tau_B^{-1} + \tau_U^{-1} + \tau_r^{-1} + \tau_{PD}^{-1} + \tau_{ep}^{-1} \qquad \text{(Eq. 4.42)}$$

τ_B is the boundary scattering relaxation time, which is determined by the speed of sound in the material v_s and average grain size L.

$$\tau_B^{-1} = \frac{v_s}{L} \qquad \text{(Eq. 4.43)}$$

τ_U is the Umklapp scattering relaxation time. Empirically it can be expressed as:

$$\tau_U^{-1}(\omega) = \frac{\hbar\gamma^2\omega^2}{Mv^2\Theta} T\exp(-\Theta/3T) = \frac{k_B^2\gamma^2}{\hbar M v^2\Theta} x^2 T^3 \exp(-\Theta/3T) \qquad \text{(Eq. 4.44)}$$

where $x = \frac{\hbar w}{k_B T}$, ω is phonon frequency, M is the average mass of a single atom, and γ is the Grüneisen parameter that characterizes the anharmonicity of lattice vibration.

There are two types of phonon-phonon scattering mechanisms: Umklapp scattering and Normal scattering. Both processes involve three phonons. The difference is that in Normal scattering process, the total phonon momentum is conserved and is generally considered as having no contribution to the thermal resistance, whereas in Umklapp scattering process, with increasing phonon momentum of the incoming wave vectors ($\vec{k}_1, \vec{k}_2$), the outgoing wave vector $\vec{k}_3$ can point out of the Brillouin zone, which can be equivalently transferred into a phonon wave vector inside the Brillouin zone $\vec{k}_3'$ but with a smaller magnitude ($\vec{k}_3 = \vec{G} + \vec{k}_3', \vec{G}$ is a reciprocal lattice vector). This leads to a change in the phonon momentum, and results in energy loss and adds thermal resistivity. Umklapp scattering is the main mechanism for thermal resistance at high temperatures for materials with low defect concentration.

As discussed previously, τ_r denotes empirically the resonant scattering time: $\tau_r^{-1} = C_0 \frac{w^2}{(w^2 - w_0^2)^2}$ (section 4.2.1); τ_{PD} denotes the point defect scattering time $\tau_{PD}^{-1} = \frac{\Omega}{4\pi v^3}\omega^4\Gamma$ (section 4.2.2); τ_{ep} denotes the electron phonon scattering time $\tau_{ep}^{-1} = C_{ep}\omega^2$ (section 4.2.3). Note that the nature of rattling remains unclear, given that both the relaxation time reduction (due to resonant scattering) and the group velocity reduction (because of the avoided crossing in the phonon spectra) can lead to similar reduction in lattice thermal conductivity (Figure 4.1). However here we are using the resonant scattering for simplicity.

4.4 Results and discussion

4.4.1 Possible electron-phonon scattering in $R_xCo_4Sb_{12}$

A series of Yb-doped $CoSb_3$ skutterudites were synthesized with nominal doping level x = 0.005 to 0.30[49]. Their room temperature transport data are shown in Table 4.2.

Table 4.2. Room temperature transport properties of $Yb_xCo_4Sb_{12}$ skutterudites (with nominal x from 0.0025 to 0.3).

Nominal x	EPMA x	n_H (cm^{-3})	Seebeck (μVK^{-1})	Mobility ($cm^2V^{-1}s^{-1}$)	Resistivity ($10^{-5}\Omega m$)	κ ($Wm^{-1}K^{-1}$)	κ_L ($Wm^{-1}K^{-1}$)
0.0025		6.8E+17	-369.2	150.3	61.16	-	
0.005	0.002	3.5E+18	-320.8	79.4	22.27	8.68	8.66
0.0075	0.003	5.7E+18	-306.4	82.4	13.34	6.85	6.82
0.01	0.009	7.4E+18	-298.8	80.1	10.54	6.93	6.89
0.025	0.019	2.1E+19	-241.8	98.1	3.08	5.59	5.44
0.05	0.047	4.6E+19	-196.8	86.0	1.57	4.81	4.50
0.075	0.071	7.37E+19	-172.8	78.5	1.08	3.86	3.39
0.1	0.1	1.24E+20	-152.4	69.4	0.73	4.02	3.32
0.2	0.2	2.87E+20	-120.6	36.4	0.60	2.99	2.07
0.25	0.25	4.26E+20	-102.2	39.5	0.37	3.63	2.1
0.3	0.25	5.08E+20	-95.0	35.9	0.34	3.64	1.95

The experimental lattice thermal conductivity was calculated using Eq. 4.39.

Now two methods can be applied to calculate the lattice thermal conductivity. The first is the Callaway model descried in Section 4.3.3. The other is using the Klemens model introduced in Section 4.2.2. The latter conveniently allows us to use the experimental value of the lattice thermal conductivity of pure (or very lightly doped) skutterudites as input. By comparing the ratio of lattice thermal conductivity between heavily doped $CoSb_3$ and the pure one, the effect of point defect scattering can be estimated. If we consider only the contribution of mass contrast between the void and Yb filler atom (Γ_M) to the scattering parameter Γ, the modeling result is shown in Figure 4.3a. Note here that we are using Yang's formula (Eq. 4.12) for Γ_M as discussed in Section 4.2.2, which will give a lower estimated lattice thermal conductivity. Yet the modeling result still highly overestimates the lattice thermal conductivity, so in the next step the effect of strain (Eq. 4.7) is also considered.

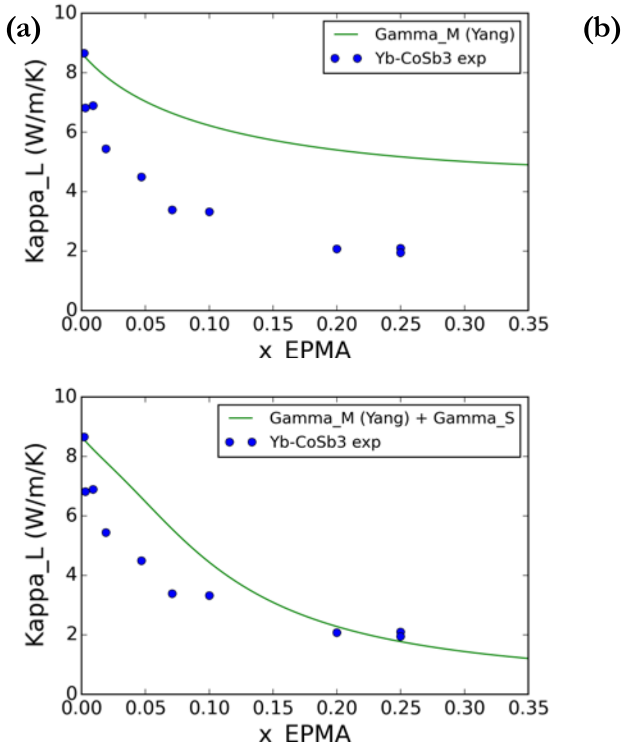

Figure 4.3. Lattice thermal conductivity versus doping level *x* with both experimental and calculated results from Klemens model. The green line represents the modeling results with a) only mass effect considered and b) both mass and strain effects considered (Γ_M calculated from Yang's formula, Γ_S with ε = 5E5). The blue dot represents experimental value (*x* from EPMA measurements listed in Table 4.2).

To assess the strain induced by the addition of fillers, the influence of filler atom on the lattice constant is studied, as shown in Figure 4.4. A linear dependence can be obtained,

$$a = a_0 + 0.08x \qquad \text{(Eq. 4.45)}$$

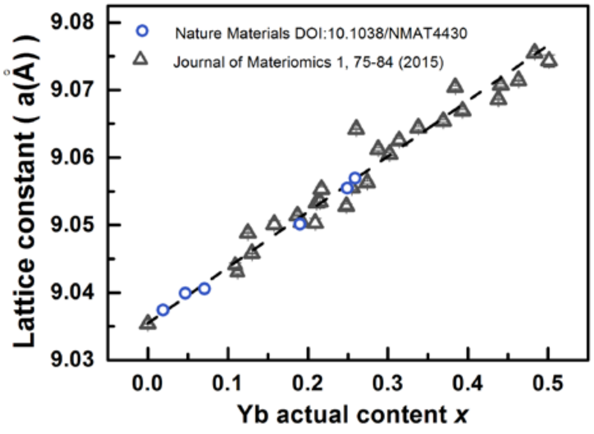

Figure 4.4. Dependence of lattice constant of $Yb_xCo_4Sb_{12}$ skutterudites on the Yb actual content x. With this relationship (Eq. 4.45) we can calculate the scattering parameter from strain effect (Eq. 4.7). However, we cannot get a reasonable fit unless ε is as large as 5E5 (Figure 4.3b). This value is not physical, and thus other effects must be contributing besides the point defect scattering. Among common scattering mechanisms (discussed in Section 4.3.3), Umklapp scattering is not prominent at room temperature. The grain size is on the same level for all samples so no additional boundary scattering rises from filled samples compared to pure skutterudite sample. What remains is the rattling effect and electron-phonon scattering. We investigate the possibility of electron-phonon scattering due to filler addition first.

By subtracting the thermal resistance due to point defect scattering from mass effect (the strain effect is ignored because of its small magnitude), we get the good linear dependence of remaining thermal resistance $W_{\exp} - W_{pd}$ on the carrier concentration n_H shown in Figure 4.5.

$$W_{ep} = W_{\exp} - W_{pd} \propto n_H^{1/2} \tag{Eq. 4.46}$$

This is possibly due to electron phonon scattering $W_{ep} \propto n_H^{\alpha}$ as discussed in section 4.2.3. However, the exponent coefficient obtained here $\alpha = 1/2$ is smaller than previously reported values (4/3 or 2) [103,104]. This might be due to the carrier concentration dependence of E_{def}, m^*. The increasing dependence of m^* on carrier concentration can counteract with the influence of carrier concentration on the scattering constant C_{ep}, thus leading to a lower dependence.

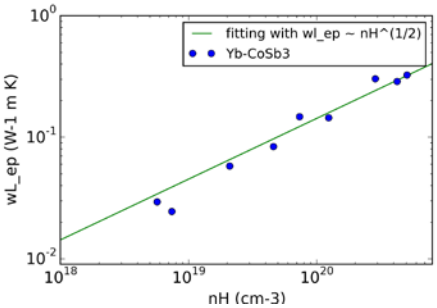

Figure 4.5. Thermal resistivity due to electron-phonon scattering versus measured Hall carrier concentration in $Yb_xCo_4Sb_{12}$. The blue dot represents experimental value (n_H listed in Table 4.2). The green line represents modeling result from Klemens model with only mass effect considered.

More research is required both on more precise theoretical estimation of electron-phonon scattering and on experimental evidence as well. Before we can conclude about the electron-phonon scattering, it would be difficult to assess the effect of resonant scattering and/or group velocity reduction due to fillers.

4.4.2 Lattice softening due to fillers

By adding a filler atom in the void site, not only it will change the density of skutteurdites, but also it may change the elastic modulus by either softening or stiffening the framework. Both will contribute to the change of sound velocities. The longitudinal v_L and transverse v_T sound velocities can be expressed in equations 4.47 and 4.48, respectively.

$$v_L = \sqrt{\frac{K + \frac{4}{3}G}{d}} \qquad \text{(Eq. 4.47)}$$

$$v_T = \sqrt{\frac{G}{d}} \qquad \text{(Eq. 4.48)}$$

where *K*, *G*, and *d* represent the bulk and shear moduli, and theoretical density, respectively.

The theoretical density can be calculated using EPMA determined doping content *x* and lattice parameter *a* derived from XRD measurements, as shown in Eq. 4.49. Note that the factor 2 equals the number of primitive cells per unit cell. For samples listed in Table 4.2, their calculated theoretical densities are listed in Table 4.3.

$$d = \frac{\left(xM_{Yb} + 4M_{Co} + 12M_{Sb}\right)\times 2}{N_A a^3} \qquad \text{(Eq. 4.49)}$$

where M_{Yb}, M_{Co}, and M_{Sb} are molar masses for the Yb, Co, and Sb atom, respectively, and N_A is the Avogadro's constant.

Table 4.3. Theoretical density calculated from EPMA doping content *x* and XRD-derived lattice parameter *a* of $Yb_xCo_4Sb_{12}$ skutterudites (with nominal *x* from 0.0025 to 0.3)[49].

Nominal *x*	EPMA *x*	*a* (Å)	*d* (g cm^{-3})
0.0025		9.035	7.642
0.005	0.002	9.035	7.644
0.0075	0.003	9.036	7.643
0.01	0.009	9.036	7.648
0.025	0.019	9.037	7.652
0.05	0.047	9.040	7.668
0.075	0.071	9.041	7.685

0.1	0.1	9.044	7.699
0.2	0.2	9.050	7.753
0.25	0.25	9.055	7.785
0.3	0.25	9.057	7.788

From Table 4.3, we can extract a linear relationship between the theoretical density *d* and EPMA doping content *x:*

$$d = 0.572x + 7.642 \qquad \text{(Eq. 4.50)}$$

By substituting Eq. 4.50 into Eq. 4.49, we can get a relationship between the lattice parameter and EPMA doping content *x*. Here *a* is in Å and *M* is in g/mol.

$$x = \frac{80M_{Co} + 240M_{Yb} - 7.642 * a^3 * 6.02}{0.572 * a^3 * 6.02 - 20M_{Yb}} \qquad \text{(Eq. 4.51)}$$

With *x* value from Eq. 4.51. By using Eq. 4.50 again we can get the theoretical density of any sample that has only one of the two variables *a* and *x* measured.

Unfortunately the speed sound measurements were not performed on this set of samples ($Yb_xCo_4Sb_{12}$ skutterudites, with nominal *x* from 0.0025 to 0.3). However, there is indeed another set of $Yb_xCo_4Sb_{12}$ samples synthesized by ball milling whose XRD (all samples are phase-pure according to XRD analysis) and speed sound measurements were performed but without EPMA results. To solve this problem, we can either use Eq. 4.51 or Eq. 4.45 to get an estimate of the EPMA doping content *x* from XRD-derived lattice parameter *a*. The results obtained from both methods are close to each other. The measured speed sound velocities as well as calculated elastic moduli (Eq. 4.47 and Eq. 4.48) and theoretical densities (Eq. 4.50) for this set of ball-milled samples are listed in Table 4.4.

Table 4.4. Speed sound measurement data as well as calculated elastic moduli and theoretical density of ball-milled $Yb_xCo_4Sb_{12}$ skutterudites (with nominal *x* from 0 to 0.6). EPMA values *x* listed are calculated using Eq. 4.51 from lattice constant *a*.

Nominal *x*	EPMA_calc *x*	*a* (Å)	*d* (g cm^{-3})	V_L (m/s)	V_T (m/s)	K (GPa)	G (GPa)
0	-	9.035	7.638	4743	2830	90.22	61.18
0.2	0.165	9.049	7.737	4600	2764	86.47	58.52
0.3	0.222	9.053	7.769	4534	2700	83.74	56.49
0.4	0.281	9.058	7.803	4469	2672	83.19	55.84
0.45	0.310	9.060	7.819	4447	2646	82.07	54.78
0.5	0.350	9.063	7.842	4418	2643	81.39	54.41

0.6	0.382	9.066	7.860	4343	2622	81.00	53.79

A decreasing linear trend in elastic moduli (both K and G) with doping content x_{EPMA} can be observed in Figure 4.6. For the maximum doping $x = 0.38$, the decrease reaches about 10%. This clearly indicates the softening nature of fillers on the framework. Whether it is due to lattice expansion or increased electron screening remains unclear, and more research effort is required to reach a solid conclusion. The decrease in speed sound velocities with doping is another proof that supports the avoided crossing mechanism in reducing thermal conductivity by fillers.

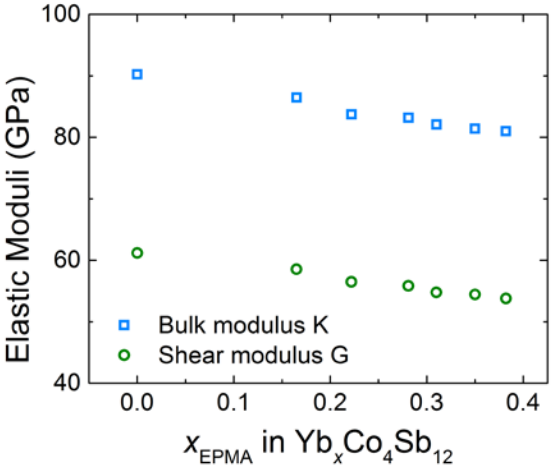

Figure 4.6. Dependence of elastic moduli on doping content x in $Yb_xCo_4Sb_{12}$.

4.5 Conclusion and future work

It can be concluded that in $R_xCo_4Sb_{12}$, besides the point defect scattering due to partial filling, the role of fillers in reducing lattice thermal conductivity possibly involves some electron-phonon scattering as well. To precisely determine the extent of this scattering such that we can comment on the effect of “rattling”, more research effort needs to be performed. Synthesis of Ni or Te-doped $CoSb_3$ samples is proposed to study the carrier concentration dependence of thermal resistance due to electron-phonon scattering, since the effect of rattling is excluded in this case. Assuming the carrier concentration dependence of thermal resistance does not vary much in unfilled and filled $CoSb_3$, this shall allow us to understand better the effect of rattling on thermal conductivity reduction, whether it is there and if it does, to what extent. It is also encouraged to measure the speed of sound velocities on Ni or Te-doped $CoSb_3$ samples. The closeness in lattice constant between undoped and doped samples will tell more about the mechanism in lattice softening (decrease of elastic moduli) with doping.

Chapter 5

Phase diagram studies in *n*-$CoSb_3$ skutterudites

5.1 Summary

In Chapter 3 the electronic origin of high thermoelectric performance of $CoSb_3$ skutterudties was investigated. In Chapter 4 the role of fillers in thermal transport was also discussed. So far we have gained some insight of physics as for why high *zT* can be achieved in skutterudites, the next step would be how we can synthesize high *zT* skutterudites from a materials scientist perspective. To optimize both electronic and thermal transport properties, precise doping control is required. This leaves us a few questions that need to be addressed. Firstly, when filler atom R is added to the $CoSb_3$ matrix, is the void the only soluble site? If not what are the other possibilities? Secondly, what is the solubility limit (equals to commonly known filling fraction limit (FFL) when the void is the only soluble site) for each type of filler? Is it a single value? Thirdly, how can we achieve precise doping control with large tolerance of synthesis uncertainty in a repeatable manner? This is important for large-scale commercialization of skutterudites in the future. Because solubility limit is a variable that exists at thermodynamic equilibrium, all the questions mentioned above cannot be answered without a careful and complete phase diagram study. By adding R into $CoSb_3$, a ternary system is under study, which leads to the breakdown of previous experiences in determining solubility limit in binary systems (impurity detection, Vegard's law etc.). In the following sections, Section 5.2 shall describe in great details the methodology of how to apply phase diagram study in studying skutterudites. Sections 5.3 to 5.5 lays out the experimental results of several ternary systems (R-Co-Sb, with R = Ga, In, Yb, Ce), which answers the questions listed above. The results presented here are mainly reproduced based on the following published papers with copyright permission acquired:

Advanced Functional Materials **23**, 3194-3203 (2013,
Copyright Wiley-VCH Verlag GmbH & Co. KGaA.)[16];
Energy and Environmental Science **7**, 812-819 (2014,
http://pubs.rsc.org/en/Content/ArticleLanding/2014/EE/c3ee43240h#!divAbstract)[17];
Journal of Materiomics 1, 75-84 (2015,
http://www.sciencedirect.com/science/article/pii/S235284781500009X)[50];

Nature Communications **6**, 7584(1-7) (2015, http://www.nature.com/ncomms/2015/150720/ncomms8584/full/ncomms8584.html)[20].

The readers are welcome to refer to these papers for more details. Section 5.6 discusses the influence of precipitation on the stability and lifetime performance of optimized compositions. Section 5.7 is the conclusion and discusses possible future work.

5.2 Methodology

The goal of phase diagram study of these R-Co-Sb ternary systems is to map out their isothermal sections at various temperatures lower than 874℃ (peritectic temperature of $CoSb_3$ decomposition)[106]. From these isothermal sections, not only phase regions near the skutterudite phase can be revealed, but also solubility of R as well as its temperature dependence can be extracted. To lower the experimental burden, only a subsection with $CoSb_3$ phase included of the full isothermal section is studied, e.g., $YbSb_2$-$CoSb_2$-Sb rather than Yb-Co-Sb. The methodology is explained in nine steps with the Yb-Co-Sb ternary system illustrated as an example.

Step one: Gather binary phase diagram information

Knowledge of binary phase diagrams is required, as shown in Figure 5.1. Most binary phase diagrams are available on the website: http://www1.asminternational.org/asmenterprise/apd/. Occasionally there are more than one phase diagram available for the same system. Either the most updated phase diagram determined from experimental work is preferred or it is recommended to choose the ones determined by the same group (Okamoto in this case) for systems in the study to keep it consistent.

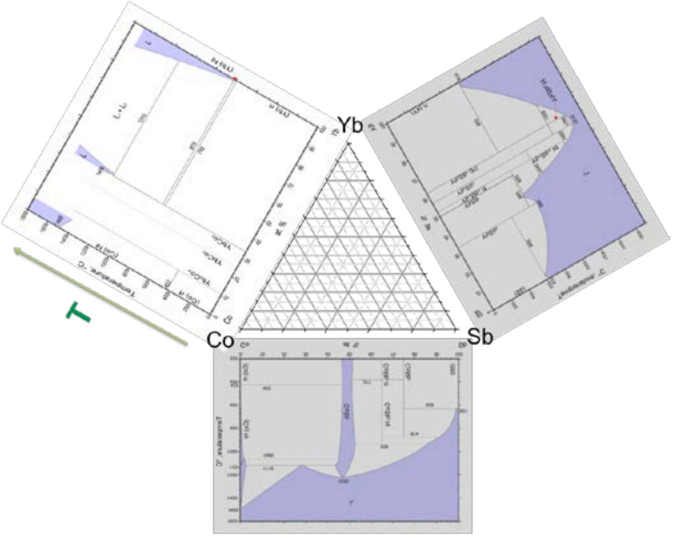

Figure 5.1 Binary phase diagrams of Yb-Co, Yb-Sb and Co-Sb systems[106-108]. Green arrow indicates the temperature dependence.

Step two: Select a temperature for isothermal section mapping

Samples will be annealed at the selected temperature for isothermal section mapping to reach thermodynamic equilibrium. As a result, neither should it exceed the maximum temperature of phase stability of the target phase, nor should it be too low such that thermodynamic equilibrium is hard to reach on an economic time scale. Temperatures between 500℃ and 850℃ are in the good range. Here we chose 700℃ for an example.

Step three: Determine nominal compositions for sample synthesis.

Get binary phases from binary phase diagrams (R-Co, R-Sb, Co-Sb) at the chosen temperature 700℃, which are represented as red dots along axis on the Yb-Co-Sb isothermal section in Figure 5.2. Estimate phase regions around target phase $CoSb_3$. Boundaries of phase regions are estimated and shown as black lines in the $YbSb_2$-$CoSb_2$-Sb section. Nominal compositions are chosen for sample synthesis, which are represented as black circles in the highlighted orange oval, as shown in Figure 5.2. These black circles are selected to scatter among different phase regions. The nominal compositions are listed in Table 5.1 to give an idea how off-stoichiometry they are.

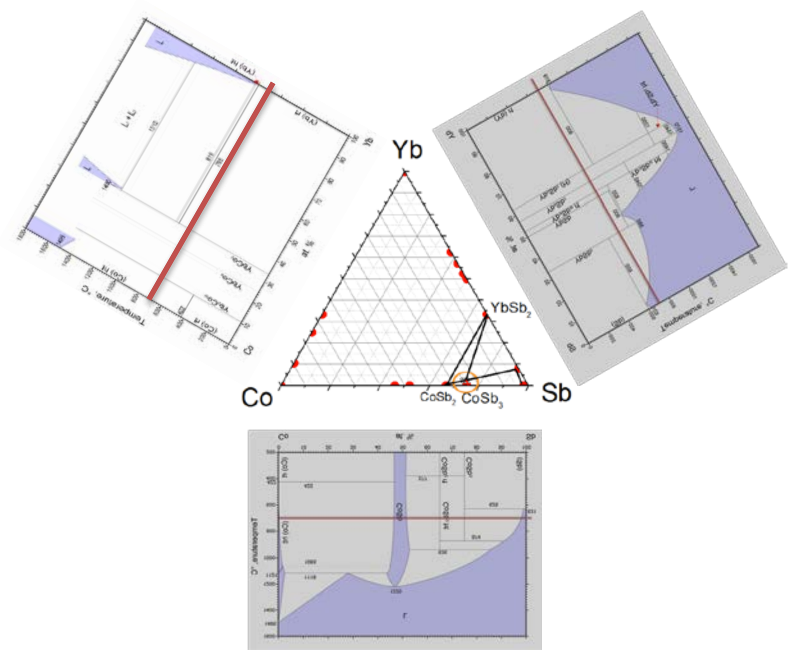

Figure 5.2 Selected nominal compositions near target phase $CoSb_3$ for phase region identification in the Yb-Co-Sb isothermal section at 700°C.

Table 5.1 Selected nominal compositions for investigation of Yb-Co-Sb isothermal section at 700°C.

Nominal	Estimated phase region
#1 $Yb_{0.25}Co_{3.8}Sb_{12.2}$	$Yb_xCo_4Sb_{12}$ + liquid Sb
#2 $Yb_{0.25}Co_4Sb_{12}$	$Yb_xCo_4Sb_{12}$
#3 $Yb_{0.25}Co_{4.2}Sb_{11.8}$	$Yb_xCo_4Sb_{12}$ + $CoSb_2$
#4 $Yb_{0.5}Co_4Sb_{12}$	$Yb_xCo_4Sb_{12}$ + $CoSb_2$ + $YbSb_2$
#5 $Yb_{0.5}Co_{4.2}Sb_{11.8}$	$Yb_xCo_4Sb_{12}$ + $CoSb_2$ + $YbSb_2$
#6 $Yb_{0.5}Co_{3.9}Sb_{12.1}$	$Yb_xCo_4Sb_{12}$ + $YbSb_2$
#7 $Yb_{0.5}Co_{3.8}Sb_{12.2}$	$Yb_xCo_4Sb_{12}$ + $YbSb_2$ + liquid Sb

Step four: Sample synthesis.

Synthesize samples with selected nominal compositions in step three in a melting and annealing method. The annealing temperature has to be the same as selected isothermal section temperature, which is 700°C. The annealing time is chosen to be one week to ensure thermodynamic equilibrium and homogenization of filler distribution. For more synthesis details please refer to Chapter 2 (Section 2.2).

Step five: Phase identification and chemical composition characterization.

Check the vacuum inside the ampoule. If it is good then proceed to break the ampoule and take the ingot out. Cut the ingot in halves. Take one half to X-ray diffraction and the other half to scanning electron microprobe for phase identification. The actual filler content in the matrix skutterudite phase is determined by electron probe microanalysis. Samples should be characterized in one single experimental routine to avoid any unwanted discrepancies in experimental conditions, such as stability of the electron beam, sample surface contamination, etc. The thermodynamic equilibrium is achieved when the standard deviation of filler content is less than the precision limit of EPMA, which is confirmed in all samples from experimental results.

Step six: Determine phase region relations.

With determined compositions of the equilibrium phases for each nominal composition, the phase regions near $CoSb_3$ can be determined, as shown in Figure 5.3. The solubility limit of R in $CoSb_3$ can be found in the composition on the furthest point of $CoSb_3$ phase region extending towards R (red dot in Figure 5.4). The solubility limit of Yb in $Yb_xCo_4Sb_{12}$ at 700℃ is determined to be $x = 0.44 \pm 0.01$.

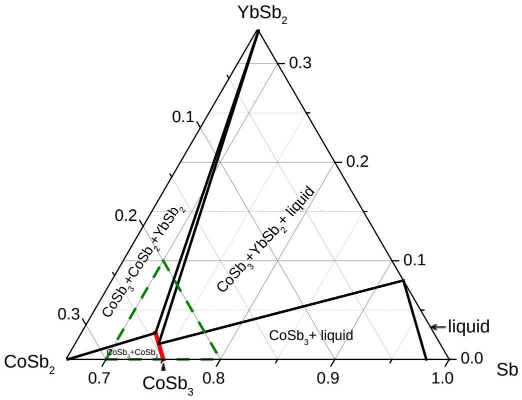

Figure 5.3 Phase regions near $CoSb_3$ determined from synthesized samples in a section of Yb-Co-Sb isothermal ternary phase diagram at 700℃ ($YbSb_2$-$CoSb_2$-Sb). The red line represents the solubility region of $CoSb_3$. A magnification of the triangle area formed by green dashed lines is shown in Figure 5.4, 5.6, and 5.7 at different temperatures (973K, 873K, and 1023K, respectively).

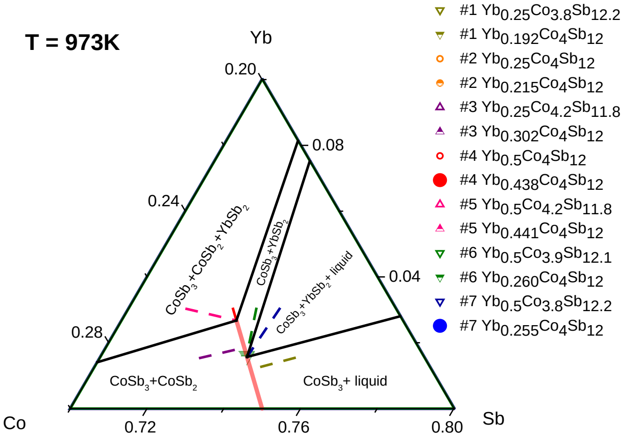

Figure 5.4 Magnification of phase regions near $CoSb_3$ of isothermal section of Yb-Co-Sb ternary phase diagram system at 973K. The solid red line indicates the void filling in the direction $(Yb_{VF})_xCo_4Sb_{12.}$ The red point represents the stable composition (with maximum solubility x = 0.44±0.01) of the skutterudite phase obtained when the nominal composition is in the Co-rich three-phase region ($YbSb_2$, $CoSb_2$, and $Yb_xCo_4Sb_{12}$). The blue point represents the stable composition of the skutterudite phase obtained when the nominal composition is in the Sb-rich three-phase region ($YbSb_2$, liquid Sb, and $Yb_xCo_4Sb_{12}$). The nominal sample compositions are shown as open symbols. Solid symbols represent the composition of the skutterudite majority phase using the experimental EPMA value for Yb content, and positioned on the red line. The nominal (open symbols) and experimental compositions (solid symbols) are connected with a dotted line.

Step seven: Determine temperature dependence of solubility.

Repeat step 2-6 for different annealing temperatures to get the temperature dependence of solubility. Note that since the phase relations do not change drastically with temperature and our interest is mainly about solubility, nominal compositions can be chosen in the phase regions that will produce stable compositions of skutterudites (discussed later in Section 5.4). Maximum solubility is often related to stable compositions and this can allow us to minimize experimental load. The temperature dependence for Yb solubility in $CoSb_3$ is shown in Figure 5.5 for example. As we can see in Figure 5.5, as temperature increases, Yb solubility increases with about five times difference (x = 0.11±0.02 at 773K and x = 0.49±0.02 at 1073K). This large variance gives us another degree of freedom to tune the carrier concentration and thus allows us to optimize thermoelectric properties.

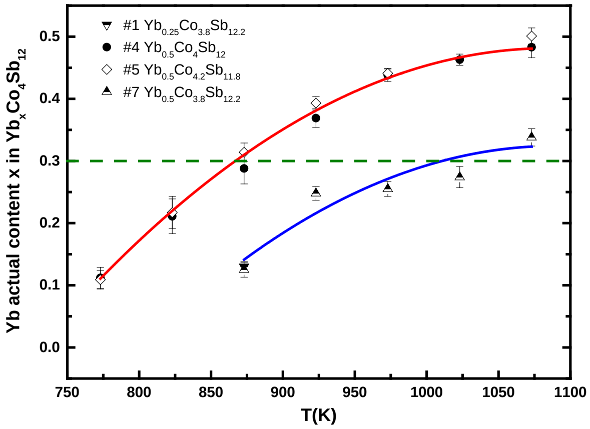

Figure 5.5 Temperature dependence of solubility limit of Yb in Yb-doped skutterudites $Yb_xCo_4Sb_{12}$. The red line indicates the temperature dependence of the actual Yb content in the stable skutterudite composition represented as a red point (maximum solubility) in Figure 5.4. The blue line shows the temperature dependence of the actual Yb content in the stable skutterudite composition represented as a blue point in Figure 5.4. The dashed green line is the actual Yb content ($x = 0.3$) targeted for optimized thermoelectric properties, which crosses the solubility lines at 873K and 1023K, respectively.

Step eight: Determine synthesis parameters for optimized compositions.

Choose an annealing temperature at which the solubility line crosses the optimized composition line. Then select corresponding phase region such that the resulting stable compositions will produce optimized doping content. For example, if the annealing temperature in the Yb-Co-Sb system is chosen to be 873K, then the nominal composition (red triangular and diamond samples in Figure 5.6) should stay in the Co-rich three-phase region ($YbSb_2$, $CoSb_2$, and $Yb_xCo_4Sb_{12}$). If the annealing temperature is chosen to be 1023K, then the nominal composition (blue circle sample in Figure 5.7) should stay in the Sb-rich three-phase region ($YbSb_2$, liquid Sb, and $Yb_xCo_4Sb_{12}$).

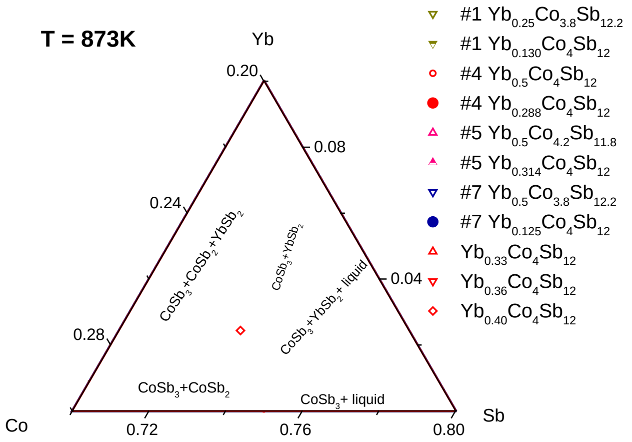

Figure 5.6 Magnification of phase regions near $CoSb_3$ of isothermal section of Yb-Co-Sb ternary phase diagram system at 873K. Samples with nominal compositions $Yb_xCo_4Sb_{12}$ (x = 0.33, 0.36, 0.40) are in Co-rich three-phase region and annealed at 873K, which gives desired optimum Yb content x = 0.30 (red dot).

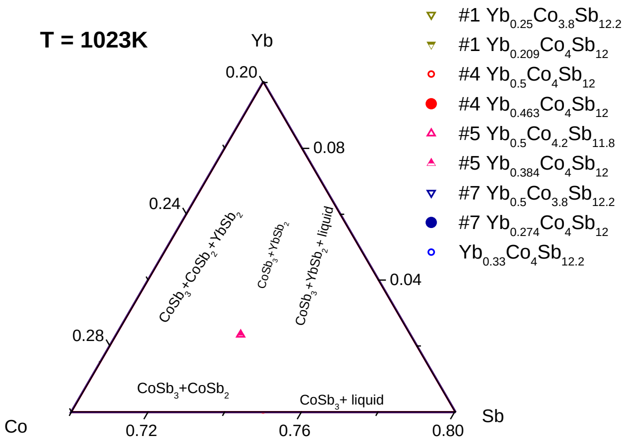

Figure 5.7 Magnification of phase regions near $CoSb_3$ of isothermal section of Yb-Co-Sb ternary phase diagram system at 1023K. Sample with nominal composition $Yb_xCo_4Sb_{12.2}$ (x = 0.33) is in Sb-rich three-phase region and annealed at 1023K, which gives desired optimum Yb content x = 0.30 (blue dot).

Step nine: TE performance characterization.

Characterize thermoelectric properties of samples with optimized compositions synthesized in step eight. As shown in Figure 5.8, the thermoelectric performance does not vary much among different compositions. Thus it enables the production of optimized skutterudites at an easily reproducible and commercial scale.

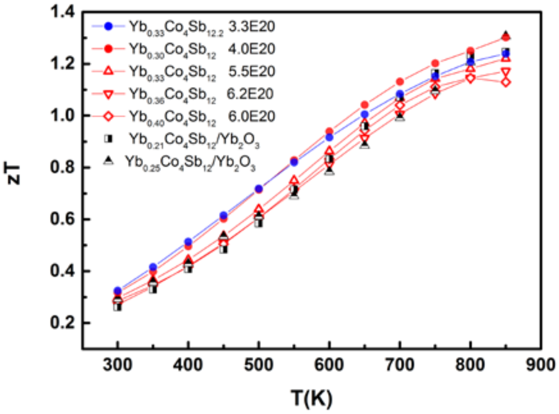

Figure 5.8 Temperature dependence of the thermoelectric figure of merit *zT* for Yb-doped skutterudites targeting the same $Yb_xCo_4Sb_{12}$ composition with samples annealed at 873K without excess Sb (red stable point) and 1023K with excess Sb (blue stable point). The dark symbols are reference data from Zhao *et al*[109].

5.3 Soluble site other than the void

5.3.1 Solubility debate of In and Ga

One important criterion in determining which site to go to for foreign atom R in $CoSb_3$ sktterudites is the size and electronegativity difference between R and possibly soluble sites. The void site (radius 1.89Å)[9] is usually large enough for most alkali, alkaline earth, group 13, and rare earth elements to go in, as shown in Table 4.1 [87]. Due to the electro-positivity of alkali, alkaline earth, and rare earth elements, it is impossible for them to substitute Sb. The large size difference between Co^{3+} and these filler ions also hinders them from substituting Co. As a result, the void site is the only soluble site for all the atoms listed in Table 4.1 except for two elements, that is, group 13 elements Ga and In.

The soluble sites as well as doping nature for both Ga and In generate a lot of debate. Theoretically, a selection rule based on the electronegativity difference between Sb and R[110] was proposed by Shi *et al*. It was predicted that Ga and In could not be filled into the void site. Experimentally, it was assumed that group 13 elements occupy the void position exclusively and donate electrons, resulting in *n*-type ternary materials. Tl was expected to donate one electron in $CoSb_3$ [111], but for In and Ga it is not clear how many electrons are donated from these void-filling atoms.[112-115] Several studies have shown GaSb- and InSb- containing composites were formed and concluded that Ga and In have virtually no solubility in $CoSb_3$.[51,116] There was yet another report claiming that In could possibly substitute for Sb in $CoSb_3$ and hardly fill into the void position.[117] Finally, since Ga^{3+} and In^{3+} are similar in size to Co^{3+}, it may also be possible for these atoms to substitute for the transition metals. The close electronegativity values among In (1.78), Ga (1.81), Sb (2.05), and Co (1.88) also support the possibility of both Co and Sb substitution.

Complicating this debate is the possibility that there is no dominant single defect type in skutterudites with group 13 impurities, but that compound defects form as commonly found in wide-gap oxides. Amphoteric impurities were also observed in a few thermoelectric materials, in which one single-type impurity forms both donor and acceptor defects.[118] If both defects exist, even separately, and form in equal amounts the material will be nearly fully compensated with few free carriers, as found in Ga-doped $CoSb_3$ skuterudites.[113]

5.3.2 DFT calculations of In-doped $CoSb_3$ systems

Before taking on experimental study, DFT calculations were applied to help navigate the research direction. Two types of calculations were performed, the first being the band structures of $CoSb_3$ and different Ga/In-doped systems. Due to the similarity between band structures of Ga- and In-doped systems, only the results on In-doped systems are shown in Figure 5.9. The second is the formation energies of possible defects as a function of both doping level and Fermi level. Results are shown in Figure 5.10 and 5.11.

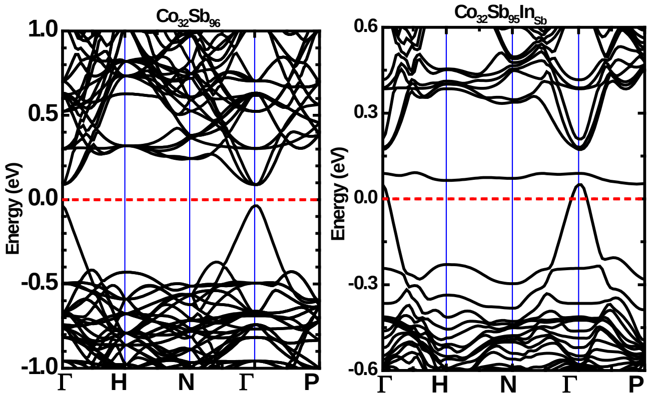

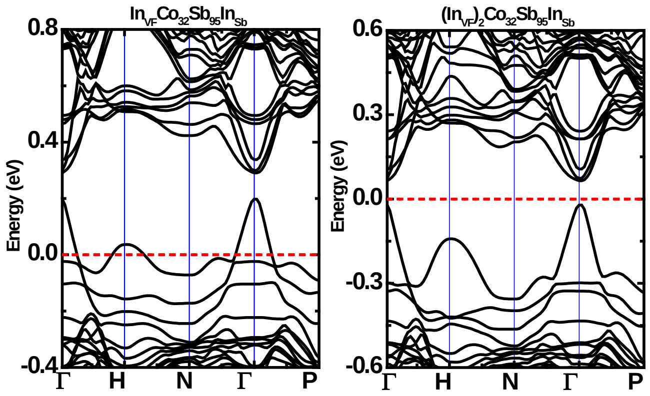

Figure 5.9 Band structures of $CoSb_3$ and different In-doped systems. The dashed lines are the Fermi levels.

Figure 5.9 shows the band structures of pure $CoSb_3$, $Co_{32}Sb_{95}In_{Sb}$, $In_{VF}Co_{32}Sb_{95}In_{Sb}$, and $(In_{VF})_2Co_{32}Sb_{95}(In_{Sb})$. Results show that In doping at different sites has different effect on band structures. Pure $CoSb_3$ is a semiconductor with small band gap. One In atom at the Sb substitution site generates a deficiency of two electrons and one In atom at the void-filling position adds one extra electron compared to pure $CoSb_3$. As a result, one In substituting for Sb leads to imbalanced charge and pushes up one Sb-based band above the Fermi level, which brings the system to an unstable state at no charge compensation. For the same reason $In_{VF}Co_{32}Sb_{95}In_{Sb}$ is also hardly stable whereas $(In_{VF})_2Co_{32}Sb_{95}(In_{Sb})$ is charge-balanced and is thus a semiconductor. Intuitively $In_xCo_4Sb_{12-x/3}$, equivalently $(In_{VF})_{2x/3}Co_4Sb_{12-x/3}(In_{Sb})_{x/3}$, is expected to be a stable skutterudite phase. Similar results are also observed in Ga-doped $CoSb_3$, namely, $(Ga_{VF})_{2x/3}Co_4Sb_{12-x/3}(Ga_{Sb})_{x/3}$, is expected to be a stable skutterudite phase as well.

The charged defects from In-containing $CoSb_3$, such as In_{Co}, In_{Sb} substitutions in the Co-Sb framework, In_{VF} on the crystal void site, and their combinations, with different charge states *q* are calculated by *ab initio* methods. The defect formation Gibbs free energy per impurity can be written as follows:

$$\begin{aligned}\Delta G_f(y,w,z,q) = [&E_{tot}(In_yCo_{32-w}In_wSb_{96-z}In_z,q) - E_{tot}(CoSb_3,bulk)\\ &+z\mu_{Sb} + w\mu_{Co} - (Vy+w+z)\mu_{In} + q(\varepsilon_F + E_V + \Delta V)]/(y+w+z)\end{aligned} \qquad \text{(Eq. 5.1)}$$

where $E_{tot}(In_yCo_{32-w}In_wSb_{96-z}In_z,q)$ is the total energy of a 2×2×2 supercell $In_yCo_{32-w}In_wSb_{96-z}In_z$. $E_{tot}(CoSb_3,bulk)$ is the total energy of supercell of bulk $CoSb_3$. y is the filling fraction of In in crystal voids, w is the substituting fraction at Co sites, and z is the substituting fraction at Sb sites. μ_R is chemical potential for R ($R = In, Co, Sb$), q is the charge state of the point defect, ε_F is the

Fermi level, referring to the valence band maximum E_v in $CoSb_3$, and ΔV is the correction term to align the reference potential in the defect supercell with that in the perfect supercell.

Figure 5.10(a) shows the calculated ΔG for $(Ga_{VF})_xCo_4Sb_{12-x/2}(GaSb)_{x/2}$ at 923 K possesses the lowest values and stays negative at about $x \leq 0.25$. The formation energy (-0.116 eV) of GaSb, a known secondary phase in Ga-contained $CoSb_3$, is also shown in Figure 5.10(a), and it becomes lower than ΔG_f for $(Ga_{VF})_xCo_4Sb_{12-x/2}(GaSb)_{x/2}$ after $x \geq 0.08$, indicating that $(Ga_{VF})_xCo_4Sb_{12-x/2}(GaSb)_{x/2}$ is the most stable phase when x is less than 0.08. In other words, the maximum filling fraction for Ga in Co_4Sb_{12} should be around 0.08, and the total Ga atoms in a unit of Co_4Sb_{12} should be around 0.12 (=1.5x) at 923 K. Similarly, a solubility of In in a unit of Co_4Sb_{12} at around 0.27 (=1.5*0.18, x = 0.18 is the filling fraction limit) at 873K is predicted.

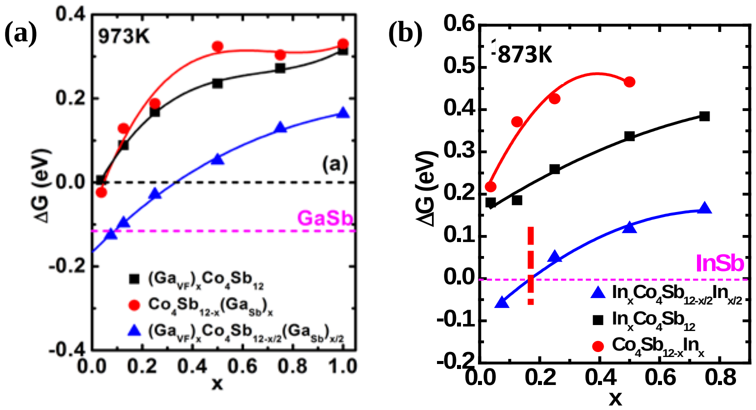

Figure 5.10 Calculated Gibbs free energy (ΔG) as a function of doping content x of (a) Ga in Ga-$CoSb_3$ skutterudite at 923K and (b) In in In-$CoSb_3$ skutterudite at 873K.

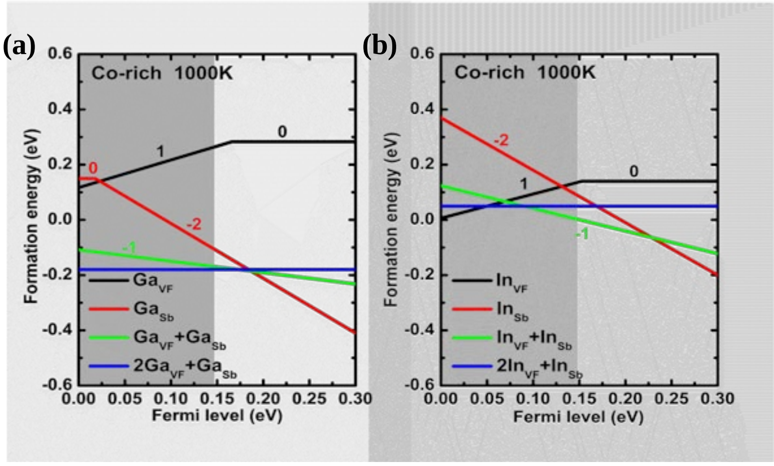

Figure 5.11 Formation energies of possible defects as a function of Fermi level at the Co-rich limit in Ga-containing (a) and In-containing (b) skutterudites. The zero Fermi level corresponds to the top of the valence band, and the width of shadowed area indicates the energy gap. The number for labeling is the charge state of the point defect.

Figure 5.11 shows the defect formation energy as a function of Fermi level at the Co-rich limit, where the system is connected to a Co reservoir. Ga-containing skutterudites form stable charge-compensated compound defects (CCCD) $(Ga_{VF})_{2x/3}Co_4Sb_{12-x/3}(Ga_{Sb})_{x/3}$ when the Fermi level falls in the gap area. The formation energy of the single filling defect $(Ga_{VF})_xCo_4Sb_{12}$ is always very high. In contrast, In-containing skutterudite favors In-filling into the void at relatively low Fermi level instead, and dual-site In occupancy can form as the Fermi level increases. In the gap area 0~0.17eV (shadow in Figure 5.11), Ga always forms the charge compensated defect, and In forms either a single filling, or a dual-site defect with or without charge compensation, at different Fermi levels which likely corresponds to different experimental conditions such as the amount of indium impurity or the stoichiometric ratio of Co/Sb.

The results from theoretical study above can be summarized as follows. Firstly, unlike for other fillers, the void is NOT the only soluble site for both In and Ga. Secondly, Ga or In-doping in $CoSb_3$ based skutterudites results in both void filling and Sb substituting, which leads to compound defects (charge-compensated in the Ga case and not fully charge-compensated in the In case). Thirdly, the solubility limit is predicted to be 0.12 for Ga in a Co_4Sb_{12} unit at 923K and 0.27 for In at 873K.

The solubility region can then be estimated to be mainly directed along the direction of $(R_{VF})_{2x/3}Co_4Sb_{12-x/3}(R_{Sb})_{x/3}$ to $CoSb_3$ (R = Ga, or In). This is different from the commonly known direction of $(R_{VF})_x$ Co_4Sb_{12} to $CoSb_3$ when the void is the only soluble site for alkali, alkaline earth, and rare earth element fillers. The experimental phase diagram study is accordingly designed as shown in Section 5.3.3 below.

5.3.3 Phase diagram study of In-Co-Sb system

Due to the similarity between Ga and In-doped $CoSb_3$, we will only take the In-doped $CoSb_3$ system as an example for phase diagram study illustration. Samples with nominal compositions along or off the solubility direction $(R_{VF})_{2x/3}Co_4Sb_{12-x/3}(R_{Sb})_{x/3}$ to $CoSb_3$ are synthesized. Two sets of samples were prepared by a process of melting followed by high-temperature annealing at 873K for 7 days. One set of samples has nominal compositions $In_xCo_4Sb_{12-x/3}$ (or equivalently $(In_{VF})_{2x/3}Co_4Sb_{12-x/3}(In_{Sb})_{x/3}$ where In_{VF} and In_{Sb} stand for void-filling, and Sb-substituting In atom, respectively) with x changing from 0.075 to 0.60. The other set is $In_{0.3}Co_{4-y}Sb_{11.9+y}$ (equivalently $(In_{VF})_{0.20}Co_{4-y}Sb_{11.9+y}(In_{Sb})_{0.10}$) with y changing from -0.20 to 0.20. High-purity elements Co

(99.99%, shot), Sb (99.9999%, piece), and In (99.999%, shot) were used as raw materials. XRD, SEM, and EPMA were performed to identify phases and determine chemical compositions.

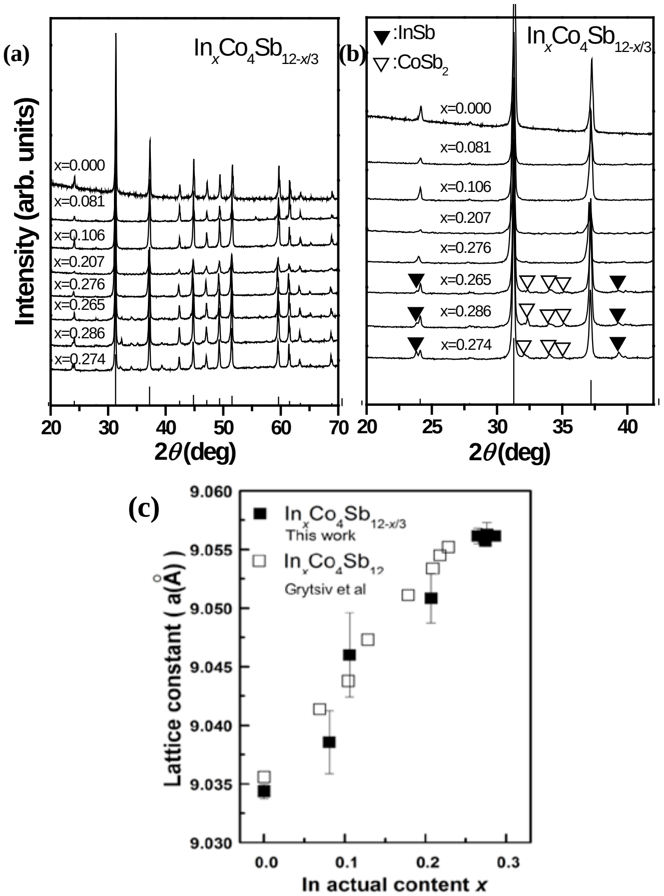

Figure 5.12 (a) XRD patterns of the In-containing skutterudites with nominal compositions $In_xCo_4Sb_{12-x/3}$ (x=0, 0.075, 0.15, 0.225, 0.30, 0.375, 0.45, 0.60) and corresponding actual compositions x=0, 0.081, 0.106, 0.207, 0.276, 0.265, 0.286, 0.274. (b) Magnification of the XRD patterns. (c) Dependence of lattice parameter on actual indium content x. Filled symbols are from this work; open squares denote data from Grytsiv *et al*[119].

Figure 5.12(a, b) shows the X-ray diffraction results of annealed $In_xCo_4Sb_{12-x/3}$ samples with actual compositions x, as determined from electron probe microanalysis. All major diffraction peaks are indexable to the skutterudite phase, as identified using JCPDS File No. 65-3144 for $CoSb_3$. However, in samples with the nominal indium content x higher than 0.30 (lower three patterns), small amount of impurity phases (secondary phases other than skutterudite phase), especially InSb and $CoSb_2$, are always observed, which indicates that those samples are outside the single-phase region.

Figure 5.12(c) plots the dependence of the lattice parameter calculated from the XRD data on the actual indium content x. The dependence in the current work agrees with the data of Grytsiv et al[119].

As x increases, the lattice parameter increases and becomes saturated when nominal $x \geq 0.30$, strongly supporting that the solubility limit of indium is around 0.30.

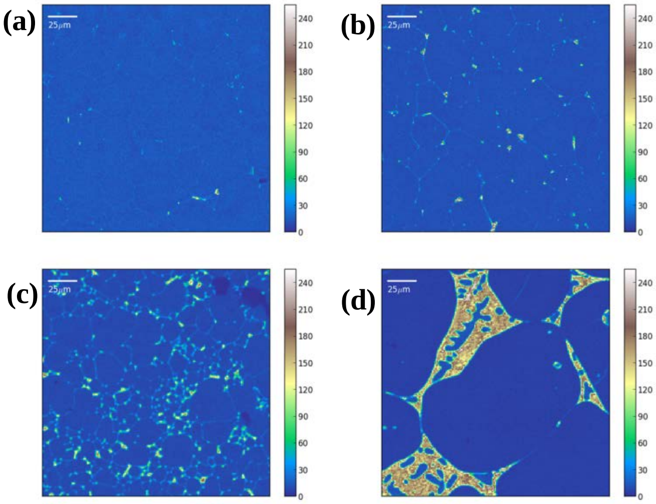

Figure 5.13 Electron probe microanalysis (EPMA) indium maps in samples with different nominal compositions. (a) $In_{0.225}Co_4Sb_{11.925}$, (b) $In_{0.30}Co_4Sb_{11.90}$, (c) $In_{0.30}Co_{4.2}Sb_{11.7}$, and (d) $In_{0.30}Co_{3.8}Sb_{12.1}$.

Electron probe microanalysis (EPMA) measurements were carried out at ten different locations on the skutterudite phase region in samples and the average total indium contents are listed in Table 5.2. The EPMA maps show that there is a significant volume fraction of In-rich impurity phases in the $In_{0.3}Co_{4-y}Sb_{11.9+y}$ samples with compositions that are off the Co/Sb ratio of the CCCD sample $(In_{VF})_{0.20}Co_4Sb_{11.90}(In_{Sb})_{0.10}$ (see Figure 5.13c and 5.13d). However, in CCCD samples, the indium is nearly completely homogeneously distributed (see Figure 5.13a and 5.13b) with few secondary phases and the solubility limit of indium is estimated to be around x=0.27±0.01 according to EPMA data. When the indium amount exceeds 0.27 in CCCD samples, secondary phase such as liquid and $CoSb_2$ is observed in SEM, which is consistent with XRD data presented above. The sensitivity of formation of secondary phases to the ratio of Co/Sb in samples strongly supports the hypothesis that impurity indium atoms form compound defects in $CoSb_3$ by occupying both the void and Sb sites.

Table 5.2 Nominal indium content and total indium content in the skutterudite phase estimated by EPMA for In-containing skutterudites with different compositions. Boldface indium contents correspond to the same skutterudite phase composition $In_{0.27\pm0.01}Co_4Sb_{11.9}$ represented by a magenta circular symbol in Figure 5.14b.

Samples	**Nominal In content**	**EPMA In content**
$In_{0.075}Co_4Sb_{11.975}$	0.075	0.081±0.004
$In_{0.15}Co_4Sb_{11.95}$	0.15	0.106±0.016

$In_{0.225}Co_4Sb_{11.925}$	0.225	0.207±0.013
$In_{0.30}Co_4Sb_{11.90}$	0.30	**0.276±0.014**
$In_{0.375}Co_4Sb_{11.875}$	0.375	**0.265±0.010**
$In_{0.45}Co_4Sb_{11.85}$	0.45	**0.286±0.012**
$In_{0.60}Co_4Sb_{11.80}$	0.60	**0.274±0.009**
$In_{0.30}Co_{3.8}Sb_{12.1}$	0.30	0.086±0.005
$In_{0.30}Co_{3.9}Sb_{12}$	0.30	0.148±0.011
$In_{0.30}Co_{4.1}Sb_{11.8}$	0.30	**0.287±0.020**
$In_{0.30}Co_{4.2}Sb_{11.7}$	0.30	**0.261±0.012**
$In_{0.20}Co_4Sb_{11.8}$	0.20	0.084±0.016
$In_{0.20}Co_4Sb_{12}$	0.20	0.150±0.020

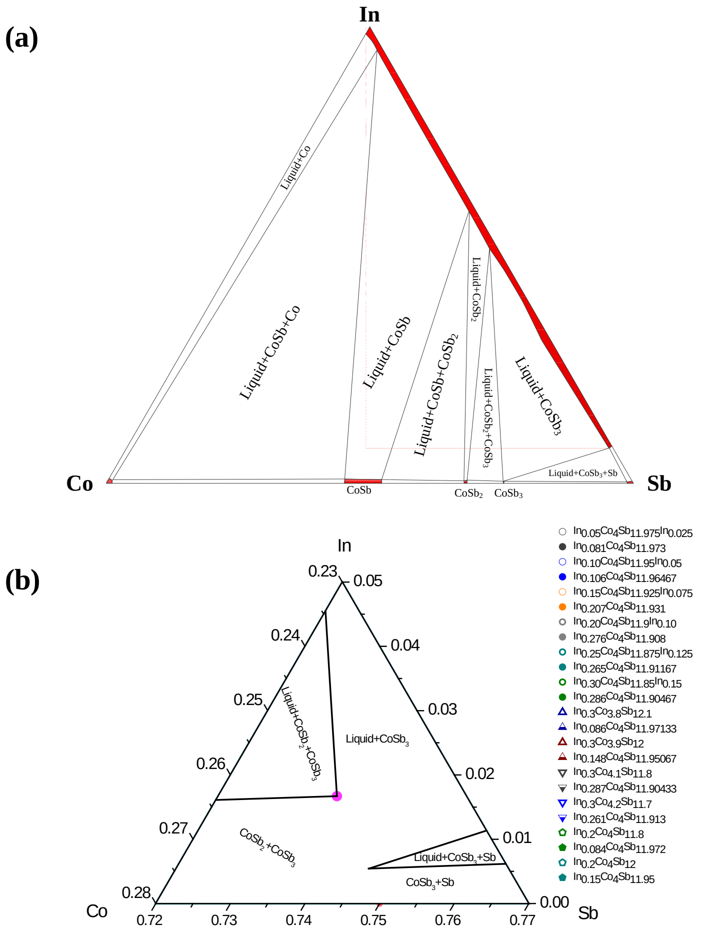

Figure 5.14 Proposed phase diagram for In-containing skutterudites at 873K. (a) Full diagram with related binary phases and approximate regions of solubility indicated by red regions. (b) Phase regions enlarged near $CoSb_3$. Because of the stability of indium in dual sites (CCCD compositions) the region of indium solubility is extended as a red line in the direction of $(In_{VF})_{2x/3}Co_4Sb_{12-x/3}(In_{Sb})_{x/3}$ up to x=0.27. The solid purple line indicates the void filling in the direction $(In_{VF})_xCo_4Sb_{12}$ up to x=0.27. The magenta circular symbol represents the composition of skutterudite phase $In_{0.27}Co_4Sb_{11.9}$ obtained when the nominal composition is in the three-phase region (liquid, $CoSb_2$ and In-$CoSb_3$). The nominal sample compositions are shown as open symbols. Solid symbols represent the

composition of the skutterudite majority phase using the experimental EPMA value for indium content which is below 0.27 for all samples, and positioned on the red CCCD line. The nominal (open symbols) and experimental compositions (solid symbols) are connected with a dotted line. The samples with nominal CCCD compositions when $x<0.30$ appear to be within the solubility limit, the closed symbols of which are shifted away from the red solubility line according to the observed carrier concentration as explained later.

The proposed phase diagram of the In-containing skutterudites at 873K is shown in Figure 5.14a, and is based on general knowledge of the binary phase diagrams. The related binary phases of In, Co, and Sb are shown on the axes including the known regions of solid or liquid solubility for the binary compounds and a rough estimate of the solubility of the ternary compounds. The exact regions of solid solubility of $CoSb_2$ and $CoSb_3$ are not known but they are enlarged for clarity in Figure 5.14a. The white regions of Figure 5.14a designate regions that are expected to contain two or three phases in equilibrium at 873K.

The region near $CoSb_3$ is enlarged in Figure 5.14b. Our experimental data suggest that the region of indium solubility extends toward the CCCD samples, $(In_{VF})_{2x/3}Co_4Sb_{12-x/3}(In_{Sb})_{x/3}$, with an estimated maximum x value around 0.27. When x exceeds 0.27, the CCCD samples contain an In-dual-site-doped skutterudite phase with indium doping level around x=0.27 and impurity phases InSb and $CoSb_2$. When the nominal composition is off the Co/Sb ratio of CCCD $(In_{VF})_{2x/3}Co_4Sb_{12-x/3}(In_{Sb})_{x/3}$ samples, significant impurity phases form from x= 0.30 samples.

When the nominal composition is slightly Sb-rich ($In_{0.3}Co_{4-y}Sb_{11.9+y}$, $y>0$), the nominal composition is in a two-phase region between In-$CoSb_3$ and liquid In-Sb where both phases have variable indium content in this region. According to the phase rule, the degrees of freedom F=C-P+0=3-2=1 where C means the number of components and P means the number of phases, 0 indicates both temperature and pressure are fixed. Thus this two-phase region has an additional degree of freedom to describe the tie line between which phases with variable In content form. We observe that the tie line connecting the nominal composition and the skutterudite phase is quite steep, which leads to a much lower In content in the skutterudite phase with an In-rich liquid In-Sb impurity phase. It is reasonable that In prefers the high entropy of the liquid rather than the solid skutterudite phase.

In contrast to the Sb rich side, when the nominal composition is slightly Co-rich ($In_{0.3}Co_{4-y}Sb_{11.9+y}$, $y<0$), it is in a three-phase region between three phases with fixed compositions, approximately liquid InSb, $In_{0.27}Co_4Sb_{11.9}$ and $CoSb_2$. The compositions in a three-phase region are fixed because of the phase rule, F=C-P+0=3-3=0. The composition of the liquid InSb ($In_{0.53}Sb_{0.47}$) is fixed near the composition of the InSb phase that is stable up to 798.7K. Because the phase boundary between two-phase region and three-phase region must be a straight line, the point of contact (magenta circular symbol) between the skutterudite phase and the phase triangle must have relatively high indium content. Because of the phase rule all the compositions in this three-phase region will produce the same skutterudite composition with high actual indium content ($In_{0.27}Co_4Sb_{11.9}$). This was confirmed by the EPMA measurements to be $x=0.27\pm0.01$ as shown in Table 5.2.

The steep slope of the tie line on the Sb-rich side of the stable phase (two phase region: liquid and $CoSb_3$) results in relatively lower In content in the skutterudite phase, when compared to the fixed composition $In_{0.27}Co_4Sb_{11.9}$ obtained from samples with nominal compositions on the Co-rich side with sufficient indium content (three-phase region: liquid, $CoSb_2$, and $CoSb_3$). This indicates that being slightly Co-rich instead of Sb-rich is more favorable in order to achieve high indium content in the skutterudite phase. Moreover, it also sheds light on why there is a solubility difference when the skutterudite phase is in coexistence with different impurity phases[119]. As the phase width appears to be quite narrow, small variations of composition will lead to different two or three-phase equilibrium regions on the phase diagram which can explain why different attempts to produce the same material may in fact produce very different skutterudite materials with different filling fraction, and therefore different thermoelectric properties. In addition the Co-rich and Sb-rich sides of the single phase region (red line in figure 5.14b) will have different temperature dependent characteristics and could lead to different precipitation products as found in Zn-Sb[120]. For example, solid solubility is typically temperature dependent and can be used to form nano-scale coherent precipitates[121], which may explain the observance of InSb in some samples[51,122,123] but not others[124-127].

5.3.4 Thermoelectric Properties of In-$CoSb_3$

5.3.4.1 Electrical Transport

The temperature dependence of the Seebeck coefficients and electrical conductivities of $In_xCo_4Sb_{12-x/3}$ (EPMA determined x=0.081, 0.106, 0.207, 0.276) is shown in Figure 5.15a and 5.15b, respectively. All the samples show negative Seebeck coefficients throughout the whole temperature range, indicating *n*-type semiconductor behavior. With increasing temperature, the magnitude of the Seebeck coefficient increases first and starts decreasing after reaching a peak, which is possibly induced by the bipolar effect. Meanwhile, the electrical conductivity (Figure 5.15b) decreases smoothly as temperature increases. As In content increases, the electrical conductivity increases and the magnitude of Seebeck coefficient decreases, which suggests that some of the indium acts as an *n*-type dopant to increase the carrier concentration.

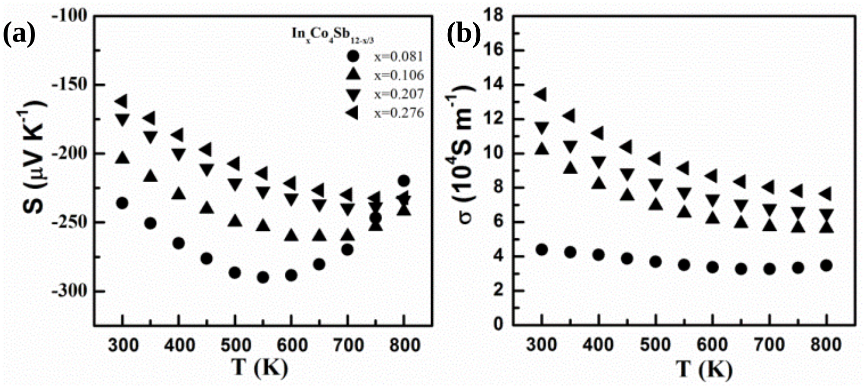

Figure 5.15 Temperature dependence of (a) the thermopower *S* and (b) electrical conductivity σ for samples of $In_xCo_4Sb_{12-x/3}$ with different indium impurity content.

Intrinsic $CoSb_3$ is a valence precise semiconductor where the doping effect of defects can be understood with Zintl chemistry[128]. Ga-containing $CoSb_3$ skutterudites $(Ga_{VF})_{2x/3}Co_4Sb_{12-x/3}(Ga_{Sb})_{x/3}$ form charge-compensated compound defects which also makes them valence precise semiconductors. An indium atom at the void filling site (In_{VF}) shows an effective charge state +1 and contributes one extra electron to the doped system. Indium atoms at the Sb-substitutional site accept two electrons. Thus, $(In_{VF})_{2x/3}Co_4Sb_{12-x/3}(In_{Sb})_{x/3}$ should also be a valence precise semiconductor as demonstrated in Figure 5.9.

However, the relatively high electron concentrations (as measured by Hall effect) and their dependence in the In-containing $CoSb_3$ samples compared to Ga-containing $CoSb_3$ samples suggests that the indium defects are not entirely charge compensated, with some excess indium as electron donor defects most likely In_{VF} (Figure 5.16a). Indeed Figure 5.11b predicts that one electron donor defects from In_{VF} are low energy defects particularly at low Fermi levels. Detailed calculations of all defects are necessary for quantitative discussion[129] and are described in detail elsewhere[130].

The mixed defect types (complex compound defects) may also lead to a slight change of the direction of the single-phase region (red line) in Figure 5.14b. For excess indium donor defects in the void filling site, the single-phase region would move toward the purple line ($In_xCo_4Sb_{12}$).

As shown in Figure 5.16b the *S*-*n* dependence in indium-containing complex compound defect samples follows the extrapolated curve of normal filled skutterudites[11,12,22,53,131]. Figure 5.16b further indicates that due to the In or Ga-rich secondary phases on the grain boundary (as observed in SEM), the $G_xCo_4Sb_{12}$ (G=In, or Ga) samples have very low electron concentrations and large thermopowers from low G content in the skutterudite phase[113,132]. That all the data fall on the same curve in Figure 5.16b also provides strong evidence that the band structure in In-containing skutterudites is virtually unchanged near the Fermi level because the same trend is observed in the normally filled as well as in the Ga-containing skutterudites. This is fully consistent with our band structure calculations shown in Figure 5.9 and discussions in Section 5.3.2.

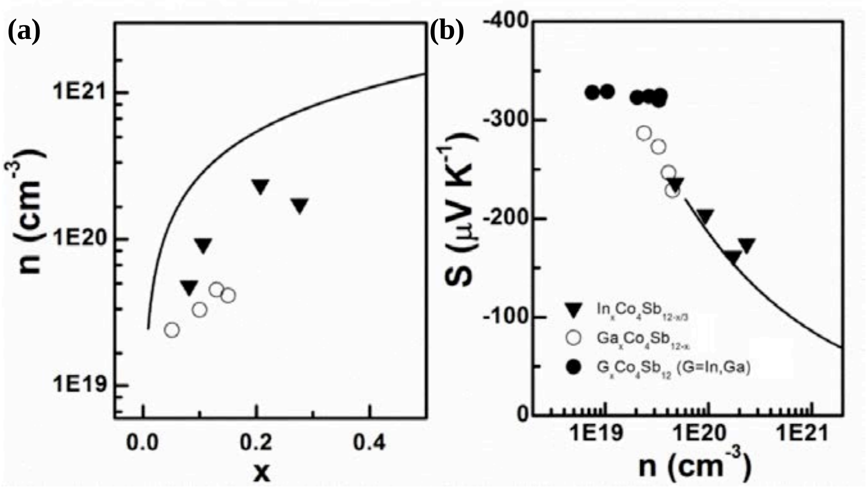

Figure 5.16 (a) Room temperature electron concentration (*n*) as a function of indium impurity fraction *x* in In-containing complex compound defect (CCD) skutterudites. The solid line represents the theoretical curve calculated by using $n=2x/a^3$ where *a* is the lattice constant of $CoSb_3$. (b) Room temperature *S* as a function of electron concentration for In-containing CCD skutterudites at 300 K. The *x* values are estimated by EPMA for CCD samples and CCCD samples from Qiu *et al*'s work[16] while they are the nominal values for the single-type defect samples from references (Harnwunggmoung *et al*[113] and Du *et al*[132]). The solid line represents the general trend for single filled-$CoSb_3$ with those typical electropositive filler species taken from literature[11,12,22,53,131].

5.3.4.2 Thermal Transport

Figure 5.17 shows the temperature dependence of total thermal conductivity (κ) of the samples $(In_{VF})_{2x/3}Co_4Sb_{12-x/3}(In_{Sb})_{x/3}$ with nominal charge-compensated compound defects. In the whole temperature range investigated, the total thermal conductivity for all samples are lower than 3.5 $Wm^{-1}K^{-1}$. As usual, κ_L is obtained by subtracting the electronic contribution from the total thermal conductivity using the Wiedemann-Franz law. We adopted a Lorentz number of 2.0×10^{-8} V^2K^{-2} to simplify the estimation of electronic thermal conductivity, and this value is also consistent with the experimentally estimated value based on our previous work on skutterudites[53]. All In-containing samples present strongly reduced κ_L as compared to binary $CoSb_3$ with κ_L ~ 10 $Wm^{-1}K^{-1}$ at 300 K. Compared with the observed dependence of κ_L on impurity filling fraction in the normal alkaline- or alkaline-earth-filled $CoSb_3$, κ_L reduction in the In-containing samples has a strong dependence on impurity content, as shown in Figure 5.17b. At In content as low as 0.106, κ_L could be reduced to 2.62 $Wm^{-1}K^{-1}$, which is even lower than that for $Ga_xCo_4Sb_{12-x/3}$ (x=0.15). Interestingly, the lattice thermal conductivity for the In-containing systems is close to the κ_L for the normal rare earth-filled $CoSb_3$.

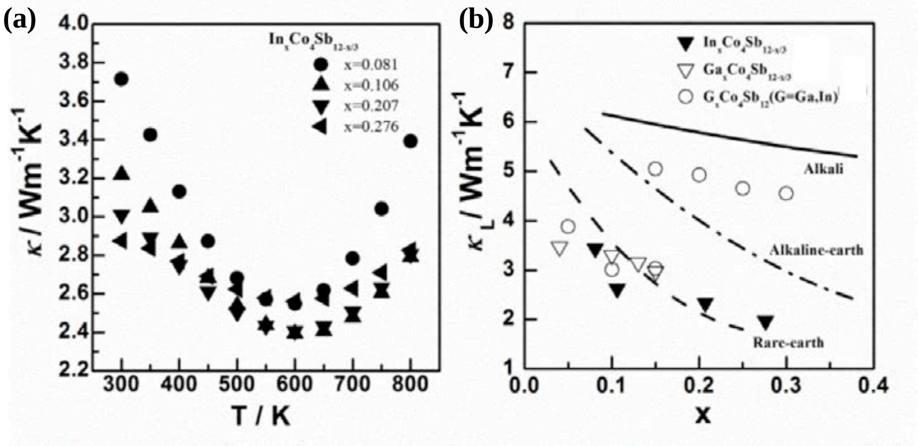

Figure 5.17 (a) Temperature dependence of total thermal conductivity and (b) Room-temperature lattice thermal conductivity as a function of the indium impurity fraction in skutterudites. The κ_L trends for alkaline- (solid line), alkaline-earth- (dashed-dotted line), and rare-earth- (dashed line) fillings are shown for comparison. The black triangles are for the indium-containing skutterudites with complex compound defects in the present work. The blank triangles are for Ga-containing skutterudites with charge-compensated compound defects[16]. And the blank circles are for the group 13 element-doped skutterudites[113,132] using the as-reported compositions, presumably assumed to form a single-type defect.

The dramatic reduction of lattice thermal conductivity in samples with complex compound defects could perhaps be explained by the dual-site occupation of indium impurities and therefore a dual-character phonon scattering mechanism. The indium impurity at the Sb-substitutional site establishes a point defect with size and bonding (in addition to slight mass) mismatch from the host Sb atoms, leading to the scattering of high-frequency lattice phonons. The indium atoms at the void sites behave as a typical filler species and scatter long wavelength phonons via resonant scattering and avoided crossing mechanisms. Therefore, the effective reduction of κ_L implies that a broad spectrum of lattice phonons could be scattered in the In-containing skutterudites with a complex compound defect. The relatively high indium doping content, when counting indium impurities at both the void and Sb sites, is important as it controls the magnitude of the phonon scattering effect.

5.3.4.3 Thermoelectric Figure of Merit

Figure 5.18 shows the temperature dependence of dimensionless thermoelectric figure of merit (zT) which are consistent with prior reports[133]. The maximum zT value in $In_xCo_4Sb_{12-x/3}$ samples reaches 1.2 (at 750 K) with indium content x =0.276. The complex compound defect containing $In_xCo_4Sb_{12-x/3}$ samples presented in this work are also stable and have good repeatability of thermoelectric properties during the measurements, as shown in Figure 5.19.

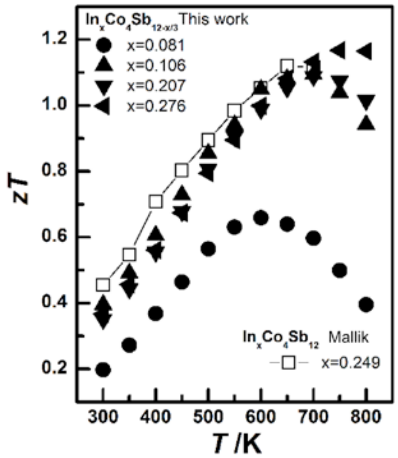

Figure 5.18 Temperature dependence of thermoelectric figure of merit zT for In-containing skutterudites with complex compound defect (CCD). The x values are the same as the ones in Figure 5.15 and 5.17.

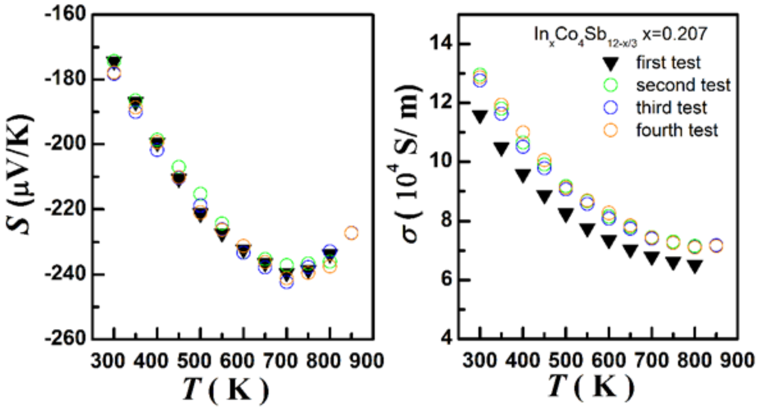

Figure 5.19 Repeatability of thermoelectric properties of In-containing skutterudite with complex compound defect (CCD) and x=0.207.

5.3.4.4 Not fully charge-compensated compound defects

Compared with $(Ga_{VF})_{2x/3}Co_4Sb_{12-x/3}(Ga_{Sb})_{x/3}$ samples, the compound defect samples of the indium system have relatively larger carrier concentrations, which may be due to the defects not being fully charge-compensated as discussed in Section 5.3.4.1. If we write the compositions in a way containing both single filling defects ($(In_{VF})_{\delta}$) and dual-site compound defects ($(In_{VF})_{2(x-\delta)/3}$ and $(In_{Sb})_{(x-\delta)/3}$) , such as $(In_{VF})_{(2x+\delta)/3}Co_4Sb_{12-(x-\delta)/3}(In_{Sb})_{(x-\delta)/3}$, where δ can be calculated using the measured Hall carrier concentration n_H and lattice constant *a*: $n_H = \frac{2\delta}{a^3}$, then we can get the value of filling fraction (2*x*+δ)/3 with *x* being the content of indium determined by EPMA, as shown in Table 5.3.

Table 5.3. Not fully charge-compensated compound defect samples $(In_{VF})_{(2x+\delta)/3}Co_4Sb_{12-(x-\delta)/3}(In_{Sb})_{(x-\delta)/3}$

Samples	**nH (10^{20} cm^{-3})**	δ	*x*	(2*x*+δ)/3
$In_{0.075}Co_4Sb_{11.975}$	0.48	0.013	0.081	0.058
$In_{0.15}Co_4Sb_{11.95}$	0.93	0.026	0.106	0.079
$In_{0.225}Co_4Sb_{11.925}$	2.35	0.065	0.207	0.160
$In_{0.30}Co_4Sb_{11.9}$	1.74	0.048	0.276	0.200

If we plot the compositions $(In_{VF})_{(2x+\delta)/3}Co_4Sb_{12-(x-\delta)/3}(In_{Sb})_{(x-\delta)/3}$ obtained in Table 5.3 in the enlarged ternary phase diagram in Figure 5.14b, we can see that the maximal solubility line will slightly change its direction to somewhere between the direction of $(In_{VF})_{2x/3}Co_4Sb_{12-x/3}(In_{Sb})_{x/3}$ – $CoSb_3$ and the direction of $(In_{VF})_xCo_4Sb_{12}$ – $CoSb_3$, which corresponds to a certain thickness of the solubility region and a ratio of void-filling/Sb-substituting of indium larger than two (with complete charge compensation this ratio is two).

5.3.5 Discussion about In-$CoSb_3$

Two sets of samples were prepared by a process of melting followed by long-term high-temperature annealing, $(In_{VF})_{2x/3}Co_4Sb_{12-x/3}(In_{Sb})_{x/3}$ with *x* changing from 0.075 to 0.30 and $In_{0.30}Co_{4-y}Sb_{11.9+y}$ with *y* changing from -0.20 to 0.20. XRD and EPMA analysis indicate that when *x* is less than 0.27, pure single phase skutterudites can be obtained, whereas if *x* is larger than 0.27 or the composition is off the direction of $(In_{VF})_{2x/3}Co_4Sb_{12-x/3}(In_{Sb})_{x/3}$ then secondary phases start to form. The maximum indium solubility limit is experimentally confirmed to be around *x*=0.27, which is in agreement with computational prediction. Thermoelectric properties were measured and a maximal *zT* value of 1.2 was obtained at 750K when *x* = 0.27. The relatively larger carrier concentrations compared to Ga-containing skutterudites indicate the possibility of not fully charge-compensated compound defects, meaning single filling defects may coexist with dual-site compound defects, which may slightly change the direction along which the solubility region is aligned.

5.4 Stable compositions and Vegard's law

In Section 5.2 we mentioned the concept of stable compositions, now we will discuss in details what stable compositions are, how they can be both misleading and powerful in guiding solubility design. We will take the Yb-Co-Sb system as an example for illustration.

5.4.1 Solubility debate of Yb

Among various kinds of filled skutterudite materials, Yb-doped skutterudites have shown good thermoelectric properties due to the heavy mass and small radius of the Yb atom compared to other fillers, and have been selected by many automotive companies, such as General Motors, as the most promising thermoelectric material for waste heat recovery[134]. Nolas *et al.* first reported a *zT* value of 1.0 for $Yb_{0.19}Co_4Sb_{12}$ at 600K[135]. Composites containing Yb-filled $CoSb_3$ and well-distributed Yb_2O_3 particles were synthesized by Zhao *et al.* with *zT* of 1.3 for $Yb_{0.25}Co_4Sb_{12}/Yb_2O_3$ at 850K[109]. Later *zT* of 1.3 for $Yb_{0.285}Co_4Sb_{12.268}$ at 800K was reported by Li *et al* [136].

Despite the good thermoelectric performance of Yb-doped skutterdites, there has been debate about the Yb solubility limit in skutterudite phase. Because of the size and chemical difference between Yb and Co or Sb atoms, substitution of Yb for Co or Sb is not likely. Instead, the Yb atoms fit nicely into the void filling site, and thus the solubility limit discussed here corresponds to the filling fraction limit (FFL). Theoretically, the filling fraction limit was calculated by Mei *et al.*[137] to be 0.30 for Yb at 0K; Shi *et al.*[138] studied the temperature dependence of filling fraction limits of fillers in $CoSb_3$ skutterudites using a plane-wave density functional method. By combining the formation energy of inserting an impurity R into the intrinsic void of $CoSb_3$ and that of secondary phases RSb_2 and $CoSb_2$, it is found that theoretically the filling fraction limit has a linear dependence on temperature, with $x = 0.2$ when R = Yb at 1000K which is close to the experimental value but the temperature dependence was not demonstrated experimentally. Dilley *et al.* synthesized $Yb_xCo_4Sb_{12}$ by induction heating samples at 1050℃ for 12min then annealing at 600℃ for 35h [139]. Lattice constant values were obtained from powder X-ray diffraction data and plotted against nominal x, from which Yb solubility limit about $x = 0.22$ was extrapolated. Xia *et al.* synthesized $Yb_xCo_4Sb_{12}$

with nominal x up to 0.4 by melting samples at 1077℃ for 10 hours and subsequent annealing at 800℃ for 7 days and observed no impurity phases[140]. Addition of oxygen to the system results in less filling due to the formation of Yb oxides[141]. In addition to traditional preparation methods (melting and long-time annealing), non-equilibrium synthesis methods were also adopted and gave different solubility limits, such as $x = 0.29$ by melt-melt-spinning (MMS) method by Li *et al.*[136] and $x = 0.5$ by ball milling by Yang *et al* [24].

In this study, the equilibrium isothermal sections of the ternary phase diagram of Yb-Co-Sb system at various temperatures are proposed in the same way as for the Ga-Co-Sb system and In-Co-Sb system, which are based on knowledge of the related binary phase diagrams and the microstructure of the samples[16,17,106-108]. The filling fraction limit derived from the ternary phase diagram and especially its temperature dependence naturally explains the solubility debate and the confusion concerning the various reports of maximum solubility of Yb in the skutterudite phase. It also leads to a strategy to synthesize optimized, high zT material.

5.4.2 Skutterudite lattice expansion due to Yb filling

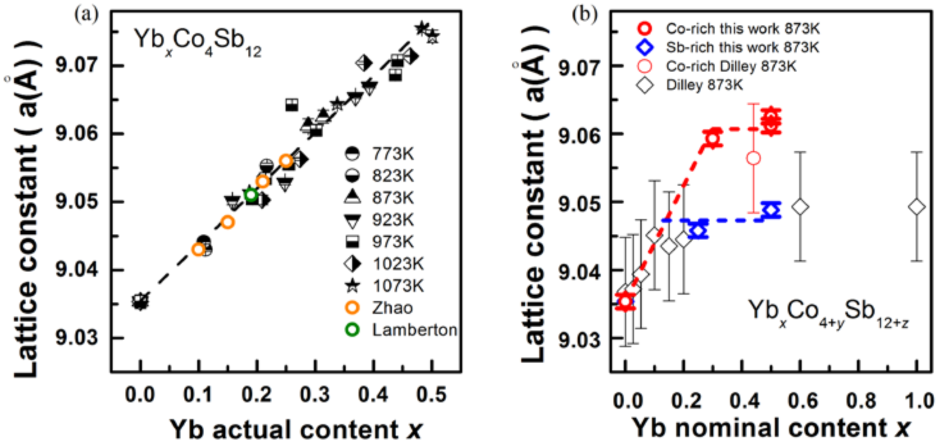

Figure 5.20 (a) Dependence of lattice constant on the actual Yb content, x, in $Yb_xCo_4Sb_{12}$ for samples annealed at various temperatures in this study and samples in references[109,142]. (b) Dependence of the lattice constant on the nominal Yb content, x, in $Yb_xCo_{4+y}Sb_{12+z}$ for samples annealed at 873K in this study and samples in reference by Dilley *et al*[139]. The red dashed line shows the increase of lattice constant followed by a plateau when x is larger than 0.30 in Co-rich samples which indicates the maximum filling fraction limit at 873K (red point in Figure 5.4). The blue dashed line shows another plateau of lattice constant indicating another stable composition $Yb_{0.13}Co_4Sb_{12}$ (blue point in Figure 5.4) in Sb-rich samples.

Lattice constants were derived from powder X-ray diffraction data and plotted against Yb actual content determined from EPMA, as shown in Figure 5.20(a). We can see that there is a good linear relationship between the actual Yb content and lattice constant of the skutterudite phase, which agrees with the literature data and is consistent with Yb going into the same site across the whole range (up to *x*=0.5), presumably the void site[109,142]. Lattice constants were also plotted against the nominal Yb content in order to compare with Dilley's data[139] in Figure 5.20(b). The two plateaus of lattice constants in this study indicate there are two stable skutterudite compositions at 873K (explained in Section 5.4.3 from Gibbs phase rule). The red dashed line shows the increase of lattice constant followed by a plateau when *x* is larger than 0.30 when the nominal composition is in a Co-rich three-phase region. Here the Yb content in the skutterudite phase reaches the maximum filling fraction limit at 873K (red point in Figure 5.4a). The blue dashed line shows another plateau of lattice constant when the nominal composition is in an Sb-rich three-phase region where the skutterudite phase has a stable composition with lower Yb content ($Yb_{0.13}Co_4Sb_{12,}$ blue point in Figure 5.4a). The lattice constants in this study (Figure 5.20(b)) are well within the same range from reference Dilley's data[139]. Moreover, for the *x* =0.44 sample from Dilley's data which has larger lattice constant than other samples, it has $YbSb_2$ and $CoSb_2$ impurities according to the XRD data, which agrees with our conclusion that the skutteridte phase with maximum filling fraction limit coexists with $CoSb_2$ and $YbSb_2$ and is thus in a Co-rich three-phase region.

5.4.3 Stable compositions in ternary phase diagram system

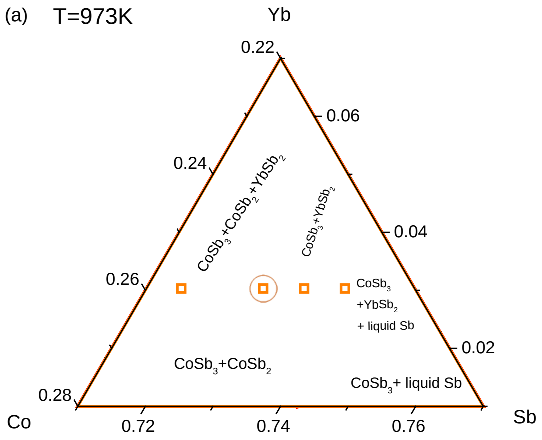

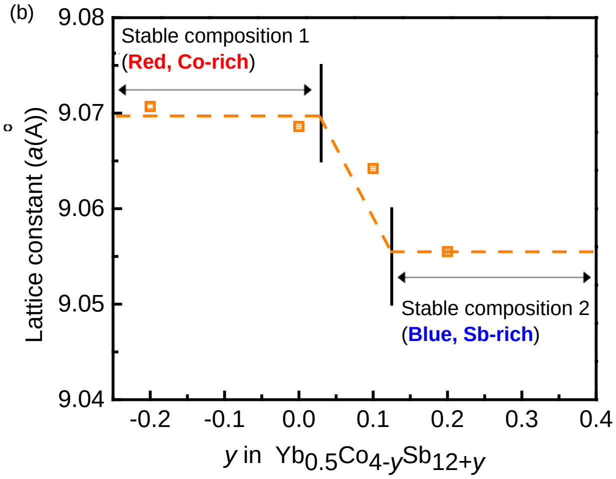

Figure 5.21 (a) Magnified region of the isothermal section at 973K near $CoSb_3$ of the Yb-Co-Sb ternary phase diagram system with two stable skutterudite compositions (red and blue points) and solubility line (red line). Scattered points (empty magenta circles) indicate possible synthesis error near the stable composition (red point) in the three-phase region of $CoSb_3$, $CoSb_2$, and $YbSb_2$. (b) Dependence of the lattice constant derived from X-ray Diffraction data on the Co/Sb ratio for nominal compositions with the same Yb content $x = 0.5$ marked as empty orange rectangles in (a).

The analysis of all samples is consistent with the proposed phase diagram for Yb-doped skutterudites shown in Figure 5.21(a), which is based on the knowledge of the related binary phase diagrams[106-108]. Our experimental data suggest that the region of Yb solubility extends toward the void filling samples, $(Yb_{VF})_xCo_4Sb_{12}$, up to the maximum solubility point. For example, at 973K the estimated maximum x value is 0.44 as shown in Figure 5.21(a) (red point). When x exceeds 0.44, the sample $Yb_{0.5}Co_4Sb_{12}$ (empty orange rectangle surrounded by empty magenta circles) contains a skutterudite phase with Yb doping level around $x = 0.44$ and impurity phases $YbSb_2$ and $CoSb_2$. When the nominal composition with $x = 0.5$ is off the Co/Sb ratio of void filling samples $(Yb_{VF})_xCo_4Sb_{12}$ (being either Co-rich or Sb-rich), more impurity phases form in the samples.

When the nominal composition contains higher Yb content than its solubility limit, it is in a three-phase region between $Yb_xCo_4Sb_{12}$, $YbSb_2$, and $CoSb_2$. According to the phase rule, there is F=C-P+0=3-3=0 degree of freedom where C is the number of components, P the number of phases, and the 0 indicates both temperature and pressure are fixed. Thus the compositions of the three equilibrium phases in a three-phase region are fixed and all the nominal compositions in this three-phase region (such as all the scattered empty magenta circles in Figure 5.21(a)) will produce the same skutterudite composition with the same actual Yb content (red point in Figure 5.21(a)). This is indicated by a plateau of the lattice constant marked as *stable composition 1* from Figure 5.21(b). At 973K it was also confirmed by the EPMA measurements to be $x = 0.44 \pm 0.01$($Yb_{0.44}Co_4Sb_{12}$).

When the nominal composition is slightly Sb-rich (for example $Yb_{0.5}Co_{3.9}Sb_{12.1}$ at 973K), it moves into a two-phase region between $Yb_xCo_4Sb_{12}$ and $YbSb_2$. Due to the phase rule, the degree of freedom F= C-P+0=3-2=1, which means that the compositions of phases at equilibrium in this two-phase region are not fixed, but vary depending on the exact starting composition within this region. As a result, the Yb content in the skutterudite phase decreases as the nominal composition becomes more Sb rich, which is confirmed by the decrease of lattice constant in Figure 5.21(b).

However, when the nominal composition is even richer in Sb (for example $Yb_{0.5}Co_{3.8}Sb_{12.2}$ at 973K), the nominal composition moves into another three-phase region between $Yb_xCo_4Sb_{12}$, $YbSb_2$ and liquid Sb. Thus the compositions of phases at equilibrium are fixed again and all the nominal compositions in this three-phase region will produce the same skutterudite composition with the same actual Yb content ($Yb_{0.26}Co_4Sb_{12}$) albeit at a much lower Yb content (blue point in Figure 5.21(a)). This was confirmed by a lower plateau of lattice constant marked as *stable composition 2* in Figure 5.21(b) and the EPMA measurements confirmed this composition to be $x = 0.26 \pm 0.02$.

In the process of synthesizing samples, exact element control is not cost-practical and thus the influence of impurity elements from low-cost starting material will lead to variations in the Co/Sb ratio and Yb content as well, shown as scattered empty magenta circles in Figure 5.21(a). If these scattered circles spill out of the three-phase region and enter into the two-phase region of $CoSb_3$ and $YbSb_2$, there will be a sharp decrease of Yb content in the skutterudite phase, resulting in a sharp decrease in lattice constant as well, which is illustrated in Figure 5.21(b).

In order to have precise control of the Yb content and thus the carrier concentration in the skutterudite phase, nominal compositions can be easily designed to remain in a three-phase region to make sure that the skutterudite phase has a stable composition. The existence of these stable compositions as well as their temperature dependence can thus be applied to facilitate the synthesis of optimized skutterudites for low-cost mass production.

5.4.4 Vegard's law in ternary phase diagram system

In materials science, Vegard's law is the empirical rule that describes the relationship between the lattice parameter of a solid solution of two constituents and those of the pure constituents. According to Vegard, the lattice parameter of a solid solution should be approximately equal to a linear combination of the two constituents' lattice parameters at the same temperature given that both pure constituents have the same crystal structure [143]:

$$a_{A_{1-x}B_x} = (1-x)a_A + xa_B \qquad \text{(Eq. 5.2)}$$

Here, $a_{A_{1-x}B_x}$ is the lattice parameter of the solid solution, a_A and a_B are the lattice parameters of the pure constituents A and B, respectively, and x is the molar fraction of B in the solution. In our case, A is the unfilled $CoSb_3$, whereas B is the fully filled $YbCo_4Sb_{12}$, which does not exist in reality due to the solubility limit of Yb. For partially filled $Yb_xCo_4Sb_{12}$, it can be regarded as:

$$Yb_xCo_4Sb_{12} = (1-x)Co_4Sb_{12} + x(YbCo_4Sb_{12}) \qquad \text{(Eq. 5.3)}$$

Thus we should be able to extract a linear relationship between the lattice parameter of partially filled $Yb_xCo_4Sb_{12}$ and the filling fraction x, as shown in Eq. 5.4.

$$a_{Yb_xCo_4Sb_{12}} = (1-x)a_{Co_4Sb_{12}} + xa_{YbCo_4Sb_{12}} = a_{Co_4Sb_{12}} + x(a_{YbCo_4Sb_{12}} - a_{Co_4Sb_{12}}) \qquad \text{(Eq. 5.4)}$$

This equation is often applied to determine the filling fraction limit (FFL) of fillers. In an experimental perspective, FFL is determined when the lattice parameter deviates from the Vegard's law as nominal filling amount x increases. Mostly this deviation is observed as a plateau[131,144]; however, sometimes it is also observed as a linear behavior with a different slope[19,145,146]. This method is valid for binary phase diagram systems, but not always true for ternary phase diagram systems.

In a binary system, as shown in Figure 5.22 below, when increasing the amount x of B in A at a given temperature, the nominal composition experiences two phase regions, first a single-phase region of the solid solution α, then a two-phase region of α and β when the amount of x exceeds the solubility limit (purple point). In a single-phase region of α, due to Gibbs phase rule, the degree of freedom F= C-P+0=2-1=1; the lattice parameter of α changes linearly with the addition of B (x). In the two-phase region, the degree of freedom F= C-P+0=2-2=0; the lattice parameter of phase α at equilibrium is fixed due to the fixed amount of B in phase α indicated by the purple point (solubility limit of B in A). Thus a linear relationship followed by a plateau will be observed between the lattice parameter of phase α and nominal content x of B.

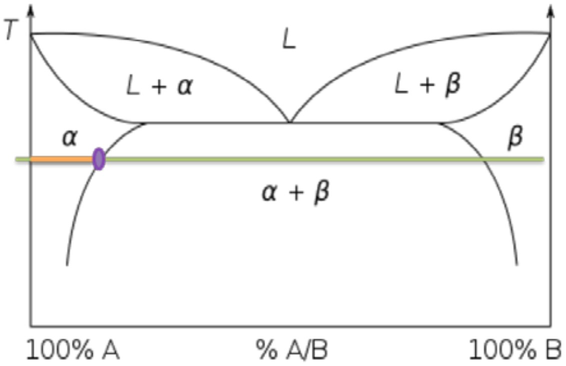

Figure 5.22 Illustration of typical eutectic phase diagram of binary *A*-*B* system. The green line represents the isothermal line. The orange section represents the solubility region of *B* in *A*. The purple dot represents the solubility limit of *B* in *A* at the selected temperature.

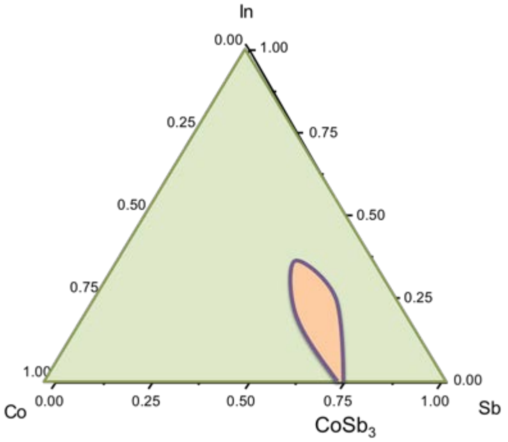

Figure 5.23 Illustration of isothermal section of ternary In-Co-Sb phase diagram. The green triangle represents the isothermal section. The orange area represents the solubility region of R-$CoSb_3$. The purple boundary represents the solubility limit of R in $CoSb_3$ at the selected temperature.

However, in a ternary system, e.g., R-Co-Sb, it is more complicated with an additional degree of freedom due to the thickness of the solubility region of $R_xCo_4Sb_{12}$, as shown in Figure 5.23. In a ternary system, the isothermal section is a surface rather than a line in a binary system, so is the solubility region. The solubility limit also changes from a single value (represented by purple dot in Figure 5.22) in a binary system to a boundary represented by the purple contour of the orange solubility region in Figure 5.23. The experimentally determined solubility limit is thus largely dependent on the phase regions adjacent to skutterudite phase where the nominal compositions are, as illustrated in Figure 5.24. For the Vegard's law to be applicable in a ternary system, the nominal compositions should be along the solubility direction, e.g., $(In_{VF})_{2x/3}Co_4Sb_{12-x/3}(In_{Sb})_{x/3}$ – $CoSb_3$, so it can be considered as in a pseudo-binary system. If nominal compositions are off the solubility direction, e.g., $(\mathrm{In_{VF}})_x\mathrm{Co_4Sb_{12}}$ – $\mathrm{CoSb_3}$ for In-Co-Sb system (purple solid line in Figure 5.14b) and $(\mathrm{Yb_{VF}})_x\mathrm{Co_4Sb_{12.2}}$ – $\mathrm{Co_4Sb_{12}}$ for Yb-Co-Sb system (yellow dashed line in Figure 5.25a), then deviations from the Vegard's law can result from nominal compositions entering either two-phase (2-p in Figure 5.24) or three-phase region (3-p' in Figure 5.24) other than the one that will give the maximum solubility limit (x_{max} in 3-p, Figure 5.24). As a result, the solubility limit observed will be smaller than the maximum solubility limit, because its determination is misled by slope change or false plateau in the relationship between lattice parameter and nominal filler content x.

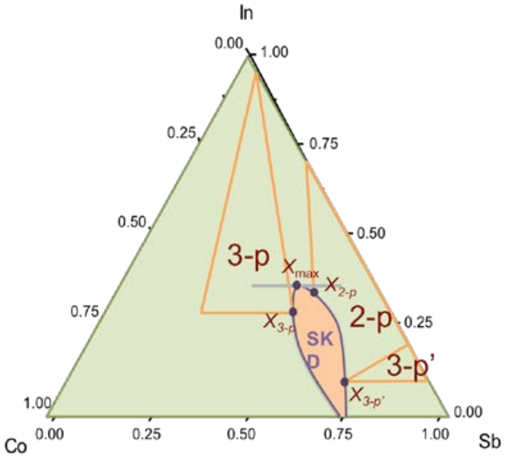

Figure 5.24 Dependence of solubility limit on adjacent phase regions in a ternary phase diagram system. Triangles enclosed in yellow lines are three-phase regions (on the Co-rich side: 3-p; on the Sb-rich side: 3-p'), with x_{3-p} and $x_{3-p'}$ indicating respectively the solubility limit of R in equilibrium skutterudite phase when nominal compositions are in these phase regions. A two-phase region (2-p) is located right above the Sb-rich three-phase region. The solubility limit of R in equilibrium skutterudite phase when nominal compositions are in this two-phase region is represented by the purple dot marked at x_{2-p}. The maximum solubility limit x_{max} is represented by the purple dot that is the furthest point along the elongated direction (solubility direction).

Figure 5.25 serves as a good example to illustrate the inapplicability of Vegard's law when the nominal compositions are off the solubility direction in a ternary Yb-Co-Sb system. It demonstrates that reaching a plateau of lattice constant could be because of the existence of stable compositions and thus does not necessarily imply reaching the solubility limit.

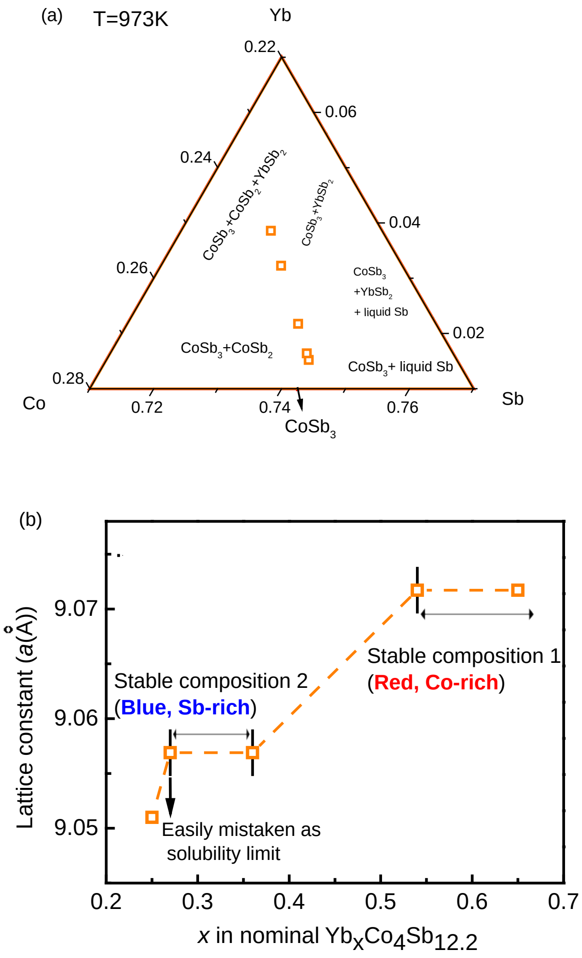

Figure 5.25 Samples with different nominal Yb content x in $Yb_xCo_4Sb_{12.2}$ (marked as empty orange rectangles) but the same Sb excess lead to a nonlinear dependence of lattice constant (b) due to the sample traversing different two- and three- phase regions of the phase diagram (a).

Excess of Sb is often added when synthesizing $CoSb_3$ skutterudites due to the high volatility of Sb. In samples with even a slight Sb excess (depicted in Figure 5.25(a)), increasing the nominal Yb content will lead to samples in the Sb-rich three-phase region of $Yb_xCo_4Sb_{12}$, $YbSb_2$, and liquid Sb first, then samples in the two-phase region of $Yb_xCo_4Sb_{12}$ and $YbSb_2$ before reaching samples in the Co-rich three-phase region of $Yb_xCo_4Sb_{12}$, $YbSb_2$, and $CoSb_2$. Thus the actual Yb content in Yb filled $CoSb_3$ as measured by the lattice constant of the skutterudite phase will stop increasing and be constant for a period (first plateau in Figure 5.25(b), or blue dashed line in Figure 5.20(b)) while the nominal composition is in the Sb-rich three-phase region and the resulting skutterudite phase has stable composition (blue point in Figure 5.25(a)). This Yb content at which lattice constant stops increasing can be easily mistaken as the Yb solubility limit[139]. However, as seen from Figure

5.25(b), further Yb addition can change the Yb actual content in the skutterudite phase dramatically as the nominal composition moves away from the Sb-rich three-phase region and into the two-phase region, and consequently the lattice constant would resume the increasing trend. As the nominal composition moves into the Co-rich three-phase region, the actual Yb content reaches the maximum solubility (red point in Figure 5.25(a)) and thus the lattice constant reaches a plateau again (second plateau in Figure 5.25(b) or red dashed line plateau in Figure 5.20(b)). An overall investigation of the phase relations near the targeted phase is thus needed in order to make a conclusion about solubility limit because: observing a plateau in lattice constant is insufficient in determining the solubility limit in a ternary system, nor is observing impurity phases sufficient (the nominal composition might just be in a two- or three-phase region).

5.4.5 Discussion about Yb-$CoSb_3$

The equilibrium isothermal sections of the ternary phase diagram of Yb-Co-Sb system at various temperatures are studied. XRD, SEM, and EPMA analysis indicates that there is a three-phase region on the Co-rich side of Yb-doped skutterudites ($Yb_xCo_4Sb_{12}$, $CoSb_2$, and $YbSb_2$) which results in a stable skutterudite composition $Yb_xCo_4Sb_{12}$ with maximum Yb content (any nominal composition in this three-phase region will produce a skutterudite phase with the same Yb content, for example $x = 0.11 \pm 0.02$ at 773K and $x = 0.49 \pm 0.02$ at 1073K), and another three-phase region ($Yb_xCo_4Sb_{12}$, $YbSb_2$ and liquid Sb) on the Sb-rich side with a stable composition $Yb_xCo_4Sb_{12}$ with relatively lower Yb content (for example $x = 0.13 \pm 0.01$ at 873K and $x = 0.34 \pm 0.01$ at 1073K). The existence of these stable compositions can be misleading when applying Vegard's law to interpret solubility limit in ternary systems while samples are off the solubility direction. Full phase diagram investigation is thus necessary to avoid such misinterpretation. At higher temperatures, the equilibrium Yb content in both stable compositions is also higher, which can be used to form nano-scale precipitates in the matrix skutterudite phase (discussed in Chapter 8).

Skutterudite material with the optimized thermoelectric composition can be produced from a range of nominal compositions with appropriate annealing, which has great potential in enabling low-cost large-scale production. Figure of merit zT values greater than 1.1 were obtained at and above 800K in all samples targeting $Yb_xCo_4Sb_{12}$ with $x = 0.3$. The highest zT value reaches 1.3 at 850K in $Yb_{0.30}Co_4Sb_{12}$.

5.5 Solubility design strategies

So far we have demonstrated the possibility of soluble sites other than the void site for fillers (Section 5.3), e.g., Sb substitution on the $CoSb_3$ matrix, as a result of which the solubility direction can be shifted away from common direction along $(In_{VF})_xCo_4Sb_{12}$ – $CoSb_3$ but towards the Co-rich side. The difference of solubility in binary and ternary phase diagram systems is also discussed (Section 5.4). It has to be noted that the dependence of observed solubility on the phase regions adjacent to the skutterudite phase as well as the temperature dependence of solubility might be the reason for many solubility debate.

Three solubility design strategies could then be proposed regarding high performance thermoelectric materials design. First of all, stay on the right solubility direction. Secondly, choose the phase region that will result in the maximum filler solubility limit. Thirdly, vary the annealing temperature. Among the strategies mentioned, the large temperature dependence of solubility especially expands our choice of optimized compositions for thermoelectric application, which can be helpful in changing thermoelectric materials with dopant solubility barrier into promising ones instead. We will take Ce-doped $CoSb_3$ as an example for illustration in this section.

5.5.1 Solubility barrier of Ce in Ce-$CoSb_3$

The intermediate temperature range (400-600℃) at which filled skutterudites have optimum thermoelectric performance makes this material a perfect candidate for automotive industry applications. Due to the heavy mass and small radius of the Yb atom compared to other fillers, Yb-$CoSb_3$ skutterudites have excellent thermoelectric properties (zT = 1.3 at 850K for $Yb_{0.3}Co_4Sb_{12}$)[50] and have been selected by many automotive companies, such as General Motors, Ford, and BMW, as the most promising thermoelectric material for waste heat recovery[147]. However, the deficiency of the rare earth element Yb (abundance in earth's crust 3ppm) could potentially be a problem in large-scale commercialization. Unlike Yb, Ce is the most earth abundant element of the rare earths (abundance in earth's crust 68ppm)[148]. In fact, there are huge resources of cerium because it is more abundant than other commonly known elements like lead (14ppm), tin (2ppm), silver (0.07ppm), tellurium (0.005ppm), and gold (0.001ppm). The price of cerium is also more competitive compared to that of ytterbium. For large quantities, the difference is a factor of 10 (Ce: \$5000/ton, Yb: \$50000/ton [149]), placing Ce in the category of other commonly used elements such as Ni.

With its larger earth abundance and fairly low cost, use of Ce would help the commercialization of *n*-type skutterudites for automotive industry only if the thermoelectric properties of Ce-doped skutterudites can match those of Yb-doped skutterudites.

Interestingly, single filled Ce-$CoSb_3$ skutterudites have been considered as unsuitable thermoelectric materials and there has yet been little report of high temperature thermoelectric properties of pure Ce-$CoSb_3$ skutterudites. Ce has been considered to be a good auxiliary filler in multiple filled skutterudites, such as in (In, Ce)-$CoSb_3$ skutterudites (zT of 1.43 for $In_{0.2}Ce_{0.15}Co_4Sb_{12}$ at 800K)[51] or (Ba, Ce)-$CoSb_3$ skutterudites (zT of 1.26 for $Ba_{0.18}Ce_{0.05}Co_4Sb_{12.02}$ at 850 K)[150]. Ce has not typically been considered as single filler. This is most likely due to its reported small filling fraction limit $x = 0.09$ in $Ce_xCo_4Sb_{12}$[19], which would prevent Ce-containing skutterudites to achieve the optimum carrier concentration for *n*-type skutterudites.[53] However, the filling fraction limit of Ce was concluded[19] based on the observance of a plateau in the lattice constant against nominal Ce content, as well as observation of impurity phases. These phenomena, as we have discussed in Section 5.4, are not sufficient proof to conclude about solubility limit in a ternary system. Thus the filling fraction limit of Ce is worth re-investigation by solubility design using an equilibrium phase diagram approach. This approach introduces both the annealing temperature and nominal composition as variables in determining the filling fraction limit, which leads to the possibility of enhancing filling fraction of fillers thermodynamically rather than consider it as a fixed single value. Using this phase diagram approach, a temperature dependent solubility like the Yb in Yb-$CoSb_3$ sheds light on optimizing Ce-$CoSb_3$.[50]

To increase the filling fraction limit of Ce in $CoSb_3$ skutterudites, charge-compensational doping such as Fe or Mn-doping has been largely applied which can dope the material from *n*-type to *p*-type.[28,151-154] In this study, single-filling Ce-$CoSb_3$ skutterudites without charge-compensational doping are prepared under equilibrium conditions and their thermoelectric properties are measured up to 850K. In other works, our focus is on the intrinsic solubility limit of Ce in $CoSb_3$ system without any compensational effect.

5.5.2 Optimum doping of Ce-CoSb$_3$ skutterudites

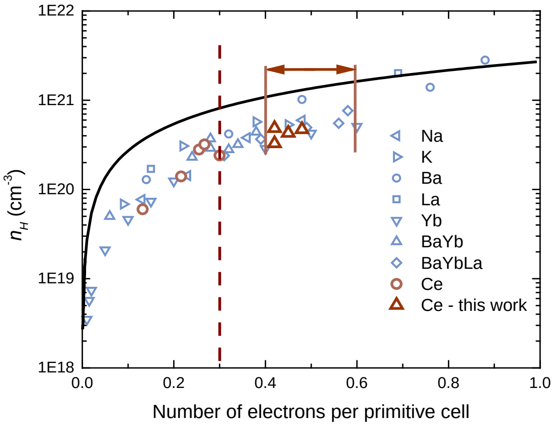

Figure 5.26 Hall carrier concentration vs number of electrons per primitive cell Co$_4$Sb$_{12}$.[11-13,19,50,53,155-157] The number of electrons per primitive cell is calculated as the sum of q_i*x_i for partially filled $(R_1)_{x1}(R_2)_{x2...}(R_n)_{xn}Co_4Sb_{12}$, where q_i is the effective charge state and x_i is the filling fraction of the ith filler R in multiple-filled skutterudites. The solid line represents the theoretical curve calculated by using $n = 2x/a^3$ where x is the total number of electrons per primitive cell and a is the lattice constant of CoSb$_3$. The red double arrow represents the estimated high power factor region (see discussions below) and the red dashed line represents the number of electrons per primitive cell limited by the previously thought Ce filling fraction limit[19].

Unfilled CoSb$_3$ is an intrinsic semiconductor with carrier concentration less than 10^{18} cm^{-3}. Rare earth filler atoms in the void sites, are nearly perfect *n*-type donors. The *n*-type carrier concentration is essentially determined by the number of filling atoms and the ionic charge state. In CoSb$_3$ a Yb filler has a valence charge +2 while Ce is +3 which is a lower oxidation state than often observed in oxides but common for Sb compounds.[158] Figure 5.26 demonstrates the trend of the carrier concentration versus the number of electrons per primitive cell, for single, double or triple-filled skutterudites. To achieve high power factor of *n*-type skutterudites 0.4 to 0.6 electrons per Co$_4$Sb$_{12}$ unit is required, as indicated by the red double arrow.[67] The carrier concentration of Ce-CoSb$_3$ samples in the previous literature study[19] is limited by the reported low filling fraction limit (x = 0.09 in Ce$_x$Co$_4$Sb$_{12}$ at 973K), consequently these samples are far from the high power factor region. In order to optimize the thermoelectric properties of Ce single filled CoSb$_3$ skutterudites, a higher filling fraction of Ce is needed. As we shall show later, the filling fraction limit of Ce can be as high as x = 0.20 at 1123K through solubility design, which is not only more than twice the reported value x = 0.09 but now allows for the optimization of Ce-

$CoSb_3$. After optimization, the four samples in this work fall in the high power factor region (nominal Ce content x = 0.17, 0.18, 0.20, 0.21, and actual Ce content measured on hot pressed pellets are x = 0.14, 0.14, 0.16, 0.15, respectively) and all of them have zT values reaching above 1.0 above 750K (see Figure 5.29e).

5.5.3 Ultra-high FFL of Ce in Ce-$CoSb_3$ skutterudites

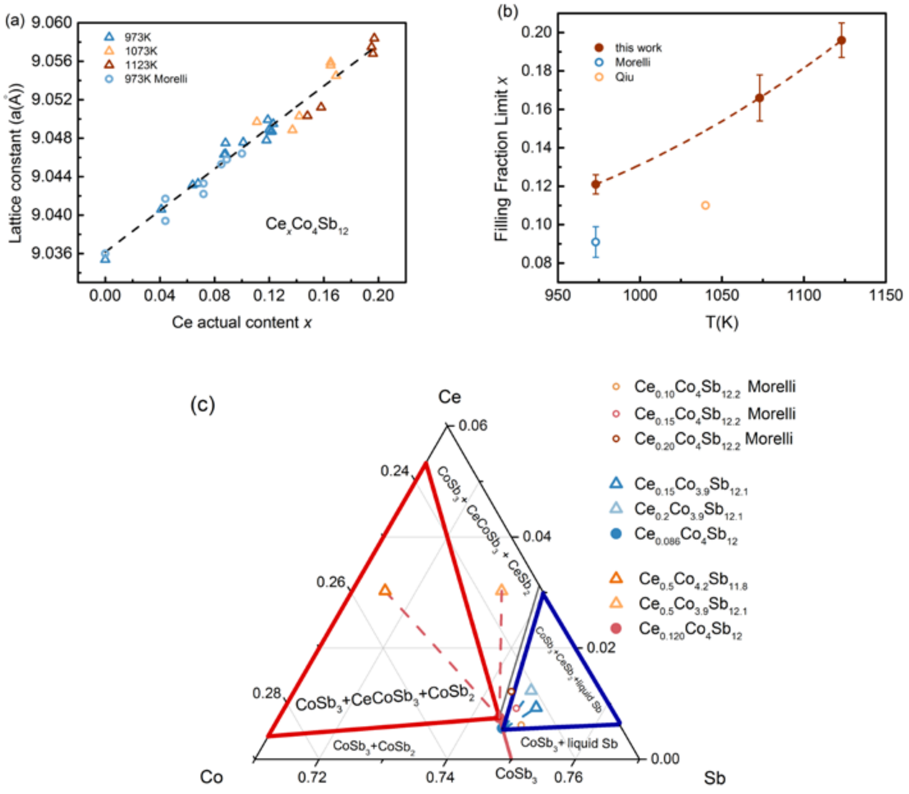

Figure 5.27 Filling fraction limit (FFL) of Ce in Ce-$CoSb_3$ skutterudites. (a) Skutterudite lattice expansion due to Ce filling. (b) Dependence of FFL on annealing temperature. Red dashed line is a guide for the eye. Error bars represent the standard deviation of filling fraction limit determined from EPMA measurements (c) Dependence of FFL on nominal composition with annealing temperature 973K. The phase region enclosed by red lines is a Co-rich three-phase region, which is related to the maximum solubility limit. The phase region enclosed by blue lines is an Sb-rich three-phase region, which is related to a lower solubility limit detected by Morelli *et al* [19].

The lattice expansion due to filling is an easy and effective way of characterizing the amount of fillers actually going into the void site in the skutterudite cell. Here lattice constants were derived from powder X-ray diffraction data and the actual Ce content was determined from EPMA. The lattice constant shows a simple linear dependence on the actual Ce content x in $Ce_xCo_4Sb_{12}$, which agrees with the literature data and is consistent with Ce going into the same site across the whole range (up to x=0.20), presumably the void site. Samples annealed at higher temperatures show both higher Ce content by EPMA as well as higher lattice constants.

The partial filling of Ce in the void site increases the entropy due to the increase of disorder of the material, and thus it can be expected that the equilibrium solubility should increase measurably with temperature. While this is known theoretically[138], the filling fraction limit (FFL) is often considered to be a temperature independent quantity; to date, there has been no report on the temperature dependence of filling fraction limit of Ce, let alone using this to design filler solubility in skutterudites. Here we show that the Ce filling fraction limit (determined from red point in Figure 5.27c) increases significantly with temperature (see Figure 5.27b). It increases to about 0.197±0.007 at 1123K and is more than twice the value reported from Morelli *et al*[19] (x = 0.09). This ultra-high filling fraction limit is verified using Atom Probe Tomography (APT) and is discussed later. This presents an opportunity for optimizing thermoelectric properties of Ce-$CoSb_3$ skutterudites. The filling fraction limit x = 0.120 at 973K is also 25% higher than the reported literature value x = 0.09, which can be explained due to the presence of separate 3-phase regions in the Ce-Co-Sb system with different Ce solubilities in $Ce_xCo_4Sb_{12}$.

Figure 5.27c shows a magnified region of an isothermal section at 973K near $CoSb_3$ of the Ce-Co-Sb ternary phase diagram. There are three two-phase regions and three three-phase regions near $CoSb_3$. The stable compositions (marked as red and blue points in Figure 5.27c) were confirmed by the EPMA measurements to be x=0.120± 0.005 for the red stable composition ($Ce_{0.120}Co_4Sb_{12}$) and x=0.086± 0.007 for the blue stable composition ($Ce_{0.086}Co_4Sb_{12}$) at 973K.

When the nominal composition is slightly Co rich (in addition to sufficient Ce, e.g. $Ce_{0.5}Co_{4.2}Sb_{11.8}$, red empty triangle) the sample is in the three-phase region between $CoSb_2$, $CeCoSb_3$[159] and $Ce_xCo_4Sb_{12}$ with x = 0.120± 0.005 (red point). Also if the nominal composition is slightly Sb rich (e.g. $Ce_{0.5}Co_{3.9}Sb_{12.1}$, yellow empty triangle) the sample is in the three-phase region between $CeSb_2$, $CeCoSb_3$, and $Ce_xCo_4Sb_{12}$ with, coincidentally, the same x = 0.120± 0.005 (red point) as found in the cobalt rich three-phase region. In both cases the equilibrium Ce content in skutterudite phase will reach the same filling fraction limit x = 0.120± 0.005 at 973K (red point) as indicated by tie lines (red dashed lines). Note that these three-phase regions (one with $CeSb_2$, $CeCoSb_3$ and $Ce_xCo_4Sb_{12}$; the other with $CoSb_2$, $CeCoSb_3$ and $CexCo_4Sb_{12}$) are different from the previous phase diagram study of Ce-Co-Sb system at 400°C.[159] No similar ternary phase such as $CeCoSb_3$ is found in the Yb-Co-Sb or In-Co-Sb system, but the Ga-Co-Sb system has a ternary phase ($Co_3Ga_2Sb_4$) as well.[160]

However, when the nominal composition is very antimony rich, such as used by Morelli[19] the samples are in another three-phase region between $Ce_xCo_4Sb_{12}$, $CeSb_2$, and liquid Sb (for example $Ce_{0.2}Co_{3.9}Sb_{12.1}$ and $Ce_{0.15}Co_{3.9}Sb_{12.1,}$ marked as green and blue empty triangles respectively). Here the Ce content in the skutterudite phase remains constant with x=0.087$\pm$ 0.007(blue point) as indicated by tie lines (green and blue dashed lines). Note that two nominal compositions ($Ce_{0.10}Co_4Sb_{12.2}$ and $Ce_{0.15}Co_4Sb_{12.2}$) from Morelli's data[19] fall into this three-phase region of $Ce_xCo_4Sb_{12}$, $CeSb_2$, and liquid Sb and one ($Ce_{0.20}Co_4Sb_{12.2}$) falls into the two-phase region of $Ce_xCo_4Sb_{12}$ and $CeSb_2$. The observation of $CeSb_2$ impurity phase in those samples confirms they are in a different field from the Co-rich three-phase region, which gives the higher Ce content. The blue stable composition point coincides with the reported filling fraction limit x = 0.09, which is about 25% less of the filling fraction limit reported in this study for the same annealing temperature. As a result the first solubility design strategy in this study for enhancing the filling fraction limit of Ce in $CoSb_3$ is: focus on the Co-rich three-phase region rather than the lower Sb-rich three-phase region.

From the analysis of the temperature dependent filling fraction limit (Figure 5.27b) we can also predict that the Ce content in the skutterudite phase can be controlled through the annealing temperature when the nominal composition is in one of the three-phase regions, which has proven to be a practical strategy to optimize thermoelectric performances in Yb-$CoSb_3$ system (Section 5.2) [50]. This solubility design strategy is also applied in the study here for enhancing the filling fraction limit of Ce in $CoSb_3$: increase the annealing temperature.

Atomic Probe Tomographic (APT) measurements on $Ce_xCo_4Sb_{12}$ skutterudite was also performed to confirm the ultra-high filling fraction of x= 0.20. APT is particularly effective at chemically and structurally characterizing materials in 3D on the nanometer length scale. It provides accurate information about atomic concentrations and can identify even the smallest nanoparticles.[161] Small nanoparticles of Yb_2O_3 and InSb were observed in some Yb and In containing skutterudites, respectively.[51,109,162] Such small particles might go unnoticed in the SEM and would contribute to the EPMA signal. Here APT was utilized to verify the Ce content and homogeneity in the $Ce_xCo_4Sb_{12}$ majority phase for sample annealed at 1123K with nominal composition $Ce_{0.5}Co_4Sb_{12}$. According to EPMA, the Ce content in the majority skutterudite phase should be $x = 0.20$ or 1.2 at%. Figure 5.28a contains a 3D reconstruction of the skutterudite phase at and around a grain boundary. As can be seen in Figure 5.28b, atomic concentrations were consistent and homogeneous away from the grain boundary. No nano-precipitates of Ce-rich phases were observed. Atomic concentrations were averaged over a 30 nm diameter cylinder, from 20 to 60 nm on the scale bar in Figure 5.28a, and the Ce content was measured to be 1.4 ± 0.1 at%. This agrees with the values obtained by EPMA (x=0.20 corresponding to Ce content of 1.2 at%) and supports our conclusion that such a high filling fraction of Ce is indeed uniformly distributed in the skutterudite phase. A uniform accumulation of Ce at the grain boundary was also observed, accompanied by a reduction in Co. Such atomic segregation is frequently observed at grain boundaries.[161]

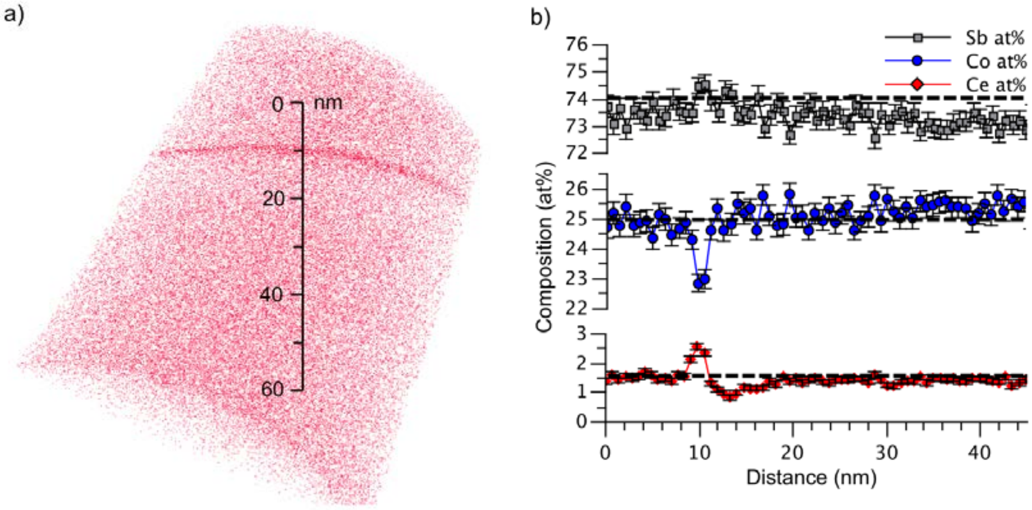

Figure 5.28 APT analysis of the most heavily doped sample $Ce_{0.2}Co_4Sb_{12}$. a) 3D reconstruction of micro-tip containing a grain boundary. Ce atoms are displayed in red; Sb and Co atoms omitted for clarity. b) Concentration profile across the grain boundary and in the grain. The black dashed lines show values measured by EPMA, and the error bars represent the statistical error, $\sqrt{c(1-c)/n}$, where c is the concentration and n is the number of atoms detected in each data point.

5.5.4 Thermoelectric properties of optimized Ce-$CoSb_3$ skutterudite

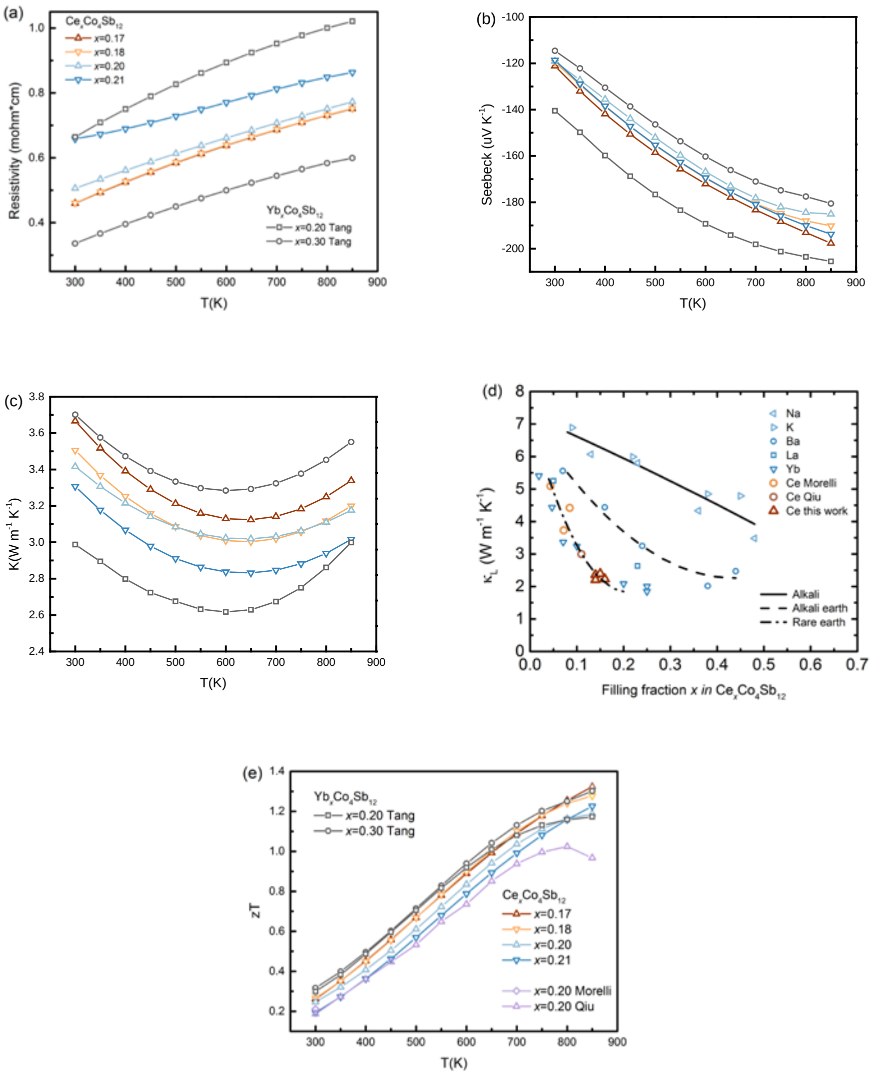

Figure 5.29 Transport properties of Ce- and Yb-doped skutterudites. The temperature dependence of : (a) electrical resistivity, (b) Seebeck coefficient, (c) thermal conductivity, and (e) thermoelectric figure of merit (zT) are plotted in the temperature range of 300K to 850K. In figure (d) the lattice thermal conductivity with a Lorentz number of 2.0×10^{-8} V^2K^{-2} is plotted against the filling fraction for various types of fillers. x denotes the nominal doping level of fillers.

The thermoelectric properties can be optimized when the filling fraction x of filler R (with valence q) in $R_xCo_4Sb_{12}$ satisfies qx = 0.4~0.6.[53,67] From Figure 5.27 we can see that when nominal compositions are in the Ce-rich three-phase regions with an annealing temperature at

1073K and 1123K, the Ce actual content in skutterudite phase is about $x = 0.17$ and 0.20 respectively. With Ce valence state being +3, qx for these materials would be in the optimum region. Thus a set of samples with nominal compositions $Ce_xCo_4Sb_{12}$ ($x = 0.17$, 0.18, 0.20, and 0.21) were prepared for thermoelectric evaluation, of which the first two samples were annealed at 1073K and the latter two were annealed at 1123K. The temperature dependence of transport properties of these samples is shown in Figure 5.29. Moreover, the transport data of two Yb-doped skutterudites with doping level $x = 0.20$ and 0.30 are also plotted for the reason of comparison.[49,50] With Yb valence state being +2, qx for these two samples are right on the boundary of the optimum region.

All the samples show negative Seebeck coefficients throughout the whole temperature range, indicating the expected *n*-type semiconductor behavior. With increasing temperature, both the electrical resistivity and the magnitude of the Seebeck coefficient increase, which is typical behavior for heavily doped semiconductors. It has to be noted that for the Ce-doped samples, the values of electrical resistivity, seebeck coefficient and thermal conductivity all fall between the values of the two Yb-doped samples, which is in agreement with Figure 5.26. κ_L is obtained by subtracting the electronic contribution from the total thermal conductivity using the Wiedemann-Franz law. We adopted a Lorentz number of 2.0×10^{-8} V^2K^{-2} to be consistent with previous work on skutterudites, and the lattice thermal conductivity calculated accordingly has less than 5% difference from the value calculated with the Lorentz number determined from a single parabolic band model.[53,163] All Ce-doped samples in this work show strongly reduced κ_L as compared to binary $CoSb_3$ with $\kappa_L \sim 10$ $Wm^{-1}K^{-1}$ at 300 K. As apparent from Figure 5.29d, Ce is as effective in reducing lattice thermal conductivity as Yb, with both much more effective than alkali and alkaline earth element fillers.

Figure 5.29e shows the continuously increasing zT indicative of the higher doping level than Qiu's sample[156]. All Ce-$CoSb_3$ samples in this work have zT values higher than 1.0 at and above 750K, with the maximum zT value in Ce-doped skutterudite samples reaching 1.3 with nominal Ce content $x = 0.17$ and $x = 0.18$ at 850K (with composition $Ce_{0.14}Co_4Sb_{12}$ for both samples determined from EPMA), which is 30% higher than that of previously reported literature value for Ce single filled skutterudites ($zT = 1.0$ for $Ce_{0.11}Co_4Sb_{12}$ at 850K)[156]. These zT are similar to those for single filled skutterudites[13,24,50,135], suggesting that Ce is a suitable earth abundant and low cost replacement for other types of fillers such as Yb, which makes the Ce single-filled skutterudites a more promising candidate for large-scale commercialization. The success of solubility design in Ce-$CoSb_3$ system is a good example that shows its potential in the optimization of thermoelectric properties in any other ternary systems with doping barriers, which allows wide applicability of this strategy.

5.5.5 Discussion about Ce-$CoSb_3$

Due to the low cost of Ce as a single filler, Ce-$CoSb_3$ skutterudites could have potential for scale-up commercialization in fields such as the automotive industry, if their thermoelectric performance can be optimized. Ce single-filled skutterudites in previous literature studies have been under-doped and fall out of the high power factor region due to the assumed low filling fraction limit of Ce (x=0.09). Here by conducting an equilibrium phase diagram study, we show that the filling fraction limit has a large temperature dependence and the value can reach as high as x=0.20 at 1123K. This clear enhancement gives a solubility value more than twice the one reported previously and thus allows optimizing Ce-$CoSb_3$ skutterudites. The ultra-high Ce content is confirmed by APT measurements. This surprisingly high filling fraction limit at high annealing temperatures breaks the solubility barrier and enables the Ce-$CoSb_3$ skutterudites to be optimized with zT of 1.3 for $Ce_{0.14}Co_4Sb_{12}$ at 850K, which is among the highest reported zT values for single-filled skutterudites and makes it an excellent substitute for Yb-doped skutterudites for waste heat recovery applications.

5.6 Stability of optimized compositions

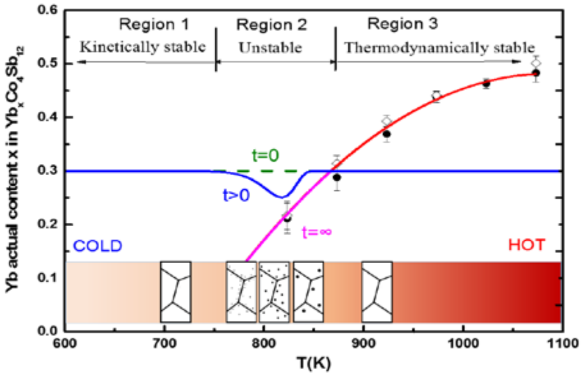

Figure 5.30 Stability of $Yb_xCo_4Sb_{12}$ skutterudite with optimum dopant composition $x = 0.3$. During operation (time $t > 0$), dopant precipitation is predicted in region 2 where the skutterudite phase is neither thermodynamically stable (as in region 3) nor kinetically stable (as in region 1).

The temperature dependent solubility limit predicts the precipitation of impurity phases at intermediate temperature, as shown schematically in Figure 5.30. Such temperature dependent solubility and precipitation has been observed in other ternary systems such as Na-doped PbTe as well[164]. In heavily doped SiGe, the precipitation and re-dissolution of dopants during high-temperature transport measurements was also reported[165]. The rate and size of the precipitates will depend on the temperature and time. As the optimum carrier concentration corresponds to approximately x = 0.3, $Yb_{0.3}Co_4Sb_{12}$ material above 873K will be stable indefinitely. The $Yb_{0.3}Co_4Sb_{12}$ material at low temperatures will be thermodynamically unstable but kinetically stable because precipitation will require the Yb diffusion, which will be low at low temperatures. In the intermediate temperature range, some precipitation of impurity phases is expected (see more discussion in Chapter 8). Reduction of the Yb content will also reduce the carrier concentration, which will raise the electrical resistivity of the material. Despite the formation of impurity phases, the maximum performance of the material may not be dramatically reduced because a lower carrier concentration at low temperature may actually increase the zT at that temperature[4]. Such a temperature dependent doping effect was found in Ag doped *n*-type PbTe-Ag_2Te nanocomposites to improve the thermoelectric performance[166]. The large difference in solubility limit at different temperatures could also be used to form nano-scale precipitates with controlled size, the results of which are also presented in Chapter 8[121,167].

5.7 Conclusion

In ternary phase diagram systems, a few concepts were cleared. Observing impurity phases are not sufficient in determining solubility limit, because the nominal composition might be just in a two- or three-phase region. This also applies for reaching a plateau of lattice constant against nominal filling content x with the plateau due to the existence of stable compositions. Three solubility design strategies are proposed based on the study of various ternary systems (In or Ga-Co-Sb in Section 5.3, Yb-Co-Sb in Section 5.4, Ce-Co-Sb in Section 5.5): firstly, stay on the correct solubility direction; secondly, aim at the right phase region; thirdly, vary annealing temperature. These strategies can be generalized to any ternary system with solubility barrier of doping elements.

Chapter 6

Defect study in intrinsic $CoSb_3$

6.1 Summary

The defect chemistry in intrinsic $CoSb_3$, to our most interest, whether intrinsic $CoSb_3$ is *p*-type or *n*-type, has been reported with large discrepancy. These reports are based on different types of materials (single-crystal or polycrystalline), which are synthesized with various methods (high temperature melting and annealing or ball milling, etc.) from different types of starting materials (in powder or ingot form, element purity). In this chapter, with a set of standard synthesis procedures, we performed a detailed Co-Sb binary phase diagram study combined with carrier concentration measurements in search of fundamental defect chemistry in $CoSb_3$ compounds. A literature review is presented in section 6.2 with previous reports. Experimental results and discussion are presented in section 6.3. Section 6.4 is the conclusion and future work.

6.2 Literature study

6.2.1 Bonding chemistry of $CoSb_3$

Skutterudite is a type of Zintl compound in which the total number of valences from both cations and anions is zero. According to Zintl chemistry[128], the formal valence of a cation and an anion can be calculated following the general valence rule[168]. As given in Eq. 6.1, e_c is the number of available valence electrons of the cation element and b_c is the number of cation-cation two-electron bonds and nonbonding lone pair electrons. Similarly, the anion formal valence is given by Eq. 6.2, where b_a is the number of anion-anion two-electron bonds.

$$V_c = e_c - b_c \qquad \text{(Eq. 6.1)}$$

$$V_a = e_a + b_a - 8 \qquad \text{(Eq. 6.2)}$$

Binary $CoSb_3$ compounds are diamagnetic semiconductors, so there should be no unpaired spin in the bonding scheme. For each Sb atom with electronic configuration $5s^2 5p^3$, it is bonded to its four nearest neighbors: two Sb atoms and two Co atoms. The Sb-Sb bonding has Sb-Sb-Sb bonding angle of 90°, which forms Sb_4 rings shown in Figure 6.2c. The remaining three valence electrons participate in the Co-Sb bonding. According to Eq. 6.2, Sb has -1 state (5+2-8 = -1). The distance between the Co atoms is too large for there to by any significant Co-Co bonding. Co atom with electronic configuration $4s^2 3d^7$ is thus only bonded to Sb atoms in an octahedral coordination (N = 6). For each Co atom, 3 electrons occupy the d^2sp^3 hybrid orbitals that are the essence of the Co-Sb bonding. The Co atom is in a 3+ state (9-6 = 3) with the remaining 6 electrons paired up leading to a low-spin d^6 state. The electronegativity of Sb (2.05) is close to that of Co (1.88), so these bonds have little ionic character. The bonding scheme is shown in Figure 6.1. The structure of [$CoSb_6$] octahedral and Sb_4 ring is shown in Figure 6.2.

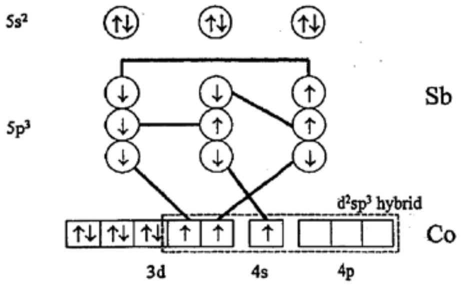

Figure 6.1 Bonding illustration in $CoSb_3$ from Dudkin's bonding model[169].

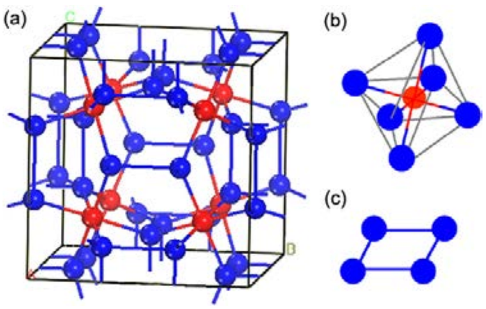

Figure 6.2. (a) Structure of skutterudite $CoSb_3$ (Co: red; Sb: blue), (b) [$CoSb_6$] octahedron, (c) Sb_4 ring. © IOP Publishing. Reproduced with permission. All rights reserved.[31]

6.2.2 Synthesis condition and defect type

Various attempts were made by previous researchers to synthesize either polycrystalline (melt-annealing method, mechanical alloying (ball milling)[31,32], high pressure assisted synthesis[34], melt-melt-spinning method[33] etc.) or single crystalline skutterudites (gradient freeze technique[5,6], flux-assisted growth[35], chemical vapor deposition[36] etc.).

The influence of synthesis methods and conditions on the defect type in $CoSb_3$ compounds is undeniable. Single crystal $CoSb_3$ can only be grown from Sb-rich melt (90 ~ 97 at% Sb) due to the phase diagram limitation[38], which is usually *p*-type[5,6,35,36]. However for polycrystalline $CoSb_3$, inconsistent results are reported among various groups. Both *p*- and *n*-type intrinsic $CoSb_3$ are reported with even the same synthesis method. Confusing though these data are, some results are still enlightening and worthy of attention.

Sharp *et al*[33] found that for samples synthesized in a melt-annealing method followed by cold/hot pressing, samples that are cold pressed show *p*-type while the ones hot pressed with the same starting powder composition show *n*-type. Deficiency of Sb due to hot pressing was speculated; however, there was no measured stoichiometry data to confirm.

Similarly, Liu *et al*[32] reported the sintering temperature can play a large role in the defects. For samples synthesized by mechanical alloying and SPS, when the sintering temperature is at 300℃, the samples show *p*-type, whereas when the sintering temperature is increased to 600℃, the samples show *n*-type. The EDS investigation shows a change in the Co:Sb ratio from 1:3.0 to 1:2.7 with increasing SPS temperature from 300℃ to 600℃, which was accounted for the *p*-*n* change. Liu *et al*[31] then studied the effect of Sb compensation on the point defects of $CoSb_3$. It was found when excess Sb was increased from zero to 8 at%, the Seebeck coefficient at room temperature changes from −430 to 40$\mu VK^{-1}$for samples synthesized with a fixed MA-SPS synthesis route. Sb-vacancy was concluded as the reason for the *n*-type behavior in Sb-deficient sample.

Nakagawa *et al*[170] tried to study the effect of stoichiometry (with nominal Sb:Co = 2.6~3.4) on thermoelectric properties of $CoSb_3$ using a melt-annealing method. Transport properties are measured on slices of annealed ingot to avoid influence of high temperature sintering process. However no clear trend was obtained. The presence of large quantities of secondary phases ($CoSb_2$ for Co-rich samples, Sb for Sb-rich samples) complicates the investigation. Recently, a study[171] on the effect of $CoSb_2$ and Sb on the electronic properties of $CoSb_3$ was revealed by a multi- band Hall effect analysis. While $CoSb_2$ increases the charge carrier density, the influence of the highly mobile charge carriers introduced by elemental Sb is worth noting as well.

By applying a high pressure (1.5GPa-3.5GPa) and high temperature (950K) assisted synthesis starting with stoichiometric Co and Sb powders, Su *et al*[34] reported that all samples synthesized are *p*-type, more interestingly, it is found that the carrier concentration can be a factor of 10 less when the pressure increases. This stress-dependent defect concentration is attributed to anti-site defects, whose formation energy may vary with the synthesis pressure. However, there was no experimental data to confirm this hypothesis. Excess Sb was observed in the lower pressure sample, which disappears for higher-pressure samples. This can be explained by the high volatility of Sb.

From the literature review we can conclude that a few factors are important in the experimental defect study of intrinsic $CoSb_3$:

1) The form and purity of starting material. Powder raw elements tend to introduce O_2 up to 1000ppm into the system. Fe or Ni impurities, which are easy to be found in Co, can contribute to *p*- or *n*-type doping as well.
2) If we compare the most common synthesis methods, traditional melt-annealing and mechanical alloying (ball milling), the latter is more prone to introduce impurities such as oxygen or Fe (if the vial is made of steel).
3) Consolidation conditions are important. The high sintering temperature can alter the stoichiometry to be Sb-deficient in $CoSb_{3,}$ resulting an *n*-type behavior. The increasing sintering pressure leads to a decreasing *p*-type carrier concentration, the reason to which remains unclear.
4) When considering the influence of off-stoichiometry (either Co-rich or Sb-rich) on defects, often large amount of secondary phases is introduced as well. The influence of these secondary phases is not fully clear yet. It is thus required to synthesis of Co-rich/Sb-rich samples with little secondary phases.

6.3 Results and discussion

6.3.1 Phase width of $CoSb_3$

With the discussion in Section 6.2.2, we orient our research as follows: 1) Powders are avoided for all starting materials. High-purity elements with slug or shot forms are chosen and purchased from Alfa Aesar (Co (99.95%, slug), Sb (99.9999%, shot)). 2) Traditional melt-annealing method rather than ball milling is used to avoid contamination. Prior to hot pressing, ingots obtained from annealing are hand grinded instead of ball milled for the same reason. 3) The sintering method was chosen to be hot pressing with a fixed set of parameters (700℃, 60MPa, and 1 hour) to minimize variance due to sintering conditions. 4) Investigated compositions are chosen to have a stoichiometry Co:Sb= 4 : (12+*x*) close to 1:3 (x = -0.06~0.17) in order to minimize quantities of secondary phases. With all these synthesis conditions determined, we hope to synthesize $CoSb_3$ in both Co-rich and Sb-rich conditions with the least amount of secondary phase, which shall allow us to study the defect type in $CoSb_3$ without influences from these impurities.

Binary $CoSb_3$ is often considered to be a line compound up to 874℃. However, we challenge this by trying to measure the temperature dependent phase width of $CoSb_3$. 21 Samples with various compositions are synthesized in a similar manner except with different annealing temperatures (See Chapter 2, Section 2.2 for more detail). The synthesized compositions as well as their annealing temperatures are shown in Table. 6.1, where × denotes the indicated composition is synthesized and annealed at the corresponding temperature.

Table 6.1 Compositions synthesized with corresponding annealing temperatures.

Annealing T(℃)	$Co_4Sb_{11.94}$	$Co_4Sb_{11.97}$	Co_4Sb_{12}	$Co_4Sb_{12.03}$	$Co_4Sb_{12.13}$	$Co_4Sb_{12.15}$	$Co_4Sb_{12.17}$
850	×	×		×			
800	×	×	×	×	×		
700	×	×	×	×		×	
650		×	×				
600		×	×				×
500		×	×				×

The phase purity of annealed ingots was checked with SEM and XRD. The stoichiometry of the $CoSb_3$ phase was confirmed by EPMA. SEM photos and XRD patterns for samples annealed at 500℃, 700℃, and 850℃ (on ingots or hot pressed samples) were chosen to show in Figures 6.3-6.8. The secondary phases (mostly determined from SEM unless otherwise specified from XRD) and EPMA compositions (on annealed ingots) are summarized and shown in Tables 6.2-6.4. After hot pressing, the phases were again checked by XRD; however, unfortunately, the stoichiometry of $CoSb_3$ phase on hot pressed samples was not double-checked. As we shall discuss in Section 6.3.2 later, this might cause problems in analyzing the correct defect type. For all the samples, the EPMA compositions for $CoSb_3$ phase confirm a stoichiometry of Co:Sb close to 1:3 after annealing and before hot pressing. The phase width can be determined from secondary phase identification for each annealing temperature.

Table 6.2 Phase purity and composition analysis of $CoSb_3$ samples annealed at 500℃.

Nominal Composition	EPMA composition	Secondary phase
$Co_4Sb_{11.97}$	12.05±0.06	$CoSb_2$
Co_4Sb_{12}	12.05±0.08	Sb
$Co_4Sb_{12.17}$	12.06±0.06	Sb

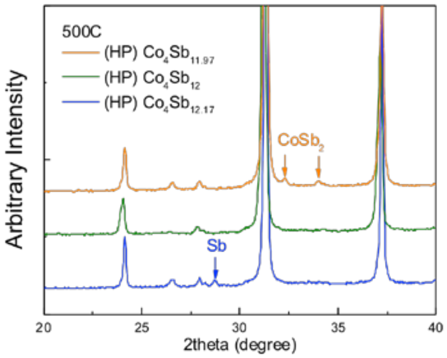

Figure 6.3 XRD patterns of $CoSb_3$ samples annealed at 500℃ (after hot pressing).

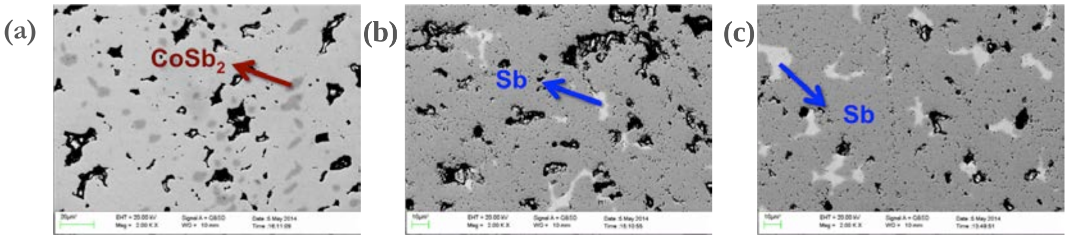

Figure 6.4 SEM photos of a) Co-rich sample $Co_4Sb_{11.97}$; b) on stoichiometry sample Co_4Sb_{12}; c) Sb-rich sample $Co_4Sb_{12.17}$ after annealing at 500℃.

As we can see from Table 6.2, the phase region of $CoSb_3$ at 500℃ should be between the compositions $Co_4Sb_{11.97}$ and Co_4Sb_{12}. The Sb secondary phase for nominal composition Co_4Sb_{12} (as can be seen in Figure 6.4b) disappears after hot pressing in Figure 6.3 (no Sb peak on the green curve), which is consistent with previous findings[34].

Table 6.3 Phase purity and composition analysis of $CoSb_3$ samples annealed at 700℃.

Nominal Composition	EPMA composition	Secondary phase

$Co_4Sb_{11.94}$	12.04±0.07	$CoSb_2$ (XRD)
$Co_4Sb_{11.97}$	12.03±0.04	None
Co_4Sb_{12}	12.05±0.04	None
$Co_4Sb_{12.03}$	12.06±0.09	Sb
$Co_4Sb_{12.15}$	12.00±0.09	Sb

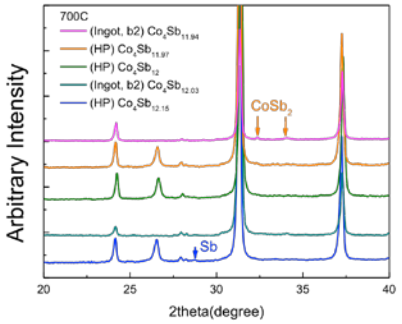

Figure 6.5 XRD patterns of $CoSb_3$ samples annealed at 700℃ (ingots or samples after hot pressing).

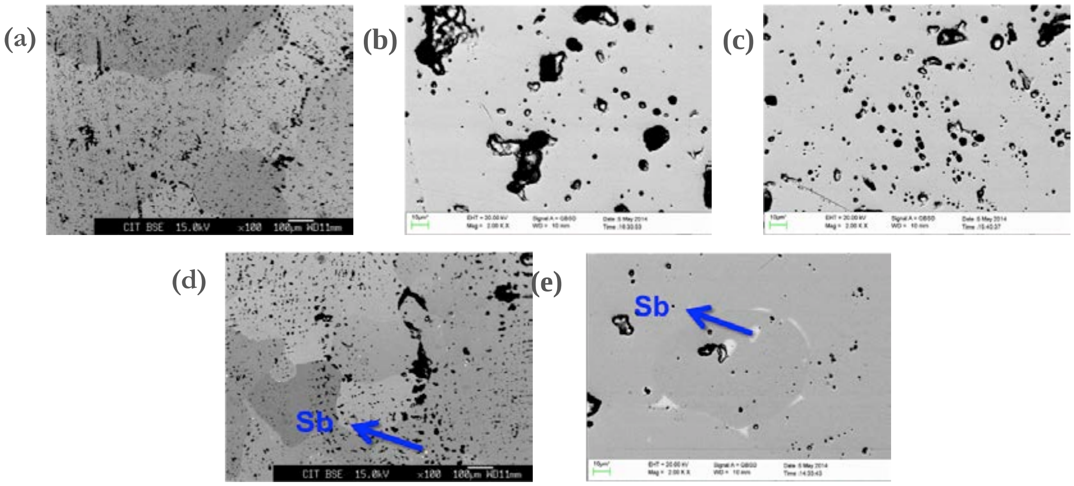

Figure 6.6 SEM photos of a) Co-rich sample $Co_4Sb_{11.94}$; b) Co-rich sample $Co_4Sb_{11.97}$; c) on stoichiometry sample Co_4Sb_{12}; d) Sb-rich sample $Co_4Sb_{12.03}$; e) Sb-rich sample $Co_4Sb_{12.15}$ after annealing at 700℃.

As we can see from Table 6.3, the phase region of $CoSb_3$ at 700℃ should be between the compositions $Co_4Sb_{11.94}$ and $Co_4Sb_{12.03}$. The $CoSb_2$ phase for nominal composition $Co_4Sb_{11.94}$ is invisible in SEM but is detected by XRD. The Sb secondary phase for nominal composition $Co_4Sb_{12.03}$ (as can be seen in SEM) disappears after hot pressing in XRD.

Table 6.4 Phase purity and composition analysis of $CoSb_3$ samples annealed at 850°C.

Nominal Composition	EPMA composition	Secondary phase
$Co_4Sb_{11.94}$	12.05±0.04	$CoSb_2$ (XRD)
$Co_4Sb_{11.97}$	11.95±0.08	$CoSb_2$ (XRD)
$Co_4Sb_{12.03}$	12.04±0.08	Sb

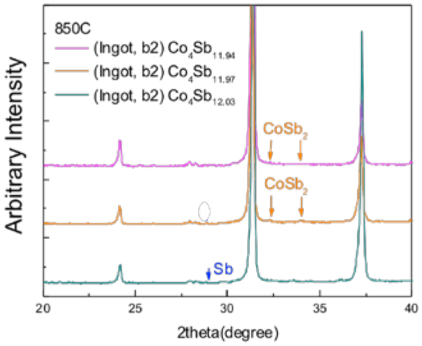

Figure 6.7 XRD patterns of $CoSb_3$ samples annealed at 850°C (ingots after annealing).

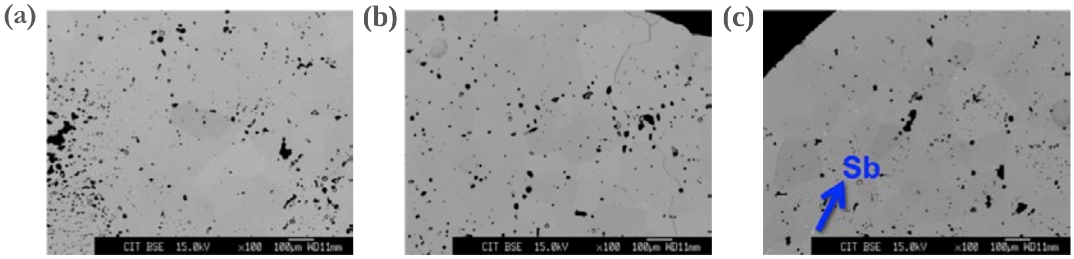

Figure 6.8 SEM photos of a) Co-rich sample $Co_4Sb_{11.94}$; b) Co-rich sample $Co_4Sb_{11.97}$; c) Sb-rich sample $Co_4Sb_{12.03}$ after annealing at 850°C.

As we can see from Table 6.4, the phase region of $CoSb_3$ at 850°C should be between the compositions $Co_4Sb_{11.97}$ and $Co_4Sb_{12.03}$.

If we combine all the information collected at each temperature, a rough estimate of the temperature dependent phase width of $CoSb_3$ can be depicted in Figure 6.9. As we can see, the phase width (where green circles are in) is very narrow throughout the temperature range investigated, with $(\Delta x)_{max} < 0.1$ for Co_4Sb_{12+x}. Due to the accuracy of EPMA measurements, it is hard to distinguish experimentally if the skutteurdite phase is Sb rich or Co rich. Appearance of secondary phases can serve as a guide, but this is true only on annealed samples because of possible modification on the stoichiometry due to high temperature sintering. This work is useful in guiding researchers to synthesize off-stoichiometry $CoSb_3$ with least secondary phases.

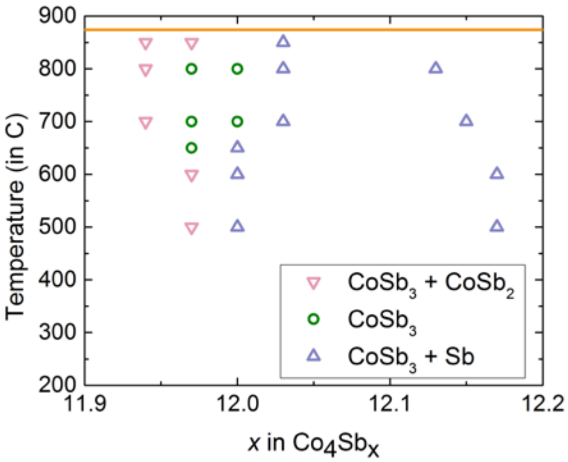

Figure 6.9 Temperature dependent phase width of $CoSb_3$. Pink downward triangle symbols represent samples in a two-phase region of $CoSb_2$ and $CoSb_3$. Green circle symbols represent samples in a single-phase region of pure $CoSb_3$. Purple upward triangle symbols represent samples in a two-phase region of $CoSb_3$ and Sb. The orange solid line represents the peritectic temperature for $CoSb_3$ 874°C.

6.3.2 Defect type in intrinsic $CoSb_3$

In this section, we will see that even though we designed the research with much care, there is still some influence from both the starting elements and synthesis condition on the defect type, which adds complexity to the interpretation of the results. Table 6.5 shows the room temperature transport data measured on samples hot pressed at 700°C with a pressure of 60MPa and pressing time of 1h.

Table 6.5 Room temperature transport data measured on Co_4Sb_x (x = 11.94 ~ 12.17) samples hot pressed at 700°C.

Annealing T (°C)	Sample Composition	nH (cm^{-3})	Resistivity (mOhm/cm)	Mobility (cm^2/Vs)	Seebeck (uV/K)	Density (g/cm^3)
500	$Co_4Sb_{11.97}$	-8.6E+17	181	-41	-300	7.41
	Co_4Sb_{12}	-3.7E+17	94	-182	-398	7.37
	$Co_4Sb_{12.17}$	-1.1E+18	116	-49	-285	7.41
600	$Co_4Sb_{11.97}$	-4.5E+17	125	-111	-337	7.45

	Co_4Sb_{12}	-4.3E+17	160	-91	-338	7.40
	$Co_4Sb_{12.17}$	-4.6E+17	95	-141	-357	7.43
650	$Co_4Sb_{11.97}$	-5.2E+17	79	-151	-381	7.28
	Co_4Sb_{12}	-4.3E+17	76	-194	-386	7.31
700	$Co_4Sb_{11.94}$	-6.0E+17	76	-136	-380	7.28
	$Co_4Sb_{11.97}$	-3.9E+17	94	-171	-398	7.41
	Co_4Sb_{12}	-3.8E+17	124	-135	-380	7.46
	$Co_4Sb_{12.03}$	-3.7E+17	94	-179	-422	7.39
	$Co_4Sb_{12.15}$	-4.2E+17	78	-192	-380	7.44
800	$Co_4Sb_{11.94}$	-5.9E+17	73	-145	-361	7.32
	$Co_4Sb_{11.97}$	-3.8E+17	89	-185	-394	7.40
	Co_4Sb_{12}	-3.8E+17	99	-168	-396	7.28
	$Co_4Sb_{12.03}$	-5.1E+17	98	-125	-423	7.32
	$Co_4Sb_{12.13}$	-5.2E+17	77	-157	-357	7.44
850	$Co_4Sb_{11.94}$	-6.2E+17	79	-128	-352	7.14
	$Co_4Sb_{11.97}$	-5.3E+17	80	-148	-376	7.26
	$Co_4Sb_{12.03}$	-4.3E+17	94	-154	-394	7.33

From the bonding chemistry of $CoSb_3$, one would expect that $CoSb_3$ with Co-rich stoichiometry would lead to *n*-type whereas Sb-rich stoichiometry would lead to *p*-type material. Yet Table 6.5 shows that all the samples synthesized show *n*-type behavior. This is quite confusing, and interesting.

Several possible reasons are speculated to explain these data:

1. Impurity doping in starting Co element.

Even though we chose a slug form of cobalt with 99.95% purity, the Co elemental analysis reveals a higher Ni impurity level compared to Fe (as shown in Figure 6.10), which might account for the unusual constant *n*-type doping.

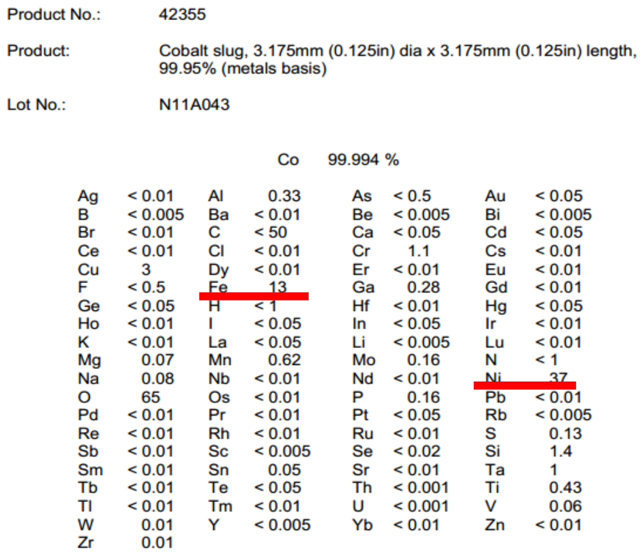

Product No.: 42355

Product: Cobalt slug, 3.175mm (0.125in) dia x 3.175mm (0.125in) length, 99.95% (metals basis)

Lot No.: N11A043

Co 99.994 %

Ag	< 0.01	Al	0.33	As	< 0.5	Au	< 0.05
B	< 0.005	Ba	< 0.01	Be	< 0.005	Bi	< 0.005
Br	< 0.01	C	< 50	Ca	< 0.05	Cd	< 0.05
Ce	< 0.01	Cl	< 0.01	Cr	1.1	Cs	< 0.01
Cu	3	Dy	< 0.01	Er	< 0.01	Eu	< 0.01
F	< 0.5	Fe	13	Ga	0.28	Gd	< 0.01
Ge	< 0.05	H	< 1	Hf	< 0.01	Hg	< 0.05
Ho	< 0.01	I	< 0.05	In	< 0.05	Ir	< 0.01
K	< 0.01	La	< 0.05	Li	< 0.005	Lu	< 0.01
Mg	0.07	Mn	0.62	Mo	0.16	N	< 1
Na	0.08	Nb	< 0.01	Nd	< 0.01	Ni	37
O	65	Os	< 0.01	P	0.16	Pb	< 0.01
Pd	< 0.01	Pr	< 0.01	Pt	< 0.05	Rb	< 0.005
Re	< 0.01	Rh	< 0.01	Ru	< 0.01	S	0.13
Sb	< 0.01	Sc	< 0.005	Se	< 0.02	Si	1.4
Sm	< 0.01	Sn	0.05	Sr	< 0.01	Ta	1
Tb	< 0.01	Te	< 0.05	Th	< 0.001	Ti	0.43
Tl	< 0.01	Tm	< 0.01	U	< 0.001	V	0.06
W	0.01	Y	< 0.005	Yb	< 0.01	Zn	< 0.01
Zr	0.01						

Figure 6.10 Co elemental analysis showing higher Ni impurity level than Fe.

To test our hypothesis, four compositions are synthesized with annealing temperature 700℃ and stoichiometry $Co_4Sb_{12.03}M_x$ (M = Fe or Ni, x = 0.002 and 0.004, which correspond to 500ppm and 1000ppm holes/electrons, respectively). The Co:Sb ratio and annealing temperature were chosen such that according to the phase diagram in Figure 6.9, the resulting samples should contain little Sb secondary phase and stay slightly Sb-rich (*p*-type expected according to bonding chemistry). XRD measurements on annealed ingot slices confirmed that all four samples contain little amount of Sb secondary phase. If the influence of the impurity (Fe, Ni) is small then all four samples should be *p*-type. However this is not the case. The room temperature transport results show *p*-type for M = Fe, yet *n*-type for M = Ni on samples sliced from annealed ingot, as shown in Table 6.6. This shows that though as small as 500pm the Ni impurity level is, it could still change completely the defect type. If we plot the carrier concentration versus the Ni content, a perfect linear relationship confirms this point; see Figure 6.11.

Table 6.6 Room temperature transport data measured on Fe, Ni doped $CoSb_3$ samples annealed and hot pressed at 700°C. Data for sample $Co_4Sb_{12.03}$ annealed at 700℃ is also shown for comparison.

Sample Composition	Impurity level	nH (cm^{-3})	Resistivity (mOhm/cm)	Mobility (cm^2/Vs)	Seebeck (uV/K)
$Co_4Sb_{12.03}Fe_{0.002}$	476 *h*	7.1E+19	1	87	32
$Co_4Sb_{12.03}Fe_{0.004}$	976 *h*	6.7E+18	1	679	62
$Co_4Sb_{12.03}$	24 *e*	-3.7E+17	94	-179	-422
$Co_4Sb_{12.03}Ni_{0.002}$	524 *e*	-1.1E+18	41	-145	-369

$Co_4Sb_{12.03}Ni_{0.004}$	1024 *e*	-1.7E+18	28	-133	-324

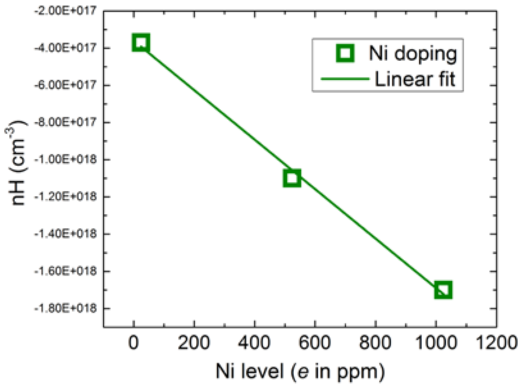

Figure 6.11 Linear relationship between carrier concentration in $CoSb_3$ and Ni impurity content.

2) Influence of hot pressing on stoichiometry.

This should be further confirmed by performing EPMA analysis on hot pressed samples, to double-check the stoichiometry. If there is indeed a large amount of Sb deficiency due to the high temperature sintering, similar to the one (Co:Sb=1:2.72) reported previously by Liu *et al*[32], it should well manifest itself on EPMA analysis. However, if the effect of hot pressing on altering the stoichiometry is actually not as significant, due to the accuracy limit of EPMA, it would hard to determine if the material is either Co-rich or Sb-rich. In any case the transport properties should be better performed on annealed ingots to eliminate the possible influence from hot pressing.

6.4 Conclusion and future work

Experimental study of the defect type was performed on samples synthesized with the guidance of phase diagram study. The phase width of $CoSb_3$ as well as its temperature dependence was discovered, with $(\Delta x)_{max} < 0.1$ for Co_4Sb_{12+x} between 500℃ and 850℃. The excess Ni impurity doping as well as the possible influence of hot pressing might alter the intrinsic defect type of $CoSb_3$. Starting elements with higher purity are needed. Transport properties are better performed on annealed ingots without hot pressing. The possible effect of oxygen on doping is worth studying as well. More research is required to reach a solid conclusion about the intrinsic defect type in both Co and Sb-rich $CoSb_3$.

Chapter 7

Phase diagram study of Ce-Fe-Co-Sb quaternary system

7.1 Summary

So far this thesis is mainly about *n*-type $CoSb_3$ based skutterudites. To enable thermoelectric application, both *n*- and *p*- legs are required, preferably from the same kind of material so that the difference in thermal expansion coefficient could be minimized to avoid detrimental strain and mechanical failure. This chapter is about the phase diagram study of the Ce-Co-Fe-Sb quaternary system, which is motivated by the need of high *zT* *p*-type skutterudite materials.

From Chapter 5 we already discussed the potential of Ce-$CoSb_3$ as good *n*-type thermoelectric material. If we substitute Co by Fe, the holes introduced by Fe (1 hole/Fe atom) will dope the material *p*-type. By tuning the ratio between *n*-type dopant Ce and *p*-type dopant Fe, we can change the $Ce_yCo_xFe_{4-x}Sb_{12}$ material to be either *n*-type or *p*-type, as discussed in Section 7.2. The thermoelectric properties of these *p*-type materials, however, are often not promising. In search of optimized compositions for *p*-type $Ce_yCo_xFe_{4-x}Sb_{12}$ material, we first investigate the phase space of skutterudite phase in this Ce-Co-Fe-Sb quaternary system. Experimental determination of isothermal sections of Ce-Fe-Sb and Co-Fe-Sb ternary systems at 700℃ is presented in Section 7.3 and 7.4 respectively. Together with previously determined Ce-Co-Sb isothermal section at 700℃, these determined ternary phase diagram isothermal sections contribute to the partial determination of phase space of $Ce_yCo_xFe_{4-x}Sb_{12}$ skutterudites as presented in Section 7.5. With a fixed Co:Fe ratio, *n*-*p* change of semiconducting type can be realized by varying the amount of Ce alone (Section 7.6). Though the thermoelectric performance of these materials needs to be further optimized, it can be potentially useful in making both *n*- and *p*- thermoelectric legs with similar compositions. Section 7.7 is the conclusion and a look at future work.

7.2 Charge-compensating defects

In $Ce_yCo_{4-x}Fe_xSb_{12}$ materials, Ce acts as a donor with each Ce atom giving three electrons to make the material *n*-type whereas Fe acts as an acceptor with each Fe atom contributing one hole to make it *p*-type. This charge-compensating effect can increase the Ce solubility limit, which was reported previously by many researchers[19,154,172]. Previous results are combined and shown in Figure 7.1. A clear increasing trend of maximum Ce solubility could be observed with the increasing amount of Co substitution by Fe.

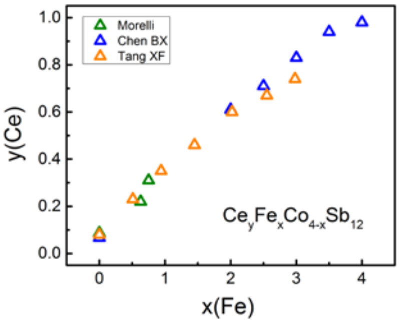

Figure 7.1 Dependence of maximum Ce solubility with Fe amount in $Ce_yCo_{4-x}Fe_xSb_{12}$ skutterudite materials[19,154,172].

The carrier concentrations for each sample are also extracted and shown in Figure 7.2.

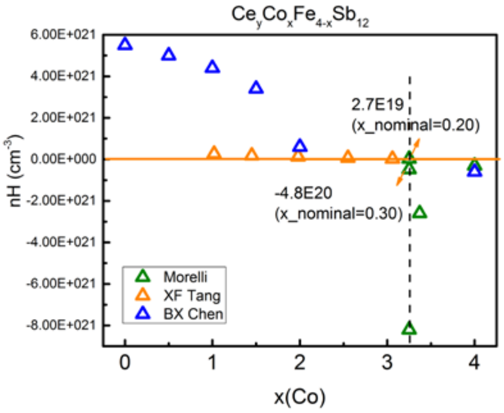

Figure 7.2 Dependence of carrier concentrations in $Ce_yCo_{4-x}Fe_xSb_{12}$ skutterudites on the amount of Co substitution[19,154,172]. The horizontal orange solid line represents carrier concentration of zero. The vertical black dashed line corresponds to x(Co) = 3.25. The carrier concentrations of two samples (green triangle symbols) lined on the dashed line of x(Co) = 3.25 are marked by orange arrows. The upper sample with nominal composition $Ce_{0.20}Co_{3.25}Fe_{0.75}Sb_{12}$ is *p*-type with carrier concentration 2.7E19 cm^{-3}, while the lower sample with nominal composition $Ce_{0.30}Co_{3.25}Fe_{0.75}Sb_{12}$ is *n*-type with carrier concentration -4.8E20 cm^{-3}.

As we can see, closer to the Co-rich side, materials are mostly *n*-type, whereas closer to the Fe-rich side, materials are mostly *p*-type. Note for a fixed cobalt content x(Co) = 3.25, both *n* and *p* type materials are observed with different Ce doping levels. This allows a good opportunity to study skutterudite materials with similar composition yet different semiconducting type (as shown in Section 7.6); however, in the literature study[19] high temperature thermoelectric properties were not measured.

For each fixed Co content, the largest amount of carriers that can be generated by Ce filling is 3**y*(Ce) electrons with *y* being the solubility limit of Ce for that specific *x*(Co) (blue dashed line) . The green line represents the amount of holes (*x*) for Co substitution by Fe in $Ce_yCo_{4-x}Fe_xSb_{12}$. Then mathematically the material can be determined to be either *n*-type or *p*-type by comparing these two quantities (blue and green lines) for a fixed Co content. To the Fe rich side (left region to the orange vertical line), the green line is higher than the blue dashed line, so materials show *p*-type behavior. To the Co-rich side (right region to the orange vertical line), the blue dashed line is higher than the green line, so materials show *n*-type behavior. The *n*-*p* crossover happens at about *x*(Co) = 2.75~3.25. Only with *x*(Co) > crossover value can both *n*- and *p*-type materials with the same Co:Fe ratio be obtained, which is in agreement with the experiment result[19]. However this value is largely dependent on the experimentally determined Ce filling solubility limit. As we have learnt from the case study of Ce-$CoSb_3$ system, the solubility limit can often be misinterpreted. So in the following sections (Section 7.3-7.5) we set out to re-investigate the phase region of skutterudites in Ce-Fe-Co-Sb system before trying to optimize thermoelectric properties.

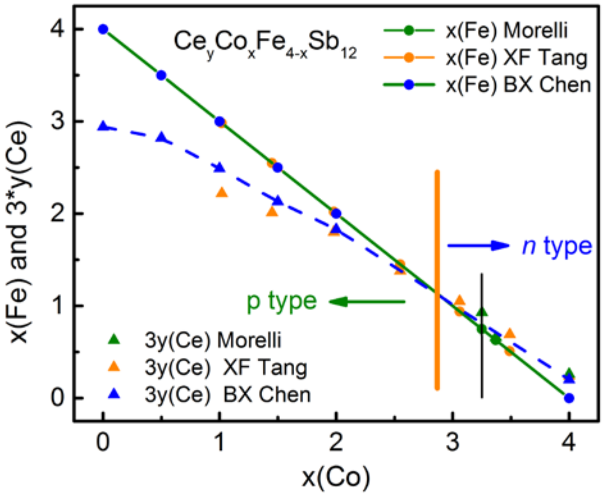

Figure 7.3 Crossover from *p*-type to *n*-type in $Ce_yCo_xFe_{4-x}Sb_{12}$ materials[19,154,172] when $x \approx 2.75 - 3.25$.

7.3 Ce-Fe-Sb isothermal section at 700℃

The isothermal section of Ce-Fe-Sb ternary system is determined following the methodology described in details in Section 5.2. To decrease the workload, only a section ($CeSb_2$-$FeSb_2$-Sb) was considered assuming the phase relations around $CoSb_3$ would not involve phases beyond this region. A sketch was first drawn based on binary phase diagram informations[173-175] and previous literature study[154], shown in. Note the large amount of excess Sb in the nominal composition $Ce_{1.05}Fe_4Sb_{12.2}$ used in literature should set it in an Sb-rich phase region. Eight nominal compositions were proposed to a first batch synthesis to determine phase regions, as listed in Table 7.1. They are also shown illustratively on the proposed isothermal section on Figure 7.4, from which we can see that the nominal compositions of our synthesis are dispersed around the previously determined skutterudite composition ($Ce_{0.98}Fe_4Sb_{12}$) and scattered in different estimated phase regions. To identify three-phase regions, at least two nominal compositions are selected in each region to confirm the equilibrium stable compositions.

Table 7.1 Selected nominal compositions for investigation of Ce-Fe-Sb isothermal section at 700℃. Bold $FeSb_2$ phase was confirmed to be FeSb phase after characterization of the samples #1-8.

Sample name	Nominal composition	Estimated phase region
Ce-Fe-Sb #1	$Ce_{0.9}Fe_{3.57}Sb_{12.43}$	$Ce_xFe_4Sb_{12}$ + liquid Sb
Ce-Fe-Sb #2	$Ce_{0.9}Fe_{3.9}Sb_{12.1}$	$Ce_xFe_4Sb_{12}$ + $FeSb_2$ + liquid Sb
Ce-Fe-Sb #3	$Ce_{0.9}Fe_4Sb_{12}$	$Ce_xFe_4Sb_{12}$ + $FeSb_2$ + liquid Sb
Ce-Fe-Sb #4	$Ce_{1.05}Fe_4Sb_{12}$	$Ce_xFe_4Sb_{12}$ + **$FeSb_2$** + $CeSb_2$
Ce-Fe-Sb #5	$Ce_{1.05}Fe_{4.1}Sb_{11.9}$	$Ce_xFe_4Sb_{12}$ + **$FeSb_2$** + $CeSb_2$
Ce-Fe-Sb #6	$Ce_{1.05}Fe_{4.2}Sb_{11.8}$	$Ce_xFe_4Sb_{12}$ + **$FeSb_2$** + $CeSb_2$
Ce-Fe-Sb #7	$Ce_{1.05}Fe_{3.9}Sb_{12.1}$	$Ce_xFe_4Sb_{12}$ + $CeSb_2$ + liquid Sb
Ce-Fe-Sb #8	$Ce_{1.05}Fe_{3.8}Sb_{12.2}$	$Ce_xFe_4Sb_{12}$ + $CeSb_2$ + liquid Sb
Ce-Fe-Sb #9	$Ce_{0.7}Fe_{4.65}Sb_{11.35}$	$Ce_xFe_4Sb_{12}$ + $FeSb_2$ + FeSb
Ce-Fe-Sb #10	$Ce_{0.7}Fe_{4.5}Sb_{11.5}$	$Ce_xFe_4Sb_{12}$ + $FeSb_2$ + FeSb
Ce-Fe-Sb #11	$Ce_{0.7}Fe_{4.1}Sb_{11.9}$	$Ce_xFe_4Sb_{12}$ + $FeSb_2$ + liquid Sb
Ce-Fe-Sb #12	$Ce_{0.7}Fe_{3.9}Sb_{12.1}$	$Ce_xFe_4Sb_{12}$ + $FeSb_2$ + liquid Sb

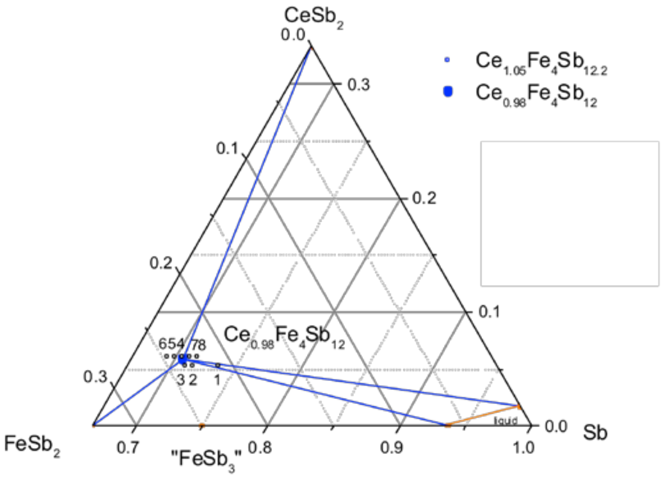

Figure 7.4 First sketch of Ce-Fe-Sb ternary phase diagram isothermal section at 700°C. Blue empty circle represents the nominal composition $Ce_{1.05}Fe_4Sb_{12.2}$ in literature[154]. The corresponding skutterudite phase compositon $Ce_{0.98}Fe_4Sb_{12}$ is shown as a blue dot. Proposed nominal compositions for the first batch 8 samples were shown as empty black circles.

After phase purity and chemical composition characterization of this batch of samples, we found that the experimental results confirm on a large part our initial estimation except for two inconsistencies.

The first is the appearance of FeSb phase that was out of our scope in the first place. For samples #4-6, the equilibrium phases are $CeSb_2$ and FeSb, not the $CeSb_2$ and $FeSb_2$ phases that we had estimated (Table 7.1). This is shown in the SEM photo (Figure 7.5c). XRD analysis of these samples (#4-6) is in agreement with SEM/EDS analysis. This suggests that the phase diagram should take into account the FeSb phase as well, and thus we enlarge the scope of our investigation to the (CeSb-FeSb-Sb) region instead. With this modification, we made a second batch of the sample (Ce-Fe-Sb #9-12). Their nominal compositions are added to Table 7.1 and shown in the enlarged isothermal section in Figure 7.6.

The second inconsistency is that the determined skutterudite phase composition $Ce_{0.96}\pm_{0.02}Fe_4Sb_{12}$ in this study is slightly different from the previous literature value $Ce_{0.98}Fe_4Sb_{12}$. This compositional change is not huge yet its influence is subtle by slightly shifting the phase boundaries downward towards the Co-Sb base line. It could well explain why the estimated phase region of sample #1 and #2 are off. As shown in Figure 7.5a, sample #1 with nominal composition $Ce_{0.9}Fe_{3.57}Sb_{12.43}$ is actually in a three-phase region ($Ce_xFe_4Sb_{12}$ + $CeSb_2$ + liquid Sb) rather than the estimated two-phase region ($Ce_xFe_4Sb_{12}$ + liquid Sb). Figure 7.5b shows sample #2 with nominal composition $Ce_{0.9}Fe_{3.9}Sb_{12.1}$ actually in a two-phase region ($Ce_xFe_4Sb_{12}$ + liquid Sb) rather than the estimated three-phase region ($Ce_xFe_4Sb_{12}$ + $FeSb_2$ + liquid Sb).

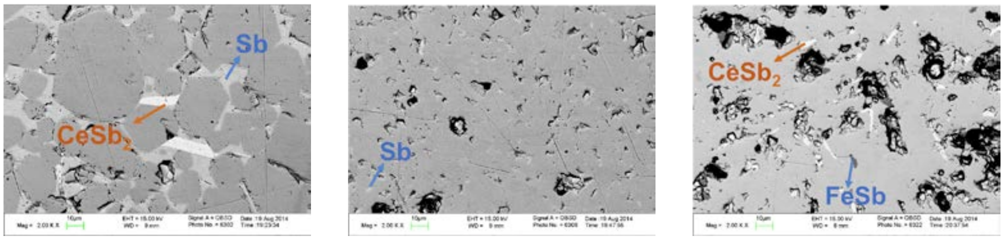

Figure 7.5 SEM photos of samples with nominal composition as a) #1 $Ce_{0.9}Fe_{3.57}Sb_{12.43}$, b) #2 $Ce_{0.9}Fe_{3.9}Sb_{12.1}$ and c) #5 $Ce_{1.05}Co_{4.1}Sb_{11.9}$. The bright white impurity phase (marked by orange arrow) is determined with EDS to be $CeSb_2$, the light white phase is Sb and the dark grey phase is FeSb.

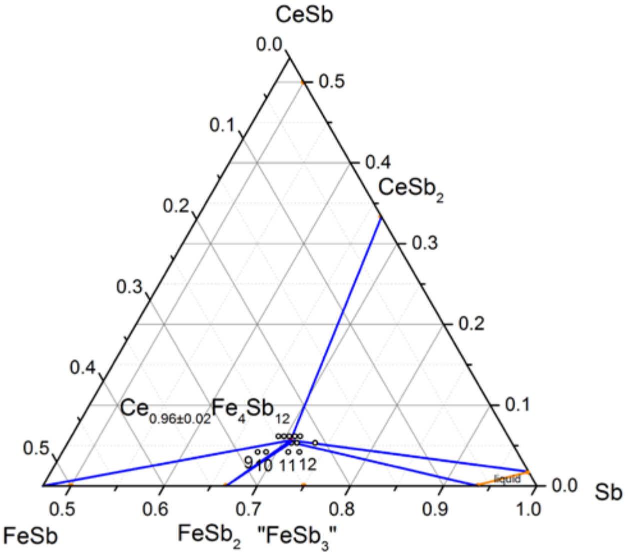

Figure 7.6 Second batch of Ce-Fe-Sb samples (#9-12) synthesized based on binary phase diagrams and results from the first batch of samples.

Note in this batch that the nominal content of Ce is much lower (x=0.7) compared to the previous synthesis. This is to make sure that samples could fall in the phase region (the one that involve FeSb phase especially) we would like to investigate and have large quantities of impurity phases to facilitate phase identification as well.

The results on these two batches of samples are self-consistent. #9 and #10 shows impurity phases of FeSb and $FeSb_2$ perfectly matching the phase diagram relations. With all the information combined we are ready to determine the isothermal section (shown in Figure 7.7) with the Ce solubility region in skutterudites being $0.917\pm0.008 < x < 0.961\pm0.018$ in $Ce_xFe_4Sb_{12}$. Note the lower solubility limt for Ce filling, meaning a minimum amount of Ce is required to stabilize the material. This is for the first time that the solubility of Ce is reported to have a width in Ce-filled Fe-based $Ce_xFe_4Sb_{12}$ skuterudites, which is quite different from the single value x = 0.98 reported earlier[154] and request some thought in synthesis.

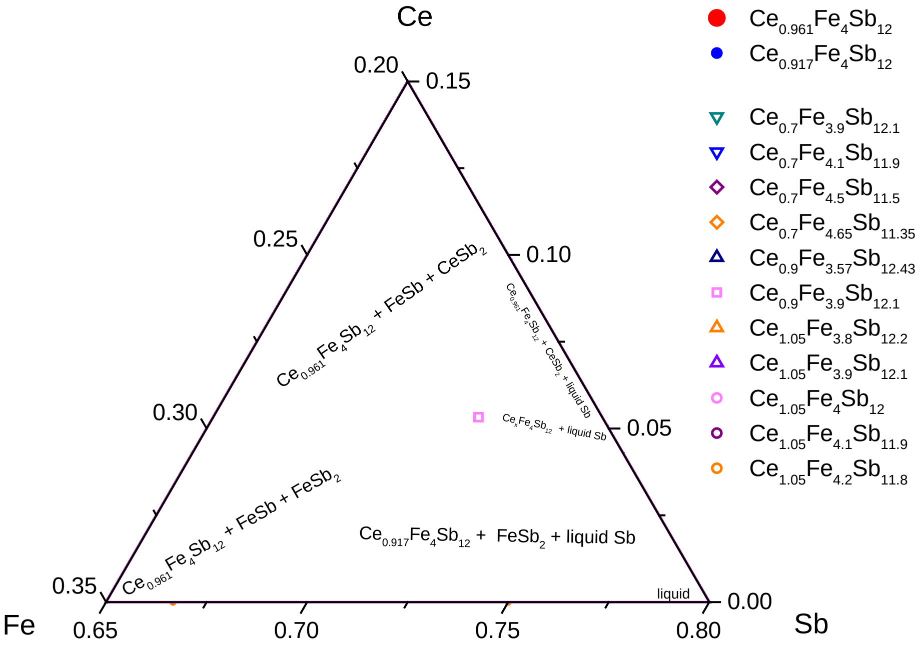

Figure 7.7 Isothermal section of Ce-Fe-Sb ternary system at 700℃.

7.4 Co-Fe-Sb isothermal section at 700℃

Due to serious deficiency of electrons, $FeSb_3$ phase does not exist in thermodynamic equilibrium form. However, these is indeed some solubility of Fe in $CoSb_3$, which makes it *p*-type material. This has been reported with x = 0.8 in $Fe_xCo_{4-x}Sb_{12}$ [176]. As we can see from the phase diagram in Figure 7.8 below, the phase region changes when the amount of substitutional Fe increases. Upon x = 0.8, the three-phase region (liquid + (Co,Fe)Sb_3 + Sb) forms for x between (0.8, 2.48); for x between

(2.48, 3.38), two-phase region of (liquid + (Co,Fe)Sb_2) forms; and lastly, another three-phase region (liquid + (Co,Fe)Sb_2 + Sb) forms for *x* between (3.38, 4). The three-phase regions with the co-existence of liquid phase and Sb phase are quite confusing because at 700℃ Sb is also in liquid form and there seems to be no miscibility gap between the Sb and liquid phase. These results are important for later comparison to our own data.

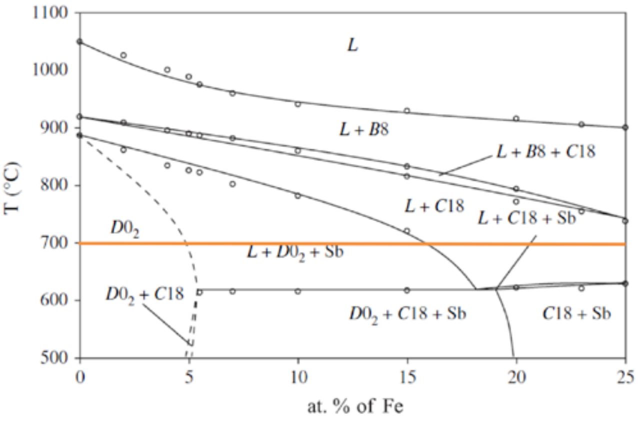

Figure 7.8 Reported phase diagram of $CoSb_3$-"$FeSb_3$" system[177]. D0$_2$ means the (Co,Fe)Sb_3 phase. C18 means the (Co,Fe)Sb_2 phase.

Isothermal section of Co-Fe-Sb ternary system is proposed based on binary phase diagram information[106,174] and literature results[177,178]. Proposed isothermal section of Co-Fe-Sb ternary system is shown in Figure 7.9. Nominal compositions for sample synthesis are listed in Table 7.2.

Table 7.2 Selected nominal compositions for investigation of Co-Fe-Sb isothermal section at 700℃. Bold phases denote that besides these phases, unexpected phases also show up for these samples (see detailed discussion in text). Samples Ce-Co-Fe-Sb #5-1 and #6-1 are proposed to investigate if a three-phase region will form on the Co-rich side. Samples (Co, Fe)Sb2 #1-4 are proposed to study the possible phase segregation between $CoSb_2$/$FeSb_2$ and the stable composition $Co_{0.33}Fe_{0.67}Sb_2$.

Sample name	Nominal composition	Estimated phase region
Co-Fe-Sb #1	$Co_{3.4}Fe_{0.3}Sb_{12.6}$	(Co, Fe)Sb_3 + liquid Sb
Co-Fe-Sb #2	$Co_{4.2}Fe_{0.3}Sb_{11.8}$	(Co, Fe)Sb_3 + (Co,Fe)Sb_2
Co-Fe-Sb #3	$Co_{3.25}Fe_{0.75}Sb_{12}$	**(Co, Fe)Sb_3**
Co-Fe-Sb #4	$Co_2Fe_2Sb_{12}$	(Co, Fe)Sb_3 + (Co, Fe)Sb_2 + liquid Sb
Co-Fe-Sb #5	$Co_{1.5}Fe_{1.5}Sb_{12}$	(Co, Fe)Sb_3 + (Co, Fe)Sb_2 + liquid Sb
Co-Fe-Sb #6	Fe_4Sb_{12}	$FeSb_2$ + liquid Sb
Co-Fe-Sb #7	$Co_6Fe_6Sb_{12}$	**(Co, Fe)Sb_2**
Ce-Co-Fe-Sb #5-1	$Ce_0Co_{2.5}Fe_{1.5}Sb_{8.5}$	(Co, Fe)Sb_3 + (Co,Fe)Sb_2

Ce-Co-Fe-Sb #6-1	$Ce_0Co_3Fe_1Sb_9$	$(Co, Fe)Sb_3 + (Co,Fe)Sb_2$
(Co, Fe)Sb2 #1	$Co_{0.30}Fe_{0.70}Sb_2$	$FeSb_2 + Co_{0.33}Fe_{0.67}Sb_2$
(Co, Fe)Sb2 #2	$Co_{0.33}Fe_{0.67}Sb_2$	$Co_{0.33}Fe_{0.67}Sb_2$
(Co, Fe)Sb2 #3	$Co_{0.36}Fe_{0.64}Sb_2$	$CoSb_2 + Co_{0.33}Fe_{0.67}Sb_2$
(Co, Fe)Sb2 #4	$Co_{0.40}Fe_{0.60}Sb_2$	$CoSb_2 + Co_{0.33}Fe_{0.67}Sb_2$

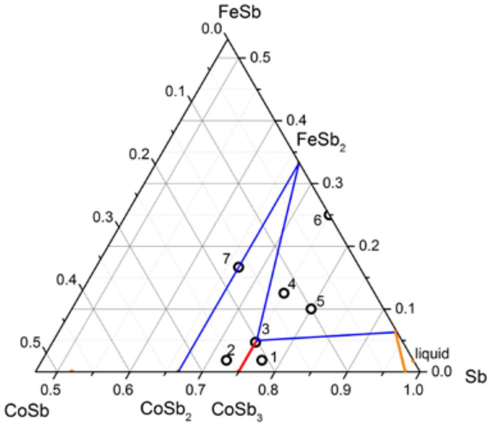

Figure 7.9 Proposed isothermal section of Co-Fe-Sb ternary system at 700℃. The solubility region of skutterudite phase $Co_{4-x}Fe_xSb_{12}$ was represented by a red solid line with solubility limit of Fe $x = 0.80$. [177]

After phase purity and chemical composition characterization of these samples, we found a few interesting discoveries.

First of all, the solubility limit is $x = 0.68$ in $Co_{4-x}Fe_xSb_{12}$, which is 15% less than the previously reported value. Secondly, stable compositions for equilibrium phases $Co_{4-x}Fe_xSb_{12}$ and $Co_xFe_{1-x}Sb_2$ are observed in samples #3-5, which are $Co_{3.32}Fe_{0.68}Sb_{12}$ and $Co_{0.33}Fe_{0.67}Sb_2$ respectively. Thirdly, the solubility regions along $CoSb_3$-"$FeSb_3$" line are single-phase skutterudite region (Co, Fe) Sb_3, three-phase region ($Co_{3.32}Fe_{0.68}Sb_{12}$ + $Co_{0.33}Fe_{0.67}Sb_2$ + liquid Sb) and two-phase region ($FeSb_2$ + liquid Sb). This is drastically different from the previous experimental results at 700℃ but more close to its lower temperature results such as 550℃. Error in temperature measurements might be a possible reason for this discrepancy.

All the findings above combined can explain why the estimated phase region for sample #3 $Co_{3.25}Fe_{0.75}Sb_{12}$ is a single-phase skutterudite phase region, yet what we observed is a three-phase region ($Co_{3.32}Fe_{0.68}Sb_{12}$ + $Co_{0.33}Fe_{0.67}Sb_2$ + liquid Sb). $Co_{0.33}Fe_{0.67}Sb_2$ phase was observed on SEM and confirmed by EPMA, and Sb phase was observed on XRD.

The determined phase region for samples #1, 2, 4, 5, and 6 matches what we estimated. Some of the SEM photos are shown in Figure 7.10. However, for sample #7, a small amount of skutterudite phase $Co_{4-x}Fe_xSb_{12}$ was observed (see Figure 7.10f) while we expect a single-phase region of (Co, Fe)Sb_2. This must be due to the compositional shift during synthesis, as we can see from the obtained phase diagram in Figure 7.11.

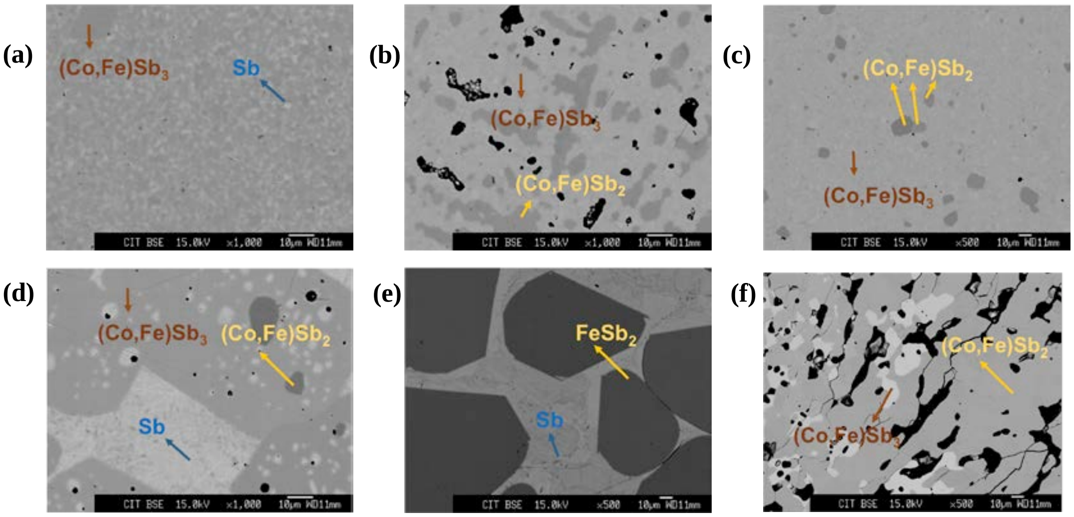

Figure 7.10 SEM photos of samples with nominal composition as a) #1 $Co_{3.4}Fe_{0.3}Sb_{12.6}$, b) #2 $Co_{4.2}Fe_{0.3}Sb_{11.8}$, c) #3 $Co_{3.25}Fe_{0.75}Sb_{12}$, d) #5 $Co_{1.5}Fe_{1.5}Sb_{12}$, e) #6 Fe_4Sb_{12}, and f) #7 $Co_6Fe_6Sb_{12}$. The impurity phases are detected by EDS and confirmed by EPMA.

The discovery of the stable composition $Co_{0.33}Fe_{0.67}Sb_2$ is quite interesting. The author could not find any published report on the crystal structure of this ternary compound. Since the two end phases $CoSb_2$ and $FeSb_2$ have completely different crystal structures[179,180] and lattice parameters, it is unlikely for them to form solid solution across the whole range[10]. To investigate if phase segregation will happen, in another way, to find out if a three-phase region ((Co, Fe)Sb_3 + Co-rich (Co,Fe)Sb_2 + $Co_{0.33}Fe_{0.67}Sb_2$) will form on the Co-rich side of skutterudite phase (see Figure 7.12), two more samples with nominal compositions $Ce_0Co_{2.5}Fe_{1.5}Sb_{8.5}$ and $Ce_0Co_3Fe_1Sb_9$ (compositions added to Table 7.2) are synthesized. Results confirm that both of them are in a Co-rich two-phase region (Co, Fe)Sb_3 + (Co,Fe)Sb_2. So no phase segregation between Co-rich (Co,Fe)Sb_2 and $Co_{0.33}Fe_{0.67}Sb_2$ seems to happen for Fe amount up to 0.53 in $Fe_xCo_{1-x}Sb_2$. Four more samples with nominal compositions close to stable composition $Co_{0.33}Fe_{0.67}Sb_2$ ($Fe_xCo_{1-x}Sb_2$, x from 0.60 to 0.70, see Table 7.2) are synthesized to study the possible segregation between stable composition

$Co_{0.33}Fe_{0.67}Sb_2$ and end phases $(Co,Fe)Sb_2$. Synchrotron XRD measurements were performed on these samples. Results are still under analysis so no conclusion can be made at this moment.

Based on the results from phase identification and compositional analysis, the experimental isothermal section of Co-Fe-Sb ternary system is determined, as shown in Figure 7.11.

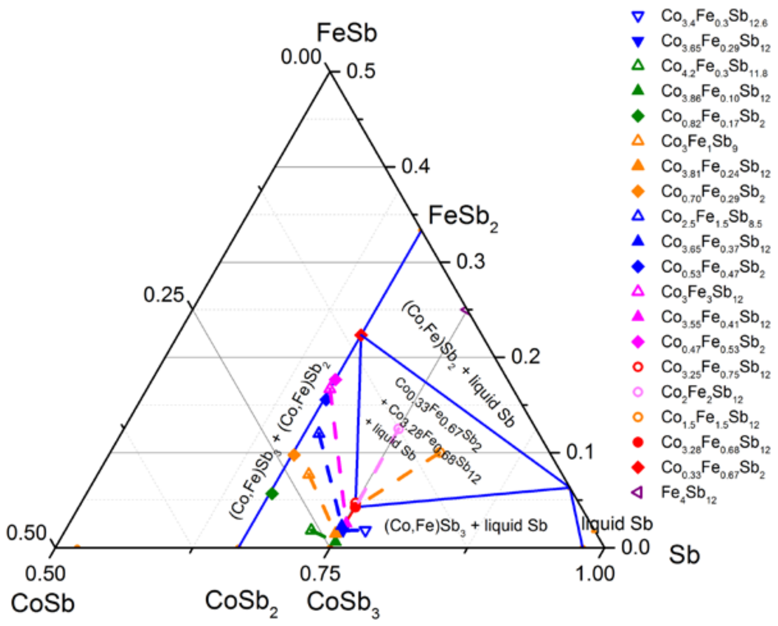

Figure 7.11 Experimental isothermal section of Co-Fe-Sb ternary system at 700℃.

7.5 Phase space of $Ce_yCo_xFe_{4-x}Sb_{12}$ skutterudites at 700℃

It would be really demanding to study the whole phase diagram of Ce-Co-Fe-Sb quaternary system at 700℃. Since the phase regions we are interested in are around $CoSb_3$, we can narrow our investigation to the region near Sb enclosed by the three ternary systems (Ce-Co-Sb, Ce-Fe-Sb and Co-Fe-Sb), which would spare us lots of time and energy. With results from sections 7.3, 7.4, and 5.5.3 and the assumption that the smooth phase boundary is almost linear, we can now set out to determine the phase space of skutterudite phase $Ce_yCo_xFe_{4-x}Sb_{12}$ in Ce-Co-Fe-Sb system at 700℃. As a first step, a series of $Ce_yCo_xFe_{4-x}Sb_{12}$ samples with exact skutterudite stoichiometry (Co+Fe):Sb =1:3 but different Co:Sb ratios (x varying from 0 to 4, each represented by a black dashed line in Figure 7.12) were synthesized, with varying amount of Ce for each selected ratio. Nominal compositions (listed in Table 7.3) are chosen to be near the phase boundary, with Ce content both below and above the estimated solubility limit for each chosen Co:Fe ratio as shown in Figure 7.13. Note that there are two solubility limits for each chosen Co:Fe ratio for the same reason we discussed in Section 7.3.

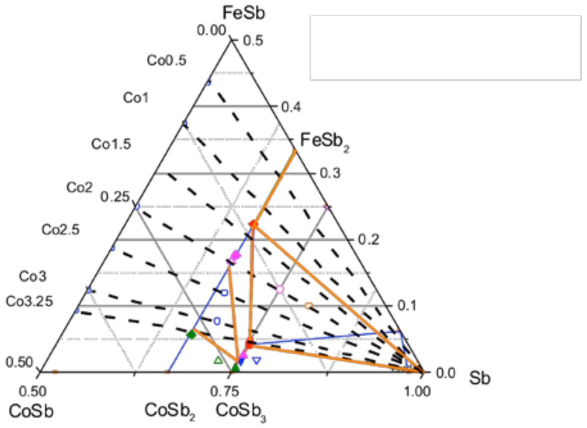

Figure 7.12 Slices of the isothermal space of Ce-Co-Fe-Sb system with different Co:Fe ratios projected to the Co-Fe-Sb plane as black dashed lines. Ce (not shown here) is perpendicular to the CoSb-FeSb-Sb phase diagram.

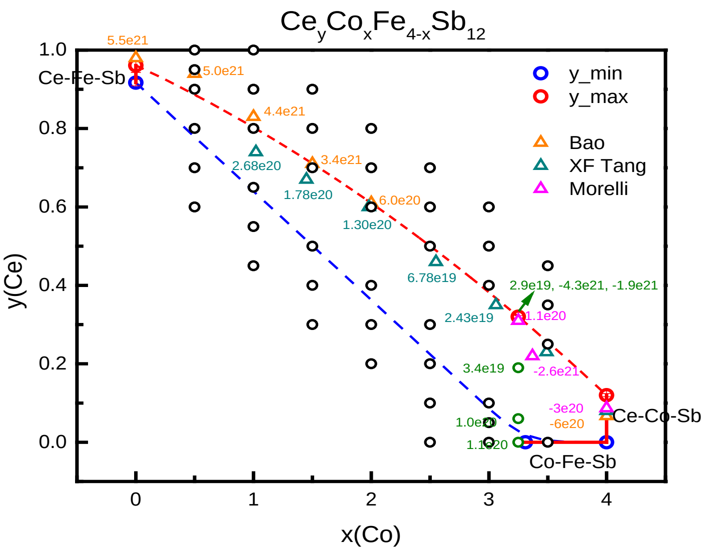

Figure 7.13 Proposed phase boundary of $Ce_yCo_xFe_{4-x}Sb_{12}$ skutterudites based on preliminary solubility results from Co-Fe-Sb, Ce-Co-Sb, Ce-Fe-Sb systems. Each dark circle represents a sample to make. Red and blue circles represent the maximum and minimum solubility limit of Ce in

$Ce_yCo_xFe_{4-x}Sb_{12}$ skutterudites determined from this study. Literature data are presented in empty triangles with carrier concentration labeled near each data point. Note here that the stoichiometry of (Co+Fe):Sb is fixed to 1:3.

Table 7.3 Nominal compositions of $Ce_yCo_xFe_{4-x}Sb_{12}$ samples for skutterudite phase space investigation in the Ce-Co-Fe-Sb quaternary system.

Sample name	Ce	Co	Sb	Fe
#1-1	0.6	0.5	12	3.5
#1-2	0.7	0.5	12	3.5
#1-3	0.8	0.5	12	3.5
#1-4	0.9	0.5	12	3.5
#1-5	0.95	0.5	12	3.5
#1-6	1	0.5	12	3.5
#2-1	0.45	1	12	3
#2-2	0.55	1	12	3
#2-3	0.65	1	12	3
#2-4	0.8	1	12	3
#2-5	0.9	1	12	3
#2-6	1	1	12	3
#3-1	0.3	1.5	12	2.5
#3-2	0.4	1.5	12	2.5
#3-3	0.5	1.5	12	2.5
#3-4	0.7	1.5	12	2.5
#3-5	0.8	1.5	12	2.5
#3-6	0.9	1.5	12	2.5
#4-1	0.2	2	12	2
#4-2	0.3	2	12	2
#4-3	0.4	2	12	2
#4-4	0.6	2	12	2
#4-5	0.7	2	12	2
#4-6	0.8	2	12	2
#5-1	0	2.5	8.5	1.5
#5-2	0.1	2.5	12	1.5
#5-3	0.2	2.5	12	1.5
#5-4	0.3	2.5	12	1.5
#5-5	0.5	2.5	12	1.5
#5-6	0.6	2.5	12	1.5
#5-7	0.7	2.5	12	1.5
#6-1	0	3	9	1
#6-2	0.05	3	12	1
#6-3	0.1	3	12	1
#6-4	0.4	3	12	1
#6-5	0.5	3	12	1
#6-6	0.6	3	12	1
#7-1	0	3.5	12	0.5
#7-2	0.25	3.5	12	0.5
#7-3	0.35	3.5	12	0.5
#7-4	0.45	3.5	12	0.5

The results are summarized in the experimentally determined phase space shown in Figure 7.14. Towards the Fe-rich part, the minimum Ce solubility limit is higher than expected, meaning the skutterudite phase space is narrower. Other than that, the solubility region has a boundary that not only overlaps roughly with our estimation but also is in agreement with literature data[19,154,172]. The EPMA determined compositions for $Ce_yCo_xFe_{4-x}Sb_{12}$ skutterudites are listed in Table 7.4.

Table 7.4 EPMA determined compositions for $Ce_yCo_xFe_{4-x}Sb_{12}$ skutterudites.

x(Co) nominal	x(Co) epma	x(Co) std	y(Ce) nominal	y(Ce) epma	y(Ce) std
1.5	--	--	0.5	--	--
1.5	1.53	0.09	0.7	0.68	0.04
1.5	1.57	0.17	0.8	0.7	0.09
1.5	1.46	0.1	0.9	0.76	0.05
2	2.45	0.09	0.2	0.3	0.04
2	2.23	0.06	0.3	0.38	0.03
2	2	0.15	0.4	0.45	0.03
2	1.95	0.02	0.6	0.62	0.03
2	1.99	0.06	0.7	0.6	0.03
2	1.97	0.11	0.8	0.65	0.05
2.5	3.65	0.02	0	--	--
2.5	2.69	0.24	0.1	0.14	0.05
2.5	2.59	0.17	0.2	0.22	0.02
2.5	2.46	0.1	0.3	0.33	0.05
2.5	2.5	0.08	0.5	0.48	0.03
2.5	2.43	0.06	0.6	0.5	0.03
2.5	2.5	0.12	0.7	0.51	0.05
3	3.81	0.02	0	--	--
3	3.08	0.1	0.05	0.03	0.04
3	3.09	0.08	0.1	0.06	0.04
3	3.06	0.11	0.4	0.32	0.05
3	3.04	0.16	0.5	0.37	0.08
3	2.92	0.14	0.6	0.42	0.07
3.5	--	--	0	--	--
3.5	3.43	0.13	0.25	0.22	0.02
3.5	3.5	0.09	0.35	0.21	0.05
3.5	3.49	0.06	0.45	0.24	0.05

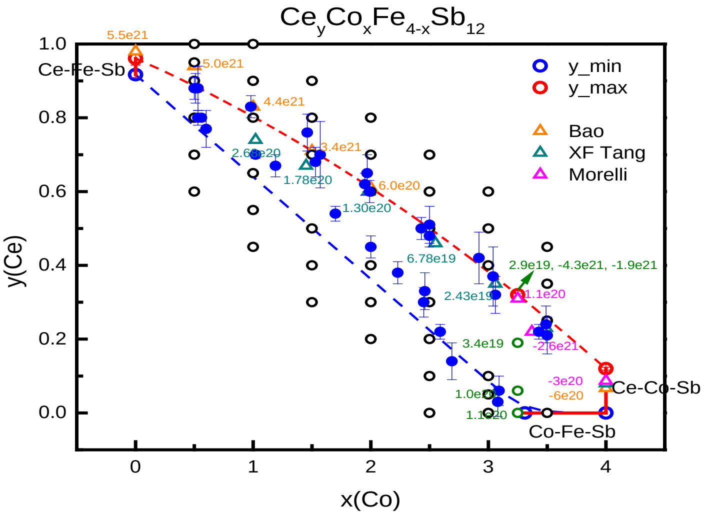

Figure 7.14 Experimentally determined phase space of skutterudite phase with exact stoichiometry (Co+Fe):Sb = 1:3 in Ce-Co-Fe-Sb system at 700°C. Each blue dot represents a measured value from EPMA listed in Table 7.4.

Figure 7.14 is only a slice of the phase space of $Ce_yCo_xFe_{4-x}Sb_{12}$ with exact skutterudite stoichiometry. To map out the full solubility region, samples similar to those listed in this section (Table 7.3) need to be synthesized with both Sb-rich and Co-rich stoichiometry instead, namely, synthesis of series of $Ce_yCo_xFe_{4-x}Sb_{12+z}$ samples with z values either larger or smaller than 0 are needed. After the full phase region is mapped out, carrier concentration needs to be measured for each sample. Ultimately, this one-to-one mapping between carrier concentration and phase space location will enable us to synthesize optimized *p*-type skutterudite material with the guidance of experimental phase diagram map.

7.6 *n-p* change in $Ce_yCo_{3.25}Fe_{0.75}Sb_{12}$ materials

As we have discussed in the end of Section 7.5, the phase diagram space is still not fully mapped out yet. However, based on the current results, a *p-n* semiconducting type change can be expected as the amount of Ce increases for x(Co) = 3.25 in $Ce_yCo_xFe_{4-x}Sb_{12}$ samples[19]. It would thus be interesting to compare their high temperature thermoelectric properties. Most importantly, by fixing the Co content, we are eliminating the influence of Co:Fe ratio on the band structure, which shall give us some insight on the electronic origin for *n*- and *p*-type conduction in $Ce_yCo_{3.25}Fe_{0.75}Sb_{12}$ skutterudites.

A set of samples with y(Ce) = 0, 0.1, 0.2, 0.3, 0.4, 0.5 are synthesized with sample named from #3-1 to #3-6. Only samples with y = 0.1, 0.2, and 0.3 are pure. For y = 0 sample, (Co,Fe)Sb_2 and liquid Sb phases are observed as impurity phases, which is consistent with results from Section 7.3. For y = 0.4, 0.5 samples, both $CeSb_2$ and Ce(Co,Fe)Sb_3 impurity phases are observed. The solubility limit is estimated to be: $y = 0.32\pm0.03$. The transport properties of these samples are measured up to 850K in our home-built high-temperature Hall system[41] and high-temperature Seebeck system[42], with data shown in Figure 7.15. Ce content measured from EPMA measurement for all samples is shown in the legend. The room temperature transport properties are also shown in Figure 7.16.

The thermoelectric performance of this set of samples are not promising, with maximum zT = 0.5 at 700K for y = 0.4 and 0.5 samples. Due to the discrepancy between our home built Seebeck system and commercial ZEM-3 system, the current data would be 15% less of measured Seebeck values on ZEM-3 systems, which will result in 20% less of zT. However, even with that into account, the zT value (maximum 0.6) is still not promising, more research needs to be performed to optimize these concentrations for both *p*- and *n*-type applications.

Even though the zT values of this set of samples are not great, there still are lots of interesting physics that request attention. From Figure 7.15a we can see that all samples except #3-4 show typical heavily doped semiconductor behavior, with increasing resistivity as temperature increases.

Sample #3-4 shows intrinsic semiconductor behavior, as can be seen from large resistivity (Figure 7.15a) and low carrier concentration (Figure 7.16a). Note that for this sample, the carrier concentration shows *p*-type, while the Seebeck coefficient is *n*-type, which might be due to the large difference in mobility between electrons and holes in $Ce_xCo_{3.25}Fe_{0.75}Sb_{12}$ and the different dependence on mobilities for Hall coefficient and Seebeck coefficient. As we can see from Appendix D, when two types of carriers coexist, the total Hall coefficient is more sensitive to the highly mobile carrier (holes in the case of skutterudites) compared to Seebeck coefficient.

Samples #3-1, #3-2 and #3-3 show *p*-type carrier concentration (Figure 7.16a), positive Seebeck coefficient (Figure 7.16d) and high mobility (Figure 7.16b). All these evidence indicate that holes are the main conducting carrier type in these samples. For samples #3-5 and #3-6, the magnitude of room temperature carrier concentrations (Figure 7.16a) are unreasonably high, which could be due to the fact that two types of carriers are conducting so the equation for calculating $n_H = -\frac{1}{eR_H}$ assuming single type carrier no longer holds.

The large Seebeck coefficient in *n*-type samples (#3-4 and #3-5) compared to *p*-type samples greatly benefit both the power factor and the *zT* even though their mobility is relatively lower compared to *p*-type samples.

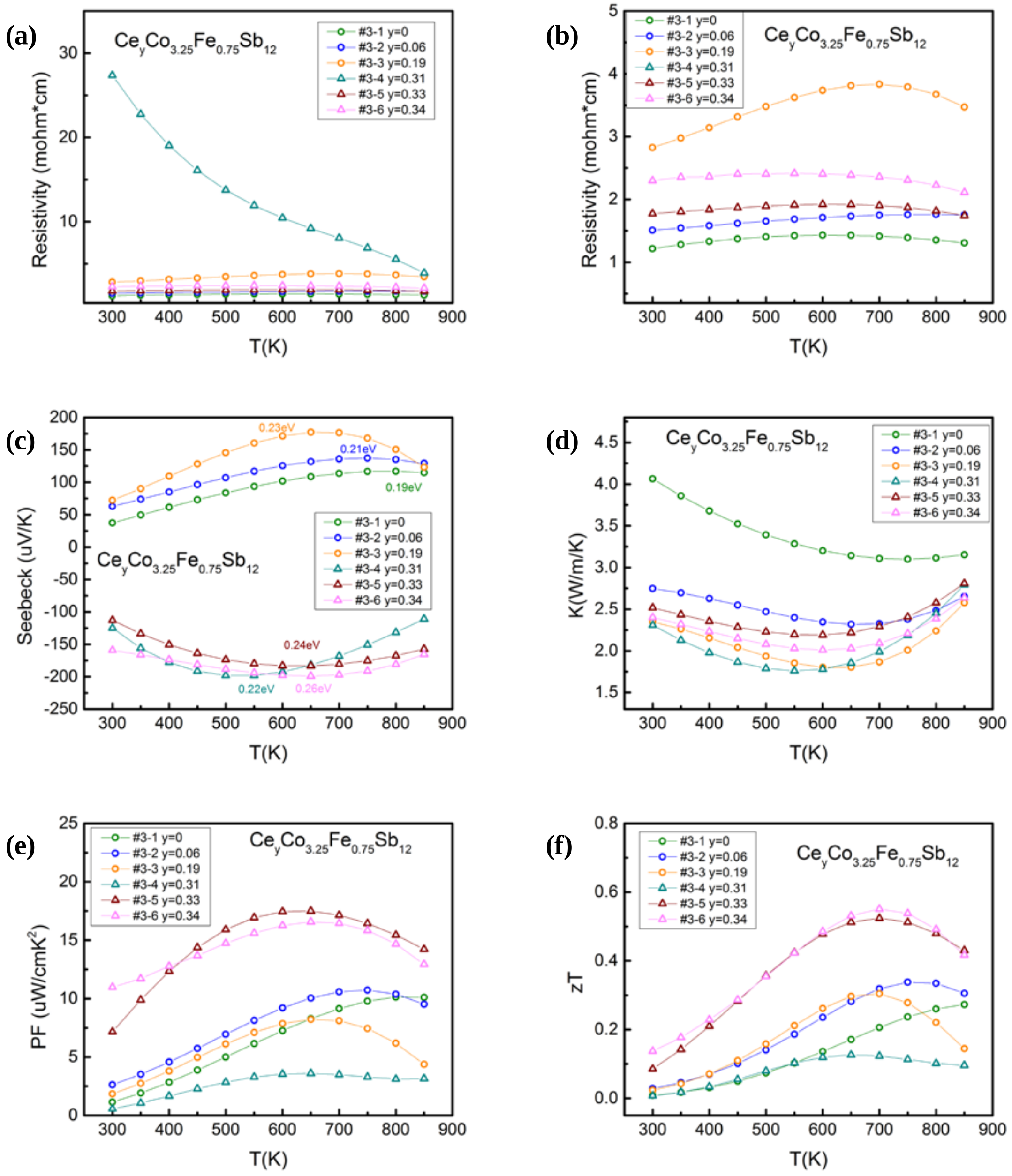

Figure 7.15 Transport properties of $Ce_yCo_{3.25}Fe_{0.75}Sb_{12}$ skutterudites. The temperature dependence of: (a) electrical resistivity (with all six samples), (b) electrical resistivity (magnification a)), (c) Seebeck coefficient, d) thermal conductivity, (e) power factor, and (f) thermoelectric figure of merit (*zT*) are plotted in the temperature range of 300K to 850K. In figure c, the numbers close to each curve is the energy band gap calculated from $E_g = 2S_{\max}T_{\max}$ [181].

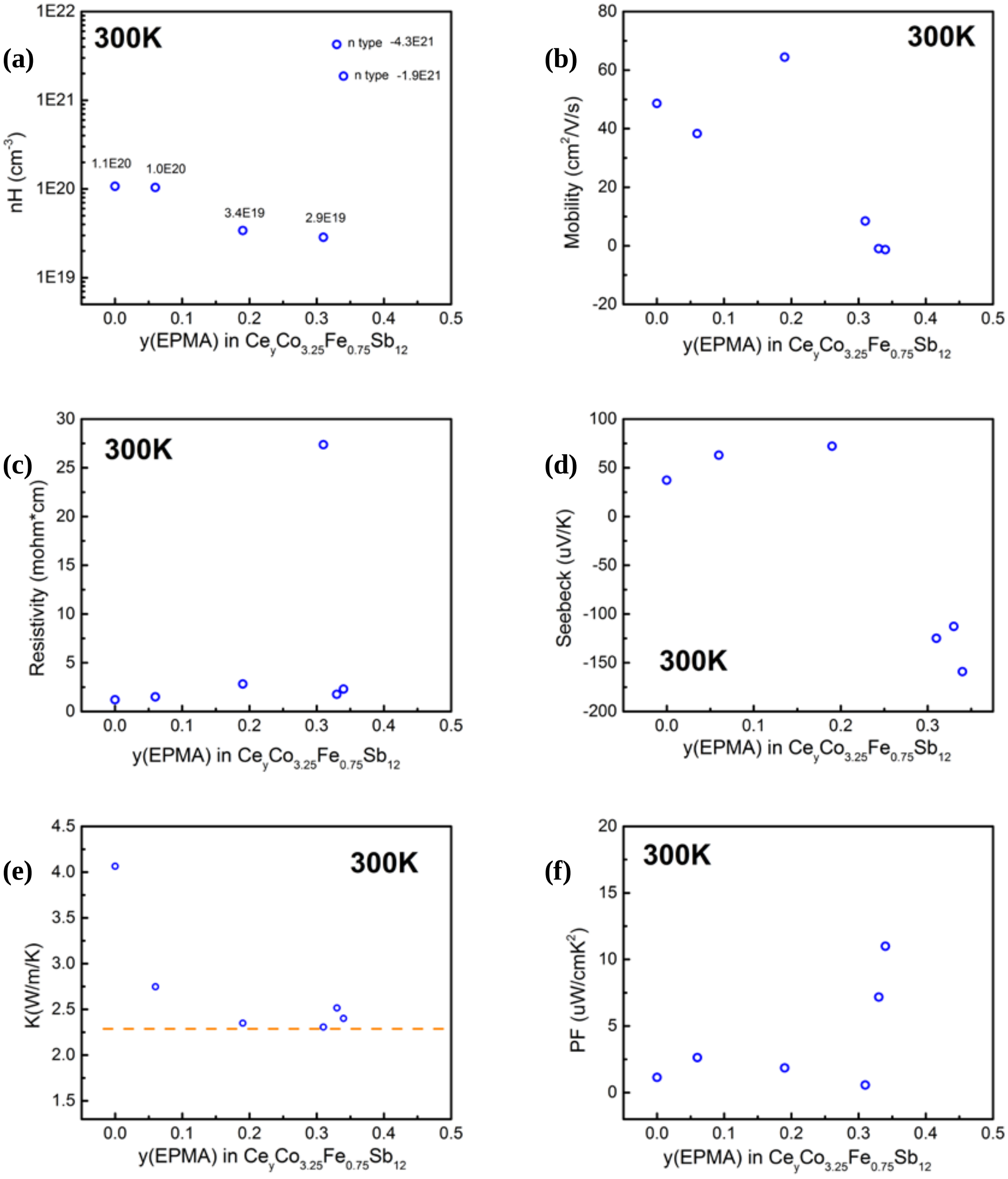

Figure 7.16 Room temperature transport properties of $Ce_yCo_{3.25}Fe_{0.75}Sb_{12}$ skutterudites. (a) Hall carrier concentration, (b) mobility, (c) electrical resistivity, (d) Seebeck coefficient, e) thermal

conductivity, and (f) power factor are plotted with Ce content y determined from EPMA measurement.

7.7 Conclusion and future work

This chapter mainly discusses the phase diagram study of Ce-Co-Fe-Sb system at 700℃. By combining results of isothermal sections of Ce-Fe-Sb, Co-Fe-Sb and Ce-Co-Sb ternary phase diagrams, the phase regions near skutterudite phase $Ce_yCo_xFe_{4-x}Sb_{12}$ are investigated. This leads to the determination of phase space of skutterudite phase on the stoichiometric section $Ce_yCo_xFe_{4-x}Sb_{12}$. A few attempts were made to synthesis both *n*- and *p*-type material with the same Co:Sb ratio, in search of good thermoelectric materials paired with similar thermal expansion coefficients. Though the obtained thermoelectric performance is not satisfying, with further study of complete mapping between the carrier concentration and the phase space, it is optimistic to obtain optimized *p*-type compositions with the guidance of the phase diagram in the future.

Chapter 8

Nano-structuring in bulk skutterudites

8.1 Summary

From the equation for $zT=\frac{S^2\sigma T}{\kappa}=\frac{S^2\sigma T}{\kappa_e+\kappa_l}$ we can see that the lattice thermal conductivity κ_l is the only parameter that allows independent tuning. Nano-structuring, as a means of bringing in nano-scale features to effectively scatter phonon prorogation thus reduce lattice thermal conductivity, has been applied in a lot of systems to improve thermoelectric properties. One mechanism is reducing the grain size to nano-scale. The introduced large density of grain boundaries leads to enhanced grain boundary scattering. This is easily realized by ball milling. Another mechanism is to introduce nano-scale foreign phases. Many efforts have been tried such as by adding more electron conductive nanoparticles or introducing filler oxides by deliberate exposure to oxygen[109]. The kinetics of these foreign phases, however, is hard to control. Here we introduce another method of nano-structuring, which is precipitation of nano-scale secondary phases according to temperature dependent filler solubility based on phase diagrams. As we have shown in Chapter 5, the solubility limit of filler atoms R in $CoSb_3$ system is not a single value but rather has a large dependence on the annealing temperature. Thus by simply combining various heat treatments, the kinetics of precipitation can be controlled such that nano-scale secondary phases may be introduced to lower lattice thermal conductivity, and even more importantly, these phases can be dissolved back into the matrix skutterudite phase in case a “reset” is needed (e.g., when precipitate size grows too large). Experimental details and results are shown in Section 8.2 and a conclusion and future work in Section 8.3.

8.2 Experimental results

Yb-doped $CoSb_3$ were chosen to perform this study with nominal compositions of $Yb_xCo_4Sb_{12}$ (x = 0.30, 0.33, 0.36 and 0.40). Samples were synthesized with similar procedures as described in Chapter 2 and 5. There are five steps. First, the raw elements are melted at 1100°C into liquid phase to maximize the mass diffusion and exchange. After 12 hours at 1100°C, the melt is quenched in water. Secondly, an annealing process at 750°C for a week follows, which allows the filler content in skutterudites to achieve its solubility limit at 750℃ and be homogenously distributed. Thirdly, the homogenized sample is quenched with water again, in order to freeze the content of Yb allowed at 750℃. Fourthly, the sample is annealed once again for 1 week, but at a lower temperature (600℃). The solubility limit at 600℃ is lower compared to that at 750℃ due to the previously experimentally determined temperature dependence of solubility limit (Section 5.2)[23]. This will drive the filler atoms out of skutterudite phase and precipitate in forms of secondary phases such as $YbSb_2$ and $CoSb_2$. Precipitation time at 600℃ was held for 1, 2, 3, and 9 days for each sample $Yb_xCo_4Sb_{12}$, respectively. For each composition, samples held at 600℃ for various precipitation times were different pieces cut from the same homogenized (at 750℃) ingot, so the only variable is the precipitation time. This shall spare us trouble if the samples are indeed homogeneous. Lastly, samples after precipitation are quenched to freeze any possible microstructural features for SEM, EDS and EPMA analysis.

The heat treatment parameters (nominal composition and heat treatment temperatures) are chosen based on the phase diagram, as shown in Figure 8.1. The larger the temperature difference between the homogenization temperature (750℃) and precipitation temperature (600℃), the larger the driving force for precipitation. According to nucleation and growth theory, this would promote more nucleation, resulting in smaller-size precipitation, which would possibly match our expectation of nano-scale secondary phases. Larger temperature difference will also lead to larger solubility difference. According to the lever rule, when the precipitation temperature decreases, for the same starting composition, the amount of secondary phases will increase, which would also facilitate our experimental observation. However, the homogenization temperature should not exceed the peritectic temperature of $CoSb_3$ (874℃), neither should the precipitation temperature be too low such that kinetics hinders the precipitation to actually happen. The nominal compositions are chosen to have an Yb content between the two solubility limits corresponding to selected temperatures.

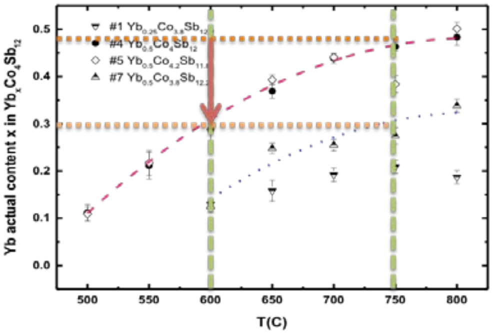

Figure 8.1 Heat treatment parameter determined based on the experimental phase diagram study (as described in Chapter 5, Section 5.2 and 5.4). The green dashed lines represent the homogenization and precipitation temperatures, 750℃ and 600℃, respectively. The orange dashed lines represent the solubility of Yb in $CoSb_3$ skutterudite phase at each temperature. The red arrow indicates the solubility difference between the two selected temperatures.

After precipitation, the amount of Yb in skutterudite phase was measured with EPMA for each composition, as shown in Figure 8.2.

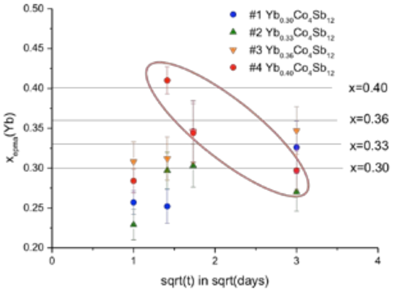

Figure 8.2 Effect of precipitation time on Yb content in skutterudites after precipitation. Each solid line represents a nominal composition.

Figure 8.2 does not show clear trend except for the data set circled in red, which exhibit a decreasing trend of Yb content in skutterudite phase as precipitation time increases. This indicates that the amount of secondary phases (especially $YbSb_2$) increases with precipitation time. However, SEM photos of these three samples are quite confusing. Although $YbSb_2$ phases did show up after 3 days' precipitation, we do not see any $YbSb_2$ phases at all after 9 days' precipitation, as shown in Figure 8.3. One possible reason might be the inhomogeneity in "homogenized" sample even after 1-week treatment at 750℃. To find out the reason, it is recommended to redo this set of synthesis.

Moreover, the size of the precipitates after 3 days' precipitation is on the order of 2-10 micrometer. Most of the precipitates observed are $YbSb_2$ phase, while the $CoSb_2$ phase is rarely observed. The reason for this phenomenon remains unclear. Although the effective scattering length for precipitates in skutterudites is not fully clear[167], the observed precipitate size is much larger if we are aiming for nano-scale precipitates in general, and thus a smaller increment on the precipitation time and or a lower precipitating temperature is recommended. The observed precipitates are mostly distributed along the grain boundaries. No in-grain precipitation is observed, which makes sense due to the high level of defects along grain boundaries and lower energy barrier.

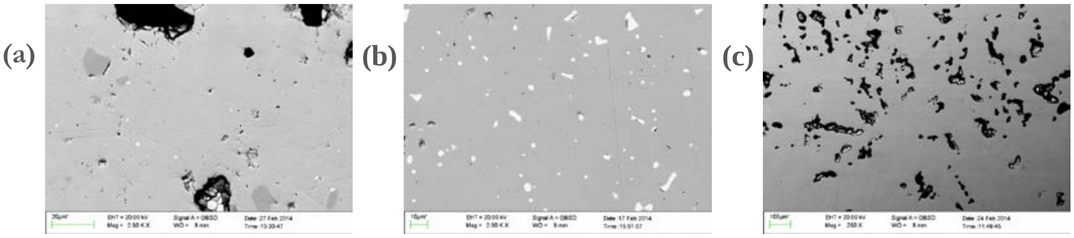

Figure 8.3 SEM photos for sample with nominal composition $Yb_{0.40}Co_4Sb_{12}$ precipitated at 600℃ with different precipitation times: (a) 2 days, (b) 3 days, and (c) 9 days.

8.3 Conclusion and future work

Although this work is not complete, it still reveals the possibility of introducing precipitates into skutterudite system based on temperature dependent solubility of fillers. To resume this work, it is recommended to re-investigate the heat treatment parameters, from possibly higher homogenization temperature, lower annealing temperature to shorter precipitation time. More experiments need to be designed in a systematic way to avoid inconsistency.

Chapter 9

Future work

In this thesis, $R_xCo_4Sb_{12}$ skutterudite has been studied successfully from two main perspectives.

First of all, why high thermoelectric performance is achievable in filled skutterudites was discussed, including both the electronic and thermal transport origin.

The electronic origin study sets a good example to find beneficial electronic band structure features of intrinsic $CoSb_3$ via both experiments and computation. This methodology can be generalized and applied to other systems in the future. It also prompts more interest on a closer investigation of the bonding chemistry of $CoSb_3$. As the temperature dependent band offset in conduction bands is speculated to be due to different temperature dependence of related bonding features. This work is undergoing with synchrotron data acquired at Argonne National laboratory just recently. More investigation is on the way.

The role of fillers on reducing lattice thermal conductivity is still open to debate, which leaves large room for future study. Either Te or Ni doped $CoSb_3$ can be synthesized to study the effect of electron-phonon scattering on phonon transport, especially the coefficient of dependence of the thermal resistance on the carrier concentration. With such information obtained, the role of fillers in terms of resonant scattering or avoided scattering can be more clearly distinguished.

The second part of this thesis elaborates on how high thermoelectric performance can be achieved through precise doping control to obtain optimized thermoelectric compositions. Phase diagram study has been proved to be a necessary and helpful method in this case. Future work can evolve around re-investigation of systems that were reported to have solubility barriers. As we have shown with Ce-$CoSb_3$, this could possibly lead to the overturn of such conclusions.

Defect study of intrinsic $CoSb_3$ is to be continued. The effect of oxygen in $CoSb_3$ defect chemistry is quite interesting and worthy of more attention. Calculation shows that the addition of oxygen will not result in any change in the defect type, yet we have one sample that shows *n*-type behavior with oxygen addition. Continued efforts are needed with special care for synthesizing conditions as detailed in Chapter 6.

Phase diagram study of quaternary system Ce-Co-Fe-Sb is mostly done, with the phase space of skutterudites on the (Co+Fe):Sb = 1:3 stoichiometry section determined at 700℃. To obtain a full phase space, similar work as described in Section 7.5 needs to be performed for both Sb-rich and Co-rich stoichiometry. To enable discovery of optimum compositions for *p*-type thermoelectric skutterudites, mapping of the carrier concentration of samples synthesized across the skutterudite phase space is needed. More detailed analysis of the $Ce_yCo_{3.25}Fe_{0.75}Sb_{12}$ samples is needed to probe possible multi-band conduction behavior in both *p*- and *n*-type $Ce_yCo_{3.25}Fe_{0.75}Sb_{12}$ skutterudite, which can be realized by magnetic field dependence of Hall effect measurements.

Nano-structuring through secondary phase precipitation in skutterudites show some promises, yet more efforts are needed to engineer the amount and size of these precipitates such that they are effective in lowing lattice thermal conductivities. It is also recommended to study the influence of common secondary phases such as $CoSb_2$, Sb and RSb_2 etc. on transport properties of intrinsic $CoSb_3$. This not only can serve as a reference in elucidating the benefits of nano-precipitates on thermal transport, but also is enlightening in the defect study of intrinsic $CoSb_3$.

Appendix A

From Boltzmann Transport Equation to Thermoelectric Properties[182-184]

Boltzmann transport equation (BTE) describes how the distribution function of a thermodynamic system changes with time when it is subjected to external forces. For an electron gas, the distribution function $f(k,r,t)$ tells us how the electrons are distributed in momentum space and from this information all of the transport properties can be evaluated. At equilibrium, the distribution function $f_0(k,r)$ is the Fermi-Dirac function:

$$f_0(k,r) = \frac{1}{1+\exp(\frac{\varepsilon-\varsigma}{k_B T})} \qquad \text{(Eq. A.1)}$$

where ε is the energy, η is the reduced electrochemical potential $\eta = \frac{\varsigma}{k_B T} = \frac{\mu - e\Phi}{k_B T}$ with μ the chemical potential (equals to Fermi energy at 0K) and Φ the electrostatic potential.

With the presence of external fields (electric field or temperature gradient), the electron distribution $f(k,r,t)$ will be subjected to two effects: one is the driving force of the external field and the other is the dissipative effect of scattering. Note that in the case of thermoelectric materials, the temperature gradient is often small such that the temperature dependence of chemical potential can be neglected, and so can the effect of diffusion on the distribution function. This can be expressed by Eq. A.2 and A.3 where s denotes “scattering process”.

$$f(k+\Delta k, r+\Delta r, t+\Delta t) = f(k,r,t) + \left(\frac{\partial f}{\partial t}\right)_s dt \qquad \text{(Eq. A.2)}$$

$$f(k+\Delta k, r+\Delta r, t+\Delta t) = f(k,r,t) + \left(\frac{\partial f}{\partial k}\right)\left(\frac{\partial k}{\partial t}\right)dt + \left(\frac{\partial f}{\partial r}\right)\left(\frac{\partial r}{\partial t}\right)dt + \left(\frac{\partial f}{\partial t}\right)dt \qquad \text{(Eq. A.3)}$$

In a steady state, there is no net change in the distribution function, $\frac{\partial f}{\partial t} = 0$.

By comparing Eq. A.2 and Eq. A.3, we get:

$$\left(\frac{\partial f}{\partial t}\right)_s = \left(\frac{\partial f}{\partial k}\right)\left(\frac{\partial k}{\partial t}\right) + \left(\frac{\partial f}{\partial r}\right)\left(\frac{\partial r}{\partial t}\right) \qquad \text{(Eq. A.4)}$$

With a relaxation time approximation, the effect of scattering process on restoring the distribution function can be described in a linear equation, shown in Eq. A.5. The scattering time τ means the amount of time required to restore the equilibrium distribution function $f_0(k,r)$ which deviates to $f(k,r,t)$ because of the external field.

$$\left(\frac{\partial f}{\partial t}\right)_s = \frac{f(k,r,t) - f_0(k,r)}{-\tau} \qquad \text{(Eq. A.5)}$$

Substitute Eq. A.5 into Eq. A.4, and we get:

$$\frac{f(k,r,t) - f_0(k,r)}{-\tau} = \left(\frac{\partial f}{\partial k}\right)\left(\frac{\partial k}{\partial t}\right) + \left(\frac{\partial f}{\partial r}\right)\left(\frac{\partial r}{\partial t}\right) \qquad \text{(Eq. A.6)}$$

It is normally considered the distribution function is not too much away from the equilibrium, so for simplicity we can replace $\left(\frac{\partial f_0}{\partial k}\right)$ and $\left(\frac{\partial f}{\partial r}\right)$ by $\left(\frac{\partial f_0}{\partial k}\right)$and $\left(\frac{\partial f_0}{\partial r}\right)$, respectively.

With the assumption of a single parabolic band model, $E = \frac{\hbar^2 k^2}{2m^*}$

In a semi-empirical model of conduction, $v = \frac{\hbar k}{m^*} = \frac{\nabla_k E_n(k)}{\hbar}$

Table. A.1 Relation between transport effect and generalized force.

Transport effect	**Acting force**	**Generalized**
Electrical conductivity	***E***	-e***E***
Hall effect R_H	***E*,*H***	-e***E***-e***v***×***H***
Seebeck effect S	∇T	-e($\nabla\mu$/e-$\nabla\phi$) =
Thermal conductivity κ	∇T	-e($\nabla\mu$/e-$\nabla\phi$) =

1. Carrier concentration *n*

$$N = \sum_k 2f(k) = \int_0^\infty 2\frac{V}{(2\pi)^3} f(k) d^3k$$

$$n = \frac{N}{V} = \int_0^\infty 2\frac{1}{(2\pi)^3} f(k) d^3k$$

$$= \int_0^\infty 2\frac{1}{(2\pi)^3} f(k) 4\pi k^2 dk = \int_0^\infty \frac{1}{\pi^2} f(k) k^2 dk$$

$$
\begin{aligned}
n &= \int_0^\infty g(\varepsilon) f_0(\varepsilon)\, d\varepsilon \\
&= \int_0^\infty 4\pi \left(\frac{2m^*}{h^2}\right)^{3/2} \sqrt{\varepsilon}\, f_0(\varepsilon) d\varepsilon \\
&= \frac{4\pi\left(2m^* k_B T\right)^{3/2}}{h^3} \int_0^\infty \sqrt{\frac{\varepsilon}{kT}} \frac{1}{1+\exp\left(\dfrac{\varepsilon-\varsigma}{kT}\right)} d\left(\frac{\varepsilon}{kT}\right)
\end{aligned}
$$

$$
\mathrm{n} = \frac{4\pi\left(2m^* k_B T\right)^{3/2}}{h^3} F_{1/2}(\eta) \qquad \text{(Eq. A.7)}
$$

2. Electrical conductivity σ

As shown in Table A.1, the external force is the electrical field ***E*** and the temperature gradient ∇T is 0.

$$
j = n(-e)v = -\int_0^\infty evg(\varepsilon)\, f(\varepsilon)\, d\varepsilon
$$

$j_0 = -\int_0^\infty evg(\varepsilon)\, f_0(\varepsilon)\, d\varepsilon = 0$ (no electric current at equilibrium)

$$
\begin{aligned}
j &= n(-e)v = -\int_0^\infty evg(\varepsilon)(f - f_0)\, d\varepsilon \\
&= -\int_0^\infty evg(\varepsilon)(-\tau)\left(\left(\frac{\partial f_0}{\partial k}\right)\left(\frac{\partial k}{\partial t}\right) + \left(\frac{\partial f_0}{\partial r}\right)\left(\frac{\partial r}{\partial t}\right)\right) d\varepsilon
\end{aligned}
$$

$\left(\dfrac{\partial f_0}{\partial r}\right)$=0 since there is no temperature gradient;

$$
\frac{\partial f_0}{\partial k} = \frac{\partial f_0}{\partial \varepsilon}\frac{\partial \varepsilon}{\partial k} = \frac{\partial f_0}{\partial \varepsilon}\frac{\hbar^2 k}{m^*} = \frac{\partial f_0}{\partial \varepsilon}\hbar v
$$

$$
v = \frac{\hbar k}{m^*},\ \frac{\partial k}{\partial t} = \frac{m^*}{\hbar}\frac{\partial v}{\partial t} = \frac{F}{\hbar} = \frac{-eE}{\hbar}
$$

$$
\begin{aligned}
j &= -\int_0^\infty evg(\varepsilon)(-\tau)\left(\left(\frac{\partial f_0}{\partial k}\right)\left(\frac{\partial k}{\partial t}\right) + \left(\frac{\partial f_0}{\partial r}\right)\left(\frac{\partial r}{\partial t}\right)\right) d\varepsilon \\
&= \int_0^\infty evg(\varepsilon)\tau\left(\frac{\partial f_0}{\partial \varepsilon}\hbar v \frac{-eE}{\hbar} + 0\right) dE = -\int_0^\infty e^2 v^2 g(\varepsilon)\tau E\left(\frac{\partial f_0}{\partial \varepsilon}\right) d\varepsilon
\end{aligned}
\qquad \text{(Eq. A.8)}
$$

v is along one direction, whereas the kinetic energy $\varepsilon = \frac{3}{2} m^* v^2$ is distributed among three directions equivalently.

$$\sigma = \frac{j}{E} = -\int_0^\infty e^2 v^2 g(\varepsilon)\tau\left(\frac{\partial f_0}{\partial \varepsilon}\right)d\varepsilon$$

$$= -\int_0^\infty \frac{2}{3m^*} e^2 \varepsilon g(\varepsilon)\tau\left(\frac{\partial f_0}{\partial \varepsilon}\right)d\varepsilon = -\int_0^\infty \frac{2e^2\sqrt{2m^*}}{3\pi^2\hbar^3}\tau_0 \varepsilon^{r+3/2}\left(\frac{\partial f_0}{\partial \varepsilon}\right)d\varepsilon$$

Note $\boldsymbol{\tau = \tau_0 \varepsilon^r}$ for acoustic phonon scattering r = -1/2

By partial integration, we get the expression of σ:

$$\sigma = -\int_0^\infty \frac{2e^2\sqrt{2m^*}}{3\pi^2\hbar^3}\tau_0 \varepsilon^{r+3/2}\left(\frac{\partial f_0}{\partial \varepsilon}\right)d\varepsilon$$

$$= \left(\frac{2e^2\sqrt{2m^*}}{3\pi^2\hbar^3}\tau_0 \infty^{r+3/2} f_0\left(\infty\right) - 0\right) + \int_0^\infty \frac{2e^2\sqrt{2m^*}}{3\pi^2\hbar^3}\tau_0 f_0 d(\varepsilon^{r+3/2})$$

$$= \int_0^\infty \frac{2e^2\sqrt{2m^*}}{3\pi^2\hbar^3}\tau_0 (r+3/2) f_0 \varepsilon^{r+1/2}\, d\varepsilon$$

$$= \frac{2e^2\sqrt{2m^*}}{3\pi^2\hbar^3}\tau_0 (r+3/2)\left(k_B T\right)^{r+3/2}\int_0^\infty f_0\left(\frac{\varepsilon}{k_B T}\right)^{r+1/2} d\left(\frac{\varepsilon}{k_B T}\right)$$

$$\sigma = \frac{2e^2\sqrt{2m^*}}{3\pi^2\hbar^3}\tau_0 (r+3/2)\left(k_B T\right)^{r+3/2} F_{r+1/2}\left(\eta\right) \qquad \text{(Eq. A.9)}$$

Thus we have the expression for electrical conductivity with the assumption that there is only one predominant scattering mechanism.

3. Hall coefficient R_H

The derivation of hall coefficient R_H is similar to that of electrical conductivity except with a different force $\boldsymbol{F}$= -e$\boldsymbol{E}$-e$\boldsymbol{v}\times\boldsymbol{H}$

$$R_H = \frac{E_y}{j_x H_z}$$

$$j = -\int_0^\infty evg(\varepsilon)(-\tau)\left(\left(\frac{\partial f_0}{\partial k}\right)\left(\frac{\partial k}{\partial t}\right) + \left(\frac{\partial f_0}{\partial r}\right)\left(\frac{\partial r}{\partial t}\right)\right)d\varepsilon$$

$$= \int_0^\infty evg(\varepsilon)\tau\left(\frac{\partial f_0}{\partial \varepsilon}\hbar v\frac{-eE - ev\times H}{\hbar} + 0\right)dE$$

$$= -\int_0^\infty e^2 v^2 g(\varepsilon)\tau\left(E + v\times H\right)\left(\frac{\partial f_0}{\partial \varepsilon}\right)d\varepsilon$$

$$v\times H=\begin{bmatrix}v_x\\v_y\\v_z\end{bmatrix}\times\begin{bmatrix}H_x\\H_y\\H_z\end{bmatrix}=\begin{bmatrix}v_yH_z-v_zH_y\\v_zH_x-v_xH_z\\v_xH_y-v_yH_x\end{bmatrix}=\begin{bmatrix}v_yH_z\\-v_xH_z\\0\end{bmatrix}$$

$j_x=-\int_0^\infty e^2v_x^2g(\varepsilon)\tau\left(E_x+v_yH_z\right)\left(\frac{\partial f_0}{\partial\varepsilon}\right)d\varepsilon=\sigma E_x$ since 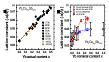

$$j_y=-\int_0^\infty e^2v_y^2g(\varepsilon)\tau\left(E_y-v_xH_z\right)\left(\frac{\partial f_0}{\partial\varepsilon}\right)d\varepsilon$$

$$=\sigma E_y+\int_0^\infty e^2v_y^2g(\varepsilon)\tau v_xH_z\left(\frac{\partial f_0}{\partial\varepsilon}\right)d\varepsilon$$

Since $-eE_x-ev_yH_z=\frac{m^*v_x}{\tau}$, in a steady state, $-eE_x=\frac{m^*v_x}{\tau}$

$$j_y=\sigma E_y+\int_0^\infty e^2v_y^2g(\varepsilon)\tau v_xH_z\left(\frac{\partial f_0}{\partial\varepsilon}\right)d\varepsilon$$

$$=\sigma E_y-\int_0^\infty\frac{e^3\tau^2E_x}{m^*}v_y^2g(\varepsilon)H_z\left(\frac{\partial f_0}{\partial\varepsilon}\right)d\varepsilon$$

$$=\sigma E_y-\int_0^\infty\frac{\sqrt{2m^*}e^3\tau_0^2E_x}{\pi^2\hbar^3}v_y^2\varepsilon^{2r+1/2}H_z\left(\frac{\partial f_0}{\partial\varepsilon}\right)d\varepsilon$$

$$=\sigma E_y+\int_0^\infty\frac{2\sqrt{2m^*}e^3\tau_0^2E_x}{3\pi^2\hbar^3m^*}H_zf_0d\left(\varepsilon^{2r+3/2}\right)$$

$$=\sigma E_y+\int_0^\infty\frac{2\sqrt{2m^*}e^3\tau_0^2E_xH_z}{3\pi^2\hbar^3m^*}(2r+\frac{3}{2})\left(k_BT\right)^{2r+\frac{3}{2}}\left(\frac{\varepsilon}{k_BT}\right)^{2r+1/2}f_0d\left(\frac{\varepsilon}{k_BT}\right)$$

$$j_y=\sigma E_y+\frac{2\sqrt{2m^*}e^3\tau_0^2E_xH_z}{3\pi^2\hbar^3m^*}(2r+\frac{3}{2})\left(k_BT\right)^{2r+\frac{3}{2}}F_{2r+1/2}\left(\eta\right)=0$$

$$E_y=-\frac{2\sqrt{2m^*}e^3\tau_0^2E_xH_z}{3\pi^2\hbar^3m^*\sigma}(2r+\frac{3}{2})\left(k_BT\right)^{2r+\frac{3}{2}}F_{2r+1/2}\left(\eta\right)$$

$$R_H=\frac{E_y}{j_xH_z}=-\frac{2\sqrt{2m^*}e^3\tau_0^2}{3\pi^2\hbar^3m^*\sigma^2}(2r+\frac{3}{2})\left(k_BT\right)^{2r+\frac{3}{2}}F_{2r+1/2}\left(\eta\right)$$

$$=\frac{-\frac{2\sqrt{2m^*}e^3\tau_0^2}{3\pi^2\hbar^3m^*}(2r+\frac{3}{2})\left(k_BT\right)^{2r+\frac{3}{2}}F_{2r+1/2}\left(\eta\right)}{\left(\frac{2\sqrt{2m^*}e^2}{3\pi^2\hbar^3}\tau_0(r+3/2)\left(k_BT\right)^{r+3/2}F_{r+1/2}\left(\eta\right)\right)^2}$$

$$R_H = -\frac{3\pi^2\hbar^3}{e\left(2m^*k_BT\right)^{3/2}}\frac{(2r+\frac{3}{2})}{(r+\frac{3}{2})^2}\frac{F_{2r+1/2}(\eta)}{\left(F_{r+1/2}(\eta)\right)^2} \qquad \text{(Eq. A.10)}$$

4. Hall factor r_H

$$r_H = -neR_H = \frac{3\pi^2\hbar^3}{e\left(2m^*k_BT\right)^{3/2}}\frac{(2r+\frac{3}{2})}{(r+\frac{3}{2})^2}\frac{F_{2r+1/2}(\eta)}{\left(F_{r+1/2}(\eta)\right)^2}e\frac{4\pi\left(2m^*k_BT\right)^{3/2}}{h^3}F_{1/2}(\eta)$$

$$r_H = \frac{3}{2}\frac{\left(2r+\frac{3}{2}\right)}{\left(r+\frac{3}{2}\right)^2}\frac{F_{2r+1/2}(\eta)F_{1/2}(\eta)}{\left(F_{r+1/2}(\eta)\right)^2} \qquad \text{(Eq. A.11)}$$

5. Drift mobility μ_d

$$\mu_d = \frac{v_d}{E} = \frac{\sigma}{-ne} = \frac{e\tau}{m^*}$$

$$\mu_d = \frac{\frac{2\sqrt{2m^*}e^2}{3\pi^2\hbar^3}\tau_0(r+\frac{3}{2})\left(k_BT\right)^{r+3/2}F_{r+1/2}(\eta)}{-e\frac{4\pi\left(2m^*k_BT\right)^{3/2}}{h^3}F_{1/2}(\eta)}$$

$$\mu_d = -(r+\frac{3}{2})\frac{2e\tau_0}{3m^*}\left(k_BT\right)^r\frac{F_{r+1/2}(\eta)}{F_{1/2}(\eta)} \qquad \text{(Eq. A.12)}$$

When r=0, $\mu_d = \frac{e\tau_0}{m^*}$ which is independent of energy.

6. Hall carrier concentration n_H

$$n_H = \frac{n}{r_H} = \frac{\frac{4\pi\left(2m^*k_BT\right)^{3/2}}{h^3}F_{1/2}(\eta)}{\frac{3}{2}\frac{\left(2r+\frac{3}{2}\right)}{\left(r+\frac{3}{2}\right)^2}\frac{F_{2r+1/2}(\eta)F_{1/2}(\eta)}{\left(F_{r+1/2}(\eta)\right)^2}} = \frac{8\pi\left(2m^*k_BT\right)^{3/2}}{3h^3}\frac{\left(r+\frac{3}{2}\right)^2}{\left(2r+\frac{3}{2}\right)}\frac{\left(F_{r+1/2}(\eta)\right)^2}{F_{2r+1/2}(\eta)} \qquad \text{(Eq. A.13)}$$

7. Hall Mobility μ_H

$$\mu_H = \frac{\sigma}{-n_He} = r_H\mu_d$$

$$\mu_H = -\frac{3}{2}\frac{\left(2r+\frac{3}{2}\right)}{\left(r+\frac{3}{2}\right)^2}\frac{F_{2r+1/2}(\eta)F_{1/2}(\eta)}{\left(F_{r+1/2}(\eta)\right)^2}\left(r+\frac{3}{2}\right)\frac{2e\tau_0}{3m^*}(k_BT)^r\frac{F_{r+1/2}(\eta)}{F_{1/2}(\eta)} \tag{Eq. A.14}$$

$$\mu_H = -\frac{e\tau_0}{m^*}(k_BT)^r\frac{\left(2r+\frac{3}{2}\right)}{\left(r+\frac{3}{2}\right)}\frac{F_{2r+1/2}(\eta)}{F_{r+1/2}(\eta)}$$

8. Seebeck coefficient

Since Seebeck coefficient is measured when there is no current, we have j=0.

The driving force for Seebeck effect is $-\nabla\zeta$ and the definition of Seebeck is $S=\frac{-\nabla\zeta}{-e\nabla T}$

$$j = -\int_0^\infty evg(\varepsilon)(-\tau)\left(\left(\frac{\partial f_0}{\partial k}\right)\left(\frac{\partial k}{\partial t}\right)+\left(\frac{\partial f_0}{\partial r}\right)\left(\frac{\partial r}{\partial t}\right)\right)d\varepsilon = 0$$

$$j = \int_0^\infty evg(\varepsilon)\tau\left(\frac{\partial f_0}{\partial \varepsilon}\hbar v\frac{-\nabla\varsigma}{\hbar}+\left(\frac{\partial f_0}{\partial r}\right)\left(\frac{\partial r}{\partial t}\right)\right)d\varepsilon$$

$$\left(\frac{\partial f_0}{\partial r}\right)\left(\frac{\partial r}{\partial t}\right)=\left(\frac{\partial f_0}{\partial \varepsilon}\right)\left(\frac{\partial \varepsilon}{\partial T}\right)\left(\frac{\partial T}{\partial r}\right)\left(\frac{\partial r}{\partial t}\right)=\left(\frac{\partial f_0}{\partial \varepsilon}\right)\frac{\left(\frac{\partial f_0}{\partial T}\right)}{\left(\frac{\partial f_0}{\partial \varepsilon}\right)}(\nabla T)v$$

$$\left(\frac{\partial f_0}{\partial r}\right)\left(\frac{\partial r}{\partial t}\right)=\left(\frac{\partial f_0}{\partial \varepsilon}\right)\left(-\frac{\varepsilon-\varsigma}{T}\right)(\nabla T)v$$

$$j = \int_0^\infty ev^2\tau g(\varepsilon)\left(\frac{\partial f_0}{\partial \varepsilon}\right)\left(-\nabla\varsigma+\left(-\frac{\varepsilon-\varsigma}{T}\right)(\nabla T)\right)d\varepsilon = 0$$

$$S = \frac{-\nabla\varsigma}{-e\nabla T} = -\frac{\int_0^\infty ev^2\tau g(\varepsilon)\left(\frac{\partial f_0}{\partial \varepsilon}\right)\left(\frac{\varepsilon-\varsigma}{T}\right)\nabla T\,d\varepsilon}{e\int_0^\infty ev^2\tau g(\varepsilon)\left(\frac{\partial f_0}{\partial \varepsilon}\right)\nabla T\,d\varepsilon}$$

$$S = -\frac{1}{e\sigma T}\left(\int_0^\infty e^2v^2\tau g(\varepsilon)\left(\frac{\partial f_0}{\partial \varepsilon}\right)(\varepsilon-\varsigma)\,d\varepsilon\right)$$

$$S=\frac{\sigma\varsigma}{e\sigma T}-\frac{\int_0^{\infty} e^2v^2\tau g(\varepsilon)\left(\frac{\partial f_0}{\partial\varepsilon}\right)\varepsilon\, dE}{e\sigma T}$$

$$=\frac{k_B}{e}\left(\eta-\frac{\frac{2e^2\sqrt{2m^*}}{3\pi^2\hbar^3}\tau_0(r+5/2)\left(k_BT\right)^{r+5/2}F_{r+3/2}\left(\eta\right)}{k_BT\frac{2e^2\sqrt{2m^*}}{3\pi^2\hbar^3}\tau_0(r+3/2)\left(k_BT\right)^{r+3/2}F_{r+1/2}\left(\eta\right)}\right)$$

$$S=\frac{k_B}{e}\left(\eta-\frac{\frac{2e^2\sqrt{2m^*}}{3\pi^2\hbar^3}\tau_0(r+5/2)\left(k_BT\right)^{r+5/2}F_{r+3/2}\left(\eta\right)}{k_BT\frac{2e^2\sqrt{2m^*}}{3\pi^2\hbar^3}\tau_0(r+3/2)\left(k_BT\right)^{r+3/2}F_{r+1/2}\left(\eta\right)}\right)$$

$$S=\frac{k_B}{e}\left(\eta-\frac{(r+5/2)F_{r+3/2}\left(\eta\right)}{(r+3/2)F_{r+1/2}\left(\eta\right)}\right) \tag{Eq. A.15}$$

9. Lorentz number L

Again the driving force is the -∇ζ and the electric current j is zero. The definition of thermal conductivity is defined by: $k=-\frac{w}{\nabla T}$

$$w=n\varepsilon v=\int_0^{\infty} v\varepsilon g(\varepsilon)\, f(\varepsilon)d\varepsilon$$

$$w=n\varepsilon v=\int_0^{\infty} v\varepsilon g(\varepsilon)\, f(\varepsilon)d\varepsilon=\int_0^{\infty} v\varepsilon g(\varepsilon)(\, f(\varepsilon)-\, f_0(\varepsilon))d\varepsilon$$

$$=\int_0^{\infty} v\varepsilon g(\varepsilon)(-\tau)\left(\left(\frac{\partial f_0}{\partial k}\right)\left(\frac{\partial k}{\partial t}\right)+\left(\frac{\partial f_0}{\partial r}\right)\left(\frac{\partial r}{\partial t}\right)\right)d\varepsilon$$

$$=\int_0^{\infty} v^2\varepsilon g(\varepsilon)(-\tau)\left(\frac{\partial f_0}{\partial\varepsilon}\right)\left(-\nabla\varsigma+\left(-\frac{\varepsilon-\varsigma}{T}\right)(\nabla T)\right)d\varepsilon$$

$$k=-\frac{w}{\nabla T}=\int_0^{\infty} v^2\varepsilon g(\varepsilon)\tau\left(\frac{\partial f_0}{\partial\varepsilon}\right)\left(-\nabla\varsigma\,/\,\nabla T+\left(-\frac{\varepsilon-\varsigma}{T}\right)\right)d\varepsilon$$

$$\frac{\nabla\varsigma}{\nabla T}=-\frac{\int_0^{\infty} v^2\tau g(\varepsilon)\left(\frac{\partial f_0}{\partial\varepsilon}\right)\left(\frac{\varepsilon-\varsigma}{T}\right)dE}{\int_0^{\infty} v^2\tau g(\varepsilon)\left(\frac{\partial f_0}{\partial\varepsilon}\right)dE}$$

$$k=\int_0^\infty v^2\varepsilon g(\varepsilon)\tau\left(\frac{\partial f_0}{\partial\varepsilon}\right)\left(\frac{\int_0^\infty v^2\tau g(\varepsilon)\left(\frac{\partial f_0}{\partial\varepsilon}\right)\left(\frac{\varepsilon-\varsigma}{T}\right)d\varepsilon}{\int_0^\infty v^2\tau g(\varepsilon)\left(\frac{\partial f_0}{\partial\varepsilon}\right)d\varepsilon}-\left(\frac{\varepsilon-\varsigma}{T}\right)\right)d\varepsilon$$

$$k=\int_0^\infty v^2\varepsilon g(\varepsilon)\tau\left(\frac{\partial f_0}{\partial\varepsilon}\right)\left(\frac{\int_0^\infty v^2\tau g(\varepsilon)\left(\frac{\partial f_0}{\partial\varepsilon}\right)\left(\frac{\varepsilon}{T}\right)d\varepsilon}{\int_0^\infty v^2\tau g(\varepsilon)\left(\frac{\partial f_0}{\partial\varepsilon}\right)d\varepsilon}-\left(\frac{\varepsilon}{T}\right)\right)d\varepsilon$$

$$k=\frac{1}{T}\left(\frac{\left(\int_0^\infty \varepsilon v^2\tau g(\varepsilon)\left(\frac{\partial f_0}{\partial\varepsilon}\right)d\varepsilon\right)^2}{\int_0^\infty v^2\tau g(\varepsilon)\left(\frac{\partial f_0}{\partial\varepsilon}\right)d\varepsilon}-\int_0^\infty \varepsilon^2 v^2\tau g(\varepsilon)\left(\frac{\partial f_0}{\partial\varepsilon}\right)d\varepsilon\right)$$

$$\sigma=\frac{j}{E}=-\int_0^\infty e^2v^2g(\varepsilon)\tau\left(\frac{\partial f_0}{\partial\varepsilon}\right)d\varepsilon$$

$$\sigma=\frac{2e^2\sqrt{2m^*}}{3\pi^2\hbar^3}\tau_0(r+3/2)\left(k_BT\right)^{r+3/2}F_{r+1/2}\left(\eta\right)$$

$$L=\frac{k}{\sigma T}=\frac{1}{T^2}\left(-\frac{\left(\int_0^\infty \varepsilon v^2\tau g(\varepsilon)\left(\frac{\partial f_0}{\partial\varepsilon}\right)d\varepsilon\right)^2}{\int_0^\infty v^2\tau g(\varepsilon)\left(\frac{\partial f_0}{\partial\varepsilon}\right)d\varepsilon\int_0^\infty e^2v^2g(\varepsilon)\tau\left(\frac{\partial f_0}{\partial\varepsilon}\right)d\varepsilon}+\frac{\int_0^\infty \varepsilon^2v^2\tau g(\varepsilon)\left(\frac{\partial f_0}{\partial\varepsilon}\right)d\varepsilon}{\int_0^\infty e^2v^2g(\varepsilon)\tau\left(\frac{\partial f_0}{\partial\varepsilon}\right)d\varepsilon}\right)$$

$$L=\frac{k}{\sigma T}=\frac{1}{e^2T^2}\left(-\frac{\left(\int_0^\infty \varepsilon v^2\tau g(\varepsilon)\left(\frac{\partial f_0}{\partial\varepsilon}\right)d\varepsilon\right)^2}{\int_0^\infty v^2\tau g(\varepsilon)\left(\frac{\partial f_0}{\partial\varepsilon}\right)d\varepsilon\int_0^\infty v^2g(\varepsilon)\tau\left(\frac{\partial f_0}{\partial\varepsilon}\right)d\varepsilon}+\frac{\int_0^\infty \varepsilon^2v^2\tau g(\varepsilon)\left(\frac{\partial f_0}{\partial\varepsilon}\right)d\varepsilon}{\int_0^\infty v^2g(\varepsilon)\tau\left(\frac{\partial f_0}{\partial\varepsilon}\right)d\varepsilon}\right)$$

Thus the Lorenz number can be written as:

$$L=\left(\frac{k_B}{e}\right)^2\left[\frac{r+7/2}{r+3/2}\times\frac{F_{r+5/2}(\eta)}{F_{r+1/2}(\eta)}-\left(\frac{r+5/2}{r+3/2}\right)^2\times\frac{F_{r+3/2}(\eta)^2}{F_{r+1/2}(\eta)^2}\right] \qquad \text{(Eq. A.16)}$$

Appendix B

TE properties from SPB model with acoustic phonon scattering

From Appendix A, the expressions for thermoelectric property such as electrical conductivity, Seebeck coefficient and thermal conductivity can be calculated with a single parabolic band model (Eq. A.9-A.16), since for skutterudites at room temperatures and above electrons are mostly scattered by acoustic phonons. The scattering time can be expressed by $\tau = \tau_0 \varepsilon^r$ where ε is energy (not reduced energy), and f or acoustic phonon scattering r = -1/2. We list the equations for TE properties from SPB model and acoustic phonon scattering below.

1. The chemical carrier density

$$n = \frac{4\pi(2m^* k_B T)^{3/2}}{h^3} F_{1/2}(\eta) \qquad \text{(Eq. B.1)}$$

2. The electrical conductivity

$$\sigma = -\frac{e^2}{3\pi^2 m^*}\left(\frac{2m^*}{\hbar^2}\right)^{3/2} \left(r+3/2\right)\tau_0\left(k_B T\right)^{r+3/2} F_{r+1/2}(\eta) \qquad \text{(Eq. A.9)}$$

$$\sigma = -\frac{e^2}{3\pi^2 m^*}\left(\frac{2m^*}{\hbar^2}\right)^{3/2} \tau_0\left(k_B T\right) F_0(\eta) \qquad \text{(Eq. B.2)}$$

3. Hall coefficient R_H

$$R_H = -\frac{3\pi^2\hbar^3}{e\left(2m^* k_B T\right)^{3/2}} \frac{(2r+\frac{3}{2})}{(r+\frac{3}{2})^2} \frac{F_{2r+1/2}(\eta)}{\left(F_{r+1/2}(\eta)\right)^2} \qquad \text{(Eq. A.10)}$$

$$R_H = -\frac{3\pi^2\hbar^3}{e\left(2m^* k_B T\right)^{3/2}} \frac{1}{2} \frac{F_{-1/2}(\eta)}{\left(F_0(\eta)\right)^2} \qquad \text{(Eq. B.3)}$$

4. Hall factor r_H

$$r_H = \frac{3}{2}\frac{\left(2r+\frac{3}{2}\right)}{\left(r+\frac{3}{2}\right)^2} \frac{F_{2r+1/2}(\eta)F_{1/2}(\eta)}{\left(F_{r+1/2}(\eta)\right)^2} \qquad \text{(Eq. A.11)}$$

$$r_H = \frac{3}{4}\frac{F_{-1/2}(\eta)F_{1/2}(\eta)}{\left(F_0(\eta)\right)^2} \qquad \text{(Eq. B.4)}$$

5. Drift mobility μ_d

$$\mu_d = -(r+\frac{3}{2})\frac{2e\tau_0}{3m^*}\left(k_B T\right)^r \frac{F_{r+1/2}\left(\eta\right)}{F_{1/2}\left(\eta\right)} \qquad \text{(Eq. A.12)}$$

$$\mu_d = -\frac{2e\tau_0}{3m^*}\left(k_B T\right)^{-1/2}\frac{F_0\left(\eta\right)}{F_{1/2}\left(\eta\right)} \qquad \text{(Eq. B.5)}$$

6. Hall carrier concentration n_H

$$n_H = \frac{n}{r_H} = \frac{8\pi\left(2m^* k_B T\right)^{3/2}}{3h^3}\frac{\left(r+\frac{3}{2}\right)^2}{\left(2r+\frac{3}{2}\right)}\frac{\left(F_{r+1/2}\left(\eta\right)\right)^2}{F_{2r+1/2}\left(\eta\right)} \qquad \text{(Eq. A.13)}$$

$$n_H = \frac{16\pi\left(2m^* k_B T\right)^{3/2}}{3h^3}\frac{\left(F_0\left(\eta\right)\right)^2}{F_{-1/2}\left(\eta\right)} \qquad \text{(Eq. B.6)}$$

7. Hall Mobility μ_H

$$\mu_H = -\frac{e\tau_0}{m^*}\left(k_B T\right)^r \frac{\left(2r+\frac{3}{2}\right)}{\left(r+\frac{3}{2}\right)}\frac{F_{2r+1/2}\left(\eta\right)}{F_{r+1/2}\left(\eta\right)} \qquad \text{(Eq. A.14)}$$

$$\mu_H = -\frac{e\tau_0}{m^*}\left(k_B T\right)^{-1/2}\frac{F_{-1/2}\left(\eta\right)}{2F_0\left(\eta\right)} \qquad \text{(Eq. B.7)}$$

8. Seebeck coefficient

$$S = \frac{k_B}{e}\left[\eta - \frac{(r+5/2)F_{r+3/2}(\eta)}{(r+3/2)F_{r+1/2}(\eta)}\right] \qquad \text{(Eq. A.15)}$$

$$S = \frac{k_B}{e}\left[\eta - \frac{2F_1(\eta)}{F_0(\eta)}\right] \qquad \text{(Eq. B.8)}$$

9. Lorentz number L

$$L = \left(\frac{k_B}{e}\right)^2\left[\frac{r+7/2}{r+3/2}\times\frac{F_{r+5/2}(\eta)}{F_{r+1/2}(\eta)} - \left(\frac{r+5/2}{r+3/2}\right)^2\times\frac{F_{r+3/2}(\eta)^2}{F_{r+1/2}(\eta)^2}\right] \qquad \text{(Eq. A.16)}$$

$$L = \left(\frac{k_B}{e}\right)^2\left[\frac{3F_2(\eta)}{F_0(\eta)} - \frac{4F_1(\eta)^2}{F_0(\eta)^2}\right] \qquad \text{(Eq. B.9)}$$

Appendix C

TE properties from SPB model in non-degenerate and degenerate limit

In a non-degenerate limit, the electrochemical potential $\eta = \frac{\varsigma}{k_B T}$ lies well within the forbidden gap well away from the appropriate band edge (η<<0). In order to neglect minority carriers, it should also be far away from the opposite band edge.

In non-degenerate limit, TE properties can be expressed in equations C.1-C.5.

$$F_n(\eta) = e^{\eta}\Gamma(n+1);\ \Gamma(n+1) = n\Gamma(n);\ \Gamma(\frac{1}{2}) = \sqrt{\pi}$$

$$n = \frac{4\pi(2m^* k_B T)^{3/2}}{h^3} e^{\eta} \frac{\sqrt{\pi}}{2} \quad \text{(Eq. C.1)}$$

$$\sigma = -\frac{e^2}{3\pi^2 m^*}\left(\frac{2m^*}{\hbar^2}\right)^{3/2} \tau_0 \left(k_B T\right)^{r+3/2} e^{\eta}\Gamma(r+\frac{5}{2}) \quad \text{(Eq. C.2)}$$

$$\mu_H = -\frac{e\tau_0}{m^*}(k_B T)^r \frac{\Gamma\left(2r+\frac{5}{2}\right)}{\Gamma\left(r+\frac{5}{2}\right)} \quad \text{(Eq. C.3)}$$

$$S = \frac{k_B}{e}\left[\eta - \frac{\Gamma(r+7/2)}{\Gamma(r+5/2)}\right] = \frac{k_B}{e}[\eta - (r+5/2)] \quad \text{(Eq. C.4)}$$

$$L = \left(\frac{k_B}{e}\right)^2\left[(r+7/2)(r+5/2) - (r+5/2)^2\right] = \left(\frac{k_B}{e}\right)^2 (r+5/2) \quad \text{(Eq. C.5)}$$

In a degenerate limit, the electrochemical potential $\eta = \frac{\varsigma}{k_B T}$ is way above the appropriate band edge and into the band (η>>0). The material is so heavily doped that it shows metallic behavior. In the non-degenerate limit, TE properties can be expressed in equations C.6-C.10.

$$F_n(\eta) = \frac{\eta^{n+1}}{n+1} + n\eta^{n-1}\frac{\pi^2}{6} + n(n-1)(n-2)\eta^{n-3}\frac{7\pi^4}{360} + \ldots$$

$$n = \frac{8\pi(2m^* k_B T)^{3/2}}{3h^3}\eta^{3/2} \quad \text{(Eq. C.6)}$$

$$\sigma = -\frac{e^2}{3\pi^2 m^+}\left(\frac{2m^*}{\hbar^2}\right)^{3/2} \tau_0 \left(k_B T\right)^{r+3/2} \eta^{r+3/2} \quad \text{(Eq. C.7)}$$

$$\mu_H \approx \mu_D = -\frac{e\tau_0}{m^*}(k_B T)^r \eta^r$$ (Eq. C.8)

$$S = \frac{k_B}{e}\left[\frac{-\frac{\pi^2}{3}\left(r+\frac{3}{2}\right)\eta^{r+\frac{1}{2}}}{\eta^{r+\frac{3}{2}}+\left(r+\frac{3}{2}\right)\left(r+\frac{1}{2}\right)\eta^{r-\frac{1}{2}}\frac{\pi^2}{6}}\right]$$ (Eq. C.9)

$$L = \left(\frac{k_B}{e}\right)^2\left[\frac{\frac{\pi^2}{3}\eta^{2r+3}-\frac{\pi^4}{18}\eta^{2r+1}\left(r+\frac{3}{2}\right)\left(r+\frac{5}{2}\right)}{\left(\eta^{r+3/2}+\left(r+\frac{3}{2}\right)\left(r+\frac{1}{2}\right)\eta^{r-1/2}\frac{\pi^2}{6}\right)^2}\right]$$

$$\kappa = -\frac{w}{\nabla T} = -\frac{\sum_i w_i}{\nabla T} = -\frac{\sum_i (S_i T J_i - \kappa_i \nabla T)}{\nabla T}$$

$$\kappa = \sum_i \kappa_i - \frac{\sum_i (S_i T \sigma_i (E - S_i \nabla T))}{\nabla T} = \sum_i \kappa_i - \sum_i \left(S_i T \sigma_i (\sum_i S_i - S_i) \right)$$ (Eq. C.10)

$$n_H = \frac{1}{eR_H} = \frac{e\left(\sum_i \sigma_i\right)^2}{\sum_i R_{H,i}\sigma_i^2} =$$

$$\mu_H = \frac{\sigma}{en_H} = \frac{\sum_i R_{H,i}\sigma_i^2}{\sigma}$$

$$\kappa = \kappa_1 + \kappa_2 + \frac{\sigma_1\sigma_2}{\sigma_1+\sigma_2}(S_2 - S_1)^2 T$$

when r=-1/2 (for acoustic phonon scattering),

$$S = -\frac{\pi^2 k_B}{3e}\frac{1}{\eta}$$ (Eq. C.11)

$$L \approx \frac{\pi^2}{3}\left(\frac{k_B}{e}\right)^2$$ (Eq. C.12)

Appendix D

TE properties from a multi-band model

For a multi-band system, the electric current density j_i and heat flux rate w_i for each band *i* can be represented as:

$$j_i = \sigma_i (E - S_i \nabla T) \qquad \text{(Eq. D.1)}$$

$$w_i = S_i T j_i - \kappa_i \nabla T \qquad \text{(Eq. D.2)}$$

In terms of electric conduction, $j = \sum_i j_i$ with $\nabla T = 0$, thus we get the expression for electrical conductivity for a multi-band system:

$$j = \sum_i j_i = \sum_i \sigma_i (E - S_i \nabla T) = \sum_i \sigma_i E = \sigma E$$

$$\sigma = \sum_i \sigma_i \qquad \text{(Eq. D.3)}$$

$$R_H = \frac{\sum_i R_{H,i} \sigma_i^2}{\sigma^2} \qquad \text{(Eq. D.4)}$$

$$n_H = \frac{1}{eR_H} = \frac{e\left(\sum_i \sigma_i\right)^2}{\sum_i R_{H,i} \sigma_i^2} \qquad \text{(Eq. D.5)}$$

$$\mu_H = \frac{\sigma}{en_H} = \frac{\sum_i R_{H,i} \sigma_i^2}{\sigma} \qquad \text{(Eq. D.6)}$$

For Seebeck coefficient and thermal conductivity, $j = \sum_i j_i = 0$

$$j = \sum_i j_i = \sum_i \sigma_i (E - S_i \nabla T) = E \sum_i \sigma_i - \nabla T \sum_i \sigma_i S_i = 0$$

$$S = \frac{E}{\nabla T} = \frac{\sum_i \sigma_i S_i}{\sum_i \sigma_i} \qquad \text{(Eq. D.7)}$$

$$j = \sum_i j_i = \sum_i \frac{w_i + \kappa_i \nabla T}{S_i T} = \frac{\prod_i S_i \left(\sum_i \frac{w_i}{S_i} + \nabla T \sum_i \frac{\kappa_i}{S_i} \right)}{T \prod_i S_i} = 0$$

$$\sum_i \frac{w_i}{S_i} + \nabla T \sum_i \frac{\kappa_i}{S_i} = 0$$

$$\kappa = -\frac{w}{\nabla T} = -\frac{\sum_i w_i}{\nabla T} = -\frac{\sum_i (S_i T j_i - \kappa_i \nabla T)}{\nabla T} \qquad \text{(Eq. D.8)}$$

$$\kappa = \sum_i \kappa_i - \frac{\sum_i (S_i T \sigma_i (E - S_i \nabla T))}{\nabla T} = \sum_i \kappa_i - \sum_i \left(S_i T \sigma_i (\sum_i S_i - S_i) \right)$$

For a two-band model, we get:

$$\kappa = \kappa_1 + \kappa_2 + \frac{\sigma_1 \sigma_2}{\sigma_1 + \sigma_2} \left(S_2 - S_1 \right)^2 T \qquad \text{(Eq. D.9)}$$

If 1 represents the electron band and 2 represents the valence band, then Eq. D.9 is just the thermal conductivity for a material with bipolar conduction term included.

Appendix E

Mott relation for SPB and SKB with acoustic phonon scattering

In Chapter 3, we have shown that the non-parabolic Kane band relation yields a decreasing Seebeck-dependent effective mass as carrier concentration increases. This is significant because it not only shows that the common explanation of Kane bands causing the increasing mass with doping in $CoSb_3$ is inadequate, but also this should have wider implications in terms of non-parabolicity's contribution to thermoelectric performance. The well-known Mott relation is [185]:

$$S = \frac{\pi^2 k_B^2 T}{3e} \frac{1}{\sigma_E} \frac{d\sigma_E}{dE} \qquad \text{Eq. E.1}$$

where $\sigma_\mathrm{E} = \frac{\mathrm{e}^2}{3} v(E)^2 \tau(\mathrm{E}) D(E)$ is the energy dependent electronic conductivity[186] that depends on the electron drift velocity (v), the scattering time (τ), and the density of states (D). Using the relationships given previously by Young *et al.*[83] we can show that:

$$v(E) = \frac{1}{\hbar}\frac{dE}{dk} = \sqrt{\frac{2}{m_0^*}} \left(\frac{d\gamma}{dE}\right)^{-1} \gamma^{1/2}$$

$$D(E) = \frac{\sqrt{2} {m_0^*}^{3/2}}{\pi^2 \hbar^3} \gamma^{1/2} \frac{d\gamma}{dE}$$

and $\tau = \tau_0 \gamma^{r-\frac{1}{2}} \left(\frac{d\gamma}{dE}\right)^{-1}$ where $\gamma(\mathrm{E}) = \frac{\hbar^2 \mathrm{k}^2}{2\mathrm{m}_0^*}$.

The Mott relation for a general band becomes:

$$S = \frac{2}{3} \frac{k_B^2 T}{e\hbar^2} \left(\frac{\pi}{3n}\right)^{2/3} m_0^* \frac{d\gamma}{dE} [r + 1 - \lambda] \qquad \text{Eq. E.2}$$

where $\lambda = 2\gamma \left(\frac{d\gamma}{dE}\right)^{-2} \frac{d^2\gamma}{dE^2}$ Eq. E.3

This expression (Eq.E.2) is derived by differentiating the obtained expression for $\sigma_E = \frac{2^{3/2} {m_0^*}^{1/2} e^2 \tau_0}{3\pi^2 \hbar^3} \left(\frac{d\gamma}{dE}\right)^{-2} \gamma^{r+1}$.

$$\frac{d\sigma_E}{dE} = \frac{2^{3/2} {m_0^*}^{1/2} e^2 \tau_0}{3\pi^2 \hbar^3} (\left(\frac{d\gamma}{dE}\right)^{-1} (r+1)\gamma^r - 2\left(\frac{d\gamma}{dE}\right)^{-3} \frac{d^2\gamma}{dE^2} \gamma^{r+1}) \qquad \text{Eq. E.4}$$

which upon substitution into the Mott equation (Eq. E.1) yields the energy dependent Seebeck relation:

$$S = \frac{\pi^2 k_B^2 T}{3e\gamma} \frac{d\gamma}{dE} \left(r + 1 - 2\gamma \left(\frac{d\gamma}{dE}\right)^{-2} \frac{d^2\gamma}{dE^2}\right) \qquad \text{Eq. E.5}$$

Next, we must first approximate the carrier concentration as a function of Fermi level: $n \approx \int_0^{E_F} D(E)dE = \frac{2^{\frac{3}{2}} m_0^{*\frac{3}{2}}}{3\pi^2\hbar^3}\gamma^{\frac{3}{2}}\Big|_{E=E_F}$ which can be solved for $\gamma(n) = \frac{\hbar^2}{2m_0^*}(3\pi^2 n)^{2/3}$ and substituted into Eq. E.5 to obtain the final expression (Eq. E.2).

In order to obtain the m_S^* that is presented in the main text for Kane band, we substitute $\gamma = E + E^2/E_g$ as is commonly used by Ravich *et al.* [187], $\frac{d\gamma}{dE} = 1 + 2E/E_g$, and $\frac{d^2\gamma}{dE^2} = 2/E_g$ into Eq. E.2. Upon substituting in λ (Eq. E.3) and simplifying, we obtain $m_S^*(E) = \frac{m_0^*}{1+2E/E_g}$ by inspection. It should be noted that this result only holds for *r*=0 (acoustic phonon scattering). Alternative scattering mechanisms can show increases in the energy dependent m_S^* [188].

While the derivation from the main text assumes a simpler scattering time where the matrix element coupling valence and conduction band state is independent of electron energy, Ravich *et al.* suggested an alternative form for the acoustic phonon scattering time that includes an energy dependent matrix element [187,189]. Upon simplification, the expression for the scattering time can be shown to be:

$$\tau(E) = \frac{3\hbar\, C_l N_v}{\pi k_B T D(E) E_{def}^2}\left(1+\frac{2E}{E_g}\right)^2\left(\left(1+\frac{2E}{E_g}\right)^2+2\right)^{-1} \qquad \text{Eq. E.6}$$

where $C_l = \rho v_l^2$ (v_l is the longitudinal speed of sound) and E_{def} is the acoustic phonon deformation potential. In this case, the equivalent Mott relation can be derived (using Eq. E.1 with the modified σ_E); we find the Seebeck effective mass simplifies to:

$$m_S^*(E) = \frac{3m_0^*\left(1+\frac{2E}{E_g}\right)}{\left(1+\frac{2E}{E_g}\right)^2+2} \qquad \text{Eq. E.7}$$

which also tends to decrease with energy at high Fermi levels, but initially shows a small increase (of only a few percent).

BIBLIOGRAPHY

1 Snyder, G. J. <http://www.thermoelectrics.caltech.edu/thermoelectrics/history.html> (

2 Vining, C. B. The thermoelectric limit zT = 1: Factor or artifact. *Proceedings of the 11th International Conference on Thermoelectrics*, 223-231 (1992).

3 Harman, T. C., Taylor, P. J., Walsh, M. P. & LaForge, B. E. Quantum Dot Superlattice Thermoelectric Materials and Devices. *Science* **297**, 2229-2232, doi:10.1126/science.1072886 (2002).

4 Snyder, G. J. & Toberer, E. S. Complex thermoelectric materials. *Nature materials* **7**, 105-114 (2008).

5 Morelli, D. *et al.* Low-temperature transport properties of p-type CoSb3. *Physical Review B* **51**, 9622-9628, doi:10.1103/PhysRevB.51.9622 (1995).

6 Caillat, T., Borshchevsky, A. & Fleurial, J. P. Properties of single crystalline semiconducting CoSb3. *Journal of Applied Physics* **80**, 4442, doi:10.1063/1.363405 (1996).

7 Caillat, T., Borshchevsky, A. & Fleurial, J.-P. Preparation and thermoelectric properties of p- and n-type CoSb3. **316**, 58-61, doi:10.1063/1.46835 (1994).

8 W. Jeitschko & Braun, D. LaFe4P12 with Filled CoAs3-Type Structure and lsotypic Lanthanoid-Transition Metal
Polyphosphides *Acta Cryst.* **33**, 3401-3406 (1977).

9 Arne, K. & Trond, R. Compounds with the Skutterudite Type Crystal Structure. 3. Structural Data for Arsenides and Antimonides. *Acta Chemica Scandinavica A* **28**, 99-103 (1974).

10 Slack, G. A. *CRC Handbook of Thermoelectrics*. 407 (CRC Press, 1995).

11 Pei, Y. Z. *et al.* Improving thermoelectric performance of caged compounds through light-element filling. *Applied Physics Letters* **95**, 042101, doi:10.1063/1.3182800 (2009).

12 Pei, Y. Z. *et al.* Synthesis and thermoelectric properties of K[sub y]Co[sub 4]Sb[sub 12]. *Applied Physics Letters* **89**, 221107, doi:10.1063/1.2397538 (2006).

13 Chen, L. D. *et al.* Anomalous barium filling fraction and n-type thermoelectric performance of Ba[sub y]Co[sub 4]Sb[sub 12]. *Journal of Applied Physics* **90**, 1864, doi:10.1063/1.1388162 (2001).

14 Park, K.-H. & Kim, I.-H. Thermoelectric Properties of Ca-Filled CoSb3-Based Skutterudites Synthesized by Mechanical Alloying. *Journal of Electronic Materials* **40**, 493-498, doi:10.1007/s11664-010-1400-4 (2010).

15 Bai, S. Q. *et al.* Thermoelectric properties of n-type Sr x M y Co4Sb12 (M=Yb, Ba) double-filled skutterudites. *Applied Physics A* **100**, 1109-1114, doi:10.1007/s00339-010-5711-3 (2010).

16 Qiu, Y. *et al.* Charge-Compensated Compound Defects in Ga-containing Thermoelectric Skutterudites. *Advanced Functional Materials* **23**, 3194-3203, doi:10.1002/adfm.201202571 (2013).

17 Tang, Y. *et al.* Phase diagram of In–Co–Sb system and thermoelectric properties of In-containing skutterudites. *Energy & Environmental Science* **7**, 812, doi:10.1039/c3ee43240h (2014).

18 G. S. Nolas, J. L. Cohn & Slack, G. A. Effect of partial void filling on the lattice thermal conductivity of skutterudites. *Physical Review B* **58**, 164-170 (1998).

19 Morelli, D. T., Meisner, G. P., Chen, B., Hu, S. & Uher, C. Cerium Filling and Doping of Cobalt Triantimonide. *Physical Review B* **56**, 7376-7383 (1997).

20 Tang, Y., Hanus, R., Chen, S. W. & Snyder, G. J. Solubility design leading to high figure of merit in low-cost Ce-CoSb3 skutterudites. *Nature communications* **6**, 7584, doi:10.1038/ncomms8584 (2015).

21 V. L. Kuznetsov, L. A. Kuznetsova & Rowe, D. M. Effect of partial void filling on the transport properties of NdxCo4Sb12 skutterudites. *J. phys.: Condens. Matter* **15**, 5035-5048 (2003).

22 Pei, Y. Z., Bai, S. Q., Zhao, X. Y., Zhang, W. & Chen, L. D. Thermoelectric properties of EuyCo4Sb12 filled skutterudites. *Solid State Sciences* **10**, 1422-1428, doi:10.1016/j.solidstatesciences.2008.01.016 (2008).

23 Tang, Y., Chen, S.-w. & Snyder, G. J. Temperature dependent solubility of Yb in Yb–CoSb3 skutterudite and its effect on preparation, optimization and lifetime of thermoelectrics. *Journal of Materiomics* **1**, 75-84, doi:10.1016/j.jmat.2015.03.008 (2015).

24 Yang, J. *et al.* Solubility study of Yb in n-type skutterudites YbxCo4Sb12 and their enhanced thermoelectric properties. *Physical Review B* **80**, 115329, doi:10.1103/PhysRevB.80.115329 (2009).

25 Rogl, G. *et al.* Nanostructuring of p- and n-type skutterudites reaching figures of merit of approximately 1.3 and 1.6, respectively. *Acta Materialia* **76**, 434-448, doi:10.1016/j.actamat.2014.05.051 (2014).

26 Rogl, G. *et al.* New bulk p-type skutterudites DD0.7Fe2.7Co1.3Sb12−xXx (X=Ge, Sn) reaching ZT>1.3. *Acta Materialia* **91**, 227-238, doi:10.1016/j.actamat.2015.03.008 (2015).

27 Meng, X. *et al.* Enhanced thermoelectric performance of p-type filled skutterudites via the coherency strain fields from spinodal decomposition. *Acta Materialia* **98**, 405-415, doi:10.1016/j.actamat.2015.07.027 (2015).

28 Meisner, G., Morelli, D., Hu, S., Yang, J. & Uher, C. Structure and lattice thermal conductivity of fractionally filled skutterudites: Solid solutions of Fully Filled and Unfilled End Members. *Physical Review Letters* **80**, 3551-3554 (1998).

29 Koza, M. M. *et al.* Breakdown of phonon glass paradigm in La- and Ce-filled Fe4Sb12 skutterudites. *Nature materials* **7**, 805-810, doi:10.1038/nmat2260 (2008).

30 Nolas, G. S., Fowler, G. & Yang, J. Assessing the role of filler atoms on the thermal conductivity of filled skutterudites. *Journal of Applied Physics* **100**, 043705, doi:10.1063/1.2245204 (2006).

31 Liu, W.-S., Zhang, B.-P., Li, J.-F. & Zhao, L.-D. Effects of Sb compensation on microstructure, thermoelectric properties and point defect of CoSb3 compound. *Journal of Physics D: Applied Physics* **40**, 6784-6790, doi:10.1088/0022-3727/40/21/044 (2007).

32 Liu, W.-S., Zhang, B.-P., Li, J.-F. & Zhao, L.-D. Thermoelectric property of fine-grained CoSb3 skutterudite compound fabricated by mechanical alloying and spark plasma sintering. *Journal of Physics D: Applied Physics* **40**, 566-572, doi:10.1088/0022-3727/40/2/035 (2007).

33 Sharp, J. W., Jones, E. C., Williams, R. K., Martin, P. M. & Sales, B. C. Thermoelectric properties of CoSb3 and related alloys. *Journal of Applied Physics* **78**, 1013, doi:10.1063/1.360402 (1995).

34 Su, T. *et al.* Fast Preparation and Low-Temperature Thermoelectric Properties of CoSb3. *Journal of Electronic Materials* **42**, 109-113, doi:10.1007/s11664-012-2259-3 (2012).

35 Mandrus, D. *et al.* Electronic transport in lightly doped CoSb3. *Physical Review B* **52**, 4926-4931, doi:10.1103/PhysRevB.52.4926 (1995).

36 Arushanov, E., Respaud, M., Rakoto, H., Broto, J. M. & Caillat, T. Shubnikov–de Haas oscillations in CoSb3 single crystals. *PHYSICAL REVIEW B* **61**, 4672 (2000).

37 Ctirad, U. in *Semiconductors and semimetals* Vol. 69 Ch. 5, (Academic Press, 2001).

38 Okamoto, H. Co-Sb. *J. Phase Equilib* **12**, 244-245 (1991).

39 LaLonde, A. D., Ikeda, T. & Snyder, G. J. Rapid consolidation of powdered materials by induction hot pressing. *The Review of scientific instruments* **82**, 025104, doi:10.1063/1.3534080 (2011).

40 Miller, M. K., Russell, K. F., Thompson, K., Alvis, R. & Larson, D. J. Review of Atom Probe FIB-Based Specimen Preparation Methods. *Microscopy and Microanalysis* **13**, 428-436, doi:10.1017/s1431927607070845 (2007).

41 Borup, K. A. *et al.* Measurement of the electrical resistivity and Hall coefficient at high temperatures. *The Review of scientific instruments* **83**, 123902, doi:10.1063/1.4770124 (2012).

42 Iwanaga, S., Toberer, E. S., LaLonde, A. & Snyder, G. J. A high temperature apparatus for measurement of the Seebeck coefficient. *The Review of scientific instruments* **82**, 063905, doi:10.1063/1.3601358 (2011).

43 Perdew, J. P., Burke, K. & Ernzerhof, M. Generalized Gradient Approximation Made Simple. *Phys Rev Lett* **77**, 3865-3868 (1996).

44 Giannozzi, P. *et al.* QUANTUM ESPRESSO: a modular and open-source software project for quantum simulations of materials. *Journal of Physics: Condensed Matter* **21**, 395502 (2009).

45 Sofo, J. O. & Mahan, G. D. Electronic structure of CoSb3: A narrow-band-gap semiconductor. *Phys Rev B* **58**, 15620-15623, doi:DOI 10.1103/PhysRevB.58.15620 (1998).

46 Agapito, L. A., Ferretti, A., Calzolari, A., Curtarolo, S. & Buongiorno Nardelli, M. Effective and accurate representation of extended Bloch states on finite Hilbert spaces. *Physical Review B* **88**, 165127 (2013).

47 WanT code by A. Ferretti, B. Bonferroni, A. Calzolari, and M. Buongiorno Nardelli, (http://www.wannier-transport.org)

48 Kokalj, A. Computer graphics and graphical user interfaces as tools in simulations of matter at the atomic scale. *Computational Materials Science* **28**, 155-168, doi:http://dx.doi.org/10.1016/S0927-0256(03)00104-6 (2003).

49 Tang, Y. *et al.* Convergence of multi-valley bands as the electronic origin of high thermoelectric performance in CoSb3 skutterudites. *Nature materials* **advance online publication**, doi:10.1038/nmat4430 http://www.nature.com/nmat/journal/vaop/ncurrent/abs/nmat4430.html - supplementary-information (2015).

50 Tang, Y., Chen, S. W. & Snyder, G. J. Temperature Dependent Solubility of Yb in Yb-CoSb$_3$ Skutterudite and its Effect on Preparation, Optimization and Lifetime of Thermoelectrics. *Journal of Materiomics* **1**, 74-83, doi:http://dx.doi.org/10.1016/j.jmat.2015.03.008 (2015).

51 Li, H., Tang, X., Zhang, Q. & Uher, C. High performance In[sub x]Ce[sub y]Co[sub 4]Sb[sub 12] thermoelectric materials with in situ forming nanostructured InSb phase. *Applied Physics Letters* **94**, 102114, doi:10.1063/1.3099804 (2009).

52 Rogl, G. *et al.* n-Type skutterudites (R,Ba,Yb)yCo4Sb12 (R=Sr, La, Mm, DD, SrMm, SrDD) approaching ZT≈2.0. *Acta Materialia* **63**, 30-43, doi:10.1016/j.actamat.2013.09.039 (2014).

53 Shi, X. *et al.* Multiple-filled skutterudites: high thermoelectric figure of merit through separately optimizing electrical and thermal transports. *Journal of the American Chemical Society* **133**, 7837-7846, doi:10.1021/ja111199y (2011).

54 Pei, Y. *et al.* Convergence of electronic bands for high performance bulk thermoelectrics. *Nature* **473**, 66-69, doi:10.1038/nature09996 (2011).

55 Zhao, L. D. *et al.* All-scale hierarchical thermoelectrics: MgTe in PbTe facilitates valence band convergence and suppresses bipolar thermal transport for high performance. *Energy & Environmental Science* **6**, 3346, doi:10.1039/c3ee42187b (2013).

56 Wang, H., Gibbs, Z. M., Takagiwa, Y. & Snyder, G. J. Tuning bands of PbSe for better thermoelectric efficiency. *Energ Environ Sci* **7**, 804-811, doi:10.1039/C3EE43438A (2014).

57 Liu, W. *et al.* Convergence of Conduction Bands as a Means of Enhancing Thermoelectric Performance of n-Type Mg2Si1-xSnx Solid Solutions. *Phys Rev Lett* **108**, 166601 (2012).

58 Parker, D., Chen, X. & Singh, D. J. High Three-Dimensional Thermoelectric Performance from Low-Dimensional Bands. *Phys Rev Lett* **110**, 146601 (2013).

59 Pei, Y., Wang, H. & Snyder, G. J. Band engineering of thermoelectric materials. *Advanced materials* **24**, 6125-6135, doi:10.1002/adma.201202919 (2012).

60 Singh, D. J. & Pickett, W. E. Skutterudite antimonides: Quasilinear bands and unusual transport. *Phys Rev B* **50**, 11235-11238 (1994).

61 Pei, Y., LaLonde, A. D., Wang, H. & Snyder, G. J. Low effective mass leading to high thermoelectric performance. *Energy & Environmental Science* **5**, 7963, doi:10.1039/c2ee21536e (2012).

62 Kuznetsov, V. L., Kuznetsova, L. A. & Rowe, D. M. Effect of partial void filling on the transport properties of NdxCo4Sb12 skutterudites. *Journal of Physics: Condens. Matter* **15**, 5035-5048 (2003).

63 Salvador, J. R., Yang, J., Wang, H. & Shi, X. Double-filled skutterudites of the type Yb[sub x]Ca[sub y]Co[sub 4]Sb[sub 12]: Synthesis and properties. *Journal of Applied Physics* **107**, 043705, doi:10.1063/1.3296186 (2010).

64 Anno, H., Matsubara, K., Notohara, Y., Sakakibara, T. & Tashiro, H. Effects of doping on the transport properties of CoSb3. *J Appl Phys* **86**, 3780-3786, doi:doi:http://dx.doi.org/10.1063/1.371287 (1999).

65 Dyck, J. S. *et al.* Thermoelectric properties of the n-type filled skutterudite Ba[sub 0.3]Co[sub 4]Sb[sub 12] doped with Ni. *Journal of Applied Physics* **91**, 3698, doi:10.1063/1.1450036 (2002).

66 Zhou, A., Liu, L.-s., Zhai, P.-c., Zhao, W.-y. & Zhang, Q.-j. Electronic Structures and Transport Properties of Single-Filled CoSb3. *Journal of Electronic Materials* **39**, 1832-1836, doi:10.1007/s11664-010-1073-z (2010).

67 Yang, J., Xi, L., Zhang, W., Chen, L. D. & Yang, J. Electrical Transport Properties of Filled CoSb3 Skutterudites: A Theoretical Study. *Journal of Electronic Materials* **38**, 1397-1401, doi:10.1007/s11664-009-0703-9 (2009).

68 Takagiwa, Y., Pei, Y. Z., Pomrehn, G. & Snyder, G. J. Validity of rigid band approximation of PbTe thermoelectric materials. *Apl Materials* **1**, 011101, doi:Artn 011101

Doi 10.1063/1.4809545 (2013).

69 Yang, J. *et al.* Solubility study of Yb in n-type skutterudites Yb_xCo4Sb12 and their enhanced thermoelectric properties. *Phys Rev B* **80**, 115329 (2009).

70 Liu, W.-S., Zhao, L.-D., Zhang, B.-P., Zhang, H.-L. & Li, J.-F. Enhanced thermoelectric property originating from additional carrier pocket in skutterudite compounds. *Appl Phys Lett* **93**, -, doi:doi:http://dx.doi.org/10.1063/1.2965123 (2008).

71 Nagamoto, Y., Tanaka, K. & Koyanagi, T. in *Thermoelectrics, 1998. Proceedings ICT 98. XVII International Conference on.* 302-305.

72 Kajikawa, Y. Refined analysis of the transport properties of Co1−xNixSb3 according to a model including a deep donor level and the second lowest valleys of the conduction band. *Journal of Alloys and Compounds* **621**, 170-178, doi:10.1016/j.jallcom.2014.09.173 (2015).

73 Chaput, L., Pécheur, P., Tobola, J. & Scherrer, H. Transport in doped skutterudites: Ab initio electronic structure calculations. *Physical Review B* **72**, doi:10.1103/PhysRevB.72.085126 (2005).

74 Gnutzman, U. & Clauseck, K. Theory of Direct Optical-Transitions in an Optical Indirect Semiconductor with a Superlattice Structure. *Appl Phys* **3**, 9-14 (1974).

75 Ackermann, J. & Wold, A. The preparation and characterization of the cobalt skutterudites CoP3, CoAs3 and CoSb3. *J Phys Chem Solids* **38**, 1013-1016, doi:http://dx.doi.org/10.1016/0022-3697(77)90203-7 (1977).

76 Kliche, G. & Lutz, H. D. Temperature dependence of the FIR reflection spectra of the skutterudites CoAs3 and CoSb3. *Infrared Phys* **24**, 171-177, doi:http://dx.doi.org/10.1016/0020-0891(84)90066-6 (1984).

77 Kane, E. O. Band Structure of Indium Antimonide. *J Phys Chem Solids* **1**, 249-261 (1957).

78 Smith, S. D., Moss, T. S. & Taylor, K. W. The energy-dependence of electron mass in indium antimonide determined from measurements of the infrared Faraday effect. *J Phys Chem Solids* **11**, 131-139, doi:http://dx.doi.org/10.1016/0022-3697(59)90051-4 (1959).

79 Cardona, M. Electron Effective Masses of InAs and GaAs as a Function of Temperature and Doping. *Physical Review* **121**, 752-758, doi:10.1103/PhysRev.121.752 (1961).

80 Dixon, J. R. & Riedl, H. R. Electric-Susceptibility Hole Mass of Lead Telluride. *Physical Review* **138**, A873-A881, doi:10.1103/PhysRev.138.A873 (1965).

81 Dionne, G. & Woolley, J. C. Optical Properties of Some Pb1-Xsnxte Alloys Determined from Infrared Plasma Reflectivity Measurements. *Phys Rev B* **6**, 3898-3913 (1972).

82 Harman, T. C. Galvano-thermomagnetic effects in semiconductors and semimetals—IV. mercury selenide. *J Phys Chem Solids* **25**, 931-940, doi:http://dx.doi.org/10.1016/0022-3697(64)90030-7 (1964).

83 Young, D. L., Coutts, T. J., Kaydanov, V. I., Gilmore, A. S. & Mulligan, W. P. Direct measurement of density-of-states effective mass and scattering parameter in transparent conducting oxides using second-order transport phenomena. *Journal of Vacuum Science & Technology A* **18**, 2978-2985, doi:doi:http://dx.doi.org/10.1116/1.1290372 (2000).

84 Pshenaĭ-Severin, D. A. & Fedorov, M. I. Effect of the band structure on the thermoelectric properties of a semiconductor. *Phys Solid State+* **49**, 1633-1637, doi:10.1134/S1063783407090053 (2007).

85 Callaway, J. Model for Lattice Thermal Conductivity at Low Temperatures. *Physical Review* **113**, 1046-1051, doi:10.1103/PhysRev.113.1046 (1959).

86 Holland, M. G. Analysis of Lattice Thermal Conductivity. *Physical Review* **132**, 2461-2471, doi:10.1103/PhysRev.132.2461 (1963).

87 Shannon. <http://abulafia.mt.ic.ac.uk/shannon/ptable.php> (

88 Xi, L., Zhang, W., Chen, L. & Yang, J. Filled skutterudites: from single to multiple filling. *Journal of the Korean Ceramic Society* **47**, 54-60 (2010).

89 Slack, G. A. & Tsoukala, V. G. Some properties of semiconducting IrSb3. *Journal of Applied Physics* **76**, 1665, doi:10.1063/1.357750 (1994).

90 Sergueev, I. *et al.* Quenching rattling modes in skutterudites with pressure. *Physical Review B* **91**, doi:10.1103/PhysRevB.91.224304 (2015).

91 Cao, D. *et al.* Evidence for rattling behavior of the filler atom(L)in the filled skutteruditesLT4X12(L=Ce,Eu,Yb;T=Fe,Ru;X=P,Sb)from EXAFS studies. *Physical Review B* **70**, doi:10.1103/PhysRevB.70.094109 (2004).

92 Feldman, J. L. *et al.* Lattice vibrations inLa(Ce)Fe4Sb12andCoSb3: Inelastic neutron scattering and theory. *Physical Review B* **73**, doi:10.1103/PhysRevB.73.014306 (2006).

93 Toberer, E. S., Zevalkink, A. & Snyder, G. J. Phonon engineering through crystal chemistry. *Journal of Materials Chemistry* **21**, 15843, doi:10.1039/c1jm11754h (2011).

94 Callaway, J. & von Baeyer, H. Effect of Point Imperfections on Lattice Thermal Conductivity. *Physical Review* **120**, 1149-1154, doi:10.1103/PhysRev.120.1149 (1960).

95 Klemens, P. Thermal Resistance due to Point Defects at High Temperatures. *Physical Review* **119**, 507-509, doi:10.1103/PhysRev.119.507 (1960).

96 Klemens, P. G. The scattering of low-frequency lattice waves by static imperfections. *Proc. Phys. Soc. A* **68**, 1113-1128 (1955).

97 Yang, J., Meisner, G. P. & Chen, L. Strain field fluctuation effects on lattice thermal conductivity of ZrNiSn-based thermoelectric compounds. *Applied Physics Letters* **85**, 1140, doi:10.1063/1.1783022 (2004).

98 Dudkin, L. D. & Abrikosov, N. K. *Zh. Neorg. Khim.* **2**, 212 (1957).

99 Stokes, K. L., Ehrlich, A. C. & Nolas, G. S. Thermal Conductivity of Fe-Doped Cosb3 Skutterudites. *MRS Proceedings* **545**, 339, doi:10.1557/PROC-545-339. (1998).

100 Anno, H., Matsubara, K., Notohara, Y., Sakakibara, T. & Tashiro, H. Effects of doping on the transport properties of CoSb[sub 3]. *Journal of Applied Physics* **86**, 3780, doi:10.1063/1.371287 (1999).

101 Yang, J. *et al.* Influence of electron-phonon interaction on the lattice thermal conductivity ofCo1−xNixSb3. *Physical Review B* **65**, doi:10.1103/PhysRevB.65.094115 (2002).

102 Pippard, A. B. On Ultrasonic attenuation in metals. *Philos. Mag.* **46**, 1104-1114 (1955).

103 Shi, X., Pei, Y., Snyder, G. J. & Chen, L. Optimized thermoelectric properties of Mo3Sb7−xTex with significant phonon scattering by electrons. *Energy & Environmental Science* **4**, 4086, doi:10.1039/c1ee01406d (2011).

104 Poujade, A. M. & Albany, H. J. Carrier-Concentration Dependence of Electron-Phonon Scattering in Te-Doped GaSb at Low Temperature. *Physical Review* **182**, 802-807, doi:10.1103/PhysRev.182.802 (1969).

105 Cahill, D., Watson, S. & Pohl, R. Lower limit to the thermal conductivity of disordered crystals. *Physical Review B* **46**, 6131-6140, doi:10.1103/PhysRevB.46.6131 (1992).

106 Okamoto, H. Co-Sb (Cobalt-Antimony). *J. Phase Equilib.* **12**, 244-245 (1991).

107 Okamoto, H. in *Binary Alloy Phase Diagrams* Vol. 2 (ed T. B. Massalski) Ch. 1261-1262, 2 (1990).

108 Okamoto, H. in *Binary Alloy Phase Diagrams* Vol. 3 (ed T. B. Massalski) 3317-3320 (1990).

109 Zhao, X. Y. *et al.* Synthesis of Yb[sub y]Co[sub 4]Sb[sub 12]/Yb[sub 2]O[sub 3] composites and their thermoelectric properties. *Applied Physics Letters* **89**, 092121, doi:10.1063/1.2345249 (2006).

110 Shi, X., Zhang, W., Chen, L. & Yang, J. Filling Fraction Limit for Intrinsic Voids in Crystals: Doping in Skutterudites. *Physical Review Letters* **95**, doi:10.1103/PhysRevLett.95.185503 (2005).

111 Harnwunggmoung, A., Kurosaki, K., Ohishi, Y., Muta, H. & Yamanaka, S. Effects of Tl-filling into the voids and Rh substitution for Co on the thermoelectric properties of CoSb3. *Journal of Alloys and Compounds* **509**, 1084-1089, doi:10.1016/j.jallcom.2010.09.207 (2011).

112 Mallik, R. C., Stiewe, C., Karpinski, G., Hassdorf, R. & Muller, E. Thermoelectric Properties of Co4Sb12 Skutterudite Materials with Partial In Filling and Excess In Additions. *Journal of Electronic Materials* **38**, 1337-1343, doi:10.1007/s11664-009-0663-0 (2009).

113 Harnwunggmoung, A. *et al.* Thermoelectric properties of Ga-added CoSb3 based skutterudites. *Journal of Applied Physics* **110**, 5, doi:10.1063/1.3606417 (2011).

114 Visnow, E. *et al.* On the True Indium Content of In-Filled Skutterudites. *Inorganic chemistry* **54**, 7818-7827, doi:10.1021/acs.inorgchem.5b00799 (2015).

115 Zhao, W. *et al.* Multi-localization transport behaviour in bulk thermoelectric materials. *Nature communications* **6**, 6197, doi:10.1038/ncomms7197 (2015).

116 Xiong, Z., Chen, X., Huang, X., Bai, S. & Chen, L. High thermoelectric performance of Yb0.26Co4Sb12/yGaSb nanocomposites originating from scattering electrons of low energy. *Acta Materialia* **58**, 3995-4002, doi:10.1016/j.actamat.2010.03.025 (2010).

117 Sesselmann, A., Dasgupta, T., Kelm, K. & Muller, E. Transport properties and microstructure of indium-added cobalt–antimony-based skutterudites. *J. Mater. Res.* **26**, 1820-1826, doi:10.1557/jmr.2011.102 (2011).

118 Jaworski, C. M., Tobola, J., Levin, E. M., Schmidt-Rohr, K. & Heremans, J. P. Antimony as an amphoteric dopant in lead telluride. *Physical Review B* **80**, doi:10.1103/PhysRevB.80.125208 (2009).

119 Grytsiv, A., Rogl, P., Michor, H., Bauer, E. & Giester, G. In y Co4Sb12 Skutterudite: Phase Equilibria and Crystal Structure. *Journal of Electronic Materials* **42**, 2940-2952, doi:10.1007/s11664-013-2679-8 (2013).

120 Pomrehn, G. S., Toberer, E. S., Snyder, G. J. & van de Walle, A. Entropic stabilization and retrograde solubility in Zn4Sb3. *Physical Review B* **83**, doi:10.1103/PhysRevB.83.094106 (2011).

121 Ikeda, T., Ravi, V. & Snyder, G. Formation of Sb2Te3 Widmanstätten precipitates in thermoelectric PbTe. *Acta Materialia* **57**, 666-672, doi:10.1016/j.actamat.2008.10.005 (2009).

122 GRAFF, J. *et al.* High-Temperature Thermoelectric Properties of Co4Sb12-Based Skutterudites with Multiple Filler Atoms: Ce0.1InxYbyCo4Sb12. *Journal of ELECTRONIC MATERIALS* **40**, 696-701, doi:10.1007/s11664-011-1514-3 (2011).

123 Ballikaya, S., Uzar, N., Yildirim, S., Salvador, J. R. & Uher, C. High thermoelectric performance of In, Yb, Ce multiple filled CoSb3 based skutterudite compounds. *Journal of Solid State Chemistry* **193**, 31-35, doi:10.1016/j.jssc.2012.03.029 (2012).

124 Zhao, W. *et al.* Enhanced Thermoelectric Performance in Barium and Indium Double-Filled Skutterudite Bulk Materials via Orbital Hybridization Induced by Indium Filler. *J. AM. CHEM. SOC.* **131**, 3713-3720 (2009).

125 Zhao, W. Y. *et al.* Synthesis and high temperature transport properties of barium and indium double-filled skutterudites BaxInyCo4Sb12−z. *JOURNAL OF APPLIED PHYSICS* **102**, 6, doi:10.1063/1.2821364 (2007).

126 Peng, J. Y. *et al.* Thermoelectric properties of (In,Yb) double-filled CoSb3 skutterudite. *JOURNAL OF APPLIED PHYSICS* **104**, 5, doi:10.1063/1.2975184 (2008).

127 Peng, J. *et al.* High temperature thermoelectric properties of double-filled InxYbyCo4Sb12 skutterudites. *JOURNAL OF APPLIED PHYSICS* **105**, 5, doi:10.1063/1.3116151 (2009).

128 Toberer, E. S., May, A. F. & Snyder, G. J. Zintl Chemistry for Designing High Efficiency Thermoelectric Materials. *Chem. Mater.* **22**, 624-634, doi:10.1021/cm901956r (2010).

129 Pomrehn, G. S., Zevalkink, A., Zeier, W. G., van de Walle, A. & Snyder, G. J. Defect-Controlled Electronic Properties in AZn2Sb2 Zintl Phases. *Angew. Chem. Int. Ed.* **53**, 3422-3426, doi:10.1002/anie (2014).

130 Xi, L. *et al.* Complex doping of group 13 elements In and Ga in caged skutterudite CoSb3. *Acta Materialia* **85**, 112-121, doi:10.1016/j.actamat.2014.11.022 (2015).

131 He, T., Chen, J., Rosenfeld, H. D. & Subramanian, M. A. Thermoelectric Properties of Indium-Filled Skutterudites. *Chem. Mater.* **18**, 759-762 (2006).

132 DU, Y., CAI, K. F., CHEN, S., QIN, Z. & SHEN, S. Z. Investigation on Indium-Filled Skutterudite Materials Prepared by Combining Hydrothermal Synthesis and Hot

Pressing. *Journal of ELECTRONIC MATERIALS* **40**, 1215-1220, doi:10.1007/s11664-011-1603-3 (2011).

133 Mallik, R. C., Jung, J.-Y., Ur, S.-C. & Kim, I.-H. Thermoelectric Properties of InzCo4Sb12 Skutterudites. *METALS AND MATERIALS International* **14**, 223-228, doi:10.3365/met.mat.2008.04.223 (2008).

134 Meisner, G. P. in *Directions in Engine-Efficiency and Emissions Research.*

135 Nolas, G. S., Kaeser, M., Littleton, R. T. & Tritt, T. M. High figure of merit in partially filled ytterbium skutterudite materials. *Applied Physics Letters* **77**, 1855-1857, doi:10.1063/1.1311597 (2000).

136 Li, H., Tang, X., Zhang, Q. & Uher, C. Rapid preparation method of bulk nanostructured Yb[sub 0.3]Co[sub 4]Sb[sub 12+y] compounds and their improved thermoelectric performance. *Applied Physics Letters* **93**, 252109, doi:10.1063/1.3054158 (2008).

137 Mei, Z., Zhang, W., Chen, L. & Yang, J. Filling fraction limits for rare-earth atoms in CoSb3: An ab initio approach. *Physical Review B* **74**, doi:10.1103/PhysRevB.74.153202 (2006).

138 Shi, X., Zhang, W., Chen, L. D., Yang, J. & Uher, C. Thermodynamic analysis of the filling fraction limits for impurities in CoSb3 based on ab initio calculations. *Acta Materialia* **56**, 1733-1740, doi:10.1016/j.actamat.2007.12.012 (2008).

139 Dilley, N. R., Bauer, E. D., Maple, M. B. & Sales, B. C. Thermoelectric properties of chemically substituted skutterudites Yb[sub y]Co[sub 4]Sn[sub x]Sb[sub 12−x]. *Journal of Applied Physics* **88**, 1948-1951, doi:10.1063/1.1305837 (2000).

140 Xia, X. *et al.* High-Temperature Oxidation Behavior of Filled Skutterudites Yb y Co4Sb12. *Journal of Electronic Materials* **41**, 2225-2231, doi:10.1007/s11664-012-2038-1 (2012).

141 Salvador, J. R. *et al.* Transport and mechanical properties of Yb-filled skutterudites. *Philosophical Magazine* **89**, 1517-1534, doi:10.1080/14786430903019099 (2009).

142 Lamberton, G. A., Tedstrom, R. H., Tritt, T. M. & Nolas, G. S. Thermoelectric properties of Yb-filled Ge-compensated CoSb[sub 3] skutterudite materials. *Journal of Applied Physics* **97**, 113715, doi:10.1063/1.1927702 (2005).

143 Vegard, L. Die Konstitution der Mischkristalle und die Raumfüllung der Atome. *Zeitschrift für Physik* **5**, 17-26 (1921).

144 Li, X. Y. *et al.* Thermoelectric properties of Te-doped CoSb[sub 3] by spark plasma sintering. *Journal of Applied Physics* **98**, 083702, doi:10.1063/1.2067704 (2005).

145 Wojciechowski, K. T., Toboła, J. & Leszczyński, J. Thermoelectric properties and electronic structure of CoSb3 doped with Se and Te. *Journal of Alloys and Compounds* **361**, 19-27, doi:10.1016/s0925-8388(03)00411-0 (2003).

146 Liu, W.-S., Zhang, B.-P., Li, J.-F., Zhang, H.-L. & Zhao, L.-D. Enhanced thermoelectric properties in CoSb[sub 3-x]Te[sub x] alloys prepared by mechanical alloying and spark plasma sintering. *Journal of Applied Physics* **102**, 103717, doi:10.1063/1.2815671 (2007).

147 Fairbanks, J. W. in *Directions in Engine-Efficiency and Emissions Research.*

148 Emsley, J. *Nature's Building Blocks: An A-Z Guide to the Elements.* New Edition 2011 edn, 120, 614 (Oxford University Press Inc., 2011).

149 *The Chinese Rare Earth Website*, <http://www.zg-xtw.com/> (2015).

150 Bai, S. *et al.* Enhanced Thermoelectric Performance of Dual-Element-Filled Skutterudites $Ba_xCe_yCo_4Sb_{12}$. *Acta Materialia* **57**, 3135-3139, doi:10.1016/j.actamat.2009.03.018 (2009).

151 Zhang, L. *et al.* Thermoelectric performance of mischmetal skutterudites MmyFe4−xCoxSb12 at elevated temperatures. *Journal of Alloys and Compounds* **490**, 19-25, doi:10.1016/j.jallcom.2009.10.033 (2010).

152 Liu, R., Qiu, P., Chen, X., Huang, X. & Chen, L. Composition optimization of p-type skutterudites CeyFexCo4−xSb12 and YbyFexCo4−xSb12. *Journal of Materials Research* **26**, 1813-1819, doi:10.1557/jmr.2011.85 (2011).

153 Tang, X., Zhang, Q., Chen, L., Goto, T. & Hirai, T. Synthesis and thermoelectric properties of p-type- and n-type-filled skutterudite R[sub y]M[sub x]Co[sub 4−x]Sb[sub 12](R:Ce,Ba,Y;M:Fe,Ni). *Journal of Applied Physics* **97**, 093712, doi:10.1063/1.1888048 (2005).

154 Chen, B. *et al.* Low-temperature transport properties of the filled skutterudites CeFe4-xCoxSb12. *Physical Review B* **55**, 1476-1480 (1997).

155 Nolas, G. S., Cohn, J. L. & Slack, G. A. Effect of partial void filling on the lattice thermal conductivity of skutterudites. *Physical Review B* **58**, 164-170 (1998).

156 Qiu, P. *et al.* Enhancement of thermoelectric performance in slightly charge-compensated CeyCo4Sb12 skutterudites. *Applied Physics Letters* **103**, 062103, doi:10.1063/1.4817720 (2013).

157 Shi, X. *et al.* Low thermal conductivity and high thermoelectric figure of merit in n-type Ba[sub x]Yb[sub y]Co[sub 4]Sb[sub 12] double-filled skutterudites. *Applied Physics Letters* **92**, 182101, doi:10.1063/1.2920210 (2008).

158 Uher, C. in *Semiconductors and Semimetals* Vol. 69 (ed T. M. Tritt) Ch. 5, 14-16 (Academic Press, 2000).

159 Luo, R. M., Liu, F. S., Li, J. Q. & Feng, X. W. The isothermal section of the Ce–Co–Sb ternary system at 400°C. *Journal of Alloys and Compounds* **471**, 60-63, doi:10.1016/j.jallcom.2008.03.061 (2009).

160 Gierlotka, W. *et al.* The Co-Sb-Ga system: isoplethal section and thermodynamic modeling. *Metallurgical and Materials Transactions* (2015).

161 Kim, Y.-J. *et al.* Three-Dimensional Atom-Probe Tomographic Analyses of Lead-Telluride Based Thermoelectric Materials. *Jom* **66**, 2288-2297, doi:10.1007/s11837-014-1155-0 (2014).

162 Ding, J. *et al.* Creation of Yb2O3 Nanoprecipitates Through an Oxidation Process in Bulk Yb-Filled Skutterudites. *Journal of Electronic Materials* **42**, 382-388, doi:10.1007/s11664-012-2370-5 (2013).

163 Kim, H.-S., Gibbs, Z. M., Tang, Y., Wang, H. & Snyder, G. J. Characterization of Lorenz number with Seebeck coefficient measurement. *APL Materials* **3**, 041506, doi:10.1063/1.4908244 (2015).

164 Aminorroaya-Yamini, S. *et al.* Rational Design of p-Type Thermoelectric PbTe: Temperature Dependent Sodium Solubility. *Journal of Materials Chemistry A* **1**, 8725-8730 (2013).

165 Vining, C. B. A model for the high-temperature transport properties of heavily doped n-type silicon-germanium alloys. *Journal of Applied Physics* **69**, 331-341, doi:10.1063/1.347717 (1991).

166 Pei, Y., May, A. F. & Snyder, G. J. Self-Tuning the Carrier Concentration of PbTe/Ag2Te Composites with Excess Ag for High Thermoelectric Performance. *Advanced Energy Materials* **1**, 291-296, doi:10.1002/aenm.201000072 (2011).

167 Heinz, N. A., Ikeda, T., Pei, Y. & Snyder, G. J. Applying Quantitative Microstructure Control in Advanced Functional Composites. *Advanced Functional Materials* **24**, 2135-2153, doi:10.1002/adfm.201302899 (2014).

168 Pearson, W. B. The crystal structures of semiconductors and a general valence rule. *Acta Crystallographica* **17**, 1-15, doi:10.1107/S0365110X64000019 (1964).

169 Dudkin, L. D. *Sov. Phys.-Tech. Physics* **3**, 216 (1958).

170 Nakagawa, H. *et al.* Thermoelectric Properties of CoSb3 prepared by copper mold quenching technique. *15th International Conference on Thermoelectrics* 117-121 (1996).

171 Ikeda, M. *et al.* Multiband Transport in CoSb3 Prepared by Rapid Solidification. *ZEITSCHRIFT FUR ANORGANISCHE UND ALLGEMEINE CHEMIE* **641**, 2020-2028, doi:10.1002/zaac.201500179 (2015).

172 Tang, X. F. *et al.* Effects of filling atoms Ba, Ce, Y and substituting atoms Fe, Ni on lattice thermal conductivity of RyMxCo4─xSb12. *Journal of Alloys and Compounds* **394**, 259-264, doi:10.1016/j.jallcom.2004.08.105 (2005).

173 Okamoto, H. Ce-Sb (Cerium-Antimony). *J. Phase Equilib.* **22**, 88 (2001).

174 Okamoto, H. in *Binary Alloy Phase Diagrams* Vol. 2 (ed T. B. Massalski) 1763-1767 (1990).

175 Su, X. & Tedenac, J.-C. Thermodynamic modeling of the ternary Ce-Fe-Sb system: assessment of the Ce-Sb and Ce-Fe systems. *CALPHAD: Comput. Coupling Phase Diagrams Thermochem.* **30**, 455-460 (2006).

176 Zhu, T., Fu, C., Xie, H., Liu, Y. & Zhao, X. High Efficiency Half-Heusler Thermoelectric Materials for Energy Harvesting. *Advanced Energy Materials*, n/a-n/a, doi:10.1002/aenm.201500588 (2015).

177 Amornpitoksuk, P., Li, H., Tedenac, J.-C., Fries, S. G. & Ravot, D. Experimental determination of phase equilibrium in the Fe–Co–Sb ternary system. *Intermetallics* **15**, 475-478, doi:10.1016/j.intermet.2006.07.004 (2007).

178 Geller, W. Das System Eisen-Kobalt-Antimon. *Arch. Eisenhuettenwes.* **13**, 263-266 (1939/40).

179 Li, J.-Q. *et al.* Solvothermal synthesis of nano-sized skutterudite Co4-x Fex Sb12 powders. *Materials Chemistry and Physics* **112**, 57-62, doi:10.1016/j.matchemphys.2008.05.017 (2008).

180 Chumak, I. V., Pavlyuk, V. V., Dmytriv, G. S. & Stepen' Damm, Y. Phase equilibria and crystal structure of compounds in the Fe - Zn - Sb system at 570 K. *Journal of Alloys and Compounds* **307** (2000).

181 Goldsmid, H. J. & Sharp, J. W. Estimation of the Thermal Band Gap of a Semiconductor from Seebeck Measurements. *Journal of Electronic Materials* **28**, 869-872 (1999).

182 Nolas, G. S., Sharp, J. W. & Goldsmid, H. J. *Thermoelectrics Basic Principles and New Materials Developments*. (Springer, 2001).

183 Ioffe, A. F. *Physics of Semiconductors*. (Academic Press Inc., 1960).

184 Fistul, V. I. *Heavily Doped Semiconductors*. (Plenum Press, 1969).

185 Heremans, J. P. *et al.* Enhancement of thermoelectric efficiency in PbTe by distortion of the electronic density of states. *Science* **321**, 554-557, doi:DOI 10.1126/science.1159725 (2008).

186 Mizutani, U. *Introduction to the electron theory of metals*. (Cambridge University Press, 2001).

187 Ravich, Y. I., Efimova, B. A. & Smirnov, I. A. *Semiconducting Lead Chalcogenides* Vol. 5 (Plenum Press, 1970).

188 Gibbs, Z. M. *Band Engineering in Thermoelectric Materials Using Optical, Electronic, and Ab-initio Computed Properties* PhD thesis, California Institute of Technology, (2015).

189 Wang, H., Pei, Y., LaLonde, A. D. & Snyder, G. J. Weak electron–phonon coupling contributing to high thermoelectric performance in n-type PbSe. *Proceedings of the National Academy of Sciences* **109**, 9705-9709, doi:10.1073/pnas.1111419109 (2012).